Geodätisch-geophysikalische Arbeiten in der Schweiz

(Fortsetzung der Publikationsreihe
«Astronomisch-geodätische Arbeiten in der Schweiz»)

herausgegeben von der

Schweizerischen Geodätischen Kommission
(Organ der Schweizerischen Akademie der Naturwissenschaften)

Siebenundfünfzigster Band
Volume 57

Astrometry and Satellite Orbits: Theoretical Considerations and Typical Applications

Urs Hugentobler

1998

Geodätisch-geophysikalische Arbeiten in der Schweiz

(Fortsetzung der Publikationsreihe
«Astronomisch-geodätische Arbeiten in der Schweiz»)

herausgegeben von der

Schweizerischen Geodätischen Kommission
(Organ der Schweizerischen Akademie der Naturwissenschaften)

Siebenundfünfzigster Band
Volume 57

Astrometry and Satellite Orbits: Theoretical Considerations and Typical Applications

Urs Hugentobler

1998

Adresse der Schweizerischen Geodätischen Kommission:

Institut für Geodäsie und Photogrammetrie
Eidg. Technische Hochschule Zürich
ETH Hönggerberg
CH-8093 Zürich, Switzerland

Redaktion des 57. Bandes:
Dr. U. Hugentobler, Dr. B. Bürki

Druck: Print-Atelier E. Zingg, Zürich

Vorwort

Die vorliegende Publikation von Herrn Dr. Hugentobler kann als Weiterführung der Arbeiten von Herrn Dr. Schildknecht (Geodätisch-geophysikalische Arbeiten in der Schweiz, Bd. 49) betrachtet werden. Herr Hugentobler fragt, wozu "heute" genaue Richtungsbeobachtungen überhaupt noch nutzen. Die Frage entbehrt nicht einer gewissen Brisanz, entspricht doch ein Fehler von 0.1" einer Richtungsbeobachtung bei einem 6'000 km entfernten Satelliten einem tangentialen Fehler von 3m. Vergleicht man diese Zahl mit dem Fehler von etwa einem Zentimeter einer LASER-Distanzbeobachtung zu Satelliten, scheint die Frage berechtigt. Dieses Argument führte Mitte der 70-er Jahre weltweit zum Verschwinden der Richtungsbeobachtungen aus der Satellitengeodäsie.

Die Untersuchungen von Herrn Hugentobler geben eine Reihe von Antworten auf diese zentrale Frage. In der Einleitung wird uns bewusst, dass bei passiven, kleinen Objekten in grosser Entfernung (z.B. im geostationären Gürtel) Richtungsbeobachtungen, wenn nicht die einzige, so doch bei weitem die zuverlässigste und genaueste Informationsquelle sind. Auch für Objekte des Planetensystems ist diese Aussage richtig.

Nach einer Übersicht über moderne CCD-Methoden wird eine weitere Antwort auf die zentrale Frage dieser Arbeit gegeben: Distanz- und Distanzdifferenzbeobachtungen, wie sie mit LASER-Beobachtungen von Satelliten oder bei der Beobachtung von Quasaren mit VLBI-Methoden gewonnen werden, sind erst in der Kombination quasi-gleichzeitiger Beobachtungen von mehreren weit auseinanderliegenden Stationen aussagekräftig. Bei der Bearbeitung von Richtungsbeobachtungen gelingt es hingegen, mit Beobachtungen von nur einer Station wichtige Resultate, z.B. genaue Bahnen, zu bestimmen.

Die erste Bahnbestimmung spielt in der Satellitengeodäsie im allgemeinen eine untergeordnete Rolle, besitzt man doch meistens für die wissenschaftlich interessierenden Objekte schon gute Näherungsbahnen. Anders sieht es aus, wenn man auch die Verteilung von "space-debris" studieren will. Es geht darum, ein Beobachtungs- und Auswertekonzept zu entwickeln, das der Entdeckung und Sicherung einer grossen Zahl passiver Objekte dient. Die Analyse geht weit über eine "rein akademische Übung" hinaus und enthält, neben wichtigen Algorithmen zur Bahnbestimmung, ein Beobachtungskonzept, das bei der ESA zur Anwendung kommen soll.

Von rein wissenschaftlichem Interesse ist die Analyse der Bahnstörungen von Satelliten, deren Umlaufzeiten "fast" kommensurabel mit der siderischen Rotationsperiode der Erde sind. Beispiele sind geostationäre Satelliten (1:1 Kommensurabilität) oder GPS-Satelliten (2:1 Kommensurabilität). Es zeigt sich, dass Richtungsbeobachtungen signifikant zur Bestimmung gewisser Terme des Gravitationspotentials der Erde und dessen zeitlicher Änderung beitragen können.

Schliesslich wird auch eindrücklich gezeigt, dass Richtungsbeobachtungen zur Kalibration anderer Beobachtungstechniken (im konkreten Fall eines Radarteleskops in Deutschland) verwendet werden können. Dieses abschliessende Kapitel weckt die Neugierde auf weitere ähnlich gelagerte Fragen: Was liesse sich beispielsweise aus der Kombination von Laser- und Richtungsbeobachtungen herausholen? Eine Frage, die in Zimmerwald mit dem neuen Teleskop bestimmt aktuell wird.

Herr Hugentobler hat mit dem vorliegenden Band einen weiteren wichtigen Meilenstein in der Weiterentwicklung von optischen Richtungsbeobachtungen gesetzt. Die Schweizerische Geodätische Kommission (SGK) dankt Herrn Hugentobler für seinen richtungsweisenden Beitrag. Die Schweiz. Akademie der Naturwissenschaften hat die Druckkosten für diesen Band übernommen, wofür die SGK ihren Dank ausspricht.

Prof. Dr. G. Beutler
Direktor des Astronomischen Instituts der Universität Bern

Direktor F. Jeanrichard
Bundesamt für Landestopographie
Vizepräsident der SGK

Prof. Dr. H.-G. Kahle
ETH Zürich
Präsident der SGK

Préface

La présente publication de Monsieur Hugentobler, dr ès sc., fait suite aux travaux de Monsieur Schildknecht, dr ès sc., parus dans le volume no 49 de la série "Geodätisch-geophysikalische Arbeiten in der Schweiz". La question de Monsieur Hugentobler "Les observations de directions ont-elles encore un sens aujourd'hui ?" est pertinente. En effet, une erreur de 0.1" d'une direction mesurée vers un satellite à 6'000 km de distance correspond à une erreur tangentielle de 3 m, tandis que la précision d'une distance mesurée par LASER est de l'ordre de grandeur du cm. On comprend dès lors pourquoi, dans les années septante, la géodésie par satellites a abandonné les mesures de directions.

Les recherches de Monsieur Hugentobler apportent une série de réponses à la question posée. Ainsi, dans l'introduction, on apprend que les observations de directions sont de loin les seules sources d'informations fiables, sinon les seules possibles, pour les petits objets passifs situés à de grandes distances (par exemple sur la ceinture géostationnaire). Cette affirmation est également valable pour les objets du système planétaire.

Après une récapitulation des méthodes modernes CCD, une nouvelle réponse est donnée à la question clef de cette étude: les distances ou les différences de distances obtenues par LASER pour les satellites ou par les méthodes VLBI pour les quasars, ne sont fiables que si les observations sont faites quasi simultanément à partir de stations très éloignées les unes des autres. Par contre, le traitement d'observations de directions à partir d'une seule station permet déjà d'obtenir des résultats importants, par exemple, les éléments exacts d'orbites.

La première détermination d'orbites ne joue pas un grand rôle en géodésie par satellites puisque l'on connaît en général de bonnes approximations pour tous les objets intéressants au point de vue scientifique. Par contre, il en va autrement si l'on veut déterminer la répartition de "débris spatiaux". Dans ce cas, il s'agit de développer une méthode d'observations et d'analyses permettant la découverte et la documentation d'un grand nombre d'objets passifs. Cette étude va bien au-delà d'un simple exercice académique et présente, à côté d'algorithmes très intéressants pour la déterminations des orbites, un concept d'observations qui sera appliqué par l'ESA.

L'analyse des perturbations d'orbites de satellites dont les révolutions sont presque commensurables avec la période de rotation sidérale de la terre, est très intéressante au point de vue scientifique. Par exemple, les satellites géostationnaires présentent une commensurabilité de 1:1 et les satellites GPS de 2:1. Il apparaît aussi que les observations de directions peuvent contribuer de façon significative à la détermination des termes du potentiel de gravité et de sa variation dans le temps.

Enfin, il apparaît que les observations de directions peuvent aussi servir à étalonner d'autres techniques d'observation (dans le cas concret, un télescope-radar en Allemagne). Ce dernier chapitre éveille également l'intérêt pour d'autres questions. Par exemple, que peut-on attendre de la combinaison de mesures de directions et de mesures de distances ? Question dont la réponse est d'actualité pour le nouveau télescope de Zimmerwald.

Avec cette étude, Monsieur Hugentobler a posé un jalon important du développement des observations optiques de directions. La Commission géodésique suisse remercie Monsieur Hugentobler d'avoir, par sa contribution, ouvert de nouvelles voies. Elle exprime sa reconnaissance à l'Académie suisse des sciences naturelles (ASSN) d'avoir pris les frais d'impression de ce volume à sa charge.

Prof. Dr. G. Beutler, Directeur
de l'Institut d' astronomie
de l'Université de Berne

F. Jeanrichard, Directeur
de l'Office fédéral de topographie
Vice-président de la CGS

Prof. Dr. H.-G. Kahle
ETH Zürich
Président de la CGS

Foreword

The publication by Dr. Urs Hugentobler may be viewed as a continuation of Dr. Schildknecht's work geodätisch-geophysikalische Arbeiten in der Schweiz, Vol. 49). "What is the scientific use of precise optical observations today?" is the central question addressed in this Volume. Keeping in mind that an error of 0.1 arcsec corresponds to a tangential error of about 3m for a satellite at a distance of about 6000km, the question is certainly justified -- in particular when compared to errors of about one centimeter routinely achieved by SLR (Satellite Laser Ranging). This argument led, by the way, to the "extinction" of optical observations in satellite geodesy in the mid-seventies.

Urs Hugentobler's analyses give a series of answers to this central question. The introduction makes us aware of the fact that optical observations are the most reliable and accurate source of information for small, passive, and remote objects like satellites or space debris in or near the geostationary belt. The same is of course true for objects in the planetary system.

After an overview of CCD-methods we are given a next answer to the central question of this work: Distance and distance difference observations, like those acquired by SLR or the observation of Quasars using VLBI (Very Long Baseline Interferometry), require (almost) simultaneous observations from several observatories. When processing optical observations, important results may already be extracted using the observations from only one station (satellite or debris orbits are one example).

First orbit determination is in general not a very important topic in satellite geodesy because usually, for objects of scientific interest, good a priori information is readily available. The situation changes when the distribution of space debris is in the center of interests. In this publication an observation and analysis concept for the detection of space debris is developed. This concept is not only of academic interest: It shall be used by the uropean Space Agency (ESA). In addition one can find sophisticated algorithms for first orbit determination.

The analysis of optical observations to satellites in deep resonance with Earth rotation (1:1 resonance for geostationary satellites, 2:1 resonance for GPS satellits) is fascinating. The author demonstrates that such observations may significantly contribute to the determination of certain terms (and their time development) of the earth's gravity potential.

Last but not least it emerges from Dr. Hugentobler's analysis that optical observations may be used to calibrate other observation techniques (in the particular case observations of a radar telescope in Germany). This analysis leads us to the question what might be achieved by combining accurate SLR and CCD observations? This question will certainly be dealt with using the new combined Zimmerwald SLR/CCD telescope in the future.

Dr. Hugentobler's work presents a milestone in the development of CCD-based optical observations. The Swiss Geodetic Commission (SGC) thanks Urs Hugentobler for his important contribution. Funds for printing this volume were provided by the Swiss Academy of Sciences, which is gratefully acknowledged by the SGC.

Prof. Dr. G. Beutler
Director of the Astronomical Institute, University of Berne

F. Jeanrichard
Federal Office of Topography
Vice President of SGC

Prof. Dr. H.-G. Kahle
ETH Zurich
President of SGC

Contents

Introduction

Since the beginning of the space age with the launch of Sputnik I on Oct. 4, 1957, astrometric observations of satellites played an important role for orbit determination and, initially, also geodetic research. In the earliest days even visual observations — carried out by amateurs within the 'moonwatch' program — and measurements with theodolites were useful for improving the models of the Earth's upper atmosphere and the geopotential. Optical astrometric observations, having a long tradition in fundamental astronomy, were frequently used between 1964 and 1975 for the establishment of regional, continental, and global geometrical networks. Already in 1958 the Smithsonian Astrophysical Observatory (SAO) operated a global network of 12 observatories equipped with Baker-Nunn cameras for satellite tracking (Veis, 1963).

In 1961 the first (passive) balloon satellite Echo I with a diameter of 30 m was launched and in 1964 Echo II (diameter 40 m) followed. The two satellites, designed for telecommunication experiments, with a visual magnitude up to about -1 mag, were widely used for geodetic purposes. In 1966 a dedicated geodetic balloon satellite, PAGEOS (Passive Geodetic Satellite) with a diameter of 30 m was put into orbit for spacial triangulation in the BC4 network consisting of 45 globally distributed stations of the National Geodetic Survey (NGS) and operated between 1966 and 1970 (Schmid, 1974).

Starting in 1962, with the launch of ANNA-1B, GEOS-1 (1965) and GEOS-2 (1968), *active* satellites were available for geodetic research. These satellites were able to generate series of intensive light flashes with a duration of about 1 msec.

Existing photographic camera systems were modified or specially designed for the measurement of high precision satellite positions relative to the stars. Large fields of view are common to all systems. Shutters or rotating blades 'chopped' the trails of the satellites and/or the stars allowing the time tagging of the positions. Depending on the mount of the camera, different observation concepts could be applied: With instruments mounted azimuthally (such as the BC4-Camera from Wild, Heerbrugg, Switzerland, which was used worldwide, in particular for the PAGEOS observations within the US NGS geometric satellite world network), tracking of satellites or stars was not possible. On the exposures both objects left trails which were chopped by shutters. Parallactically mounted instruments (e.g. the BMK camera of Carl Zeiss, Oberkochen, Germany) allowed tracking of the stars while the satellites generated trails on the photographic plates. Triaxially mounted instruments (such as the Baker-Nunn camera, primarily operated by the Smithsonian Astrophysical Observatory in its global network) allowed tracking a satellite by moving the instrument around a single axis.

Because of the time consuming processing and measuring of the photographic plates, astrometric methods for geodetic applications were gradually replaced by other techniques. Since the first artificial satellites were in orbit their telemetry data was used for orbit determination and improvement of the Earth's gravity model. Satellite-borne transponders allow distance measurements from the receiver to the satellite. The SECOR technique

(Sequential Collation of Ranges) was developed for geodetic applications and was first used with the satellite ANNA-1B (1962).

ANNA-1B was also the first satellite to carry a transmitter emitting radiowaves with stabilized frequencies for Doppler measurements. Initially Doppler measurements of geodetic satellites were used for orbit determination and for the improvement of the geopotential. The TRANSIT spacecraft of the Navy Navigation Satellite System (NNSS) were of particular importance. These satellites carried a stable radio beacon and were designed for navigation based on Doppler measurements. The first of these satellites were launched in 1960, and the system was operational until 1996. It was eventually replaced by the Global Positioning System (GPS) which became fully operational in 1994. Since about 1967 the TRANSIT Doppler system was eventually used for geodetic applications. Today the GPS navigation system is used worldwide for geodesy and the control of local and global networks. Due to the high temporal resolution and the reliability of geodetic GPS measurements these are of increasing importance also for geodynamic studies (see e.g. Beutler et al. (1996a)).

Shortly after the invention of the Laser by Maiman in 1960, Lasers were used for the measurement of distances to satellites. The first satellite equipped with Laser reflecting corner cubes, Explorer 22, was launched in 1964 and in the same year the first reflected Laser pulses were successfully detected at the NASA Goddard Space Flight Center (Plotkin et al., 1965). Today, Satellite Laser Ranging (SLR) is, together with satellite altimetry, the standard tool for the study of the geopotential as well as ocean and solid Earth tides. An increasing number of satellites is equipped with Laser retro-reflectors.

Optical observations of artificial satellites played an important role in the historical development of satellite geodesy, but due to the great effort necessary for acquiring and processing the observations based on photographic plates and due to their rather low accuracy, they were completely replaced by the new techniques for satellite tracking by the mid-seventies. The progress made in the development of position sensitive electronical sensors, in particular of the Charge Coupled Device (CCD), lead to a revival of optical observations of satellites in the last decade.

The observatory of the Astronomical Institute of the University in Berne (AIUB) in Zimmerwald has a long tradition in astrometry as well as in satellite tracking. Since the installation of the astronomical Schmidt camera (aperture 40 cm, focal length 104 cm) in 1959 and to this day astrometric positions of minor planets, comets, and supernovae have been measured on photographic plates. Since 1965 the Zimmerwald observatory has participated in programs for optical tracking of passive and active satellites, in particular in the WEST (West European Satellite Triangulation) project. Echo 1 and Echo 2, PAGEOS, Explorer 19, and Explorer 39 as well as GEOS 1 and GEOS 2 were observed photographically using the Schmidt camera. For this purpose a tilting plane-parallel glass plate in front of the plateholder was used for time tagging of the trails of passive satellites. The last observations of PAGEOS were made in 1974 in Zimmerwald.

In 1970 the first experiments of distance measurements to satellites with a ruby Laser

were performed using the astronomical Cassegrain telescope (aperture 60 cm, focal length 12.6 m) of the Zimmerwald observatory. Because the mount of the instrument did not allow tracking of the satellites the tests were not too successful. In 1975/76 a Satellite Laser Ranging Station was built adjacent to the astronomical observatory and routine SLR operations were made in Zimmerwald. In addition the Zimmerwald station participated in several TRANSIT campaigns. Since 1992 Zimmerwald also hosts a GPS permanent receiver.

First tests of optical observations of artificial satellites using a first generation photoelectric image intensifier and photographic film were performed in 1985 with the Cassegrain telescope. After these first experiences a CCD camera was mounted at the prime focus of the Zimmerwald SLR telescope in 1990 (Schildknecht, 1994). In 1995 the SLR telescope was replaced by a 1-meter combined Laser Ranging and Astrometry Telescope (ZIMLAT) (TELAS (1992), Gurtner et al. (1996)). The Coudé path of the instrument is used for SLR operations while the four ports on the Nasmyth platform are designed for optical satellite tracking and astrometry.

The driving idea for CCD astrometric observation of artificial satellites was proposed by Ivo Bauersima (1984), the so-called *Coupled Quasar, Satellite, and Star Positioning* (CQSSP). By observing artificial satellites together with reference stars a link can be established between different celestial reference frames: The orbits of geodetic or GPS satellites are known with high precision in the terrestrial reference frame, the orientation of which is well defined in the extragalactic reference frame, based on distant radio quasars, by Very Long Baseline Interferometry (VLBI). The CQSSP project proposes to observe such satellites together with reference stars with well defined coordinates in the celestial reference frame. Such observations allow an independent determination of the link between the extragalactic reference frame (defined by radio telescopes) and the celestial reference frame (defined by optical telescopes) by using the satellites as transfer objects (acting as 'moving quasars').

The CQSSP project is based on the fact that optical tracking of satellites is the only technique in satellite geodesy which directly accesses the inertial (or quasi-inertial) reference frame. Any satellite may be tracked optically as long as it is sunlit, therefore allowing a number of different applications of the technique. For instance resonant geopotential terms can be derived from observations of geostationary satellites; high precision orbit determination is used to support scientific missions; telemetry antennas may be calibrated and space debris in high altitude orbits monitored. In the present work some of these applications are addressed and studied in detail.

The instrumentation of the observatory in Zimmerwald and the observation technique used for precise astrometry of moving objects are presented in Chapter 1. A detailed review of the technique as well as a discussion of the error budgets of the new CCD measurement technique may be found in Schildknecht (1994). After a short review of the existing astrometric catalogues and of the reduction procedures to be used for artificial satellites we put the emphasis on the differences of the procedures for the astrometry of

satellites, minor planets, and stellar objects.

One application of optical observations is the survey of, or search for orbiting objects. Space debris represent a growing threat to space vehicles. This leads to an increasing interest on the part of the space agencies and commercial telecommunication companies in the space debris population. Low Earth orbits are accessible to survey Radars whereas optical sensors are more appropriate for surveys of objects in high Earth orbits. Algorithms for automatic detection of faint objects were developed at the AIUB for the 1-meter Zeiss telescope installed by the European Space Agency (ESA) in Tenerife for space debris observations (Schildknecht et al., 1995a). The algorithms are very well suited for the detection of slow moving objects in high orbits. Astrometry of moving objects leads to very precise results if the relative angular velocity of the objects with respect to the reference stars is small. All applications presented subsequently therefore deal with slow moving objects. In the last section of Chapter 1 orbital characteristics of slow moving satellites are summarized. Special attention is payed to geostationary orbits and geostationary transfer orbits.

After the detection of a moving object an initial orbit has to be determined in order to compute ephemerides for acquiring additional observations and to eventually identify the object. Three algorithms for initial orbit determination are presented in Chapter 2 and the accuracy of the determined orbits is assessed.

After acquiring observations in several nights for a given object an orbit improvement procedure may be invoked. In Chapter 3 the programs developed for orbit improvement and for the combination of observations from different satellites are presented. The accuracy of the determined osculating elements and the radiation pressure coefficients is discussed and the distribution of observations required for an optimum determination of orbit parameters is studied.

The determination of resonant geopotential terms is a fascinating application of the high precision orbit determination of geostationary satellites. The ellipticity of the Earth's equator causes a resonant librating motion of geostationary satellites which are in 1:1-resonance with Earth's rotation. The resonant geopotential terms C_{22} and S_{22} can therefore be determined using astrometric observations of small geostationary satellites (Catalano et al., 1983). In Chapter 4 the theory of resonance is developed for geostationary satellites as well as for GPS satellites, which are in deep 2:1-resonance with Earth's rotation. The pseudo-secular variations of the elements of GPS satellites are in good agreement with the values computed from theory.

Astrometric observations of Meteosat 4 and Meteosat 5 acquired in winter 1994/95 in Zimmerwald and covering a time interval of 111 days are presented in Chapter 5. All observations were used to determine the resonant geopotential terms C_{22} and S_{22}. The results indicate that astrometric observations of geostationary satellites are competitive with other methods for the determination of these coefficients.

Astrometric observations of geostationary satellites acquired in Zimmerwald are combined with Radar observations obtained at the 34 m-Radar dish antenna of the Forschungs-

gesellschaft für Angewandte Naturwissenschaften (FGAN) in Wachtberg-Werthhoven in Chapter 6. The orbital parameters determined using the different observation types are compared, and the magnitude of systematic biases in the Radar observations as well as the methods for their determination using optical observations are assessed.

A number of additional applications, including the precision necessary for the CQSSP project, remain to be studied. Combination of observations of different type or from different observatories represent the next logical step for fully exploiting the astrometric possibilities of the new 1-meter Zimmerwald Laser Ranging and Astrometry Telescope (ZIMLAT).

1 Astrometry of Artificial Satellites

1.1 Optical Observations and Reduction Methods

1.1.1 Instrumentation in Zimmerwald

Optical observations of artificial satellites are performed at the observatory of the Astronomical Institute of the University of Bern (AIUB) in Zimmerwald, some 8 km south of the city of Bern at an altitude of about 950 m above sea level. For this purpose the 0.5m SLR (Satellite Laser Ranging) telescope was used until its dismantling in May 1995. Most of the observations presented in this work were acquired with this 'old' telescope.

The telescope was in routine operation since 1975 contributing data to the NASA Crustal Dynamics Project (CDP) and other geodynamic projects mainly through SLR observations. For astrometric observations a CCD camera was mounted in the telescope's primary focus. The telescope had a primary mirror of 0.52 m diameter, a focal length of 1.0 m and was mounted on a computer-controlled alt-azimuthal mount.

The CCD camera (still in use today) is a product from Photometrics. The chip PM512 has 512 x 512 pixels with a quadratic size of 20 μm giving the camera in the prime focus of the old SLR telescope a field of view of 35 arcmin and a 'poor' mapping scale of 4.1"/pixel (for astrometric purposes). The camera is cooled thermoelectrically to $-45°$ with a secondary liquid cooling.

Since summer 1996 a new telescope has been installed in the observatory in Zimmerwald, the so-called Zimmerwald Combined Laser Ranging and Astrometric Telescope (ZIMLAT) (TELAS (1992), Gurtner et al. (1996)). It is a Ritchey-Chrétien telescope with an aperture of 1.0 m and a focal length of 10.3 m. The Coudé path of the alt-azimutally mounted instrument is used for SLR operations while CCD cameras for astrometric purposes are mounted on the derotated Nasmyth platform. Reductors are available for reducing the focal length to 4 m and to 8 m, respectively. The Photometrics CCD camera used with the old telescope is still in use together with an Astrocam camera with a EEV chip of 2048 x 2048 pixels with a size of 15 μm and two readout nodes. In the 4 m focus this camera has a field of view of 26 arcmin (37 arcmin diagonal) and a mapping scale of 0.77"/pixel. Both cameras are cooled thermoelectrically with a secondary liquid cooling.

1.1.2 Observation Technique for Fast Moving Objects with CCD

The technique developed and used at the AIUB for the measurement of astrometric positions of fast moving objects is described in detail in Schildknecht (1994) and in several papers (Schildknecht et al. (1992), Schildknecht et al. (1993), Schildknecht et al. (1996a), Hugentobler et al. (1995)). Therefore we confine ourselves to a brief overview of the technique in this section.

In the classical procedure for the astrometric measurement of astronomical objects the image of the object is measured on a photometric plate together with reference stars in its neighbourhood. Usually, about six reference stars are used; with their plate coordinates (in mm) the exact pointing direction of the telescope, the distortions of the photographic plate and the celestial coordinates of the object(s) of interest are computed using a conventional parameter estimation procedure (e.g., a least squares procedure).

At the observatory in Zimmerwald a CCD camera is used for the astrometric observation of artificial satellites. As in classical relative astrometry the satellite of interest is observed together with reference stars on the same exposure. The detector provides the frames containing the images of the satellite and of the stars in electronical form. The CCD coordinates of the satellite image and the reference star images are determined using object image recognition and centroiding algorithms (see Schildknecht et al. (1995a)) and the procedure of astrometric reduction gives the celestial coordinates of the satellite. In Figure 1.1 a CCD frame from the Zimmerwald instrument is shown which was acquired with fixed telescope and an exposure time of 3.2 seconds. It shows the four geostationary satellites Astra A – D as well as an unidentified, drifting object.

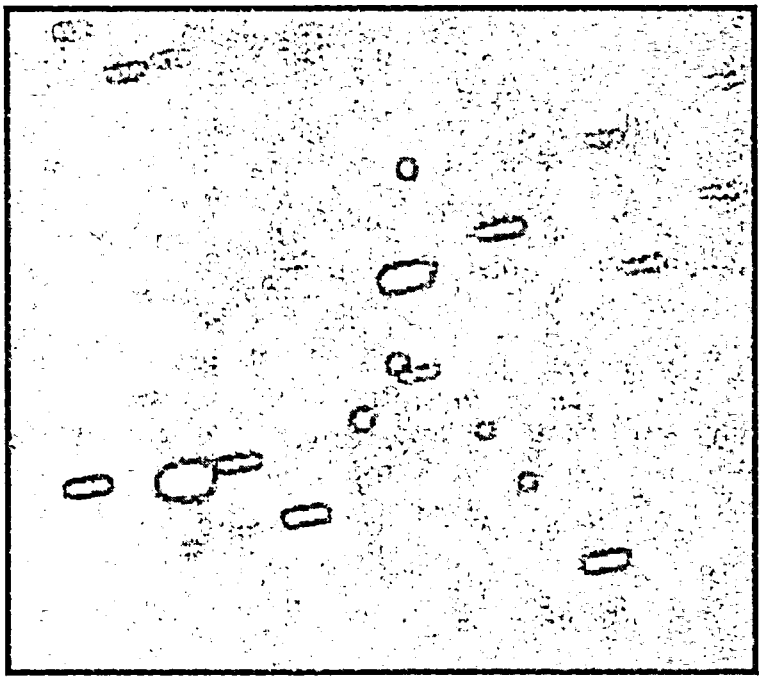

Figure 1.1: Five geostationary objects on one CCD frame covering a field of view of 17′ x 15′ (180 x 160 km in the geostationary ring): The four TV-satellites Astra A to D and an unidentified drifting object. The frame was acquired on Feb. 28, 1995 at the Zimmerwald observatory with fixed telescope and an exposure time of 3.2 seconds.

Due to the small field of view of the CCD detector the classical approach of astrometric measurement has to be adapted because in general only one reference star is in the field of view at a given instant of time: Satellite positions are measured on series of frames acquired whenever a reference star happens to have a close encounter with the satellite on the celestial sphere.

For the measurement of geostationary satellites a series of about 10 short exposed frames (exposure time of one second or less) is acquired with fixed telescope (drives off) during the close encounter. Because of the slow motion of a geostationary object in the Earth-fixed frame its image appears pointlike and at about the same place on all frames whereas the reference star moves across the field of view due to the Earth's rotation. A superposition of nine single frames documenting a close encounter of a reference star with the geostationary satellite Meteosat 5 is shown in Figure 1.2.

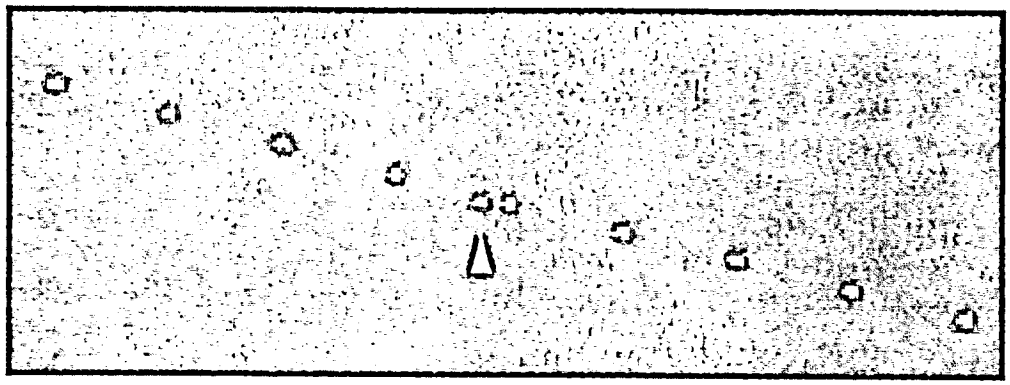

Figure 1.2: Close encounter of a reference star with the geostationary satellite Meteosat 5 (Arrow). The Figure was generated by superposition of nine single frames spaced by 8 seconds and exposed by 0.5 seconds each. The frame covers 16 arcmin. The frames were acquired in Zimmerwald on Aug. 16, 1994.

Knowing the angular velocity and the direction of the motion of the stars across the field of view due to the Earth's rotation it is possible to determine the mapping scale and the orientation of the camera. In addition the exact pointing direction of the optical axis of the telescope (realized through the coordinates of a selected pixel on the CCD chip) as well as the precise celestial coordinates of the satellite(s) may be calculated.

Usually several observation series within a given time interval (several hours up to one night) are reduced together if the mapping scale did not change (e.g. due to refocussing). In an iterative parameter estimation procedure

- the common mapping scale for all series,
- one camera orientation angle and one telescope pointing direction for each series, and
- one set of celestial coordinates for the satellite(s) for each frame

are determined together with rms errors and residuals for the measured object images. The result consists of about 10 sets of satellite coordinates for each close encounter.

In Figure 1.3 astrometric positions and their formal 1-sigma errors obtained from the astrometric reduction are given for the satellite Meteosat 5 observed in the night of Jan. 13/14, 1995 with the old SLR telescope in Zimmerwald. The rms errors are between 0.5" and 0.6" (1-sigma error in each coordinate). In the Figure showing hour angle vs. declination each cluster of points represents one or several close encounters with up to ten single measurements. In Figure 1.4 we magnify the first cluster of positions of 21:37 from Figure 1.3. The positions were measured during three close encounters with different reference stars within 15 minutes. The dotted line in both figures shows the best fitting orbit determined from astrometric measurements covering several nights. For details we refer to Chapter 5.

The observation technique as described above proved to be appropriate for geostationary objects as well as for high orbiting satellites such as GPS satellites or objects in a geostationary transfer orbit (GTO) at apogee. For a faint and not strictly geostationary satellite it might be necessary to track the object during the close encounter series in order to increase its signal-to-noise ratio. In this case a calibration series with fixed telescope has to be performed immediately before and/or after the astrometric measurement of the

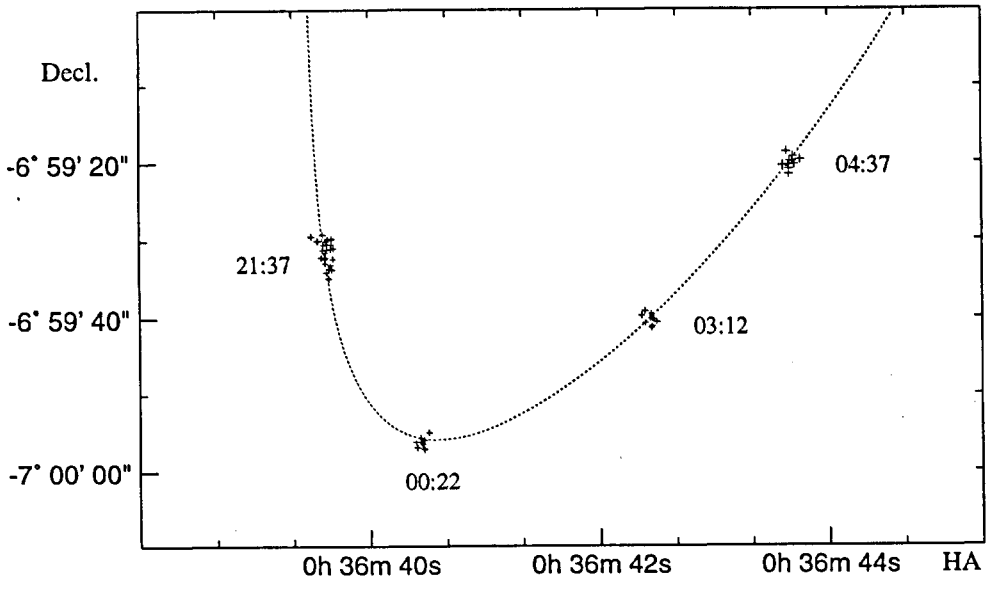

Figure 1.3: Reduced astrometric positions and their formal 1-sigma errors for Meteosat 5 observed in the night of Jan. 13/14, 1995 with the old SLR telescope in Zimmerwald (Hour angle (HA) vs. declination). Each cluster of positions is the result from one or more close encounter series. The dotted line represents the best fitting orbit (using observations from several nights, for details we refer to Chapter 5).

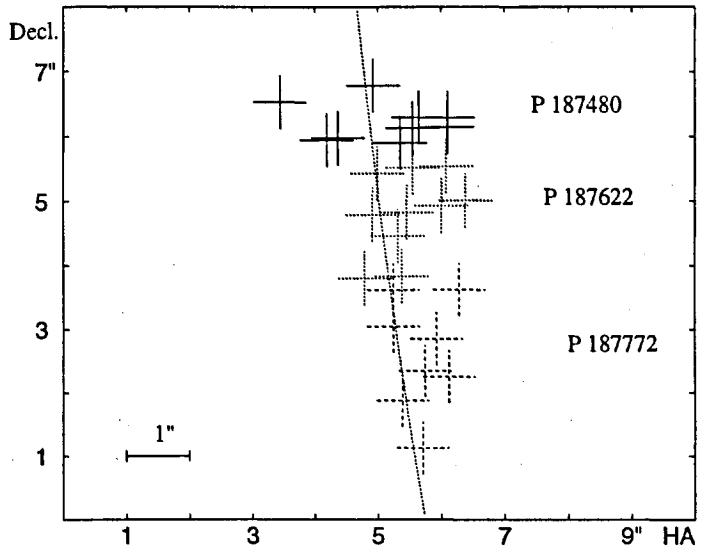

Figure 1.4: Enlarged view of the astrometric positions around 21:37 from Figure 1.3. Different symbols are used to distinguish positions measured during three close encounters series within 15 minutes. Each close encounter is labeled with the corresponding PPM reference star designation.

satellite (e.g. using the same reference star) for determining the mapping scale and the camera orientation.

The accuracy of the astrometric measurements is limited by the following three factors:

(1) The accuracy of the determination of the center of light for the object image on the CCD frame for not too faint objects — even for a simple 'center of mass' algorithm — is of the order of a tenth of a pixel (Verdun, 1993) because the object image is spread over several pixels. For a mapping scale of 4″/pixel (for the old telescope) the centroid accuracy is therefore about 0.4″ to 0.5″. For the new 1 m ZIMLAT telescope a centroiding accuracy of about 0.1″ is expected.

(2) The uncertainty in the mapping scale and in the orientation of the camera affects in particular observations with a large separation of satellite and reference star. The two parameters are determined with an accuracy corresponding to the centroiding accuracy reduced by a factor depending on the number of frames used for their determination. For observations with the old telescope the relative rms error for the scale is of the order of 10^{-4}, for the camera orientation the rms error is between 0.3′ and 3′.

(3) The astrometric accuracy depends directly on the accuracy of the catalogue positions of the reference stars used. For PPM stars an uncertainty of about 0.3″ has to be expected (Röser et al., 1991). As soon as the Hipparcos catalogue with stellar

positions with milliarcsecond accuracy (Kovalevsky et al., 1995) is available, the accuracy of astrometric positions will almost entirely be determined by the observation and measuring technique.

1.1.3 Astrometric Catalogues

FK5 The Fifth Fundamental Catalogue was compiled by the *Astronomisches Rechen-Institut Heidelberg* following a resolution adopted by the International Astronomical Union at its XV General Assembly in Sydney, 1973. The catalogue consists of two parts, the 1'535 fundamental stars of the FK5 Basic Catalogue (Fricke et al., 1988) and the 3'117 stars of the FK5 Extension (Fricke et al., 1991). The FK5 Basic Catalogue covers a magnitude range from −1.5 to +7.5 mag, the FK5 Extension covers the magnitude interval 4.5 to 9.5 mag. The mean rms errors in position and proper motion are about 0.02″ and 0.06″/century for the stars in the Basic Catalogue with declinations above −30° and 0.03″ and 0.11″/century for the stars with declinations below −30°. The mean rms errors for the stars in the FK5 Extension are about 0.06″ and 0.27″/century. The epochs of the observations lie in the interval between 1941 and 1958. The density of FK5 stars is about 0.1 stars per square degree.

PPM The astrometric catalogue 'Positions and Proper Motions (PPM)' (Röser et al., 1991) contains 384'866 stars of 6–11 mag in both hemispheres. The astrometric accuracy is of the order of 0.3″ in position and 0.43″/century in proper motion, 0.12″ and 0.24″/century for the high precision subset, and 0.05″ and 0.010″/century for the FK5 stars included into the catalogue. Systematic errors are estimated to be of the order of 0.05″ in position and 0.2″/century for proper motion. The catalogue is based on the FK5 system. The density is about 9 stars per square degree. Therefore, on average about every 2.5 minutes a PPM star passes closer than 5 arcmin to a geostationary satellite.

ACRS The catalogue of Astrometric Catalogue Reference Stars (ACRS) (Corbin et al., 1991) was compiled as a base for a new reduction of the Astrographic Catalogue (AC) plates. It is an all-sky catalogue based on the Second Cape Photographic Catalogue (CPC2) and the AGK3. It contains 320'211 stars (250'000 in Part 1, the stars with good observation history, and 70'159 in Part 2, the stars with bad observation history). Mean rms errors in proper motion are about 0.47″/century for the stars with good observation history (Part 1). The catalogue was compiled in the FK4 system and then transformed to the FK5 system. The average star density is 7.8 stars per square degree.

CMC The Carlsberg Meridian Catalogue (CMC) (CMC, 1984) contains at present 80'393 stars (volumes 1–8) in the declination range from −40° to +90°. It is compiled from observations acquired with the Carlsberg Automatic Meridian Circle on La Palma.

With the ongoing measuring program the density of available stars is still increasing. The accuracy of stellar positions ranges between 0.08" and 0.34" depending on the declination. Around the declination of $-7°$ for geostationary objects the accuracy is of the order of 0.2". Proper motions are accurate to 0.2 – 0.4"/century. The catalogue is based on the FK5 system. The average star density is 2.4 stars/deg^2.

Hipparcos The Hipparcos Catalogue is based on measurements collected by ESA's astrometric satellite HIPPARCOS (High Precision Parallax Collecting Satellite) between 1989 and 1993. The catalogue contains a total of 107'504 stars with mean standard errors of 1.2 mas in position and 1.7 mas/year in proper motion (Kovalevsky et al., 1995). The coordinates are linked to the extragalactic frame of Quasar sources. The bulk of the Hipparcos stars are in the magnitude interval from 8 mag to 10 mag. The star density is 2–7 stars per square degree. The catalogue will be published in April 1997.

Tycho The Tycho Catalogue is based on observations made with the star mapper slit system of the HIPPARCOS satellite and is nearing completion. The catalogue will contain 1'067'560 stars in the magnitude interval from 4.5–11.7 mag (Høg et al., 1995). The expected rms accuracy of the stars is 0.03" at magnitude 10.5 mag. The star density is 25 stars per square degree.

1.1.4 Reduction of Satellite Positions to Standard Coordinates

Because of the small field of view of a CCD camera at a telescope (35" for the old Zimmerwald instrument) it is in general not possible to determine the mapping parameters using a single frame. These parameters are therefore determined using series of frames. This process requires assumptions concerning the time variations of these parameters. The mapping parameters are assigned to different 'variability classes' depending on the time scale of variation: The camera orientation may be dependent on the pointing direction, if the mount model is not absorbing such a dependence; the mapping scale depends on the focus position which in turn is temperature dependent. These two parameters are 'quickly varying' parameters. They are determined for each close encounter series or for a group of encounter series.

Decentering, tilt terms and other higher order mapping terms may be constant over longer periods of time. They are determined using dedicated calibration sessions only once per night, once per week, or even less frequently, depending on the particular necessities. To be able to assume stability for these 'slowly varying' mapping terms it is essential that all distortions of the field stemming from known sources are modelled. It is, e.g., not possible to include distortions from differential refraction or aberration into the mapping model as in classical astrometry where a complete set of mapping parameters can be determined for each plate. It is therefore mandatory that the coordinates of the reference stars used for astrometric measurements are referred to the true topocentric system of

epoch. The coordinates of the satellites obtained from the astrometric reduction of the CCD coordinates are consequently in the same system.

For the purpose of orbit determination and improvement the satellite coordinates have to be in an inertial system such as J2000. When transforming the satellite coordinates from the system of date to the system J2000 care has to be taken to use the same algorithms which have been used for the computation of the apparent coordinates of the reference stars from standard coordinates. This is true in particular for refraction because refraction can only be modelled with limited accuracy. Using the same formula for the 'forward' and the 'backward' transformation eliminates the major part of the uncertainties.

The transformation of apparent coordinates of artificial satellites to standard coordinates (e.g. in the system J2000) is in several respects somewhat different from the transformation of coordinates for stars and minor planets. In Table 1.1 the individual transformation elements for the transformation between the apparent and the standard coordinate system are listed together with the influence on the coordinates of an object (a stellar object, a minor planet, an artificial Earth orbiting satellite) measured with respect to a reference star, given that the corresponding transformation element is neglected in both transformation directions, for the computation of the apparent position of the reference star and the back-transformation of the object's coordinates into the standard coordinate system.

Neglected Part of Transformation	Effect on Position of		
	Star	Minor planet	Satellite
Precession	rotation	rotation	rotation
Nutation	rotation	rotation	rotation
Annual aberration	differential	differential	total
Daily aberration	differential	differential	differential
Proper motion	total	total	total
Light travel time	no	total*	total*
Parallax	(total)	total*	total*
Light deflection	(differential)	(total)	(total)
Refraction	differential	differential	differential
Color refraction	total	total	total
Parallactic refraction	no	(total)	total*

Table 1.1: Effects of neglected parts of system transformations on the standard coordinates for different objects for differential astrometry (see text). Transformations marked with '*' are contained in the object's standard coordinates. They are taken into account during the orbit determination procedure.

Precession and Nutation

Because precession and nutation rotate the coordinate system, the relative position of the reference star and the program object is rotated with respect to the direction of sidereal motion. The coordinate components of a measured object are affected in a differential way if precession or nutation are neglected (i.e., the magnitude of the introduced position error depend on the distance to the reference object). Coordinates of all types of celestial objects are affected in a similar way. In addition, indirect effects may be caused when neglecting the precession: The coordinate argument for subsequent transformations may not be correct.

Aberration

The effect of aberration is a time and position dependent deformation of the coordinate system. In differential astrometry aberration therefore gives a differential contribution which results in a distortion of the field, if not applied.

For Earth orbiting satellites the effect is somewhat different than for stellar objects or for minor planets. The question is the following: If a satellite is observed exactly when it 'occults' a reference star, what are its coordinates in the system J2000? In fact, the coordinates are not the same as for the reference star (see Figure 1.5) because the satellites are *not* subjected to annual aberration. As opposed to positions of stars and minor planets, their positions are expressed in the geocentric and not in the barycentric system. Aberration is the change of direction of a light ray when applying a Lorentz transformation from a moving system to the system of the observer. It is therefore the origin of the coordinate system within which the ephemerides are computed (more precisely: the system in which the propagation of light reflected from the satellite is described) deciding whether or not annual aberration must be applied. Because the coordinate system within which the positions of the satellites are expressed moves around the Sun together with the Earth, only the daily aberration has to be applied.

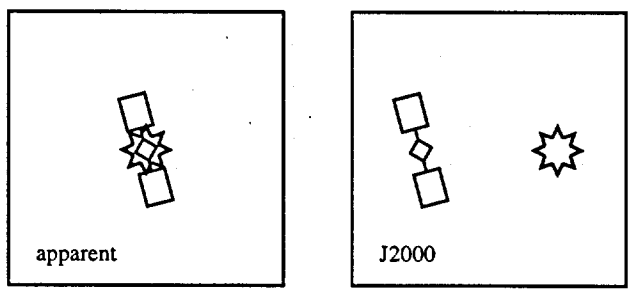

Figure 1.5: A satellite with the same coordinates as a reference star in the apparent system has not the same coordinates in the system J2000.

The fact that the motion of the satellite is expressed in a non-inertial (but quasi-inertial) coordinate system which orbits around the Sun is compensated by introducing tidal forces exerted by Sun and Moon.

Proper Motion

The proper motion of reference stars directly affects the position of the measured object if not taken into account. When transforming the coordinates of a measured stellar object back into the system J2000 it is not possible to transform the epoch of the coordinates to the same system if no positions measured at earlier epochs are available. Coordinates of these objects are therefore expressed in the system J2000 while the coordinate epoch is the epoch of observation.

Light Travel Time

For objects within the planetary system the light travel time enters directly into the position of the objects. The observed direction to an object is the geometrical direction from the observer at time t to the object at time $t - \tau$, where τ is the light travel time ('retarded direction'). Due to the simple linear motion of stellar objects, their light travel time can be included into the catalogue positions (i.e., they must be included into the catalogue position if the distance is unknown). For minor planets and satellites it is, however, necessary to compute the effect of light travel time explicitly. Because, in order to do this, the knowledge of the distance is required the astrometric position of a minor planet or a satellite can in principle *not* contain the effect of light travel time. This correction is applied during the orbit determination or improvement procedure.

Parallax

The parallax enters directly into the position for all objects. For stellar objects it is in general not necessary to consider the annual parallax. For minor planets both, the annual and the daily parallax, for artificial Earth satellites the daily parallax are significant. Because the distance has to be known for applying this correction coordinates of moving objects can only be given in the topocentric system J2000. The parallax is corrected during the orbit determination procedure.

Light Deflection

Because light deflection due to the Sun's gravitation affects the positions of measured stellar objects in the same way as the reference objects, only differential effects affect their astrometric positions. Positions of minor planets are only partially and those of

artificial satellites are not at all affected by light deflection. Therefore the total effect from the reference star is transferred to the measured object if the effect is neglected. Light deflection plays, however, no role in astrometry with an accuracy in the range of 0.1". For all positions in the night hemisphere of the sky the light deflection is below 4 mas. It can therefore be neglected without loss of accuracy.

Refraction

Neglecting refraction or using inappropriate models introduces significant differential effects. Quantitative information for such deformations may be found in Schildknecht (1994).

Color Refraction

If observations are performed without filters the difference in refraction due to different colors of reference stars and the program object enters fully into the measured object's position. The spectral intensity distribution for a minor planet or an artificial satellite may be assumed to be (more or less) the same as that of sunlight. The energy distribution of the light from reference stars of early or late spectral types may, however, be significantly different. The color refraction for a star with given spectral energy distribution $s(\lambda)$ may be computed through

$$R_s = \frac{\int R(\lambda)\, \tau(\lambda)\, c(\lambda)\, s(\lambda)\, d\lambda}{\int \tau(\lambda)\, c(\lambda)\, s(\lambda)\, d\lambda} \tag{1.1}$$

where $R(\lambda)$ is the refraction for monochromatic light with wavelength λ, $c(\lambda)$ the spectral sensitivity of the detector system, and $\tau(\lambda)$ the atmospheric transmission. The zenith distance dependent atmospheric transmission may be computed through the following mapping function

$$\tau(\lambda) = \tau_0(\lambda)^{1/\cos(z)}$$

where τ_0 is the atmospheric transmission for unit air mass. In Table 1.2 the refraction differences to a solar type G2 spectrum are given for several spectral types and zenith distances (computed using eqn. (1.1)). The optical spectra were taken from Silva et al. (1992), the spectral atmospheric transmission τ_0 from Allen (1973), and the spectral quantum efficiency of the Photometrics CCD chip PM512 from the manufacturer's specifications. The refraction $R(\lambda)$ was computed through numerical integration using the US Standard Atmosphere (1976) for normal conditions (temperature 15°, pressure 1013 mbar, dry air, sea level).

Parallactic Refraction

Refraction does not only change the direction of an incident light ray. A ray with a fixed direction outside the atmosphere is also displaced parallely up to several meters (see

	Zenith Distance							
Spectral Type	10°	20°	30°	40°	50°	60°	70°	80°
O5	0.04″	0.08″	0.13″	0.19″	0.27″	0.39″	0.58″	1.01″
B6	0.03″	0.07″	0.11″	0.15″	0.21″	0.30″	0.45″	0.78″
A6	0.02″	0.04″	0.06″	0.09″	0.13″	0.18″	0.27″	0.45″
F6	0.00″	0.01″	0.01″	0.02″	0.03″	0.04″	0.05″	0.09″
K4	−0.01″	−0.03″	−0.04″	−0.06″	−0.08″	−0.11″	−0.17″	−0.27″
M4	−0.05″	−0.10″	−0.15″	−0.22″	−0.31″	−0.43″	−0.65″	−1.09″

Table 1.2: Color refraction for different spectral types relative to a solar type spectrum G2 based on the spectral sensitivity of the CCD chip PM512, refraction for standard conditions and using optical star spectra from Silva et al. (1992).

Table 1.3). For an observed object which is not at infinity this parallel displacement causes a parallax. (A more appropriate designation for the effect would therefore be 'refraction parallax'.) For a geostationary satellite at a zenithal distance of $z = 30°$ the change in position due to the parallactic refraction is 0.05″, for $z = 70°$ it is 0.1″. The standard coordinates of moving objects are *not* corrected for parallactic refraction because knowledge of the distance is required. The correction may or must be applied during the orbit determination or improvement procedure, depending on the required accuracy level.

Zenith distance	10°	20°	30°	40°	50°	60°	70°	80°	90°
Displacement of light ray (m)	0.4	0.9	1.6	2.6	4.3	8.0	18	70	2000

Table 1.3: Parallel displacement of a light ray outside the atmosphere due to refraction. Results from numerical integration of the US Standard Atmosphere (1976) for standard conditions at 47° latitude and sea level (15°C, 1013 mbar, 550 nm).

1.1.5 Search for Earth Orbiting Objects

When trying to observe a given satellite for the first time, the object usually has to be searched for because initial orbital elements are not good enough to 'trap' the object in a small field of view. It is in particular the alongtrack error of the satellite which increases rapidly with the age of the predicted ephemeris. The object has therefore to be searched along the projected orbital plane. After having found an object on two or more search frames initial orbital elements are determined (see Chapter 2) in order to decide whether or not the object is the correct one.

The search for orbiting objects may, in fact, be interesting by itself: In the space around the Earth a debris problem is aggravating (Interagency Report on Orbital Debris, 1995),

(Orbital Debris, 1995). More than 4'000 spacecraft have been launched into space since 1957; nearly 2'000 still are in orbit. Of these, only about 450 are operational, the others are no longer functioning or they have completed their mission. Nonfunctional spacecraft, however, constitute only a small fraction of the debris orbiting the Earth. The U.S. Space Command (USSPACECOM) catalogue currently contains more than 7000 objects. Only 6% are functioning spacecraft, 22% are nonfunctional satellites, 17% are spent rocket upper stages, and 42% are fragments from more than 120 spacecraft and rocket body breakups in orbit. The remaining 13% are mission related objects (lense caps, bolts, etc.). Only objects larger than about 10 cm in LEO (Low Earth Orbits) and 1 m in GEO (Geostationary Orbits) are contained in the catalogue. The catalogue is known to be incomplete, the actual population of debris in space being unknown. It is estimated that more than 100'000 debris in the range between 1–10 cm and more than 35'000'000 particles in the range between 0.1–1 cm orbit the Earth.

Because national and commercial interests in the development and use of space becomes more and more important, the space agencies have a growing interest to increase the current knowledge of the debris population around the Earth, to monitor the orbital debris environment, and to assess debris mitigation measures. The Space Surveillance Network (SSN) of the USSPACECOM as well as the Russian Space Surveillance System use Radar for routine survey of objects in LEO. Radar is the best suited ground-based technique for surveying LEO, but because the Radar receiving power decreases with the fourth power of the distance, optical sensors are more adequate for observing objects in high Earth orbits (above about 6'000 km). In particular, objects in GEO are only observable for large Radars (see Chapter 6) while even small optical telescopes may observe objects in GEO with a size of 1 m.

For optical observations of high orbiting objects CCDs are appropriate due to their sensitivity. For survey purposes a large field of view is required, however. The telescopes of the GEODSS (Ground Electro-Optical Deep Space System) of the Space Surveillance Network are upgraded with CCD cameras. ESA is installing a 1 m Zeiss telescope equipped with a 4k x 4k-CCD array at Teide observatory in Tenerife (Massart et al., 1997). The instrument will (among other applications) be used for surveying the geostationary ring and objects in geostationary transfer orbits (GTO). NASA developed a 3 m liquid mirror telescope which will be installed at a site close to the equator and operated in a 'staring mode' for space debris observations (Potter et al., 1996).

A special method for the automatic detection of moving objects on CCD frames was developed by Schildknecht et al. (1995a) for the ESA space debris telescope in Tenerife as well as for the telescope at the Zimmerwald observatory: On a reference frame all objects are searched and a template (mask) is generated with all pixels marked that belong to these objects (assumed to be stellar). This template is subsequently used to mask the stellar objects on search frames after transforming the mask frame to the coordinate system of the search frame. On the masked frame moving objects may be automatically detected. The process is illustrated in the sequence of frames in Figure 1.6: On the masked frame (right) the faint image of the Meteosat 4 apogee boost motor with a size of 1.3 m x 0.8 m

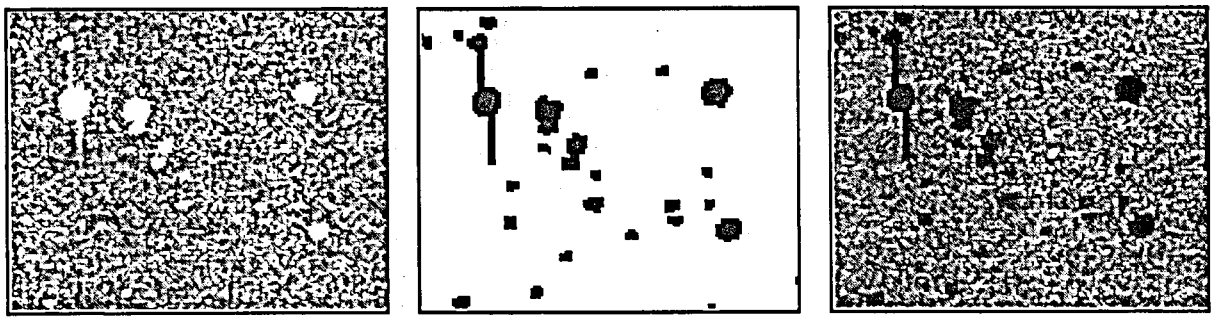

Figure 1.6: Masking technique illustrated by two frames taken at the Zimmerwald SLR telescope on June 30, 1994. A reference frame (left) is used to generate a mask (center) which is applied to a search frame (right) on which the Meteosat 4 apogee boost motor 89 020E shows up. The frames cover 14'x10' and were exposed for 1.5 seconds.

shows up. The estimated magnitude of the object is between 15 mag and 16 mag.

In order to get a good signal-to-noise ratio (SNR) faint objects should be tracked. If the object's light is integrated onto the same pixels and the readout noise of the chip is negligible the SNR increases with the square root of the exposure time. If, on the other hand, the object is moving with respect to the pixels, the maximum achievable SNR is limited by the background noise. The optimum exposure time in this case is a few pixel crossing times (Schildknecht et al., 1995b). In order to lower the detection limit spatial filtering techniques may be used (Schildknecht et al., 1995c).

If regions of the sky are surveyed for special types of objects, the telescope may track with the expected motion of the objects during exposure. E.g., objects in GEO may be searched for with fixed telescope; GTO objects may be searched for at apogee where the angular velocity is minimum and the direction and value of the motion may be calculated for a given orbital inclination. In order to use the same reference frame (mask) for a long time the sidereal motion may be compensated by repositioning the telescope during readout of the chip (see Figure 1.7). Using this 'track-and-go'-technique a declination stripe is surveyed. In this way e.g., the geostationary ring or the locations of the apogee for GTO objects may be scanned.

If approximate orbital elements shall be computed for the detected objects in order to schedule follow-up observations at least two positions have to be measured for each object. If the objects are moving slowly enough they may occur on two or more successive search frames. Objects in LEO, on the other hand, will leave behind only a trail on a single frame. The object's position at a later time has then to be inferred from the (ambiguous) direction and the length of the trail and the object has to be followed with a telescope which is capable to track at high rates.

For high orbiting objects the optical search scenarios are therefore much simpler than for objects in LEO. In addition, to get high precision astrometric positions neither the trails

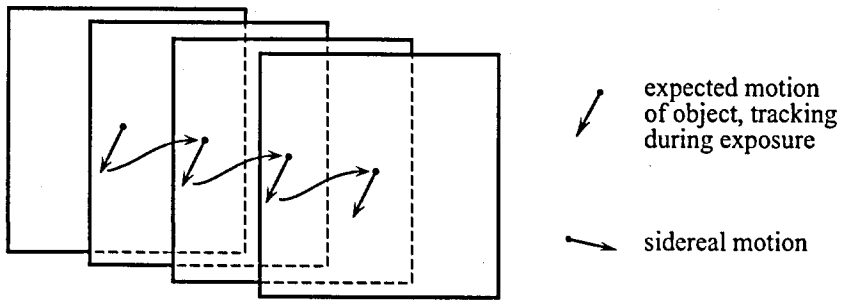

Figure 1.7: Search scenario for slow moving objects: During the exposure the telescope is tracking with the expected motion of the objects. The sidereal motion is compensated by repositioning between exposures.

for the moving objects nor the trails for the reference stars should be too long because the centroids are determined with lesser accuracy in the direction of the trails. We will therefore restrict ourself to high orbiting objects such as geostationary satellites, GTO objects, or GPS satellites.

1.2 Slow Moving Satellites

1.2.1 Geostationary Orbits

The geostationary ring with a geocentric radius of about 42'164 km is a very important region in space for telecommunication satellites and other Earth observing spacecraft such as meteorological satellites. Currently more than 600 objects are catalogued in and near this region. Only 110–130 of them are operational satellites (1996), the others are dead satellites, rocket upper stages, apogee boost motors, fragments. Every year additional 18–28 spacecraft are injected into the geostationary ring. Two explosions are known to have occurred (Kessler, 1993): on Feb. 21, 1992, the breakup of a Titan upper stage which was launched on Sept. 26, 1968, and the breakup of an EKRAN satellite in June 1978 caused by a battery failure. Other breakups are likely to have occurred. The true population in and near the geostationary ring is therefore not known. Efforts are undertaken by the space agencies of the USA (NASA), Russia (RSA), Japan (NASDA), and Europe (ESA) to get a better knowledge on the population in this region in space.

A search for uncontrolled objects in the geostationary region was performed with the NASA CCD Debris Telescope (CDT) on Mt. Haleakala, Maui, Hawaii, between 1992 and 1994 (Potter (1995), Talent et al. (1997)). A 32 cm f/1.3 Schmidt telescope equipped with a CCD camera with a limiting magnitude of 17^{mag} for a 30 seconds exposure was used. About 30% of the detected objects in a total of 252 observing hours could not be

correlated with entries in the catalogue. These objects might belong to a population of orbital debris near the geostationary ring.

The most important source of information on geostationary orbit objects are the Two Line Elements (TLE) for more than 600 objects (Feb. 96) prepared by the USSPACECOM (U.S. Space Command). They are based on observations from the three optical tracking sites GEODSS (Ground Electro-Optical Deep Space System) of the Space Surveillance Network (SSN) (Chamberlain et al., 1993). Additional 40 objects are catalogued in the RAE (Royal Aircraft Establishment) Tables of Earth Satellites. Catalogues based on these catalogues are issued by ESA (Janin, 1996) and the Institute for Theoretical Astronomy in St. Petersburg (Sochilina et al., 1996). The Russian Space Surveillance System compiles a catalogue of space objects based on independent observations (Batyr et al., 1993).

The inclinations of the geostationary orbits range between 0° and 15°. The histogram in Figure 1.8 (left) shows the distribution of the inclinations. The functioning satellites have inclinations close to 0°. The Histogram 1.8 (right) shows the distribution of the right ascensions (R.A.) of the ascending nodes for the catalogued geostationary objects. The unexpected distribution of the nodes will be discussed below. In Figure 1.9 (left) we see the distribution of the drift rates for catalogued objects in GEO. The objects in 'graveyard' orbits with negative drift rates (semimajor axis larger than geostationary radius) are clearly visible. The fraction of objects with eccentricities smaller than a given value is shown in Figure 1.9 (right). 97% of all catalogued objects have an eccentricity e below 0.01.

The geocentric space velocity of geostationary objects is about 3 km/s and the angular velocity relative to the stars is about 15″/sec. The angular velocity in the Earth-fixed frame depends on the inclination and the position of the satellite in its orbit: At the culmination

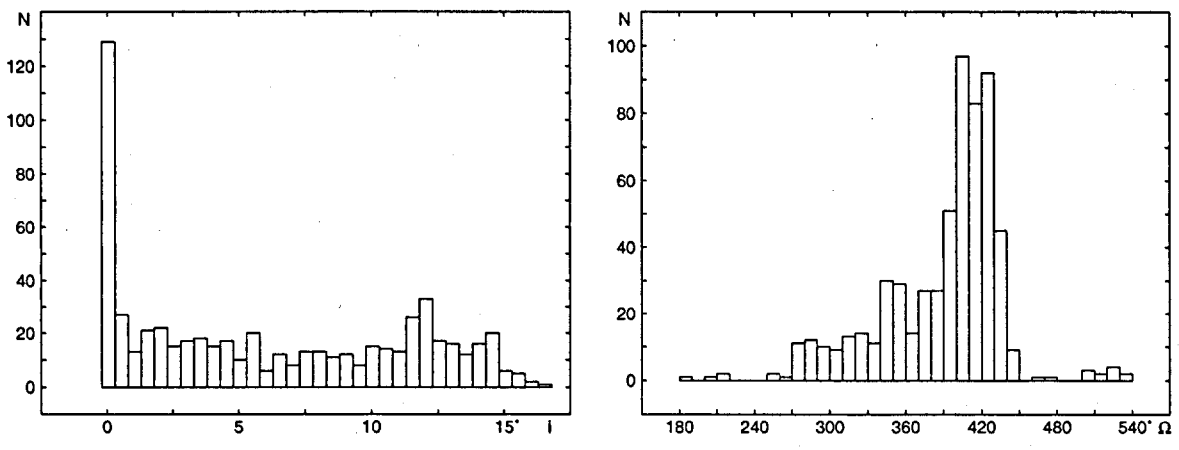

Figure 1.8: Histograms of inclination (left, bin size 0.5°) and R.A. of ascending node (right, bin size 10°) for catalogued geostationary objects.

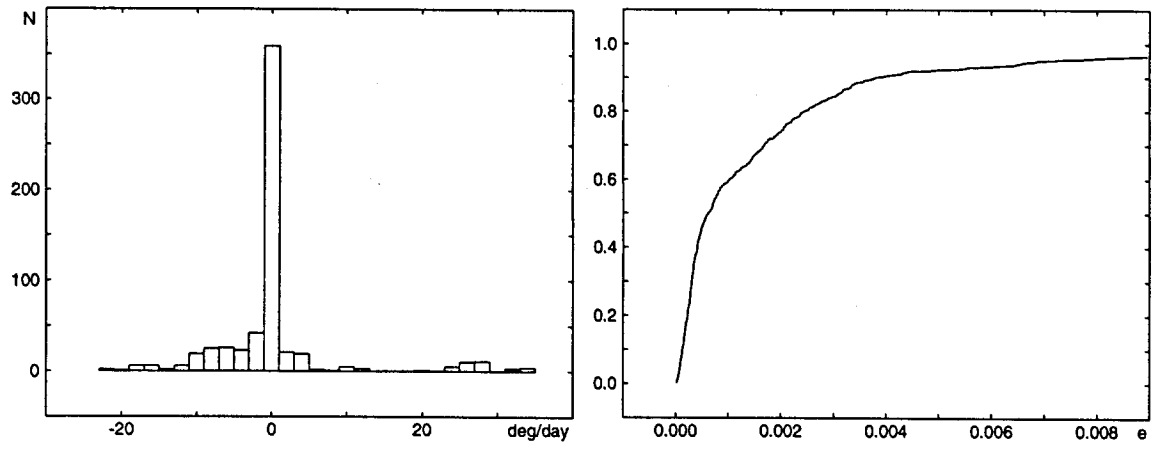

Figure 1.9: Histogram of drift rates (left, bin size 2°/day) and fraction of catalogued geostationary orbits with eccentricity smaller than a given value (right).

points (highest or lowest elevation) the relative motion (in the Earth-fixed system) is minimum. In Table 1.4 we give the corresponding values for different inclinations and semimajor axes for an object at the equator crossing and at the culmination point for an observer located in Zimmerwald. In Figure 1.10 we see the angular velocity field for geostationary objects with an orbital inclination of 15°. Azimuth and elevation refer to an observer in Zimmerwald. The dotted line represents the location of the geostationary ring which, for Zimmerwald, is at a declination of −7.2° (in the meridian) due to parallax.

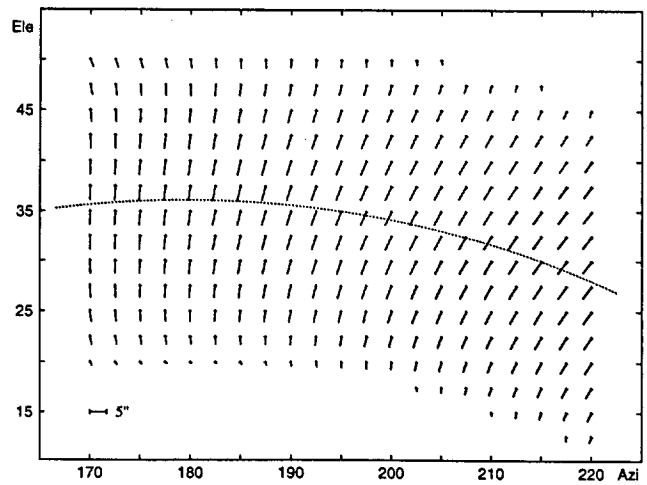

Figure 1.10: Velocity field for geostationary satellites with orbital inclination of 15° in the Earth-fixed system for an observer in Zimmerwald. The dotted line represents the geostationary ring.

Semimajor Axis	Incl.	Satellite location	Angular velocity star-fixed	Angular velocity Earth-fixed
GEO	0°	equator	14.9″/sec	0.0″/sec
	10°	equator	15.0″/sec	2.9″/sec
		culmination	15.3″/sec	0.3″/sec
	15°	equator	15.0″/sec	4.3″/sec
		culmination	15.4″/sec	0.6″/sec
GEO+ 500 km	0°	equator	14.6″/sec	0.3″/sec
	10°	equator	14.7″/sec	2.9″/sec
		culmination	15.0″/sec	0.0″/sec
	15°	equator	14.7″/sec	4.3″/sec
		culmination	15.1″/sec	0.3″/sec
GEO+ 1000 km	0°	equator	14.4″/sec	0.6″/sec
	10°	equator	14.4″/sec	2.9″/sec
		culmination	14.7″/sec	0.3″/sec
	15°	equator	14.4″/sec	4.3″/sec
		culmination	14.8″/sec	0.0″/sec

Table 1.4: Angular velocities for geostationary objects with different orbital inclinations for an observer in Zimmerwald.

From Zimmerwald (longitude 7.5°E, latitude 46.9°N) a sector of 93° of the geostationary ring is observable above 20° elevation (from 54°E to 39°W). From the stabilized objects only those inside this longitude range can be observed. Many of the abandoned objects are drifting, however, with drift rates up to 35°/day (for the catalogued objects). The drift rate may be computed from the difference Δa of the semimajor axis to the geostationary radius $a_0 \simeq 42'164$ km using Kepler's third law, to first order

$$\Delta n[\text{deg/day}] \simeq 0.0128\ \Delta a[\text{km}] \tag{1.2}$$

Depending on the drift rate an object is only visible for a certain time interval ('visibility time') and returns back into visibility after a period of invisibility. In Table 1.5 we list drift rates and the corresponding Earth-fixed revolution time ('return time') as well as the duration of the visibility periods for an observer in Zimmerwald.

From Table 1.4 and Figure 1.10 we conclude that GEO objects with specified inclinations should be 'trapped' at the upper or lower culmination point where the angular velocity in the Earth-fixed frame is lowest and the probability for detection thus maximum. Indeed, a satellite with an orbital inclination of 15° stays for about $2\frac{3}{4}$ hours within one degree in declination or during $1\frac{3}{4}$ hours within 0.4° (see Table 1.6). I.e., the alongtrack-search of an object with unknown longitude and an inclination of 15° can be performed in direction of right ascension using the same reference frame at upper or lower culmination during more than one and a half hour with a telescope which has a field of view of 0.4°.

Δa	Drift Rate	Return Time	Visibility for Zimmerwald
−1000 km	13.2 deg/day	27 days	7.0 days
−800	10.5	34	8.8
−600	7.8	46	11.9
−400	5.2	69	18.
−200	2.6	139	36.
0	0	∞	∞
200	−2.6	141	36.
400	−5.1	71	18.
600	−7.6	48	12.3
800	−10.0	36	9.3
1000	−12.5	29	7.5

Table 1.5: Return times (revolution period in the Earth-fixed system) and visibility times for an observer in Zimmerwald for drifting geostationary objects (minimum elevation above horizon: 20°).

Incl.	Field of view				
	1.0°	0.7°	0.4°	0.1°	
5°	4.9	4.1	3.1	1.5	h
10°	3.4	2.9	2.2	1.1	h
15°	2.8	2.3	1.7	0.9	h

Table 1.6: Time in hours during which geostationary objects with given orbital inclination remains within a given declination interval of the culmination point.

Satellites in orbit are subject to a number of perturbations. For geostationary satellites the most important perturbations are due to the oblateness of the Earth, the gravitational attraction from Moon and Sun, the inhomogeneous longitudinal mass distribution of the Earth, and, depending on the area-to-mass ratio, the direct solar radiation pressure. In Table 1.7 we list the magnitudes of the perturbing accelerations and the resulting alongtrack drifts for a time interval of 5 and 30 days (from Rudenko (1995)).

Active satellites have to be repositioned several times per year or even several times per month because perturbing forces are driving them away from their nominal Earth-fixed position. Perturbations due to the variation of the longitudinal mass distribution of the Earth, described by the J_{22}-term of the geopotential, give rise to longperiodic oscillations in the longitude of a geostationary satellite. These resonance effects are studied in detail in Chapter 4.

At a distance of a few Earth radii the effect of the perturbations by Sun and Moon are of the same order as the effect of the Earth's oblateness. The combined effect of these

Force	Satellite acceleration [m/s^2]	Maximum drift over 5 days [arcsec]	Maximum drift over 30 days [arcsec]
Earth's monopole (J_{00})	$2.2 \cdot 10^{-1}$		
Earth's oblateness (J_{20})	$1.7 \cdot 10^{-5}$	480.	2880.
Gravitational attraction by the Moon	$7.3 \cdot 10^{-6}$	280.	1660.
Gravitational attraction by the Sun	$3.3 \cdot 10^{-6}$	100.	570.
Direct solar radiation pressure	$2.3 \cdot 10^{-7}$	20.	120.
Earth equatorial ellipticity (J_{22})	$2.8 \cdot 10^{-8}$	70.	2590.
Earth's albedo radiation pressure	$2.1 \cdot 10^{-9}$	0.2	1.
Gravitational attraction by Venus	$4.4 \cdot 10^{-10}$	0.01	0.07
Solid Earth tides	$2.7 \cdot 10^{-10}$	0.008	0.04
Gravitational attraction by Jupiter	$5.2 \cdot 10^{-11}$	0.002	0.009
Ocean tides	$2.7 \cdot 10^{-11}$	0.0008	0.004
General relativistic correction	$2.4 \cdot 10^{-11}$	0.0008	0.004

Table 1.7: Acceleration and longitudinal drift of a geosynchronous satellite due to the forces acting on it. Orbital elements: $a = 42'164$ km, $e = 0$, $i = 0°$, $\omega = 0°$, $\Omega = 0°$, $M = 0°$. Satellite area to mass ratio $A/M = 0.05$ m^2/kg. From (Rudenko, 1995).

three perturbations cause the orbital planes of geostationary objects to precess around a stable plane (Allan et al., 1964). This plane (the so-called proper or Laplacian plane) has an inclination of about 7.5° with respect to the equatorial plane and its nodal line coincides with the direction to the vernal equinox. The first astronomer who studied a perturbation of this kind was Laplace (1805) in his discussion of the motion of Saturn's moon Iapetus whose orbit shows a similar precession due to the perturbations of the Sun and the oblateness of Saturn.

As a consequence the pole of a geostationary orbital plane (with the celestial coordinates $\alpha = \Omega - 90°$ and $\delta = 90° - i$) describes a cone with a period of about 53 years with opening angle of 15° which is tilted towards the ecliptical pole (see Figure 1.11). The orbital inclination of uncontrolled objects left in the equatorial plane will therefore steadily increase to reach 15° after about 25 years and then decrease again during the next quarter of a century. The first objects launched into geostationary orbit thirty years ago have now an orbital inclination of about 15°. This orbital precession around a common plane explains the — at first sight strange — fact, that the ascending nodes of geostationary objects (most of them uncontrolled) are clustered at a given right ascension (see Figure 1.8, right).

The fact that uncontrolled geostationary objects all have a right ascension of the ascending node Ω which is strongly correlated with the inclination i means that the location of their culmination are for a given inclination at the same right ascension. For a given epoch t the geocentric longitude λ of their upper culmination point may therefore be calculated

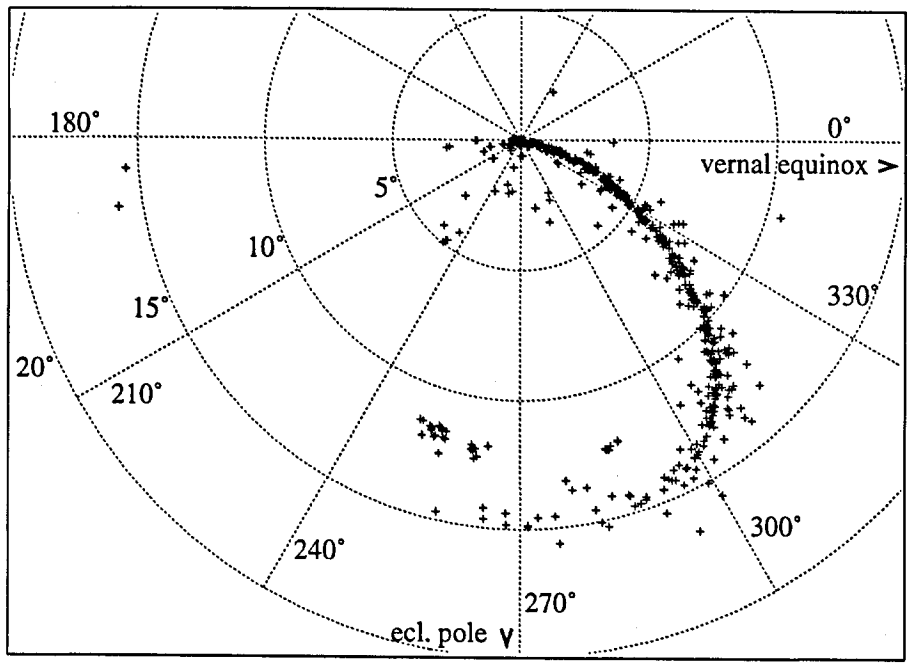

Figure 1.11: Precession of the orbits of geostationary satellites. The symbols '+'give the location of the orbital poles corresponding to inclination i and R.A. of ascending node Ω of the catalogued objects (Feb. 1996). Coordinates are right ascension $\alpha = \Omega - 90°$ and declination $\delta = i$ (same representation as in Janin (1996)).

with the formula

$$\lambda_{\text{culm}} = \Omega(i) + 90° - \Theta_0 \tag{1.3}$$

where Θ_0 is the Greenwich Mean Sidereal Time (GMST) at time t. The right ascension of the ascending node may be approximately computed as a function of i by

$$\cos\Omega = \cot(7.5°)\,\frac{1-\cos i}{\sin i} \tag{1.4}$$

(providing two solutions for Ω). When looking for uncontrolled objects one simply has to scan the culmination longitude given by eqn. (1.3) (or the corresponding lower culmination) for a given inclination. The search may be performed using a single reference frame (mask) and scanning at constant declination.

1.2.2 Density of Catalogued Objects in Geostationary Ring

The probability for finding an object in a circular orbit with arbitrary longitude of node within the declination interval δ to $\delta + d\delta$ can be computed by using the equation $\sin u \sin i = \sin\delta$ which connects the argument of latitude u (distance of the satellite

from the ascending node) and the declination δ. The result is

$$dn(\delta) = \frac{1}{\pi} \frac{\cos\delta d\delta}{\sqrt{\sin^2 i - \sin^2 \delta}} \qquad \text{for} \qquad |\delta| < i, \tag{1.5}$$

where dn is the mean density of the satellites averaged over longitude in the declination interval $d\delta$ centered at δ. The function has its minimum value of $1/\sin i$ at the equator where the satellite's declination changes fastest. For $\delta = \pm i$ the function (1.5) diverges and the detection probability of a satellite is maximum at these culmination points. (It can easily be checked that the integral of dn over declination is equal to 1.)

For a satellite population with orbital inclinations distributed according to a function $f(i)$ ($f(i)di$ is the number of orbits with inclinations in the interval i to $i + di$) we may again compute the average number of objects per declination interval $d\delta$:

$$\frac{dN(\delta)}{d\delta} = \frac{1}{\pi} \int_{\delta}^{I} f(i) \frac{\cos\delta}{\sqrt{\sin^2 i - \sin^2 \delta}} di. \tag{1.6}$$

All orbits with inclinations between δ and the maximum inclination I contribute to the integral. If we adopt (in order to integrate eqn. (1.6) analytically and to give an approximate formula) a distribution of inclinations of $f(i) = N\cos i/\sin I$ (for $i < I$; N is the total number of objects) we get a density distribution

$$dN(\delta) = \frac{N}{\pi} \frac{\cos\delta}{\sin I} \ln\left(\frac{\sin I + \sqrt{\sin^2 I - \sin^2 \delta}}{\sin\delta}\right) d\delta.$$

This function is shown in Figure 1.12 as a dotted line for $N = 480$ (i.e. the number of non-operational catalogued objects). The solid line in the figure gives the latitudinal object density for the actual distribution of orbital inclinations of the catalogued GEO objects. It was computed by adding up the functions (1.5) for the inclinations of all catalogued objects. Although the inclination distribution adopted for the analytical computation was selected only for convenience, the similarity of the two distributions is satisfactory.

If enough orbits with different inclinations are averaged the maxima at the culmination points of the individual orbits are averaged out and the maximum density occurs at the equator. This happens because every object, no matter what its orbital inclination is, has a non-zero probability to be found at the equator. In addition, all controlled objects (about 120) have very small inclinations and contribute only to the peak of the distribution in the equator.

In Figure 1.12 we see the density as number of objects per square degree (computed from declination bins of 0.2°). The density reaches 1.8 objects/deg^2 at the equator, but already at a declination of $\pm 0.2°$ the density drops to 0.2 objects/deg^2. Therefore, if we search for objects with no specific orbital inclinations, the probability for finding one is maximum at the equator. Most of the detected objects will, however, have a small inclination because the probability for finding high inclination objects at the equator is low; for objects with

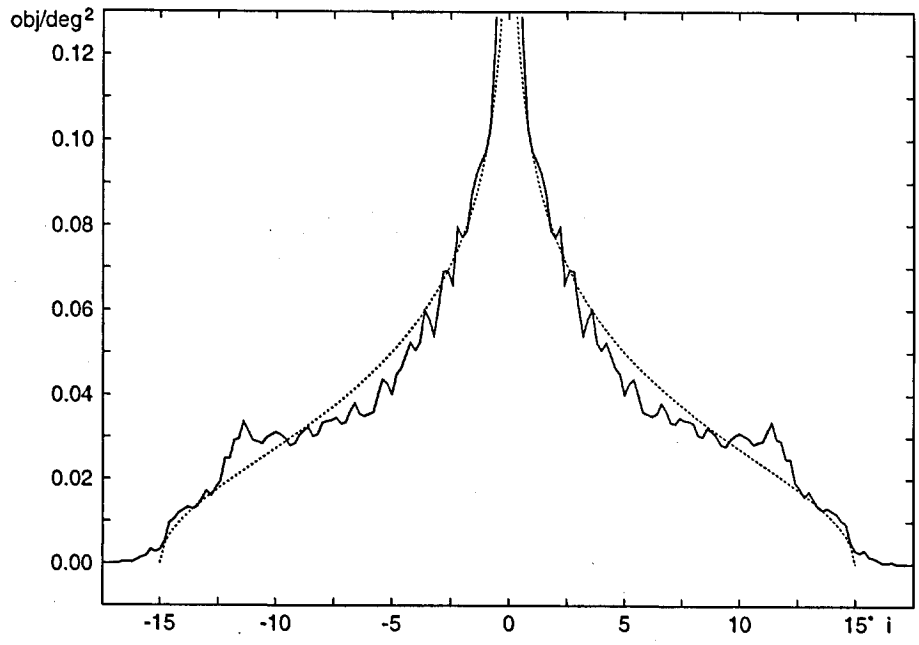

Figure 1.12: Density of catalogued GEO objects v.s. declination. The dotted line gives a theoretical distribution based on an orbital inclination density distribution $dn \sim \cos(i)$, the solid line shows the distribution computed from the density distribution of the inclinations of catalogued GEO objects. The density is given in objects/deg^2 (based on a bin width of 0.2°).

given inclination $i > 0$ the probability for finding them is maximum at the declination $\delta \simeq \pm i$.

To get a more detailed picture the sky was divided into bins, one degree wide in right ascension and half a degree wide in declination. The inclinations and ascending nodes of the objects in Janin (1996) were taken and for each orbit the relative contribution to the different bins was computed. The result is the map of the sky in Figure 1.13 which gives the object density distribution as a function of right ascension and declination. (The Figure was actually drawn for an observer at the geocenter, but parallax does not substantially alter the result.) The gray scale gives the object density in a logarithmic scale, black corresponds to the highest density.

The systematic distribution of the satellite orbits due to the orbit precession caused by perturbations is easily seen. We see again — as we already saw before — that the ascending node is drifting backwards in right ascension for increasing inclination. This systematic distribution of orbits causes a kind of a caustic of higher density, at negative declination close to the ascending nodes and at positive declination close to the descending nodes. At the location of this caustic orbits with different inclinations intersect.

The location of this caustic may be computed in the following way: The relation between inclination i and right ascension of the ascending node Ω for uncontrolled objects is

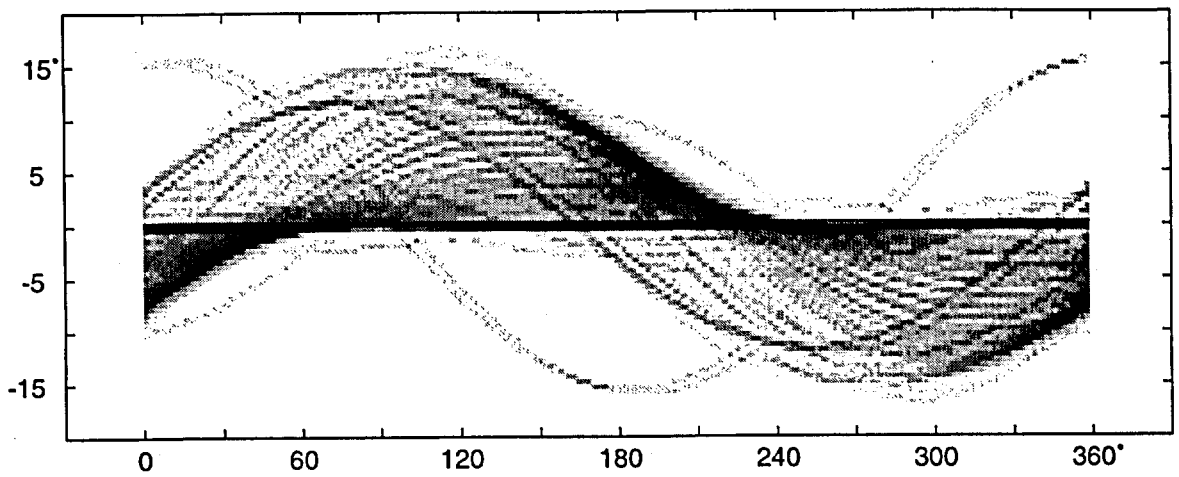

Figure 1.13: Object density as a function of right ascension (R.A.) and declination constructed from all catalogued objects given in Janin (1996). The logarithmic gray scale is a measure for density. Bin size: 1° in R. A. and 0.5° in declination.

given by eqn. (1.4). On the other hand, for given i and Ω the right ascension α and the declination δ of points in the orbit are connected by

$$\sin(\Omega - \alpha) = \tan\delta \cot i. \tag{1.7}$$

Let us determine the intersection of two adjacent orbits, one with inclination i and node Ω, the other with inclination $i + \Delta i$ and node $\Omega + \Delta\Omega$. Using eqn. (1.7) for both orbits with the same α and δ we get (to first order in Δi and $\Delta\Omega$)

$$\cos(\Omega - \alpha)\sin^2 i\, \Delta\Omega = -\tan\delta\, \Delta i \tag{1.8}$$

where α and δ are the coordinates of the intersection points. Taking the total derivative of eqn. (1.4) we get a relation between Δi and $\Delta\Omega$. We obtain

$$\tan\Omega \sin i\, \Delta\Omega = \Delta i, \tag{1.9}$$

a result which is used to eliminate Δi and $\Delta\Omega$ from eqn. (1.7). The result is

$$\cos(\Omega - \alpha)\sin i = \tan\delta \tan\Omega. \tag{1.10}$$

Finally, using eqn. (1.7), we obtain the two equations

$$\tan(\Omega - \alpha) = \cos i \cot\Omega \tag{1.11}$$

$$\tan\delta = \cos(\Omega - \alpha)\cot\Omega \sin i \tag{1.12}$$

which, together with eqn. (1.4) give α and δ describing the caustic parametrized by Ω (or i). δ is positive if α falls into the second and the third quadrants, negative if α falls into the first and the last quadrants.

According to Figure 1.13 the density is maximum at the equator where it is everywhere above 0.41 objects/deg^2 and reaches 0.83 objects/deg^2 at R. A. 65° and 245° (4h and 16h). In Figure 1.14 the average number of objects per 0.5°x0.5° along the equator is shown.

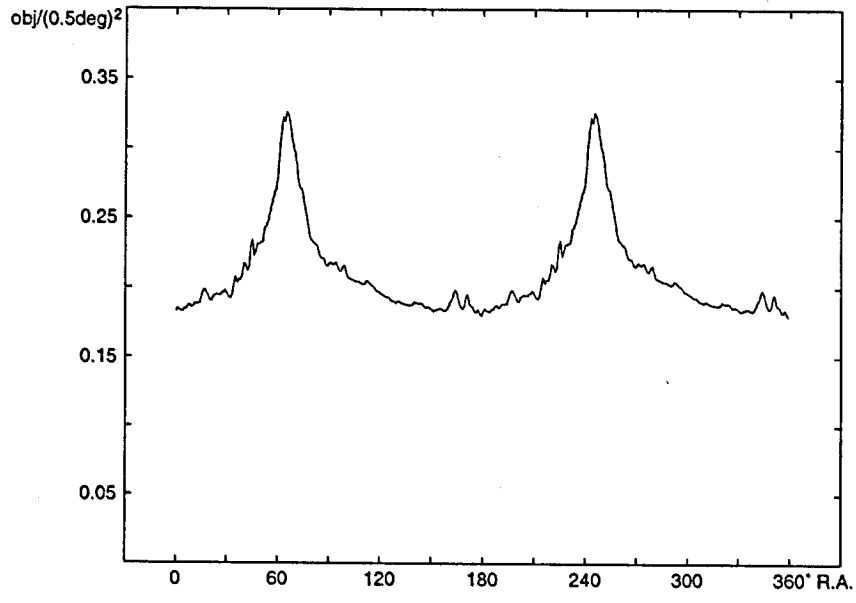

Figure 1.14: Density of catalogued geostationary objects along the equator for a field of view of 0.5°x0.5°.

At the 'caustic' off the equator the density still reaches 0.54 objects/deg^2. Objects with non-zero inclination should be 'tapped' at the location of the 'caustic'. Because the density distribution is quite inhomogeneous and a scaling for different fields of view is not straightforward, numbers for the density at some locations in the sky are given for several fields of view in Table 1.8.

Several special features in Figure 1.13 may be attributed to individual groups of objects: The orbits with an ascending node around 270° and an inclination of 15° belong to four catalogued objects with the COSPAR designation 76 032. A fourth object with the same designation, the fragment 76 023K has a different orbit, however. The group of orbits with

Field of view:	$1° \times 1°$	$0.7° \times 0.7°$	$0.5° \times 0.5°$	$0.4° \times 0.4°$
Max. at equator (α : 65°, 245°)	0.83 deg^{-2}	0.52 deg^{-2}	0.33 deg^{-2}	0.24 deg^{-2}
Min. at equator (α : 155°, 335°)	0.41 deg^{-2}	0.27 deg^{-2}	0.18 deg^{-2}	0.14 deg^{-2}
Max. at 'caustic'	0.54 deg^{-2}	0.31 deg^{-2}	0.18 deg^{-2}	0.13 deg^{-2}
$\alpha = 90°$, $\delta = 13°$	0.075 deg^{-2}	0.051 deg^{-2}	0.009 deg^{-2}	0.006 deg^{-2}

Table 1.8: Object density at different positions in the sky for several fields of view.

an ascending node of about 350° and an inclination of 12° consist of the 27 objects with COSPAR designation 66 053, 67 003, and 68 050. Finally, the orbit with an ascending node at about 70° and an inclination of 10° are attributed to the object 81 073A.

All these objects and groups of objects are easily seen in Figure 1.15. We conclude that object searches should not only be performed at the locations of highest object density (equator, caustic), because in this way entire groups of objects (e.g. fragments from break-ups) might be missed. Indeed, investigations with the NASA CDT (Talent et al., 1997) revealed groups of objects with orbital nodes and inclinations outside the 'mainstream' of the catalogued objects. In addition care should be taken to search for objects close to the Earth's shadow where the illumination of the orbiting objects by the Sun is optimal.

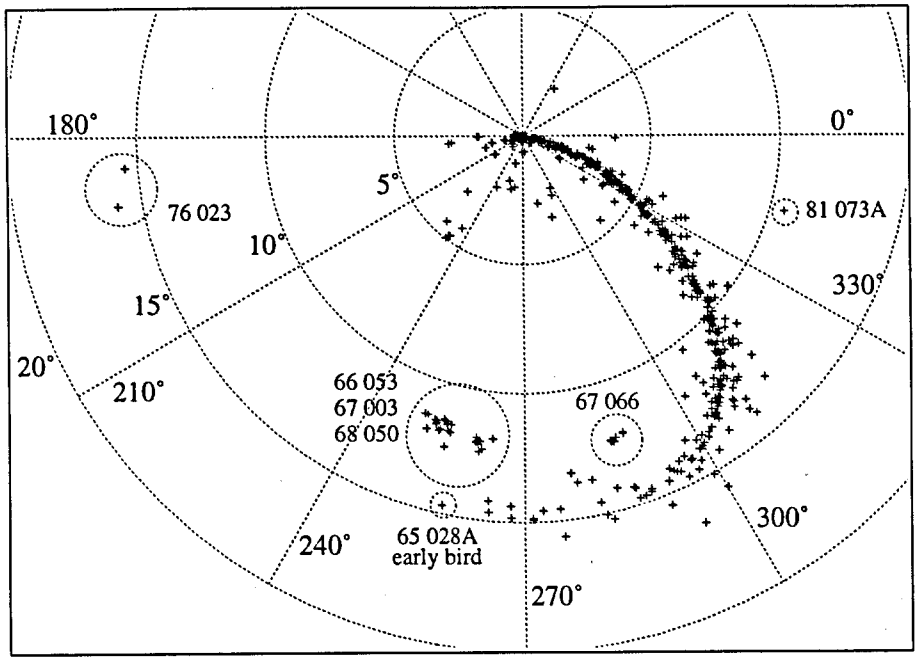

Figure 1.15: Orbital pole for geostationary satellites with groups of satellites indicated which have different inclination and/or ascending node than the 'mainstream' of the objects.

1.2.3 Geostationary Transfer Orbits

Geostationary transfer orbits (GTO) are necessary to transport payloads from a low Earth orbit into the geostationary ring. Usually the rocket upper stage remains in this highly eccentric orbit after deployment of the satellite which is injected into the GEO with an apogee boost motor (ABM) (an exception are the Russian Proton launchers which directly inject the satellites with the fourth stage of the rocket which remains unfortunately in a near geostationary orbit).

498 objects were catalogued in GTO in 1995 (Interagency Report on Orbital Debris, 1995), namely 75 spacecraft, 276 rocket bodies, and 147 fragments and debris. Until 1995 about 10 breakups in GTO were recorded (Nauer, 1995).

Initially, the height of the apogee of a GTO is at about 35'800 km while the perigee is at an altitude of a few hundred kilometers. The corresponding semimajor axis is about 24'500 km and the eccentricity is about 0.73. The orbital period of an object in GTO is close to 10.5 hours. Air drag acting at the perigee decreases the apogee height at a rate which depends on the perigee height and the solar activity (see Janin (1994)).

The launch of a geostationary satellite takes place in the following way (somewhat idealized): The rocket is launched in eastward direction to take maximum advantage of the Earth's angular momentum. The rocket upper stages therefore reaches a low Earth orbit (LEO) with an inclination corresponding to the geographical latitude of the launch site. The injection of the rocket into the GTO has to take place at the ascending or descending node in order to bring the apogee close to the equatorial plane. The argument of perigee for a GTO is therefore initially close to 0° or 180°. The inclination of the orbit remains close to the latitude of the launch site. The change of inclination for the payload to 0° is effectuated during injection into the GEO at apogee for energetic reasons. After deployment the payload is shifted along the GEO to its target position. The launch sites frequently used are given in Table 1.9. In Table 1.10 we present the standard Ariane 4 GTO elements (Ariane 4 User's Manual, 1983).

Due to the Earth's oblateness perturbations the argument of perigee changes at a rate of +0.8°/day causing the perigee to rise above the equatorial plane (for argument of perigee

Kourou (French. Guayana)	5°N
Cape Canaveral (USA)	28°N
Tanegashima (Japan)	30°N
Xichang (China)	41°N
Tyuratam (Kasachstan)	46°N

Table 1.9: Latitude of launch sites for geostationary satellites.

Apogee height	35975	km
Perigee height	200	km
Eccentricity	0.73	
Inclination	7°	
Geogr. longitude of ascending node	169°	
Argument of perigee	178°	

Table 1.10: Standard Ariane 4 GTO elements, from Ariane 4 User's Manual (1983).

Incl.	Angular velocity	
	star-fixed	Earth-fixed
7°	6.9″/sec	8.1″/sec
28°	7.2″/sec	9.9″/sec
46°	7.5″/sec	12.3″/sec

Table 1.11: Angular velocities for GTO objects with different orbital inclinations at apogee for an observer in Zimmerwald.

Incl.	Maximum elevation	Hours before or after apogee	Angular velocity	
			star-fixed	Earth-fixed
7°	37.5°	2.4 h	10.0″/sec	5.0″/sec
28°	55.7°	4.5 h	56″/sec	71″/sec
46°	88.0°	4.8 h	3.6′/sec	3.7′/sec

Table 1.12: Maximum elevation of GTO objects with different orbital inclinations for an observer in Zimmerwald.

close to 180°). Together with the drift of the node of about −0.4°/day the GTO ellipse rotates eastward at a rate of about 0.4°/day.

At their apogee GTO objects have a velocity of 1.6 km/sec. Their angular velocity relative to the stars and in the Earth-fixed system are given in Table 1.11. The elevation of the apogee for a GTO object in the meridian of Zimmerwald is 36°. The maximum elevation is reached before or after the apogee passage, however, depending on the argument of perigee. Values are given in Table 1.12.

In Zimmerwald a GTO with an inclination of 7° may stay for up to 7.2 hours above an elevation of 20°. In Figure 1.16 the velocity field of a GTO object with an inclination of 7° is shown as seen by an observer in Zimmerwald.

1.2.4 Molniya Orbits

Molniya ('lightning') satellites are Russian communication satellites in highly eccentric 12-hour orbits. Their orbits are at the critical inclination of $i = 63.4°$ in order to avoid a drift of the apsidal line, thus keeping the apogee above the northern hemisphere. The typical eccentricity is $e = 0.722$, the corresponding apogee is at an altitude of 39′356 km or at a geocentric distance of 7.2 Earth radii. A satellite in such an orbit remains for 10 hours at a geocentric distance of more than 3 Earth radii. This makes them useful for communication links at high geographic latitudes. Currently more than 100 objects are catalogued in Molniya type orbits. 15 breakups in Molniya orbits were recorded until 1995

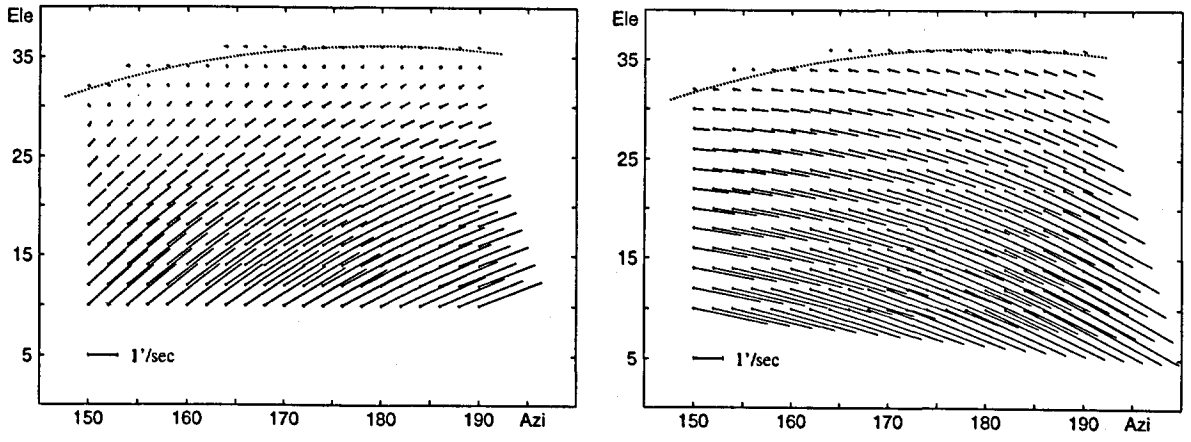

Figure 1.16: Velocity field for GTO objects with orbital inclination of 7° in the Earth-fixed system for an observer in Zimmerwald. Left: receding object, right: approaching object. The dotted line represents the geostationary ring.

(Nauer, 1995). Table 1.13 summarizes the parameters of a typical Molniya orbit (Flury, 1994).

Orbital period	11:58	h
Semimajor axis	26560	km
Eccentricity	0.722	
Height of perigee	1000	km
Height of apogee	39357	km
Inclination	63.4°	
Argument of perigee	270°	

Table 1.13: Typical characteristics for Molniya type orbits.

The velocity of a Molniya satellite at its apogee is 1.6 km/sec which corresponds to an angular velocity of 6.4″/sec relative to the stars or 0.3″/sec in the Earth-fixed system for an observer in Zimmerwald. The maximum elevation of the apogee is about 70° above the northern horizon.

1.2.5 GPS and Glonass Orbits

An important class of satellites is found in Medium Earth Orbits (MEO) in 12-hour orbits: The NAVSTAR-GPS and the GLONASS navigation satellites.

At present 25 NAVSTAR-GPS (Global Positioning System) satellites are operational, several others — in particular all Block I satellites — are in orbit but disactivated. The

GPS satellites are distributed in six orbital planes with equally distributed nodes. The orbital inclination is 63° for Block I and 55° for Block II satellites. The radius of the nearly circular orbits of about 26'560 km results in a revolution period of 11h 58min, i.e. half a sidereal day. The satellites are therefore in a deep 2:1-commensurability with the Earth rotation causing resonance effects in the orbital elements (see Chapter 4).

The Russian counterpart of the American GPS system is the GLONASS (Global Navigation Satellite System). The full configuration of 24 satellites distributed over three orbital planes was complete on Dec. 14, 1996, the launching date for the last three vehicles. Currently (December 1996) 25 satellites are operational (one spare), a number of disactivated or non-functioning satellites are in orbit as well. The semimajor axis of the near-circular orbits is around 25'500 km (about 1'100 km below the GPS satellites) giving an orbital period of 11h 15min. The orbital inclination is about 65°. Two geodetic ('cannonball') satellites, the Etalon satellites equipped with retro-reflectors, are in GLONASS-type orbits.

Medium Earth Transfer Orbits (MTO) exist for the MEOs. Rocket bodies may be found in MTOs which brought MEO objects into orbits.

1.2.6 Other High Altitude Orbits

There are a number of other high satellite orbits of interest for telecommunication and research. Let us give a few examples:

The Tundra orbits have a 24 hour period and an eccentricity of 0.2668 (Flury, 1994). They were studied for Russian telecommunication satellites. The inclination is at the critical value of 63.4°. Perigee and apogee altitudes are 24'537 km and 47'036 km respectively. An object in such an orbit would move with 8.8"/sec relative to the stars and with 2.6"/sec in the Earth-fixed frame at apogee where the space velocity is 2.3 km/s. There are no known objects in such orbits, however.

Other orbits for telecommunication satellites are studied, e.g., 16-hour orbits with critical inclination (Khan, 1993). Six satellites in three orbital planes would be sufficient to provide a continuous service to Europe, Western Europe, Middle East, Japan, Korea, China, North America. The eccentricity of the proposed orbits is 0.53, the apogee height would be at 42'851 km, the perigee height at 8'745 km.

Many scientific missions are launched into high Earth orbits in order to increase the observation window or to avoid the radiation belts. One of the most successful scientific spacecraft, the IUE (International Ultraviolet Explorer) satellite was launched on Jan. 26, 1978, into a 24-hour orbit with an eccentricity of 0.13 and a perigee height of 30'196 km, an apogee height of 41'397 km and an inclination of 35.15° (Macchetto et al., 1978). After more than 18 years of operation the satellite was switched off on Sept. 30, 1996.

The ESA satellite ISO (Infrared Space Observatory) was launched on Nov. 17, 1995 into a highly eccentric 24-hour orbit with a perigee height of 1'038 km, an apogee height of

70'569 km and an inclination of 5.17° (Kessler et al., 1991).

The Russian probe Interball-1 was successfully put into an orbit with a period of 3 days and 20 hours on Aug. 2, 1995. The perigee height is 7'879 km, the apogee height 197'609 km (31 Earth radii, half way to the Moon!), the inclination is 62.9°, the eccentricity is 0.869. At its apogee the satellite moves with only 0.5 km/s which gives an angular velocity of 0.2"/sec relative to the stars and 6.5"/sec in the Earth fixed system. The satellite investigates the Earth's magnetotail (COSPAR Bulletin, **134**, Dec. 95, p. 25.).

The high energy observatory INTEGRAL (International Gamma-Ray Astrophysics Laboratory), a mission in ESA's 'Horizon 2000' scientific long-term plan is scheduled for launch at the beginning of the next century. Because the high energy gamma ray detectors cannot operate within the radiation belts, the satellite will be lifted into a high Earth orbit. ESA plans to launch the satellite with a Russian Proton launcher into a 72-hour orbit with an apogee height of 115'000 km. If the Proton launcher would not be available the satellite would be launched with an Ariane rocket into a 24-hour orbit. (The Russian Space Agency offered the launch of INTEGRAL free of charge in the context of scientific collaboration; Space Science Newsletter, July 94.) The characteristics for the two orbits are given in Table 1.14 (Clausen et al., 1994).

Launcher:	Proton	Ariane
Orbital period	72 h	24 h
Semimajor axis	88'000 km	42'200 km
Eccentricity	0.38	0.76
Height of perigee	48'000 km	4'000 km
Height of apogee	115'000 km	68'000 km
Inclination	51.6°	65°
Argument of perigee	270°	270°

Table 1.14: Orbital parameters for the high energy observatory INTEGRAL for the options of a Proton or an Ariane launcher.

2 Initial Orbit Determination

The purpose of initial orbit determination for objects orbiting the Earth is to obtain a first estimate for the orbital elements of an object for which only a few observations were acquired within a few minutes, e.g. two astrometric positions of an object on the detection frame and on the confirmation frame exposed immediately after the first one. Initial orbital elements may be used to identify an object, e.g., if one is searching for a 'lost' object. They are necessary for extrapolating the object's position for a later recovery in the same night. Additional astrometric positions may then be used to refine the orbit. Initial orbital elements are also required as starting values for an orbit improvement process. Last but not least, the initial elements determined for objects observed during a survey campaign may be used for a statistical analysis of the distribution of the elements and for population studies of objects in given regions of space.

In the first section below three algorithms for the determination of an initial orbit are presented, one for the determination of a circular orbit and two for the determination of elliptic orbits. All three algorithms are intended to be used for short observed arcs only. In the second section emphasis is put on the performance of the algorithms. We will see that even for elliptic orbits the circular elements are a valuable tool for identification and ephemeris calculation for high orbiting objects.

2.1 The Algorithms

2.1.1 Circular Orbit

The determination of a circular orbit using two observations is well known and straightforward: For both observation times t_1 and t_2 the geocentric positions $\boldsymbol{R}_1$ and $\boldsymbol{R}_2$ of the observer are assumed known in addition to the observation unit vectors $\boldsymbol{e}_1$ and $\boldsymbol{e}_2$ pointing from the observer to the object. Both pairs of vectors are related to the unknown geocentric position vectors $\boldsymbol{r}_1$ and $\boldsymbol{r}_2$ of the satellites by

$$\boldsymbol{r}_1 = \boldsymbol{R}_1 + \Delta_1 \boldsymbol{e}_1 \quad \text{and} \quad \boldsymbol{r}_2 = \boldsymbol{R}_2 + \Delta_2 \boldsymbol{e}_2 \quad , \tag{2.1}$$

where the topocentric distances Δ_1 and Δ_2 at the two observation epochs are unknown. Assuming that the observations must lie on a circular orbit with radius a we may write

$$\boldsymbol{r}_1^2 = a^2, \qquad \boldsymbol{r}_2^2 = a^2, \qquad \boldsymbol{r}_1 \cdot \boldsymbol{r}_2 = a^2 \cos\varphi \tag{2.2}$$

where φ is the angle between the two geocentric position vectors. Using Kepler's third law we get

$$\varphi = n(t_2 - t_1) \qquad \text{with} \qquad n^2 a^3 = GM. \tag{2.3}$$

While the eqns. (2.1) and (2.2) represent pure geometrical information, eqn. (2.3) introduces the dynamics into the solution. The eleven scalar conditions in eqns. (2.1) to (2.3)

represent a non-linear system for the eleven unknowns that were introduced. The system may be solved for the unknown radius a by determining the zeros of the function

$$B(a) \equiv \boldsymbol{r}_1(a) \cdot \boldsymbol{r}_2(a) - a^2 \cos n(t_2 - t_1) \quad . \tag{2.4}$$

The $\boldsymbol{r}_i(a)$ are computed by solving the first two eqns. in (2.2) for Δ_i as a function of a and introducing these values into eqn. (2.1).

Having found a root of eqn. (2.4) the inclination i and the right ascension of the ascending node Ω may be calculated from vectors $\boldsymbol{r}_1$ and $\boldsymbol{r}_2$ (using the vector product) as well as the argument of latitude u for one of the observation times (angle measured in the orbital plane from the ascending node to the position at times t_1 resp. t_2). The algorithm is implemented in the FORTRAN subroutine OCCORD.

2.1.2 Elliptic Orbit

With three observations available it is possible to determine all six elements of a Keplerian orbit. Similar to the procedure discussed in the previous section the problem may be reduced to the determination of the roots of a function with one argument. The algorithm was developed by Beutler et al. (1987) for minor planets and comets in heliocentric orbits.

Let us assume that for three epochs t_1, t_2, t_3 the geocentric position vectors $\boldsymbol{R}_1$, $\boldsymbol{R}_2$, $\boldsymbol{R}_3$ of the observer and the observed unit vectors $\boldsymbol{e}_1$, $\boldsymbol{e}_2$, $\boldsymbol{e}_3$ are known in some (quasi-)inertial coordinate system. The three geocentric position vectors $\boldsymbol{r}_1$, $\boldsymbol{r}_2$, $\boldsymbol{r}_3$ are written in the form

$$\begin{aligned} \boldsymbol{r}_1 &= \boldsymbol{R}_1 + \Delta_1 \boldsymbol{e}_1, \\ \boldsymbol{r}_2 &= \boldsymbol{R}_2 + \Delta_2 \boldsymbol{e}_2, \\ \boldsymbol{r}_3 &= \boldsymbol{R}_3 + \Delta_3 \boldsymbol{e}_3 \end{aligned} \tag{2.5}$$

introducing three unknown topocentric distances Δ_1, Δ_2, Δ_3. As the Keplerian motion takes place in a plane we may write the position vector at any time as a linear combination of the position vector and velocity vector at time t_1

$$\boldsymbol{r}(t) = f(t)\boldsymbol{r}_1 + g(t)\boldsymbol{v}_1. \tag{2.6}$$

One easily verifies that functions $f(t)$ and $g(t)$ are solutions of the initial value problem

$$\begin{array}{lcllcl} f^{(2)} & = & -GM\dfrac{f}{r^3} & g^{(2)} & = & -GM\dfrac{g}{r^3} \\ f(t_1) & = & 1 & g(t_1) & = & 0 \\ f^{(1)}(t_1) & = & 0 & g^{(1)}(t_1) & = & 1 \quad . \end{array} \tag{2.7}$$

The solutions may be written in the form of a Taylor series

$$f(t) = \sum_{k=0}^{\infty} \frac{1}{k!} f^{(k)}(t_1) \cdot (t - t_1)^k \qquad g(t) = \sum_{k=0}^{\infty} \frac{1}{k!} g^{(k)}(t_1) \cdot (t - t_1)^k \tag{2.8}$$

with the coefficients

$$\begin{array}{lcllcl} f^{(0)} & = & 1 & g^{(0)} & = & 0 \\ f^{(1)} & = & 0 & g^{(1)} & = & 1 \\ f^{(2)} & = & -\mu & g^{(2)} & = & 0 \\ f^{(3)} & = & 3\mu\sigma & g^{(3)} & = & -\mu \\ f^{(4)} & = & -15\sigma^2\mu + \varepsilon\mu + \mu^2 & g^{(4)} & = & 6\sigma\mu \\ f^{(5)} & = & 105\sigma^3\mu - \sigma(45\varepsilon\mu + 15\mu^2) & g^{(5)} & = & -45\sigma^2\mu + 9\varepsilon\mu + \mu^2 \\ \cdots & & & \cdots & & \end{array} \tag{2.9}$$

where the so-called fundamental invariants

$$\mu = GM/r^3, \qquad \sigma = \boldsymbol{r}_1 \cdot \boldsymbol{v}_1/r_1^2, \qquad \varepsilon = v_1^2/r_1^2 - \mu, \tag{2.10}$$

are only functions of r_1^2, $\boldsymbol{r}_1 \cdot \boldsymbol{v}_1$, and v_1^2. Up to orders 2 resp. 3 the series (2.8) for f resp. g are in fact only functions of r_1^2.

Inserting eqn. (2.6) into eqn. (2.5) we obtain the equations

$$\begin{array}{rrrrcl} \boldsymbol{r}_1 & -\boldsymbol{e}_1\Delta_1 & & & = & \boldsymbol{R}_1 \\ f(t_2)\boldsymbol{r}_1 + g(t_2)\boldsymbol{v}_1 & & -\boldsymbol{e}_2\Delta_2 & & = & \boldsymbol{R}_2 \\ f(t_3)\boldsymbol{r}_1 + g(t_3)\boldsymbol{v}_1 & & & -\boldsymbol{e}_3\Delta_3 & = & \boldsymbol{R}_3. \end{array} \tag{2.11}$$

If the coefficients f and g in eqn. (2.11) were known this system of equations would be linear, i.e., one could solve for the nine unknowns, the components of $\boldsymbol{r}_1$ and $\boldsymbol{v}_1$ and the topocentric distances Δ_1, Δ_2, Δ_3. In fact, if we assume that r_1^2 is given, we can compute f and g to second and third order respectively and solve the system of equations (2.11). We obtain $\boldsymbol{r}_1$ and $\boldsymbol{v}_2$ and may then compute μ and ε. Iteratively, we then compute improved values for f and g and so we obtain the solution of eqn. (2.11) to any desired order. In other words, $\boldsymbol{r}_1$, $\boldsymbol{v}_1$, and Δ_1, Δ_2, Δ_3 are only functions of the one parameter r_1^2!

If r_1^* is a solution of eqn. (2.11), then the square of the vector $\boldsymbol{r}_1$ that we get by iteratively solving eqn. (2.11) must be equal to $(r_1^*)^2$. We therefore define the function

$$B((r_1^*)^2) \equiv (r_1^*)^2 - \boldsymbol{r}_1 \cdot \boldsymbol{r}_1 \tag{2.12}$$

where $\boldsymbol{r}_1$ is computed by iteratively solving eqns. (2.11) with $(r_1^*)^2$ as input parameter. The roots of the function (2.12) are the solutions of the problem. Looking for roots in a given range of geocentric distances provides all solutions in this range.

As a result the algorithm gives the geocentric position $\boldsymbol{r}_1$ and velocity $\boldsymbol{v}_1$ of the object (at epoch t_1) using the observations from three epochs. These vectors may then be transformed to osculating Keplerian elements by a standard procedure. The algorithm is implemented in the FORTRAN subroutine OCFORD.

2.1.3 Elliptic Orbit with Given Semimajor Axis and Eccentricity

The determination of the eccentricity of an orbit using observations covering only a short time interval is rather delicate, as will be seen later (Section 2.2.3). Therefore an algorithm was developed which determines an eccentric orbit with fixed, pre-defined values for eccentricity e and semimajor axis a. The algorithm is based on the procedure presented in Section 2.1.2 and requires only two observations. The algorithm may, e.g., be used for the determination of the orbit of a detected GTO object for which approximate values for semimajor axis and eccentricity may be assumed known.

Let us write the three fundamental invariants (2.10) as a function of the geocentric distance r_1 at the first observation epoch t_1. The first invariant μ has already the required form. From the energy equation we get the relation between r_1 and v_1 which gives us the third invariant

$$\varepsilon = \frac{v_1^2}{r_1^2} - \mu = \frac{GM}{r_1^2}\left(\frac{2}{r_1} - \frac{1}{a}\right) - \mu = \mu\left(1 - \frac{r_1}{a}\right). \tag{2.13}$$

After some transformations we get the relation

$$\sigma^2 = \frac{e^2\mu^2 - \varepsilon^2}{\mu - \varepsilon}. \tag{2.14}$$

With $a(1-e) \leq r_1 \leq a(1+e)$ we know from eqn. (2.13) that ε is within the limits $-e\mu \leq \varepsilon \leq e\mu$. Thus we are sure that eqn. (2.14) is neither singular nor negative for any $e < 1$. Taking the square root of eqn. (2.14) we have a sign ambiguity, indicating that the sign of the scalar product $\boldsymbol{r}_1 \cdot \boldsymbol{v}_1$ is undefined. As a matter of fact we will always find two solutions for two observations for one and the same semimajor axis and eccentricity, one for a receding object (sign +), the other for an approaching object (sign −).

As in the previous section we start with an adopted value for r_1^2 and compute the fundamental invariants μ, σ, and ε from eqns. (2.13) and (2.14) with pre-defined values for semimajor axis a and eccentricity e. For σ we have to select a sign. Using eqn. (2.6) we write down the two equations

$$\begin{aligned} \boldsymbol{r}_1 &= \boldsymbol{R}_1 + \Delta_1 \boldsymbol{e}_1 \\ f_2\boldsymbol{r}_1 + g_2\boldsymbol{v}_1 &= \boldsymbol{R}_2 + \Delta_2 \boldsymbol{e}_2. \end{aligned} \tag{2.15}$$

Multiplying both equations with $\boldsymbol{r}_1$ we get

$$\begin{aligned} r_1^2 &= R_1^2 + 2\Delta_1 \boldsymbol{R}_1 \cdot \boldsymbol{e}_1 + \Delta_1^2 \\ (f_2 + \sigma g_2) r_1^2 &= \boldsymbol{R}_1 \cdot \boldsymbol{R}_2 + \Delta_1 \boldsymbol{R}_2 \cdot \boldsymbol{e}_1 + \Delta_2 \boldsymbol{R}_1 \cdot \boldsymbol{e}_2 + \Delta_1 \Delta_2 \boldsymbol{e}_1 \cdot \boldsymbol{e}_2 \end{aligned} \tag{2.16}$$

from which the two topocentric distances Δ_1 and Δ_2 are computed. By back-substitution into eqns. (2.15) we obtain the vectors $\boldsymbol{r}_1$ and $\boldsymbol{v}_1$ which allow us finally to compute the osculating elements at time t_1. If the adopted value for r_1^2 introduced initially into the

algorithm was correct, the semimajor axis a_{out} and the eccentricity e_{out} that we get from eqns. (2.16) are the same as the input values a and e. To find the solution we can therefore define the two functions

$$B_1(r_1^2) = a_{out} - a \qquad \text{and} \qquad B_2(r_1^2) = e_{out} - e \tag{2.17}$$

and determine their roots in a range of r_1. Each root of the two functions corresponds to two solutions (one for an approaching, the other for an receding object) of orbits with given semimajor axis and eccentricity which represents the two observations used for their determination. The algorithm is implemented in the FORTRAN subroutine OCEORD.

2.2 How Accurate is an Initial Orbit?

In order to come up with the observation schedule for newly discovered objects it is necessary to know how far into the future an initial orbit can be used without loosing the object. The performance of the three algorithms is studied in the following sections and, based on the results, an optimal observation scenario is proposed which is optimal in the sense that an orbit with maximum accuracy is generated with a minimum number of observations.

In our context we are interested mainly in high orbiting satellites, in particular in satellites in the geostationary ring (GEO) and in satellites in geostationary transfer orbits (GTO).

2.2.1 Methods of Analysis

Because for all algorithms the number of parameters equals the number of observations it is not possible to compute formal errors for the elements. The three algorithms generate orbits which exactly represent the observations used and observational errors can therefore not be estimated.

If the observation error (i.e. the rms error of the two components of the astrometric positions) is assumed known, it is possible to define formal errors for the estimated parameters by a covariance analysis. The problem of determining the elements for an initial orbit may be formulated as a general parameter estimation problem solved by means of the method of least squares. Because the numbers of parameters and observations are equal the observation rms cannot be computed, but a realistic value for the observational rms errors may be adopted. The first design matrix for the three problems may be set up, the normal equation matrix computed and inverted. This procedure gives the variance-covariance matrix after multiplication with the a priori variance.

In practice, due to numerical problems, the inversion of the normal equation matrix is difficult because – due to the fact that the observations are usually separated by a very short time interval of the order of one minute – the matrix is almost singular. It is,

however, possible to compute analytically the inverse of the normal equation matrix! Since the numbers of parameters p and observations o are equal, the first design matrix is quadratic, though nearly singular. The components of the inverse first design matrix, i.e., the derivatives dp_i/do_k of orbit parameter i with respect to observation k may be calculate analytically using the formulas given in Section 2.1. Multiplying the matrix with its transposed and with the a priori variance eventually provides the variance-covariance matrix for the parameters.

Because the analytical computation of the derivatives dp_i/do_k is quite tedious the derivatives were calculated numerically. The resulting formal errors are in excellent agreement with the values obtained by Monte Carlo simulations and are given in Schildknecht et al. (1995a). Results will be presented in the subsequent sections below.

Using the full covariance information the formal errors are transformed into the *alongtrack* and *crosstrack* components projected onto the celestial sphere, and studied as a function of time. The formal error in position is, however, not very interesting because the difference between the true orbit and the initial orbit is after a short time dominated by systematic errors, e.g., by the adoption of a circular orbit. (The term 'short time' will be specified for the different algorithms in the following sections.) A more interesting quantity is the evolution of the difference between the true and the initial orbit with time as a function of the orbital parameters of the 'true' orbit. Of particular interest is the answer to questions such as how long an object with given (non-zero) eccentricity will remain within a given field of view centered at an ephemeris generated from initial elements.

Simulations: In order to study random and systematic errors as a function of the elements of the true orbit Monte Carlo simulations were used to generate geostationary (GEO) and geostationary transfer orbits (GTO). All or some of the elements were varied assuming a uniform random distribution within a given range. The ranges within which the elements were varied are given in Table 2.1. The mean longitude was fixed for all orbits in order to simulate observations around a given position at the sky (ele $\simeq 35°$, azi $\simeq 200°$).

Geostationary Orbits (GEO)	Geostationary Transfer Orbits (GTO)
Semimajor axis $a = 42'000$ to $42'300$ km	Apogee distance $Q = 40'000$ to $43'000$ km
Eccentricity $e = 0.0$ to 0.1	Perigee height $h = 300$ to 600 km
Inclination $i = 0$ to $15°$	Inclination $i = 5$ to $25°$
R.A. of ascending node $\Omega = 0$ to $360°$	Argument of latitude $u = -40$ to $40°$, 140 to $220°$
Argument of perigee $\omega = 0$ to $360°$	Mean anomaly $M = 150$ to $210°$

Table 2.1: Range of elements used for Monte Carlo generation of GEO and GTO orbits. The mean longitude of the first observation was in all cases fixed at $\ell = 307°$.

For the simulation of near geostationary orbits the Keplerian elements were varied within reasonable ranges to get typical orbits. For geostationary transfer orbits the perigee height h and the apogee distance $Q = a(1 + e)$ were varied within reasonable ranges. The ranges in semimajor axis a and eccentricity e are set to $a = 23340 - 24990$ km and $e = 0.70 - 0.73$, typical values for this type of orbit. The inclination was varied between $i = 5°$ and $25°$ which corresponds roughly to the geographical latitudes of the sites from which geostationary satellites are launched. The mean anomaly M for the first observation time was varied within $30°$ or $60°$ around apogee, the argument of latitude u within $40°$ around $0°$ and $180°$ in order to generate the observations close to the ascending and descending node respectively.

Two or three observations separated by different time intervals were generated. The observations always were at least $20°$ above horizon. These observations were then used to perform a covariance analysis in order to obtain formal errors. Alternatively the simulated observations were used or for an initial orbit determination in order to study systematic errors.

2.2.2 Circular Orbit

Given a circular orbit determined from two observations with given rms error σ of the observations and separated by a small time interval Δt. How well does this orbit represent the true orbit of the object? How fast does the determined orbit deviate from the true orbit for different eccentricities of the true orbit? Let us first consider the formal errors of the circular elements and their differences with respect to the true elements in order to answer these questions.

Formal Errors in the Elements: The formal error of the semimajor axis a (left) and of the inclination i (right) for GEO type orbits are given as a function of the eccentricity e in Figure 2.1. The corresponding figures for the other two elements would look very much like the figure for the inclination (Figure 2.1, right). Each of the 180 points represents the result of one Monte Carlo simulation with different sets of elements for the 'true' orbit. The time interval between the two observations used for the orbit determination was $\Delta t = 1$ minute, the adopted value for the rms error of the observations was $\sigma = 0.5''$.

The formal errors in the elements do not show a strong dependence on the eccentricity of the true orbit. This is not surprising because the formulae for computing the formal errors do not contain the eccentricity. Any dependence can only be introduced by slight changes in the observing geometry (object observed at different locations relative to perigee).

For $\Delta t = 1$ min the formal error in the semimajor axis a is around 20 km, the maximum formal errors for inclination i and for $\Omega \sin i$ are about $0.045°$; for the mean longitude ℓ it is $0.005°$ for inclinations below $15°$ (see Table 2.2). The values are proportional to Δt^{-1}.

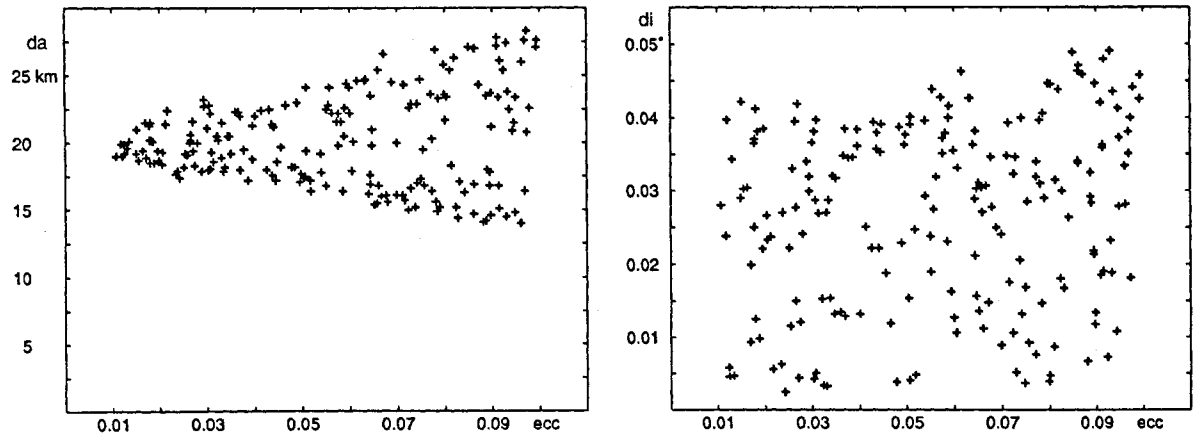

Figure 2.1: Formal errors of the semimajor axis (left) and the inclination (right) as a function of eccentricity of the true orbit. The simulated observations were separated by 1 minute, a rms value of 0.5″ was assumed for the observations. Each point represents the result of one (of 180) Monte Carlo simulations.

These results are easily understood: The observational uncertainty of the two observations introduces an error in the mean motion of $\sqrt{2}\sigma/\Delta t$ which in turn transforms via Kepler's third law into an error in the semimajor axis. I.e., we have for a circular orbit

$$\Delta a = \frac{2a}{3n}\frac{\sqrt{2}\sigma}{\Delta t} \approx 22 \text{ km} \quad . \tag{2.18}$$

Because the observation distance is not 42'000 km but only about 38'000 km, this value is reduced to 20 km which is the mean value obtained from the simulations.

The formal errors of inclination and node depend on the argument of latitude. The maximum formal error in the inclination is obtained when the object is observed close to the nodes. The formal error in the ascending node on the other hand is minimum in these cases. Maximum values result when the object is observed at maximum elongation from

Maximum formal errors for $\sigma_{obs} = 0.5''$, $i < 15°$				
Element:	a	i	$\Omega \sin i$	ℓ
$\Delta t = 1$ min:	22 km	0.045°	0.045°	0.005°
$\Delta t = 2$ min:	11 km	0.022°	0.022°	0.003°

Table 2.2: Maximum formal errors for the four circular elements obtained from simulations adopting an observational error of 0.5″ and a separation of 1 minute and 2 minutes for the two observation epochs.

the equatorial plane. A simple geometrical consideration gives the formula

$$\Delta i = \frac{180°}{\pi}\frac{\sqrt{2}\sigma}{n\Delta t} \simeq 0.09°\frac{\sigma(")}{\Delta t(\text{min})} \tag{2.19}$$

for the maximum formal error of the inclination i.

The formal error in the mean longitude ℓ depends on the argument of latitude and the inclination. It is comparable to the rms error of the observations if the object is observed close to the nodes. If the object is observed at maximum elongation from the equatorial plane (i.e. at about 90° from the nodes), the formal error in the mean longitude grows linearly with increasing inclination. For $i = 15°$ a maximum value of 0.005° is reached. This increase of the formal error is due to the error in the position of the node.

The formal errors of the parameters computed by covariance studies are by definition linear functions of the observation rms errors. From eqns. (2.18) and (2.19) one easily concludes that there must be a linear dependence of the formal errors of semimajor axis and inclination on Δt^{-1}. Simulations confirm this dependence for all four elements.

Difference Between Circular and True Elements: While the formal errors of the elements are based on statistics (errors introduced by the observation errors) the difference of the circular elements (based on exact observations) and the true elements are of systematic nature. As opposed to the formal errors the difference of the elements does not depend on the observation errors but on the eccentricity of the true orbit. For an eccentricity of 0.001 and 0.01 the maximum differences of the true and the circular elements is given in Table 2.3.

Maximum differences of the elements				
Element:	a	i	$\Omega \sin i$	ℓ
$e = 0.001$	56 km	0.007°	0.007°	0.115°
$e = 0.01$	560 km	0.07°	0.07°	1.15°

Table 2.3: Maximum difference between the four circular elements obtained from simulations and the true elements of orbits with an eccentricity of 0.001 and 0.01.

The differences for all elements are linear functions of the true eccentricity. For the semimajor axis this may be understood in the following way: If an object in an eccentric orbit is observed in its perigee (or apogee) and a circular orbit is assumed, a maximum systematic error in the mean motion arises with a value of

$$\Delta n = \dot{\nu}_{\substack{\text{perigee}\\\text{apogee}}} - n = \left(\frac{\sqrt{1-e^2}}{(1 \mp e)^2} - 1\right) n \quad , \tag{2.20}$$

where ν is the true anomaly, n the mean motion. With this expression we get for the maximum difference in the semimajor axis to the first order in e

$$\Delta a = \frac{4}{3} ae \tag{2.21}$$

which gives 56 km for $a = 42165$ km and $e = 0.001$. The difference between circular and true longitude may be written as

$$\Delta \ell = \nu - M = 2e \sin M + O(e^2) \quad , \tag{2.22}$$

where M is the mean anomaly. The maximum value for this difference is therefore $\Delta \ell = 2e$ which gives 0.115° for e=0.001. The systematic differences in i and Ω result because the object is not observed from the geocenter. They depend on the actual observation geometry.

As stated above, the differences of the elements, i.e. the systematic errors do not depend on the observation rms error σ nor on the time interval Δt between the two observation epochs.

Difference of Circular and True Elements for GTO objects: If the observed satellite is not a GEO but a GTO object the algorithm would not fail to generate elements of a circular orbit representing the two observations. The elements determined would, however, be heavily biased. For an object observed in the apogee of an orbit with eccentricity e the algorithm interprets the rate of change in the true anomaly as the mean motion n of a circular orbit. Solving for the radius of this circular orbit we obtain

$$a_c = a \left(\frac{1+e}{1-e} \right)^{2/3} \quad . \tag{2.23}$$

For a GTO object with $a \sim 24'500$ km and $e \sim 0.7$ a radius of the circular orbit of about $a_c \sim 78'000$ km would result. A somewhat more precise estimate taking into account the rotation of the Earth during the observations (and thus modifying the angular velocity of the object) gives a value of $a_c \sim 63'600$ km. The difference to the 'true' semimajor axis would be around 39'000 km!

Circular elements for observations of GTO objects were computed with 200 Monte Carlo simulations. The objects were assumed to be observed within 30° in mean anomaly from the apogee. The range of the semimajor axis determined is 60'000 km to 67'000 km. For the inclination the range of values covers ±2° around the 'true' value. The results are independent on the time interval between the two observations and the observation rms errors even for GTO objects.

There can be little doubt, however, that an object for which a semimajor axis of about 65'000 km is computed assuming a circular orbit, moves around the Earth in a highly eccentric orbit just because there are currently no objects on circular orbits with such radii (i.e., on circular 44-hour orbits). GTO objects are therefore easily distinguished from GEO objects and the operator may invoke an elliptic orbit determination algorithm (see below) to get a more realistic result.

Formal Errors in Position: Using the full covariance information of the estimated orbit parameters the formal errors of the object positions at the celestial sphere may be computed in alongtrack and crosstrack direction as a function of time. The evolution of the formal error is shown Figure 2.2 for a number of circular orbits (in alongtrack (left) and crosstrack directions (right)). The observations were generated from orbits with eccentricity $e = 0.001$: the other elements were generated at random. Obviously the variation of the elements leaves the character of the curves essentially unchanged. The formal alongtrack error grows linearly with about 0.28°/day corresponding to an error in the semimajor axis of about 22 km while the crosstrack error shows a periodic behaviour with a maximum value of about 0.045°corresponding to the error in inclination. The slope of the two curves at $t = 0$ is the same (observe the different scales in the figures).

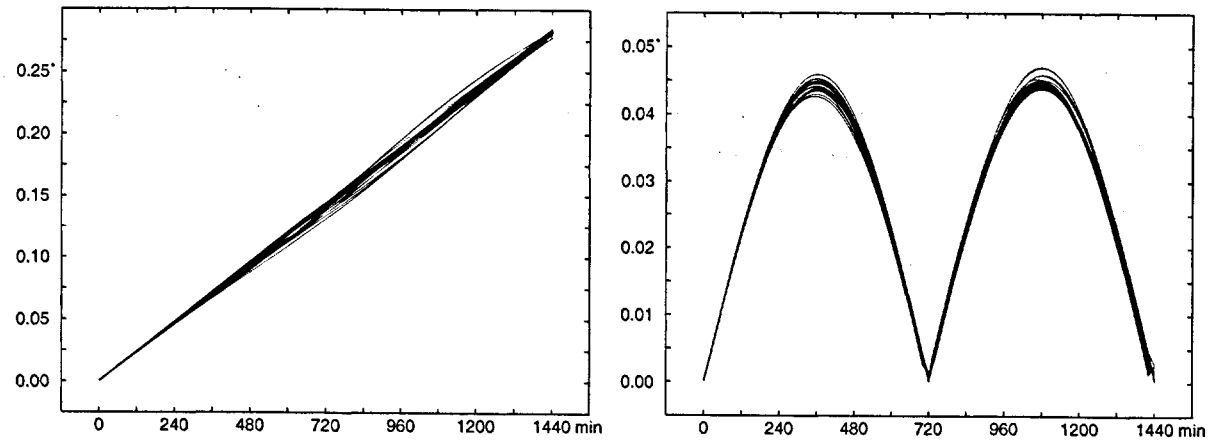

Figure 2.2: Formal errors in position as a function of time in alongtrack (left) and crosstrack directions (right). Different curves correspond to orbits with different elements and a fixed eccentricity $e = 0.001$. Observation rms error was assumed to 0.5″.

Because the formal errors do not depend on the eccentricity, the errors in position do not depend on the eccentricity either. For relatively high eccentricities (see Figure 2.3 for $e = 0.1$) we observe a large variation of the drift rates for the circular orbits, because some of the original orbits are observed close to perigee, others close to apogee. The revolution period for the determined circular orbits therefore varies in a big range and with it the periods and amplitudes of the crosstrack error.

The formal errors of the satellite position are proportional to the observation rms error and proportional to Δt^{-1}, where Δt is the time interval between the two observations. The dependence of the alongtrack (left) and crosstrack errors (right) on Δt is given in Figure 2.4.

Systematic Errors in Position: Two objects, one in an eccentric 'true' orbit, the other in a circular orbit exactly representing two observations of the eccentric orbit, will

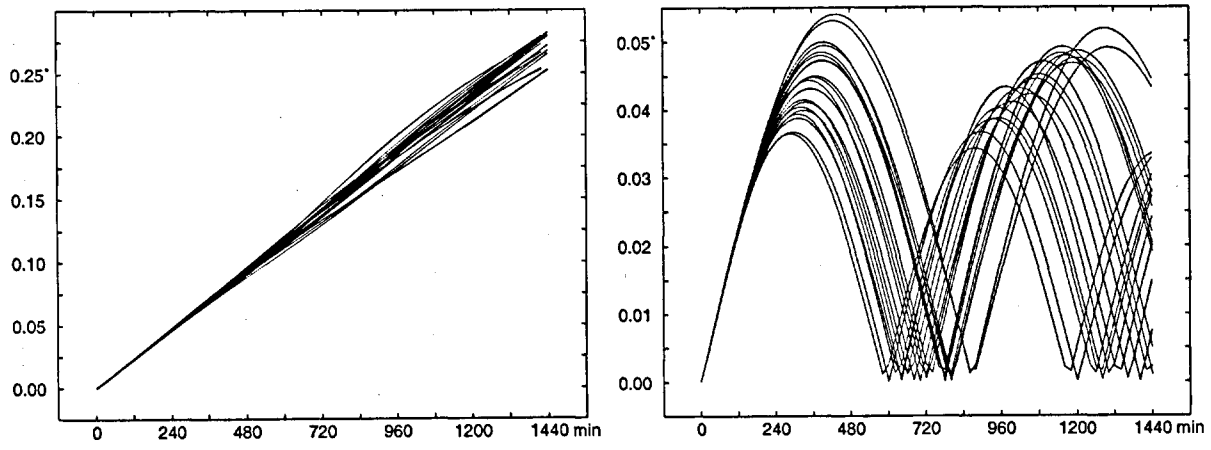

Figure 2.3: Formal errors in position as a function of time in alongtrack (left) and crosstrack directions (right). Different curves correspond to orbits with different elements and a fixed eccentricity of $e = 0.1$. Observation rms error was assumed to 0.5".

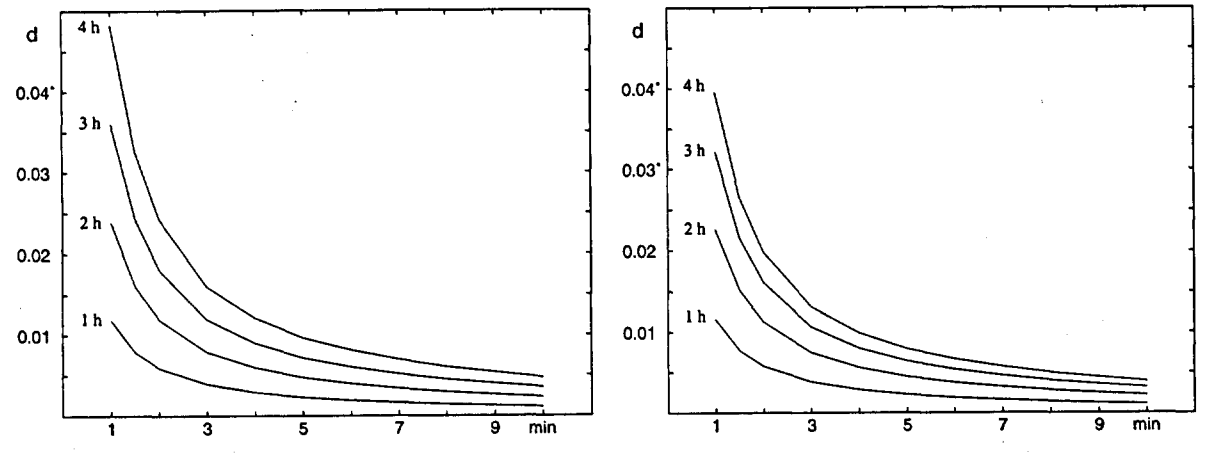

Figure 2.4: Formal errors in alongtrack (left) and crosstrack directions (right) as a function of the time interval Δt between the observations. Different curves correspond to an extrapolation of the orbit for 1, 2, 3, and 4 hours.

drift away from each other at a rate that depends on the eccentricity of the true orbit. In Figures 2.5 and 2.6 the difference between the two orbits is shown as a function of time in alongtrack and crosstrack direction for orbits with an eccentricity of $e = 0.001$ and $e = 0.1$ respectively. The different curves correspond to 'true' orbits with fixed eccentricity but otherwise random elements.

The difference (systematic error) in crosstrack direction is always one to two orders of magnitude smaller that the corresponding difference in alongtrack direction. The former

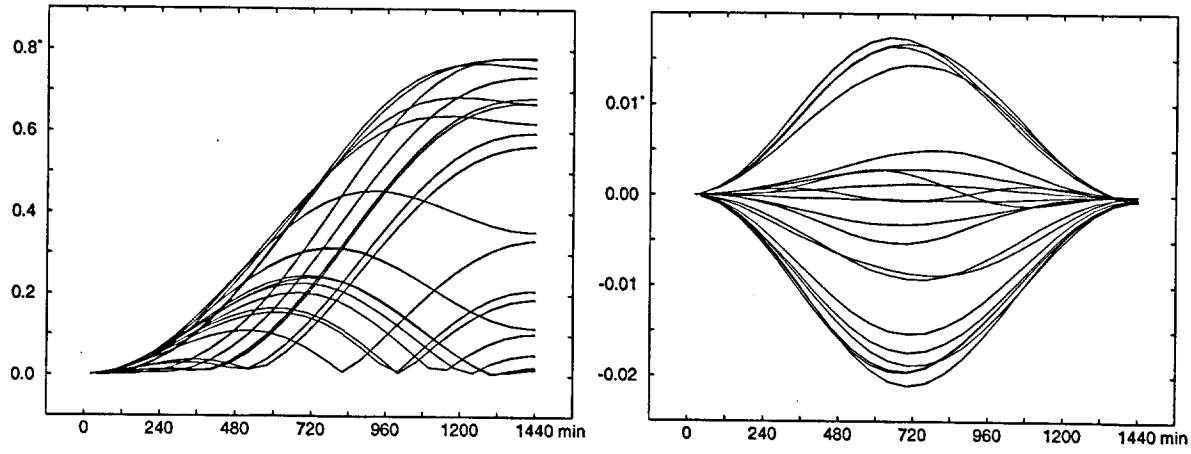

Figure 2.5: Difference in degrees between orbits with eccentricity $e = 0.001$ and a circular orbit determined from two observations on this orbit as a function of time in alongtrack (left) and crosstrack direction (right). Different curves correspond to reference orbits with different (random) elements but the same eccentricity.

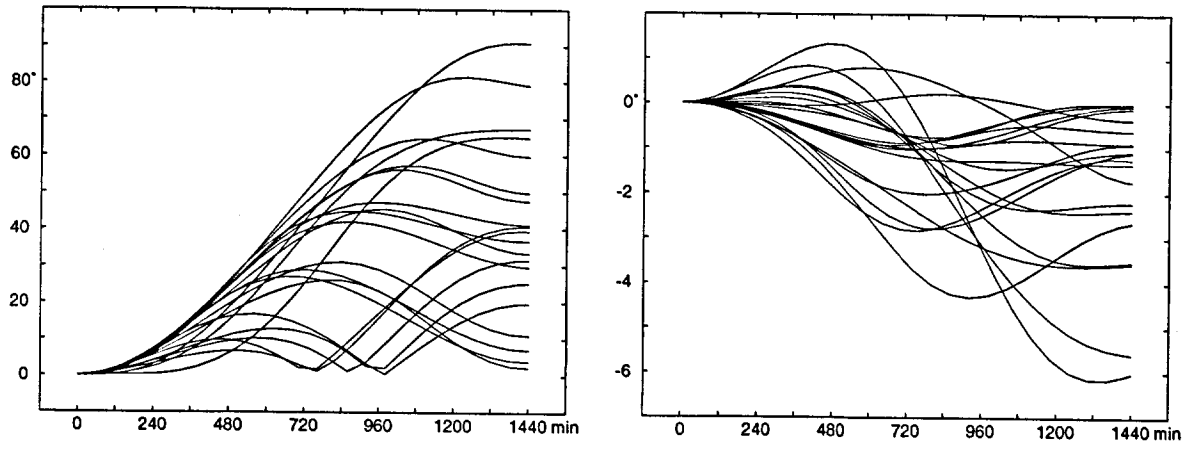

Figure 2.6: Difference in degrees between orbits with with eccentricity $e = 0.1$ and a circular orbit determined from two observations on this orbit as a function of time in alongtrack (left) and crosstrack direction (right). Different curves correspond to reference orbits with different (random) elements but the same eccentricity.

shows a periodic behaviour (the drift observed for $e = 0.1$ stems from a slightly systematic behaviour of the circular orbit determination algorithm) while the latter increases with time. The maximum rate occurs (as expected) if observations near perigee or apogee are used for the orbit determination. The drift may reach 0.8°/day for $e = 0.001$ and 90°/day for $e = 0.1$ corresponding roughly to the maximum systematic error in the semimajor axis

given in eqn. (2.21).

In Figure 2.7 (left) we see the maximum formal error in alongtrack direction as a function of time for eccentricities between $e = 0$ and $e = 0.01$ (i.e. the envelopes of curves such as those in Figure 2.5 and Figure 2.6, right). The curves have a similar shape but are scaled in the ordinate direction. In Figure 2.7 (right) we see the alongtrack error for an extrapolation of 1, 2, 3, and 4 hours as a function of eccentricity. The dependence of the systematic error in position on the eccentricity is obviously linear. The same is true for the crosstrack error but the slope is much smaller.

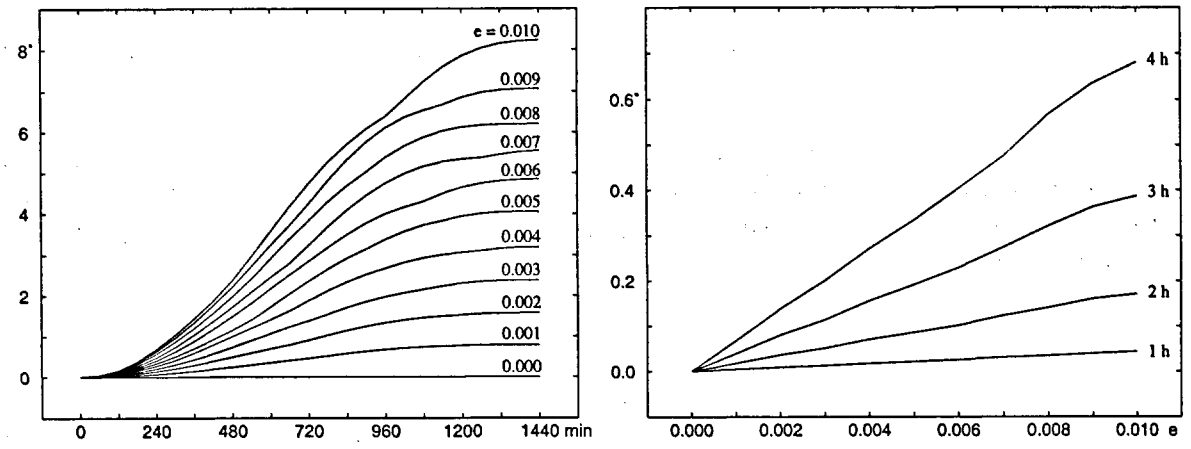

Figure 2.7: Maximum alongtrack difference in degrees between circular orbits and reference orbits with different eccentricities as a function of time (left) and eccentricity (right). The four curves in the right diagram show the difference after extrapolation for 1, 2, 3, and 4 hours.

The maximum systematic errors are given in Table 2.4 in alongtrack and crosstrack position after 1, 2, 3, and 4 hours for reference orbits with eccentricity $e = 0.001$ and $e = 0.01$. For comparison the corresponding formal errors are given assuming an observation rms error of 0.5". For short extrapolation times the formal errors are dominant, for longer ones the systematic errors.

Systematic Errors in Position for GTO Objects: A circular orbit determined from observations of a GTO object represents the 'true' orbit only over a short time around the observation epochs. In Figure 2.8 we see the difference between 'true' and circular orbit as a function of time. The left part of the figure covers an extrapolation interval of 5.5 hours, the right part magnifies the first 90 minutes. Each curve represents one of 40 Monte Carlo simulations of a GTO object observed within 30° in mean anomaly from its apogee. As expected the difference of the two orbits starts to increase rapidly after about 2 to 3 hours. Interestingly enough, the object remains within one degree of its circular ephemeris position for about one hour for most simulated orbits!

	systematic error				formal error			
after	1h	2h	3h	4h	1h	2h	3h	4h
alongtrack								
e=0.001	.004°	.017°	.039°	.067°	.012°	.024°	.036°	.049°
e=0.01	.043°	.17°	.39°	.68°	.012°	.024°	.036°	.049°
crosstrack								
e=0.001	.0003°	.001°	.003°	.004°	.012°	.023°	.032°	.040°
e=0.01	.003°	.013°	.027°	.046°	.012°	.023°	.032°	.040°

Table 2.4: Maximum systematic and formal errors in alongtrack and crosstrack directions after 1, 2, 3, and 4 hours for circular orbits determined from observations based on orbits with eccentricity $e = 0.001$ and $e = 0.01$. Observation rms error was assumed to 0.5″.

The maximum total angular difference as well as the crosstrack offset (with respect to the determined circular orbit) of GTO and circular orbit are given in Table 2.5 for extrapolation time intervals ranging between 10 minutes and 2 hours. For extrapolation times longer than about one hour the time interval on which the circular orbit determination is based is not essential, the systematic error dominates anyhow. For extrapolations below one hour the representation of the orbit is improved, however, by a longer observation time interval. An observation time interval of 1 minute gives a residuum of 1′ after 10 minutes. If after 10 minutes the object is observed again and a new circular orbit is determined the formal error after 20 minutes is 2′ instead of 4′.

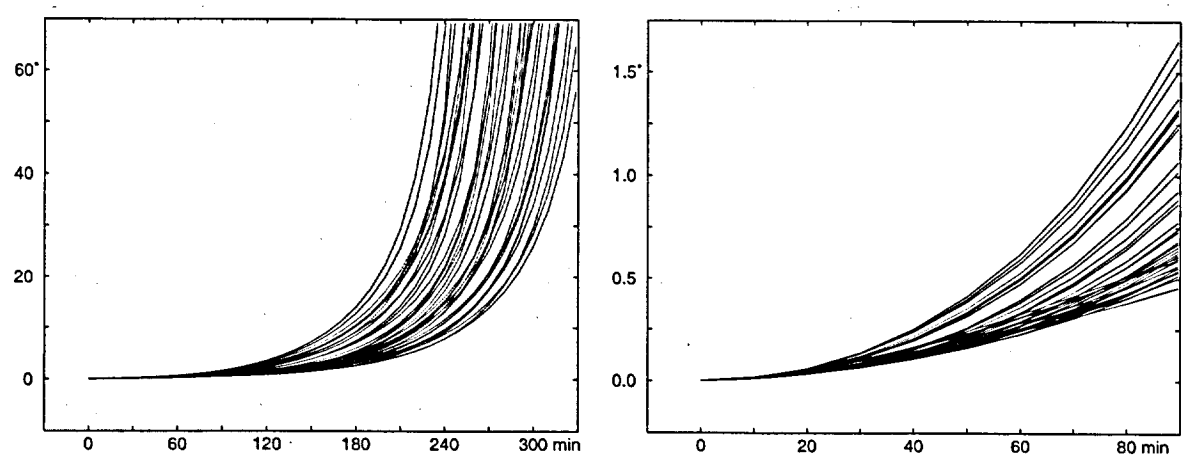

Figure 2.8: Difference between 'true' GTO orbits and circular orbit representing two observations spaced by 1 minute and located within 30° in mean anomaly from apogee. Left: Extrapolation for 5.5 hours, right: extrapolation for 1.5 hours. Each curve represents the result from one of 40 Monte Carlo simulations.

If the object of interest is observed before apogee the circular orbit representation holds for a longer time interval than for objects observed after the apogee. An object observed at mean anomaly between 150° and 180° is well within half a degree from its circular ephemeris position after one hour (because the object remains for a longer time at a large distance with a velocity which does not change dramatically).

Δt	Mean Anomaly at Obs. Time	Systematic Error in Position for GTO after: 10	20	30	40	50	60	90	120	min
Total difference:										
1 min	150,...,210°	0.018°	0.067°	0.15°	0.28°	0.46°	0.71°	1.9°	4.3°	
1 min	150,...,180°	0.019°	0.066°	0.14°	0.22°	0.33°	0.44°	1.0°	1.9°	
1 min	130,...,150°	0.027°	0.11°	0.24°	0.41°	0.62°	0.86°	1.7°	2.6°	
1 min	210,...,240°	0.029°	0.13°	0.32°	0.60°	1.0°	1.6°	4.3°	10°	
10 min	150,...,210°	—	0.032°	0.10°	0.21°	0.38°	0.60°	1.7°	3.9°	
Crosstrack difference:										
1 min	150,...,210°	-0.007°	-0.032°	-0.07°	-0.13°	-0.22°	-0.32°	-0.8°	-1.7°	
1 min	150,...,180°	-0.007°	-0.089°	-0.07°	-0.12°	-0.19°	-0.27°	-0.7°	-1.8°	
1 min	130,...,150°	-0.010°	-0.039°	-0.09°	-0.15°	-0.23°	-0.33°	-0.7°	-1.2°	
1 min	210,...,240°	-0.010°	-0.045°	-0.11°	-0.20°	-0.34°	-0.52°	-1.5°	-3.5°	
10 min	150,...,210°	—	-0.017°	-0.05°	-0.11°	-0.19°	-0.29°	-0.8°	-1.7°	

Table 2.5: Maximum angular distance of a GTO and its 'best fitting' circular orbit for extrapolation time intervals between 10 minutes and 2 hours. The circular orbit is based on two observations separated by 1 and 10 minutes, respectively, and located around the apogee within different ranges in mean anomaly. The crosstrack component refers to the circular motion. The numbers on each line are based on 400 Monte Carlo simulations.

30° in mean anomaly corresponds to only 7.5° in true anomaly at apogee for an orbit with eccentricity $e = 0.7$. If the object is observed farther away from the apogee, the range of validity for a circular orbit representation is reduced. If the object is observed between 120° and 150° in mean anomaly (7.5° – 16° in true anomaly preceeding apogee) the difference of the circular orbit with respect to the true orbit is $> 0.5°$ already after 45 minutes (see Table 2.5). If the object is observed at the same distance after the apogee passage (i.e. at 210° – 240° in mean anomaly) the situation is much worse: The circular orbit representation is good within 0.5° only for 35 minutes. (At this angle objects with the apogee close to the descending node ($\omega \sim 180°$) are close to or even below 20° elevation for a mean latitude station like Zimmerwald.)

The crosstrack offset of a GTO object (relative to the circular motion) is always negative (for an observer at northern latitudes). The object starts to leave the 'best fitting' circular orbit in southward direction. The evolution of the object's position relative to its circular ephemeris position is given for 100 simulated GTO orbits in Figure 2.9.

Maximum Alongtrack Error for a GEO Object: To get the maximum expected error in the position of an object we have to combine the formal and the systematic errors.

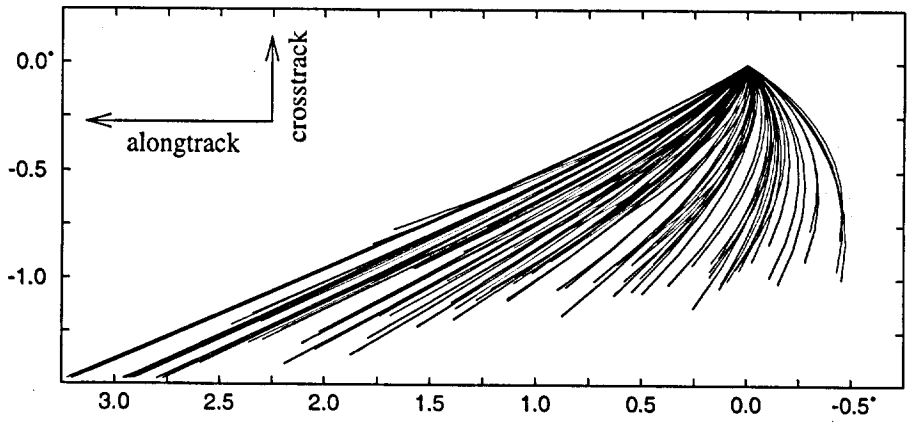

Figure 2.9: Paths of GTO objects relative to the circular orbit computed from two observations separated by 1 minute and located within 30° in mean anomaly from the apogee. The orbits were extrapolated for two hours. In negative x-direction the alongtrack offset and in y-direction the crosstrack offset (relative to the circular motion) is plotted. Each curve represents one of 100 Monte Carlo simulations.

We use the following 'rule' to compute the expected maximum error:

$$\text{total error} = \text{systematic error} + 3 \cdot \text{formal error}. \tag{2.24}$$

In Figure 2.10 we see the dependence of the maximum alongtrack error on the separation of the two observations used for the circular orbit determination for a GEO object (left, observation rms error fixed at 0.5″) and the observation rms error (right, separation of observations is 1 minute). The reference orbit has an eccentricity of $e = 0.001$. In Table 2.6 we find numerical values.

	Total Alongtrack Error for $e = 0.001$, $\sigma = 0.5''$						
Extrapolation:	1h	2h	3h	4h	6h	12h	24h
$\Delta t =$ 1 min:	.040°	.089°	.15°	.21°	.37°	.89°	1.64°
$\Delta t =$ 10 min:	.007°	.023°	.048°	.080°	.16°	.50°	.80°

Table 2.6: Maximum total alongtrack error for a circular orbit determined from observations spaced by 1 min and 10 min based on an orbit with eccentricity $e = 0.001$ and with observation rms errors of 0.5″.

How long does an object on an eccentric GEO orbit remain within a given field of view if the center of the field is set using an ephemeris which is based on a circular orbit determined from two closely spaced astrometric positions? The answer depends, as we have seen above, on the eccentricity of the true orbit, on the time interval between the two observations, and on the observation rms errors. In Figure 2.11 we see the minimum

time T for which objects on orbits with different eccentricities e will stay within a field of view with given diameter. The curves are based on extrapolated positions using circular orbits (determined with observations with rms errors of 0.5″ and a separation of 1 minute (solid lines) and 10 minutes (dashed lines)). The different shape of the solid and the dashed curves is due to a larger formal error for $\Delta t = 1$ min which influences the value of T for small eccentricities. Table 2.7 contains numerical values of T for different eccentricities.

Even for instruments with a small field of view with a diameter of 0.2° an object with true eccentricity of $e = 0.1$ will remain in the FOV for 25 minutes (for $\Delta t = 1$ minute). An object with eccentricity smaller than $e = 0.01$ will remain in a FOV with diameter of 1° for more than three hours. According to Figure 1.9 (right) on page 27 this corresponds to 97% of the catalogued objects in Janin (1996). The 60% objects with eccentricities smaller than 0.001 remain within 0.1° of the center of the FOV for two hours (all numbers for $\Delta t = 1$ min).

Obviously, even for objects in orbits with relatively big eccentricities, a circular orbit based on two closely spaced observations is a valuable tool for recovering the object within the same night. Even for GTO objects the circular orbit determined from the two detection frames is good enough to recover the object within about half an hour for a FOV of 1°.

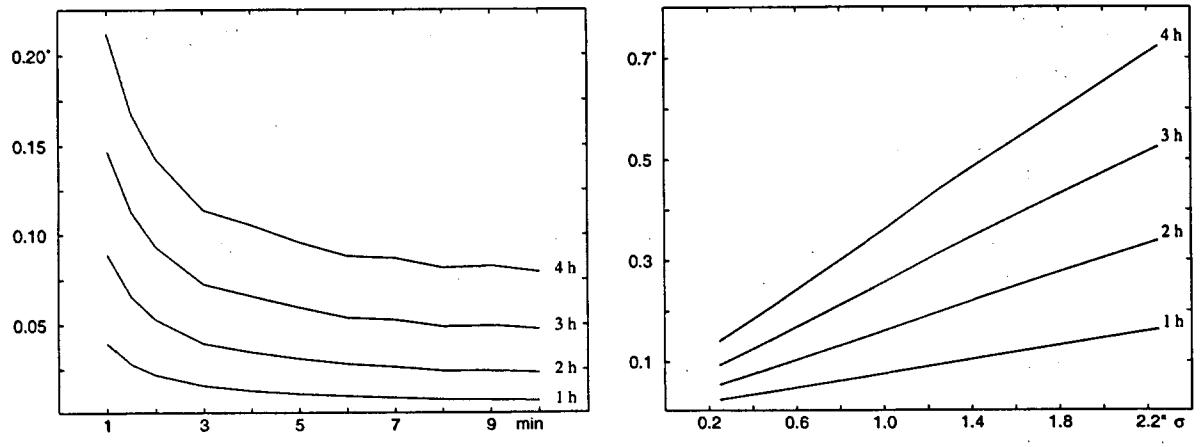

Figure 2.10: Maximum total alongtrack error for an object on an orbit with eccentricity $e = 0.001$. Left: Dependence on the separation of the two observations used for circular orbit determination with an observation rms error of 0.5″. Right: Dependence on the observation rms error σ and a separation of the two observations of 1 minute. The different curves correspond to extrapolation by 1, 2, 3, and 4 hours.

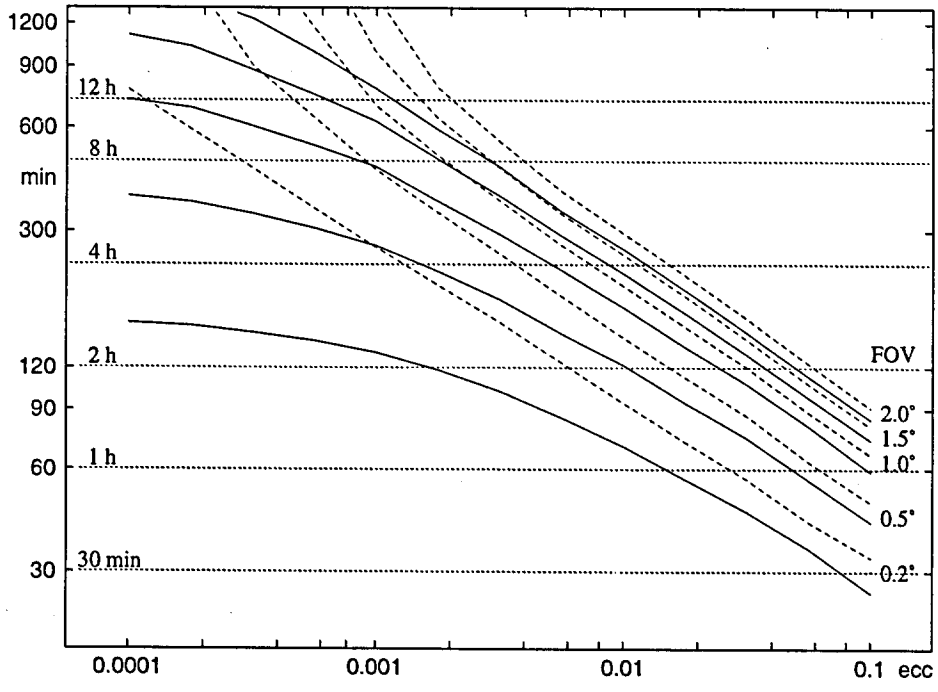

Figure 2.11: Time for which an object on an orbit with given eccentricity remains within a specific field of view (FOV), if the position is extrapolated using a circular orbit determined with two observations spaced by 1 minute (solid lined) and 10 minutes (dashed lines) with an assumed rms error of the observations of 0.5″.

		$\sigma = 0.5''$									
Time interval:		$\Delta t = 1$ min					$\Delta t = 10$ min				
Eccentricity:		0.0001	0.001	0.01	0.1	0.7	0.0001	0.001	0.01	0.1	0.7
FOV	0.2°	160	135	70	25	15	770	270	95	35	30
	0.5°	380	270	120	40	25	> 1440	455	145	50	40
	1.0°	720	460	180	60	35	> 1440	695	205	65	55
	1.5°	1110	625	225	75	45	> 1440	985	255	80	70
	2.0°	> 1440	775	265	85	50	> 1440	> 1440	295	90	80

Table 2.7: Time in minutes that an object in an orbit with given eccentricity remains within a specified field of view if its position is extrapolated with a circular orbit generated from two observations spaced by 1 minute or 10 minutes. GTO objects are assumed to be observed within 16° in true anomaly of the apogee. Observation rms errors are 0.5″.

2.2.3 Elliptic Orbit

The algorithm for elliptic orbit determination described in Section 2.1.2 determines all six Keplerian elements using the observations of the object of interest at three different (and

closely spaced) times. Because all orbital elements are determined, systematic effects in the sense of Section 2.2.1 do not exist. Monte Carlo simulations of the observations themselves (and not only of the orbital parameters) are therefore used to look for possible systematics in the determined elements. Formal errors in the elements and in the propagated positions are studied, as well.

The algorithm may produce more than one orbit representing the observations, no orbit at all, or an orbit with elements very different from the true ones. We will see that the algorithm is reliable provided the time interval containing all observations is relatively long, or, if the orbit has a high eccentricity.

Number of Solutions: As opposed to the circular orbit determination the elliptic orbit determination algorithm may fail to generate an orbit for observation epochs that are too close together or too far apart. It is clear that the algorithm must break down for observations that are too far apart because the orbit is represented by a polynomial (the functions $f(t)$ and $g(t)$ in eqn. (2.6), expanded into Taylor series). For observations which are too close together the observation errors may cause the algorithm to generate unreasonable elements or even to fail.

Figure 2.12 (left) shows — as a function of the total observation time interval — the percentage of nearly circular orbits (with $e = 0.01$) in a GEO, generated by a Monte Carlo procedure, that were successfully reconstructed by the elliptic orbit determination algorithm. 'Error-free' observations were used for the simulations. The abscissa gives the length of the time interval between the first and the last observation. The second observation is assumed to be in the center of this time interval (observe that 6 hours corresponds to 1/4 revolution).

The algorithm starts to fail for observation intervals of about 3 hours (1/8 revolution). Strangely enough the algorithm 'recovers' for time intervals longer than 4 hours to break down finally for time intervals longer than about 6 hours. This strange behaviour has its origin in the finite convergence radius of the Taylor expansion (2.6): For observation time intervals longer than 3 hours the algorithm starts to have problems with convergence and the function $B(r)$ oscillates with very large amplitude for values of r which are only slightly smaller than the true value. Nevertheless the algorithm finds solutions which, however, for longer and longer observation time interval deviate more and more from the true solution. Usually two or more 'solutions' are found. The features in Figure 2.12 (left) depend for time intervals longer than about 3 hours on the expansion order of the Taylor series (order $q = 12$ was used) and the termination criterion for the *regula falsi* used to identify the roots of the function $B(r)$. In fact, using a Taylor expansion with a reduced order $q = 7$, solutions may be found up to an observation time interval of 12 hours! It is obvious, however, that most of these solution are far from representing the true orbit of the object.

Figure 2.12 (right) gives the result of a similar analysis for GTO objects observed around apogee. The solid line corresponds to 'error-free' observations while the dotted line was

produced with observations with a rms error of 0.5". For observation time intervals longer than 1.5 hours the algorithm starts producing failures. The increase of the number of solutions for time intervals between 3 and 4 hours is due to multiple solutions at the limit of convergence of the Taylor series. In this range of observation time intervals even hyperbolic solutions may be generated.

For short observation time intervals the ability of the algorithm to generate a reasonable solution is limited by the observation errors. For an observation rms error of 0.5" all simulated orbits were reconstructed for observation time intervals longer than about 6 minutes corresponding roughly to 0.4% of the orbital period. This number confirms the experiences gained with elliptic orbit determination algorithms in the planetary system: For a 'normal' minor planet with a revolution period of about 4.7 years (semimajor axis of 2.8 au) an orbit is determined without problems if the observations cover a time interval of at least one week (0.4% of the revolution period) and up to about 6 months (10% of the revolution period).

In conclusion we may state that the observation time interval for an elliptic orbit determination should be longer than about 6 to 10 minutes but *not* exceed 3 hours for GEO objects and 1.5 hours for GTO objects. If the observations of an object are separated by such long time intervals it is a problem to assign the observations to one and the same object, anyhow.

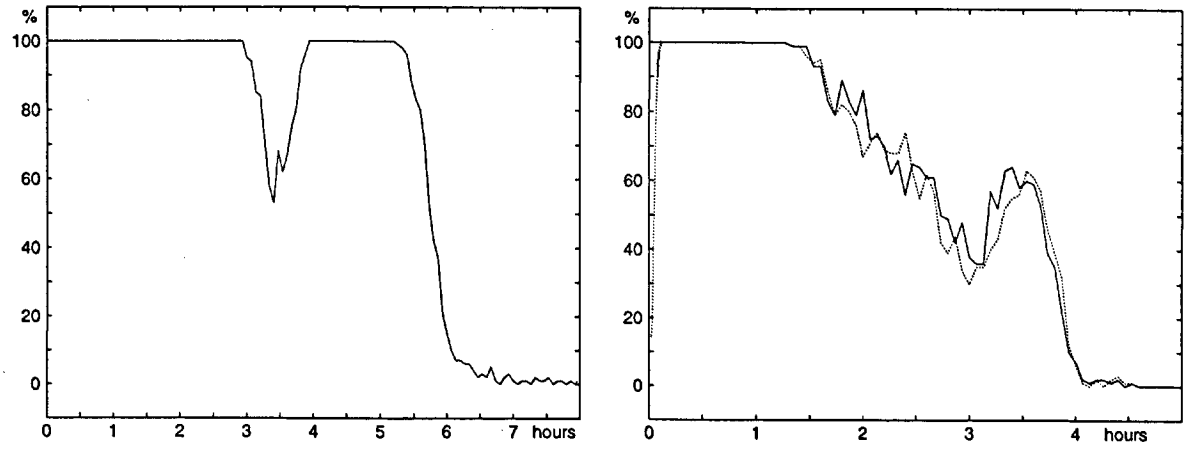

Figure 2.12: Percentage of simulated orbits reconstructed by the elliptic orbit determination algorithm as a function of the time interval between the first and last observation. Left: Orbits with eccentricity $e = 0.01$. Right: Orbits with eccentricity $e = 0.7$. Solid line: 'error-free' observations, dotted line: observation rms error $\sigma = 0.5''$. The strange features for $t > 3$ hours for GEO and $t > 1.5$ hours for GTO are caused by convergence problems of the algorithm. The solutions in these ranges are not reliable.

Systematic Differences of Elements for GEO Objects: In order to study the accuracy of elements determined by elliptic orbit determination under realistic conditions, not only the elements of the simulated orbits were varied but also the observations. The observed right ascension and declination were assumed to be normally distributed with standard deviations of 0.5″. The difference of the determined elements and the simulated elements ('determined' – 'true') was analyzed as a function of the observation time interval.

The Histogram 2.13 shows the distribution of the differences in the semimajor axis (top left), eccentricity (top right), and inclination (bottom left). The histogram (bottom right) shows the distribution of the computed mean anomaly of the first observation. All histo-

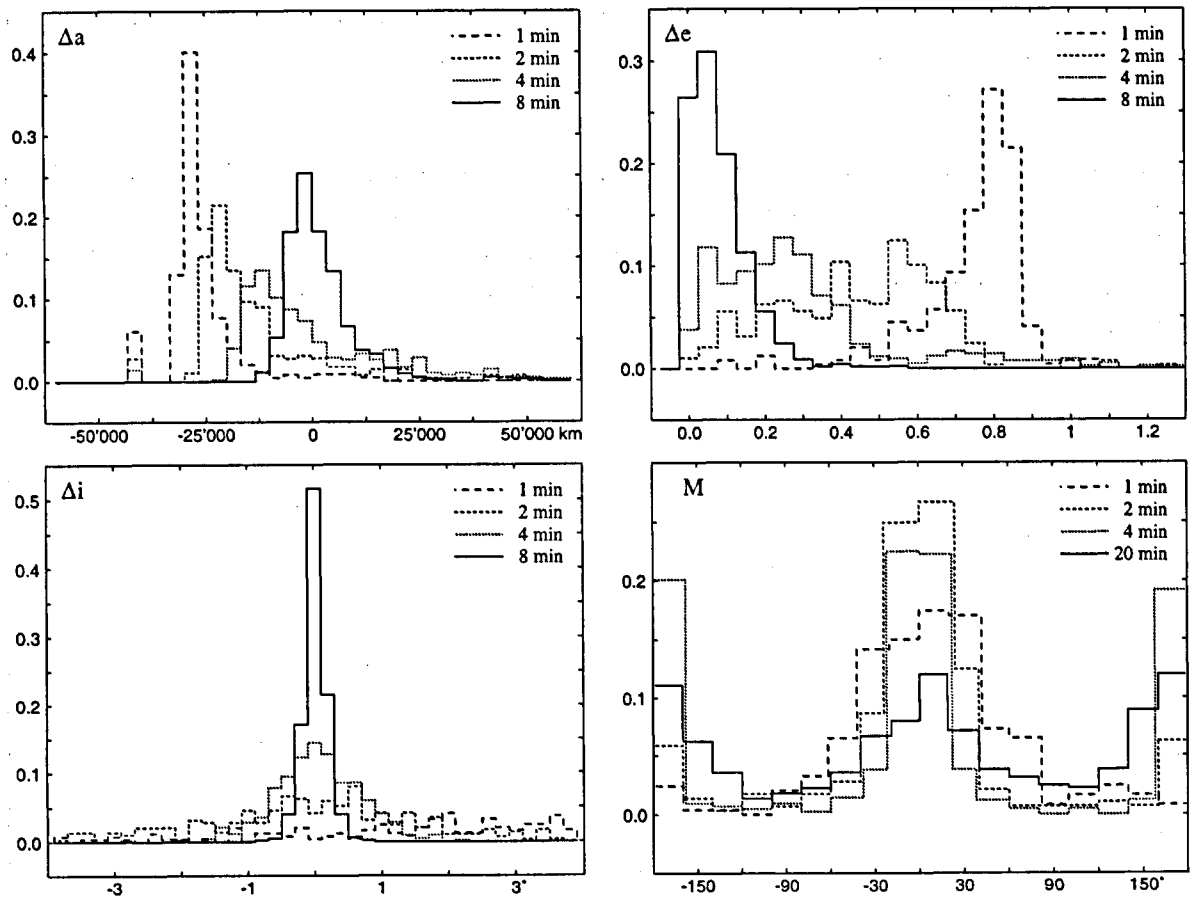

Figure 2.13: Histograms indicating the difference of determined elements to simulated elements ('determined'–'true') for different observation time intervals: Semimajor axis (top left), eccentricity (top right), inclination (bottom left) for geostationary orbits with eccentricity $e = 0.01$. The histogram (bottom right) shows the distribution of the determined mean anomaly for the first observation epoch. The histograms for each observation time interval are based on 450 Monte Carlo simulations. Observation rms 0.5″.

grams are based on simulated geostationary orbits with $e = 0.01$. The observation epochs were equally spaced.

For small observation time intervals the determined semimajor axes and the eccentricities obviously show significant systematic differences with respect to the true values. The semimajor axis is systematically underestimated ($\Delta a < 0$) while the eccentricity is overestimated ($\Delta e > 0$). For an observation time interval of $\Delta t = 1$ minute the peak value for the semimajor axes is more than 25'000 km below the actual value for geostationary orbits, i.e., at only about 17'000 km which would correspond to an orbital period of only about six hours! The corresponding eccentricities are distributed around 0.8. Some of the eccentricities are even larger than unity as already stated in the previous paragraph. Only for time intervals longer than 8 minutes the peak of the histogram is at $e = 0.1$ or below.

The Histogram 2.13 (bottom right) showing the distribution of the computed mean anomaly for observation time intervals between 1 and 20 minutes helps to understand the reason for the systematics. All histograms show peaks at 0° and 180° while the 'true' mean anomaly is randomly distributed! Obviously the algorithm has the tendency to put the object at a place in the orbit with large curvature, i.e., either into the perigee or the apogee. The argument of perigee on the other hand is randomly distributed even for long observation time intervals due to the small eccentricity of the 'true' orbit.

The inclination i (Figure 2.13, bottom left) and the right ascension of the ascending node Ω, on the other hand, are well determined for long observation time intervals. For an 8 minutes interval the inclination is within 0.5°, for 4 minutes within 1° of the true value. Even for small time intervals the distribution of the determined value around the true value is symmetrical.

Systematic Differences of Elements for GTO Objects: The same analysis (as that presented in the previous paragraph for GEO and near GEO objects) was also performed for geostationary transfer orbits with eccentricities around $e = 0.7$. The observations were simulated randomly within 40° of the apogee of the orbits with a rms of 0.5". The Histograms 2.14 show the distribution of the differences in the semimajor axis (top left), eccentricity (top right), inclination (bottom left), and mean anomaly at the first observation epoch (bottom right).

As for geostationary orbits the semimajor axis is systematically underestimated, the eccentricity overestimated for small observation time intervals. For a time interval of 1 minute the determined semimajor axes are distributed around a value which is only about half of the 'true' value, the eccentricities are distributed around 0.9. (For these orbits the perigee distance would be around 1'200 km from the geocenter.) The apogee distance, too, is underestimated by more than 15'000 km.

The determined mean anomaly on the other hand (Figure 2.14, bottom right) is fairly well distributed around the 'true' value. This is due to the large eccentricity and the fact that the object is assumed to be observed near its apogee (i.e. a place in the orbit with a big curvature).

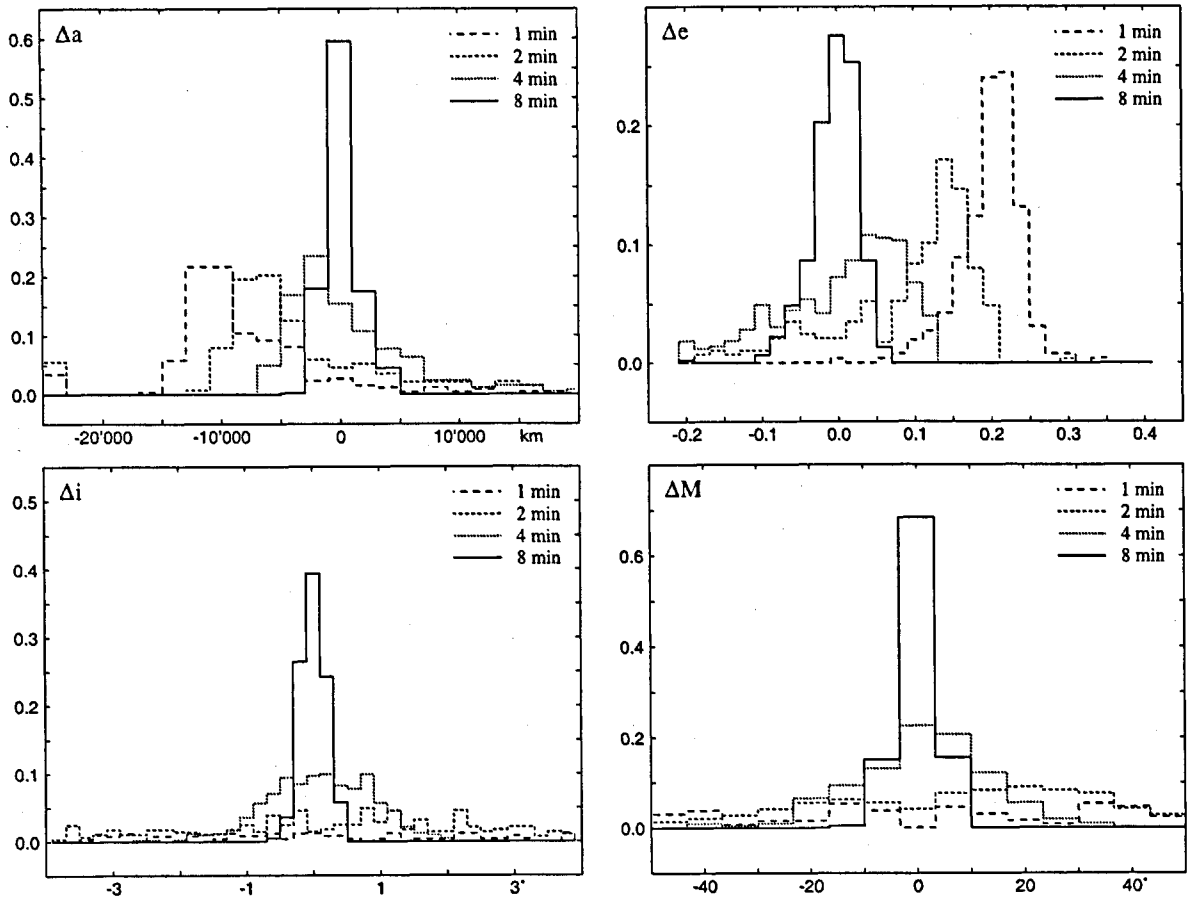

Figure 2.14: Difference of determined elements with respect to simulated elements ('determined'–'true') for different observation time intervals: Semimajor axis (top left), eccentricity (top right), inclination (bottom left), and mean anomaly (bottom right) for geostationary transfer orbits with eccentricities $e \simeq 0.7$. The histograms for each observation time interval are based on 450 Monte Carlo simulations. Observation rms error is 0.5″.

The inclination (Figure 2.14, bottom left) and the right ascension of the ascending node are fairly well determined for geostationary transfer orbits, too. For small observation time intervals the distribution is somewhat broader than for GEO objects. The corresponding histograms for GEO in Figure 2.13 and for GTO in Figure 2.14 are given in the same scale; they look fairly similar.

Formal Errors of Elements for Near Geostationary Orbits: The formal errors of the elements — determined with the method described in Section 2.1.2 — depend strongly on the orbital elements and the observation geometry. The formal errors therefore vary for different simulations in a range that may cover more than an order of magnitude for some elements. Figure 2.15 shows the formal errors for some elements. Each point represents

one simulation of a geostationary orbit. The rms error of the observation was assumed to be 0.5", the observation time interval was 10 minutes.

In Figure 2.15 (top left) the formal error of the semimajor axis is given as a function of eccentricity. The mean formal error is around 4'000 km, the distribution getting broader for larger eccentricity. This formal error is in agreement with the histogram of the distribution of the element differences in the previous paragraphs. In Figure 2.15 (top right) the formal error of the eccentricity is shown as a function of eccentricity. Obviously the formal error depends only slightly on the value of the eccentricity. This is also true for the other elements (except for the mean longitude) for which the corresponding figure would

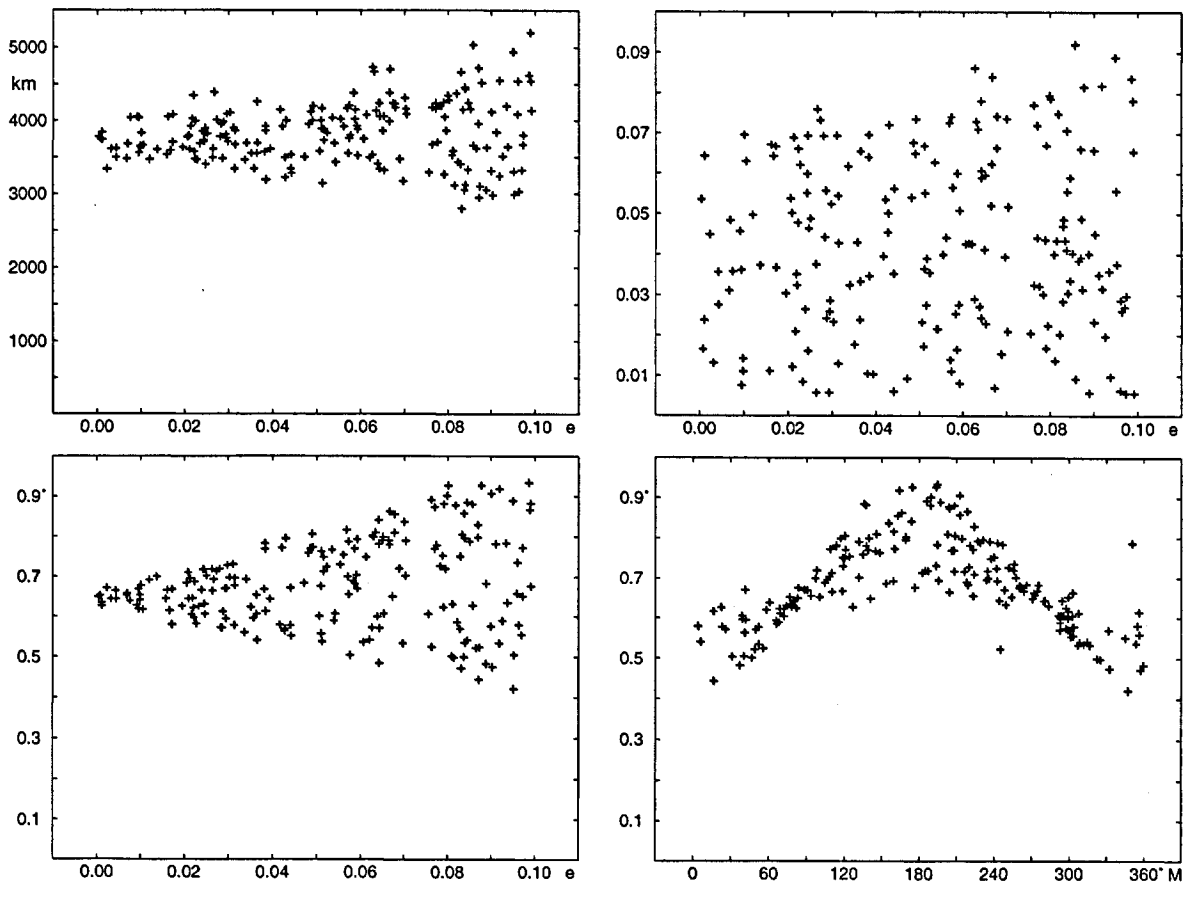

Figure 2.15: Formal errors of the elements determined with the elliptic orbit determination algorithm using three simulated observations with an rms of 0.5" in a time interval of 10 minutes of a GEO object. Top left: Formal error of the semimajor axis a as a function of the eccentricity e. Top right: Formal error of the eccentricity as a function of the eccentricity e. Bottom left: Formal error of the mean longitude ℓ at the first observation epoch as a function of e. Bottom right: Formal error of ℓ as a function of the mean anomaly M of the first observation epoch. Each point represents one of 200 Monte Carlo simulations.

look similar. The formal errors in inclination and R.A. of ascending node show a similar dependence on the argument of latitude as for the circular orbit (see previous section).

The formal errors reflect the variation of element differences obtained from Monte Carlo simulations in the previous paragraphs as soon as the distribution of the element differences is centered around the 'true' value, i.e., for not too short observation time intervals. Therefore, we will only consider observation time intervals of 5 minutes or longer.

As the formal error in the semimajor axis increases for increasing eccentricity, the formal error in the mean longitude increases too (see Figure 2.15, bottom left) because of the growing formal error in the mean motion. The big value of the formal error of about 0.7° (for an observation rms error of 0.5″) is mostly due to the badly determined size and shape of the orbit, i.e., the big formal error in the semimajor axis and the eccentricity. Figure 2.15 (bottom right) shows the dependence of the formal error in the mean longitude on the mean anomaly at the first observation epoch: Observations performed at apogee provide larger formal errors in the mean longitude than observations performed at perigee.

In Table 2.8 statistical information concerning the distribution of the formal errors of the elements calculated with our elliptic orbit determination algorithm are given for different eccentricities and time intervals between the observations. It shows the decrease of the formal errors for increasing observation time intervals.

Because the formal errors are strictly proportional to the observation rms errors (see Section 2.2.1) it is not necessary to give results for rms observation errors other than 0.5″.

	Range of Formal Errors in the Elements for $\sigma_{obs} = 0.5''$					
	$\sigma(a)$ [km]	$\sigma(e)$	$\sigma(i)$ [deg]	$\sigma(\Omega)\sin i$ [deg]	$\sigma(\omega)\cdot e$ [deg]	$\sigma(\ell)$ [deg]
$e \simeq 0.0$:						
$\Delta t =$ 5min	15′000 – 28′000	.02 – .37	.12 – .70	.11 – .68	1.4 – 18.	2.4 – 2.8
$\Delta t =$ 10min	3′400 – 4′100	.006 – .075	.03 – .18	.03 – .17	0.26 – 4.0	0.6 – 0.7
$\Delta t =$ 20min	880 – 1′120	.003 – .020	.007 – .05	.007 – .04	0.07 – 1.1	0.1 – 0.2
$e \simeq 0.1$:						
$\Delta t =$ 5min	11′500 – 45′000	.02 – .42	.12 – .81	.11 – .80	1.4 – 18.	1.7 – 3.8
$\Delta t =$ 10min	2′800 – 5′200	.006 – .09	.03 – .21	.03 – .20	0.26 – 4.5	0.4 – 0.9
$\Delta t =$ 20min	720 – 1′300	.001 – .022	.007 – .06	.007 – .06	0.07 – 1.1	0.1 – 0.3
$e \simeq 0.7$:						
$\Delta t =$ 5min	2550 – 4750	.06 – .10	.26 – .66	.41 – .72	0.9 – 5.0	5. – 8.7
$\Delta t =$ 10min	380 – 1050	.013 – .032	.07 – .20	.10 – .21	0.17 – 1.5	1.2 – 1.9
$\Delta t =$ 20min	150 – 280	.004 – .006	.018 – .05	.027 – .05	0.05 – 0.3	0.3 – 0.5

Table 2.8: Range of formal errors obtained from elliptic orbit determination. The values were determined by Monte Carlo simulations. The orbits with eccentricities between 0.0 and 0.1 correspond to near geostationary orbits, those with eccentricity around 0.7 to geostationary transfer orbits. The time interval between the first and the last of the three measurements is 5, 10, and 20 minutes. Observation rms errors are 0.5″.

Formal Errors for Geostationary Transfer Orbits: In Figure 2.16 we give the formal errors of the semimajor axis (left) and the eccentricity (right) as a function of the eccentricity for simulated GTOs. Similar pictures would result for the other elements. The formal error in the semimajor axis is around 750 km, i.e., much smaller than for a GEO object under similar observation conditions (where the formal error reaches values of 3'800 km, see Figure 2.15, top left). The difference is due to the smaller semimajor axis (resulting in a different mean motion) and the fact that the GTOs are observed only around the apogee. The latter circumstance renders the distribution of the formal errors for all elements narrower.

Minimum and maximum formal errors obtained from the simulations are given in Table 2.8 for all elements for eccentricities around 0, 0.1, and 0.7 and for total observation time intervals (with equally spaced observations) of 5, 10, and 20 minutes.

Dependence on the Observation Time Interval: Increasing the time interval between the observation epochs reduces the size of the formal errors of all elements. This is shown in Figure 2.17 for the formal error in the semimajor axis (left) and the eccentricity (right) in a logarithmic scale. For the eccentricity (as well as for the elements that are not shown) the formal errors are inversely proportional to the square of the time interval between the observations ($\sigma \propto \Delta t^{-2}$). This dependence is similar for GEO and GTO.

It is not obvious that the formal error has this dependence on the observation time interval. For the circular orbit we had a proportionality of formal errors and time interval with an

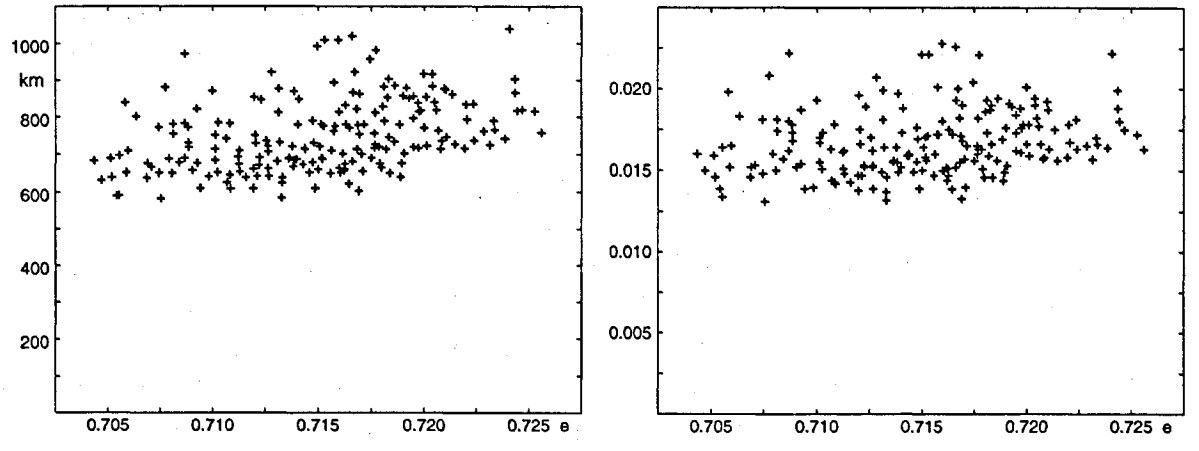

Figure 2.16: Formal error of the semimajor axis (left) and the eccentricity (right) as a function of eccentricity for geostationary transfer orbits observed near apogee. The rms error of the observations is 0.5" and the observation time interval 10 minutes. Each point represents one of 100 Monte Carlo simulations.

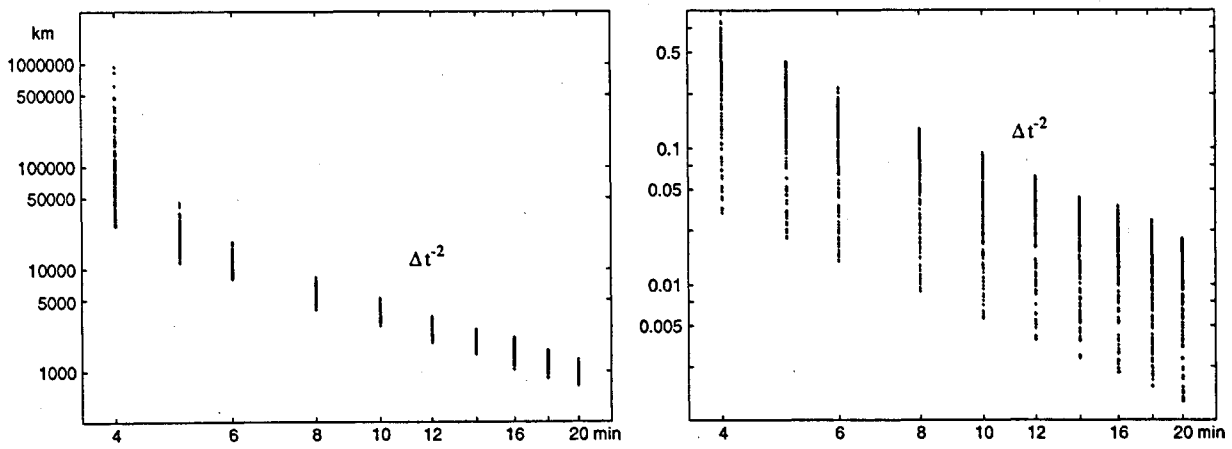

Figure 2.17: Dependence of the formal errors in the elements using our elliptic orbit determination algorithm on the observation time interval in double logarithmic scale. Left: formal error in the semimajor axis as a function of $\log \Delta t$. Right: formal error in the eccentricity as a function of $\log \Delta t$. The rms error of the observations is 0.5". Each point represents one of 200 Monte Carlo simulations.

exponent of -1 whereas for the elliptic orbit we have an exponent of -2. The stronger dependence on the time interval seemingly is due to the fact that the shape of the orbit is not fixed. An error in the shape of the orbit influences (through the observation geometry) also the accuracy of the orientation of the orbital plane.

The semimajor axis (Figure 2.17 left) shows exceedingly large formal errors for small time intervals between the observations. For an observation time interval of 4 minutes and observation rms error of 0.5" one obtains formal errors that may reach 1'000'000 km! As already stated above the formal error is meaningless for too short time intervals because the difference between computed and 'true' elements show strong systematic effects.

Dependence on the Distribution of the Observations: In the previous paragraphs it was assumed that the three observation epoch were equally spaced within the total observation interval. If this assumption is not true the formal errors of the elements grow. In Table 2.9 we see the range of the formal errors for simulated GTO for a total observation interval of 10 minutes, where the second observation was made 1, 2, and 5 minutes after the first observation. The values of the formal errors for the observation times separated by 1 and 9 minutes correspond roughly to those of a total time interval of only 5 minutes with equally spaced observations, those for the observations separated by 2 and 8 minutes are roughly equal to those of a time interval of 8 minutes with equally spaced observations.

Formal Errors in Position: The formal errors in the elements are of interest for identifying an object whereas the formal errors in position as a function of time indicate,

Intervals between the three observations	Range of Formal Errors in the Elements for $\sigma_{obs} = 0.5''$					
	$\sigma(a)$ [km]	$\sigma(e)$	$\sigma(i)$ [deg]	$\sigma(\Omega)\sin i$ [deg]	$\sigma(\omega)\cdot e$ [deg]	$\sigma(\ell)$ [deg]
$e \simeq 0.7$:						
$\Delta t = 1 + 9$ min	2'000 – 4'500	.04 – .10	.20 – .70	.35 – .65	0.5 – 5.0	3.8 – 6.0
$\Delta t = 2 + 8$ min	1'000 – 1'750	.022 – .04	.10 – .35	.19 – .38	0.3 – 2.1	2.0 – 3.2
$\Delta t = 5 + 5$ min	580 – 1'050	.013 – .023	.07 – .20	.10 – .21	0.2 – 1.5	1.2 – 1.9

Table 2.9: Range of formal errors obtained from first orbit determination for different spacings of the observation epochs within an interval of 10 minutes. The values were determined from orbits varied by Monte Carlo simulations. Observation rms errors are 0.5".

how long a set of elements is useful for recovering the object. In Figure 2.18 we show the (formal) alongtrack error for a time span of 24 hours after the first observation epoch for GEO type orbits (top left) and for GTO type orbits (top right) observed close to the apogee. Each curve corresponds to one of 40 Monte Carlo simulations of orbital elements. The results are based on an observation time interval of 10 minutes (from first to last observation) and an observation rms error of 0.5".

After a few hours the formal error in the position starts to grow very rapidly for both types of orbits. For objects in GTO approaching the apogee the error grows to exceedingly large values because, due to the small distance to the observer and the large velocity, small errors in the elements lead to big alongtrack errors. This explains the spikes in Figure 2.18 (top right).

Figure 2.18 (bottom) allows a closer look at the two types of orbits, both covering a time interval of three hours. Obviously objects of both types will remain only for a few hours (at most) within a small field of view. Three main differences between the development of the formal errors for the two types of orbits may be observed: a) The formal error at $t = 0$ is lower for the GTO type orbit as in the case of the elements, and b) remains at this low level for about one hour while the formal error for the GEO type orbits increases linearly with time; c) after about two hours the formal error for the GTO type orbits starts to increase much faster than for the GEO type orbits because the object approaches the perigee.

Maximum formal errors obtained in 200 Monte Carlo simulations are given in Table 2.10 for 1, 2, 3, and 4 hours after the first observation epoch. Both, the alongtrack and crosstrack formal errors are given. The observation rms error adopted is 0.5", observation time intervals are 5, 10, and 20 minutes. For an observation time interval of 5 minutes (or smaller) *no* acceptable orbits are obtained for a GEO in most cases (formal errors are of the order of 300°) whereas the results are reasonable for GTO.

As usual, the crosstrack error is much smaller than the alongtrack error. It may therefore be neglected in all cases where the alongtrack error is within acceptable limits.

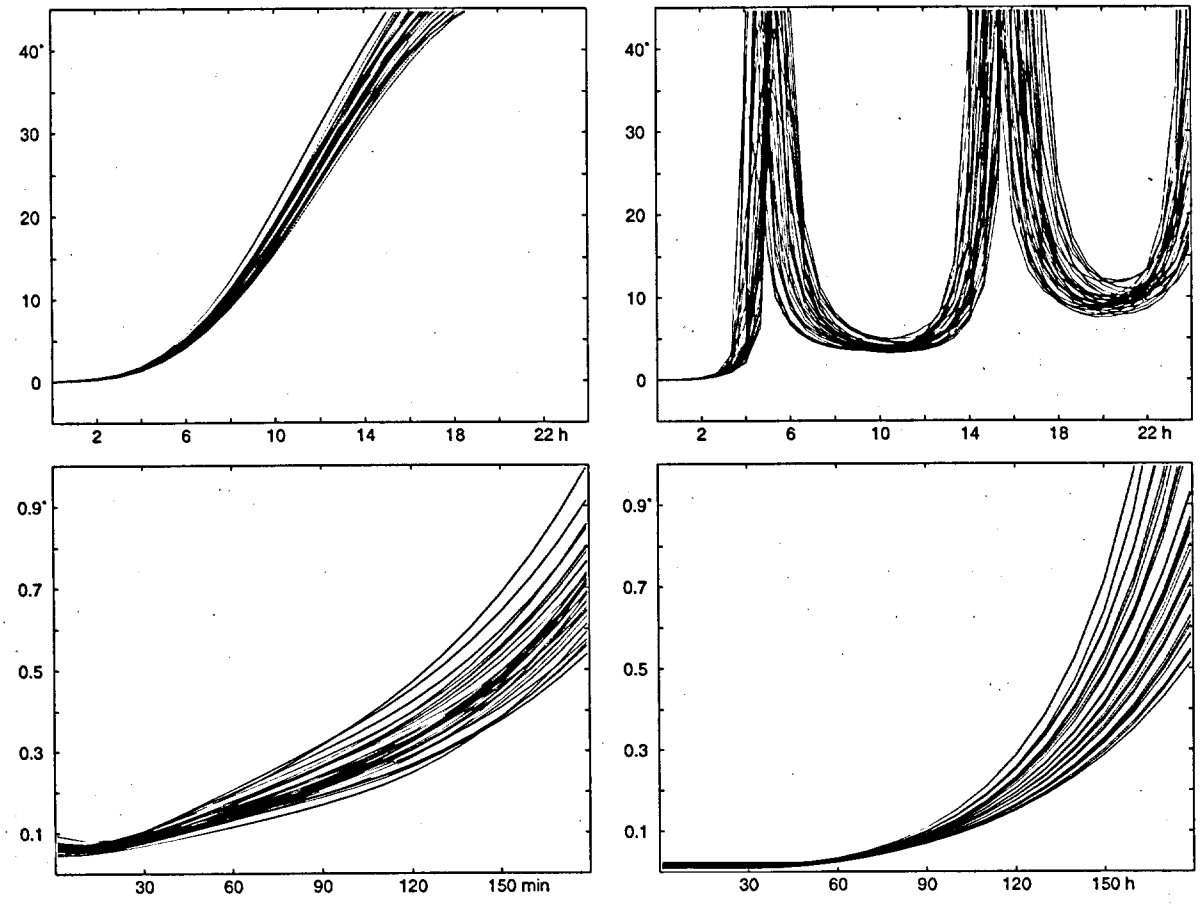

Figure 2.18: Alongtrack rms errors as a function of time for GEO (left) and GTO type orbits (right). The top row covers a time interval of 24 hours (same scale), the bottom row the first 3 hours (same scale). Different lines correspond to one of 40 Monte Carlo simulation runs. An observation time interval of 10 minutes and an observation rms error of 0.5", and observation of the GTO object near apogee were assumed.

From Table 2.11 we may extract the time during which an object remains within a given field of view, if its ephemeris was computed using the elements of an elliptic orbit determination. A GTO object observed near apogee and within a time interval of 10 minutes will remain within a small field of view of 0.2° for one hour. Obviously the increase in the observation time interval is not so important for GTO objects because errors will dramatically increase anyhow when the object approaches the perigee.

In conclusion we may state that for near circular orbits the determination of an elliptic orbit is not very helpful because the circular orbit determined from two observations is equally accurate (see previous section). For geostationary orbits with moderate eccentricity ($e \sim 0.1$) the determination of an elliptic orbit may be adequate if a long observation

Δt		alongtrack 1	2	3	4 h	crosstrack 1	2	3	4 h
5 min	GTO	0.55°	1.3°	9°	350°	0.15°	0.50°	0.9°	3.9°
10	GEO	0.16°	0.37°	0.80°	1.7°	0.012°	0.05°	0.09°	0.12°
	GTO	0.035°	0.30°	1.8°	63°	0.020°	0.07°	0.02°	1.0°
20	GEO	0.016°	0.05°	0.19°	0.5°	0.003°	0.012°	0.02°	0.03°
	GTO	0.006°	0.06°	0.36°	7.0°	0.003°	0.015°	0.04°	0.15°

Table 2.10: Maximum formal alongtrack and crosstrack errors for GEO and GTO obtained in 200 Monte Carlo simulations. The observation time interval was 5, 10, or 20 minutes (for GTO near apogee), observation rms error 0.5″.

Δt		FOV 0.2°	0.5°	1.0°	1.5°	2.0°	
5 min	GTO	—	—	< 75	< 85	< 95	min
10	GEO	—	15	45	70	90	min
	GTO	60	80	100	115	125	min
20	GEO	115	160	200	230	255	min
	GTO	100	130	155	165	175	min

Table 2.11: Minimum time during which an object remains within a given field of view centered at the ephemeris position based on an elliptic orbit. The numbers are based on 3-σ formal errors and are the maximum values observed during 200 Monte Carlo simulations. Observation rms errors are 0.5″.

interval (10 – 30 minutes) is available. For GTO type orbits the elliptic solution is more stable. It may therefore be useful to determine an elliptic orbit if the circular orbit fails to represent the observations.

In any case the elliptic orbit determination algorithm may be used to generate initial elements for an orbit improvement algorithm. For nearly circular orbits the circular elements are good enough to force orbit improvement to converge, too, however.

2.2.4 Elliptic Orbit with Given Eccentricity and Semimajor Axis

The algorithm for the determination of 'restricted' elliptic orbits (with pre-defined semimajor axis and eccentricity) is only promising for highly eccentric orbits. For almost circular orbits the probability for finding a solution is low because roots of the functions $B_1(r)$ and $B_2(r)$ (see Section 2.1.3) have to be found in the interval $a(1-e) \geq r \geq a(1+e)$.

Therefore we will study the performance of our algorithm only for GTO orbits.

The algorithm requires a priori values for semimajor axis and eccentricity. Below, we use the mean values for GTO orbits as specified in Table 2.1:

$$a_0 = 24165\text{km} \qquad \text{and} \qquad e_0 = 0.715 \quad .$$

For given values a_0, e_0, and with two observations the algorithm in general provides two possible orbits, one with a receding object (referred for as the '+ solution'), the other with an approaching object (referred for as the '− solution'). We will study the behaviour of the 'true' solution (i.e. the '+ solution' for true '+' or '− solution' for true '−') as well as of the 'false' solution (i.e. the '+ solution' for true '−' and the '− solution' for true '+') for different distances of the object from the apogee, i.e., for different ranges of the mean anomaly. We will find that the algorithm is robust like the circular orbit determination algorithm. Obviously, systematic errors dominate formal errors because a and e are kept fixed at pre-defined values.

Systematic Errors in the Elements: In Figure 2.19 we see the differences of the determined elements with respect to the 'true' elements as a function of $a - a_0$, the true semimajor axis a minus the pre-defined axis a_0. In Figure 2.19 (left) we give the difference in the inclination, in Figure 2.19 (right) the difference in the argument of perigee. Qualitatively, similar figures result for the other elements.

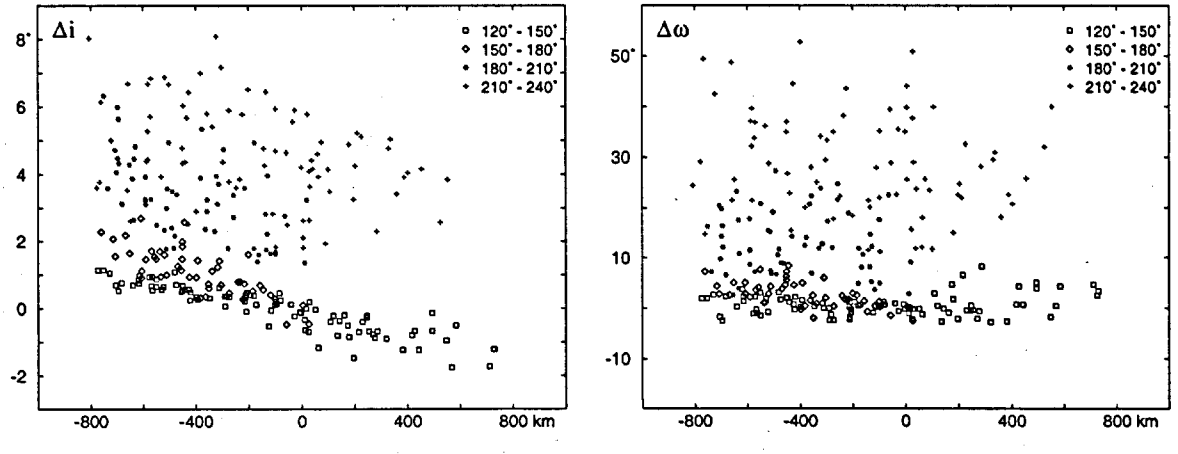

Figure 2.19: Difference between 'true' GTO elements and determined restricted elliptic orbit ('+ solution') as a function of $a - a_0$. Left: Systematic difference in inclination i, right: systematic difference in argument of perigee ω. Different symbols indicate different ranges in the mean anomalies of the 'true' orbits at the observation epochs. The time interval between the observations is 1 minute, the observation error is 0.5". Each point represents the result from one of 400 Monte Carlo simulations.

The Figures 2.19 characterize the situation for the '+ solution'. Different symbols correspond to different ranges in the mean anomaly of the simulated orbit. The boxes (□) and the diamonds (◇) indicate orbits determined from receding objects (the '+ solution' is o.k.) while the two other symbols indicate determined orbits for approaching objects for which the '+ solution' is false.

We observe a clearly systematic behaviour: Not surprisingly, the selection of the approaching solution for an object which is receding leads to orbital elements which differ very much from the 'true' ones (symbols $*$ and $+$ in Figure 2.19). But it is not possible to select the correct solution if only two observations are available. If a third observation is available, the 'false' solution would immediately show up due to large residuals (see below).

Even if the correct solution type is selected systematic differences between the 'true' and the determined elements occur if the a priori semimajor axis a_0 and eccentricity e_0 are different from the 'true' values (symbols □ and ◇ in Figure 2.19). The difference of the elements show a linear dependence on the offset of the 'true' semimajor axis from the a priori value a_0. Table 2.12 gives maximum values of the systematic differences in the four determined elements if the correct solution is selected.

All results are nearly independent on the observation time interval and the observation errors.

The restricted elliptic orbit determination algorithm fails to reconstruct orbits for objects close to the apogee when the semimajor axis a is larger than a_0. This is why in Figure 2.19 there are no results for positive values of $a - a_0$ for observations close to the apogee (symbols ◇ and $*$ for mean anomaly between 150° and 210°).

Δi	$\Delta\Omega \cdot \sin i$	$\Delta\omega$	$\Delta\ell$
±4°	±3°	±20°	±50°

Table 2.12: Maximum difference of determined elliptic elements with respect to the 'true' elements if the correct solution is selected (ℓ is the mean longitude at the osculation epoch). Observation time interval: 1 minute, observation rms errors: 0.5". The numbers are based on 800 Monte Carlo simulations.

Formal Errors in the Elements: The formal errors of the determined elements are much smaller than the systematic errors discussed in the previous paragraph (see Table 2.13). They do not at all represent the precision of the determined orbit. We observe an almost linear dependence on the length of the observation time interval. The errors are independent on the location relative to the apogee at which the object is observed.

Systematic Errors in the Position: The evolution of the systematic errors in position of a GTO object for which a restricted elliptic orbit was determined is given in Figure 2.20

	$\sigma(i)$	$\sigma(\Omega)\sin i$	$\sigma(\omega)$	$\sigma(\ell)$
1 min	0.12°	0.10°	2.0°	1.5°
10 min	0.012°	0.010°	0.18°	0.12°

Table 2.13: Formal errors in the four elements determined by the restricted elliptic orbit determination algorithm for two different observation time intervals. The observation rms error is 0.5″.

and Table 2.14. Figure 2.20 (top) shows that for most simulations the offset between the 'true' and the extrapolated position starts to increase dramatically after a few hours. If the wrong orbit was used for extrapolation the increase starts at earlier times and is more pronounced (top right). (The short dashed lines correspond to extrapolation of orbits based on the wrong solution but of objects observed close to the apogee while the long dashed lines correspond to objects observed at angular distances larger than 30° in mean anomaly from apogee.)

Figure 2.20 (bottom) shows the systematic alongtrack (left) and crosstrack error (right) for a time interval covering about one hour. The dashed lines correspond to the 'false' solution, the dotted and the solid lines to the correct solution (the dotted line to objects observed close to the apogee, the solid lines to objects observed farther away from the apogee). After half an hour the alongtrack error for the wrong solution may amount up to more than 0.4° whereas for the correct solution it may reach about 0.15°. As usual the crosstrack error is negligible compared to the alongtrack error.

In Table 2.14 we give numerical values for the maximum angular distance between the computed and the 'true' satellite position for different extrapolation time intervals. The observation time interval was assumed to be 1 minute, the observation rms error 0.5″. Different assumptions do not significantly change the results. All four combinations between receding and approaching objects for the 'true' orbit and the selected solution of the al-

'true' orbit	solution selected	Systematic Error in Position after: 10	20	30	40	50	60	90	120	min
+	+	0.015°	0.06°	0.14°	0.26°	0.40°	0.58°	1.1°	2.5°	
−	−	0.017°	0.07°	0.17°	0.31°	0.50°	0.74°	1.7°	4.1°	
+	−	0.06°	0.24°	0.57°	0.57°	1.7°	2.5°	6.5°	14°	
−	+	0.05°	0.21°	0.49°	0.49°	1.4°	2.1°	5.2°	11°	

Table 2.14: Maximum angular distance of a GTO from its 'best fitting' orbit obtained from the restricted orbit determination algorithm. The orbit determination is based on two observations separated by 1 minute. The range in the mean anomaly covers 120° – 180° ('+-orbit') and 180° – 240° ('−-orbit'). The numbers in each line are based on 400 Monte Carlo simulations.

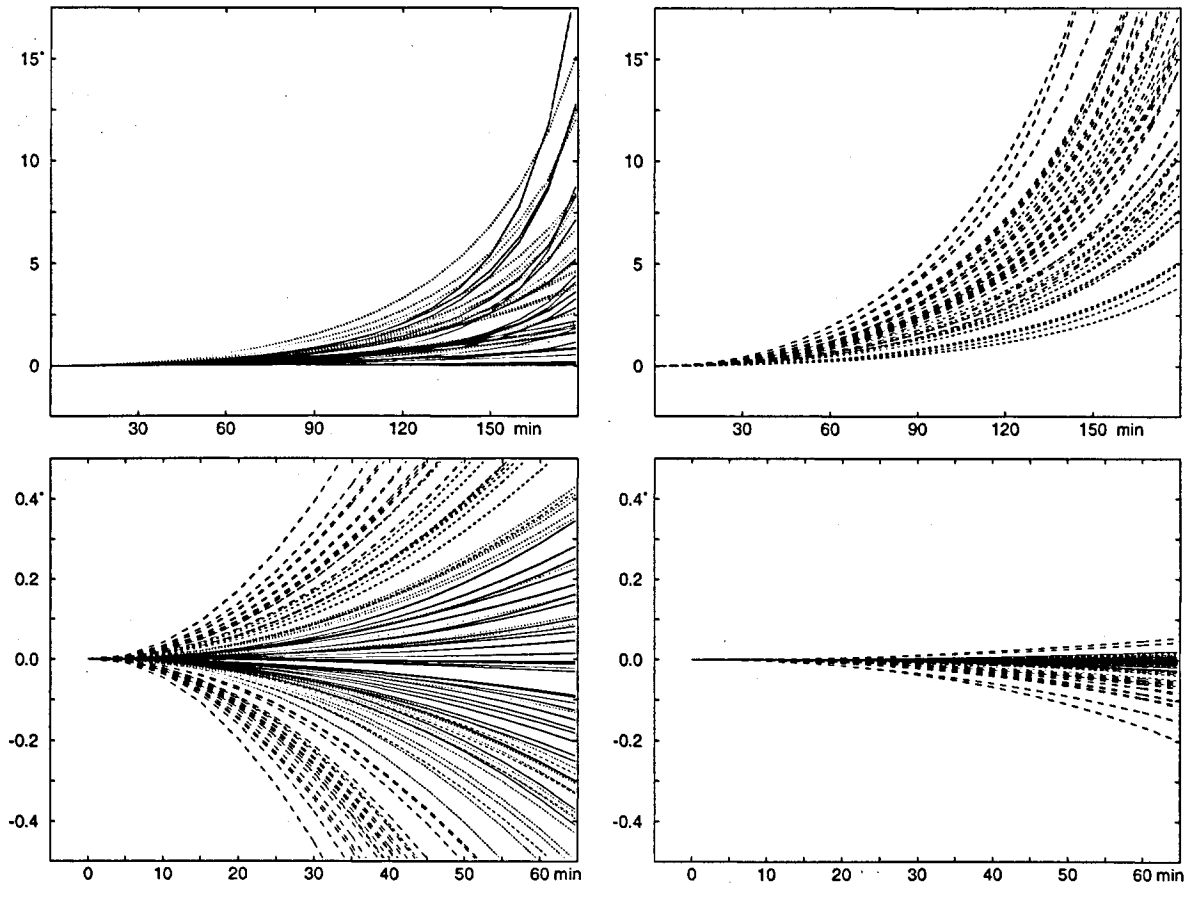

Figure 2.20: Angular separation of ephemerides based on the determined (restricted elliptic case) and the 'true' orbit as a function of time. Top left: Angular separation for the correct solution, top right: angular separation for the wrong solution. Bottom left: Alongtrack offsets for the correct solution (solid and dotted lines) and the wrong solution (dashed lines) in a zoomed time interval. Bottom right: Same for the crosstrack difference. Each curve represents one of 80 Monte Carlo simulations.

gorithm are given. Selecting the correct solution leads to ephemerides which are within one degree of the 'true' position for more than one hour. If the object is receding, the situation is slightly better because the angular velocity of the object remains low for a longer time.

If the 'false' solution is selected the mistake may show up already after a few minutes. The object remains behind its ephemeris position if the '− solution' was selected for a receding object and it is ahead if the '+ solution' was selected for an approaching object. The residuals may be up to three times larger than the value expected for the correct solution. After 30 minutes the object might be at the edge of a field of view with a diameter of 1°. If the object was observed close to the apogee, however, it may remain

close to the computed position even if the wrong solution was selected.

In Table 2.15 we find the minimum time a GTO object would remain within a given field of view for the different orbits and selected solutions. For a field of view of 1° diameter the object remains in the field for more than 45 minutes resp. one hour for approaching and receding object, if the correct solution is selected. The numbers are based on an observation time interval of 1 minute.

'true' orbit	solution selected	Time in Field of View of 0.2°	0.5°	1.0°	1.5°	2.0°	
+	+	29	47	67	81	93	min
−	−	21	34	47	57	65	min
+	−	13	20	28	34	39	min
−	+	14	22	31	38	44	min

Table 2.15: Minimum time during which an object remains within a given field of view centered at the ephemeris position based on a restricted elliptic orbit. The numbers are based on 3-σ formal errors and are the maximum values observed during 400 Monte Carlo simulations. The observation interval is 1 minute, the observation rms errors are 0.5".

2.3 Conclusions and Examples

In the previous section we discussed the performance of three initial orbit determination algorithms. Let us now compare the algorithms in order to propose an optimum observation scenario which allows to keep track of a newly detected object with a minimum number of observations, to improve its orbit in such a way that it cannot be lost again, and eventually to identify it.

Circular Orbit Determination In Section 2.2.2 we found that the circular orbit determination algorithm is very robust and provides useful orbital information even for highly eccentric orbits — at least for short extrapolation times. For two observations that are separated by only 1 minute and an rms of observations of 0.5" an object with an eccentricity $e < 0.01$ (97% of the catalogued objects) will remain for at least two hours within a field of view of 0.5° (similar to the ZIMLAT telescope, 4 m focus). Geostationary objects with eccentricities below 0.1 remain in the FOV for about 40 minutes and GTO objects (observed within 16° in true anomaly resp. 60° in mean anomaly from the apogee) will remain in the FOV for at least 15 minutes (see Table 2.7). It is therefore advisable that an initial orbit determination procedure should start with a circular orbit determination. An elliptic orbit determination algorithm may be used if, after additional observations of

the object were acquired (based on the circular orbit ephemerides), it is obvious that the object moves in a highly eccentric orbit.

Because the circular orbit determination algorithm provides the attitude of the orbital plane (i.e. inclination i and R.A. of ascending node Ω) with good accuracy, the algorithm is well suited for identifying detected objects. For an observation time interval of 1 minute and an observation rms error of 0.5" the formal and the systematic errors in the inclination i and in $\Omega \sin i$ are well below one degree (see Tables 2.2 and 2.3) for orbits with eccentricities $e < 0.01$. For GTO orbits these two elements are determined with an accuracy of about 2°.

The semimajor axis (and hence the alongtrack drift) of a geostationary satellite is not well determined. For an orbit with an eccentricity of $e = 0.01$ the uncertainty in the semimajor axis reaches 570 km (see Table 2.3) corresponding to an uncertainty in the drift of 7° per day. For a GTO object the determined circular semimajor axis is 'unreasonable' (60'000 to 67'000 km) which makes it easy to distinguish it from a GEO object.

Because inclination and node are determined with good accuracy these two elements are best suited for the identification of a newly detected object but also to look for known objects with unknown alongtrack offsets and to distinguishing them from other objects that may occasionally cross the field of view.

Examples for Circular Orbit Determination The performance of the algorithm as described in the previous section could be confirmed using real observations made at the Zimmerwald observatory. The circular orbit determination algorithm was routinely used for the identification of objects and for the generation of ephemerides required for the measurement of close encounters of the satellite and the reference stars. Let us illustrate this with a few examples.

The telecommunication satellite Olympus 1 was observed in the night of February 20/21, 1995, within a joint experiment of our observatory with the FGAN tracking Radar at Wachtberg-Werthhoven (see Section 6). The satellite was moving in an uncontrolled way. After finding an object close to the predicted position three frames were exposed within five minutes. Coarse position measurements were performed (using the cursor on the screen) with a precision of only 4". Comparing the elements from the circular orbit determination with the two line elements (TLE) immediately confirmed the identity of the object. The circular orbit was used to track the satellite for about 4.5 hours. In Table 2.16 the circular elements together with the precise elements, determined using all observations from the entire night, are given. The differences of the elements are in the expected range given in Section 2.2.2 for this orbit with eccentricity $e = 0.002$.

An unidentified geostationary object was observed in the night of January 3/4, 1995 (Figure 2.21). Approximate elements were obtained from ESOC (Massart, 1995). Two cursor measurements of the position were acquired within seven minutes. The resulting circular elements are given in Table 2.17 together with the precise elements. The difference of the elements for a satellite with a relatively high eccentricity of $e \simeq 0.023$ are in good agreements with those given in the previous section.

Olympus 1, February 20/21, 1995			
Elements	a	i	Ω
circular	41784 km	2.39°	73.80°
precise	41863 km	2.35°	73.77°

Table 2.16: Elements from the circular orbit determination algorithm compared to the precise elements (determined with more observations) of the geostationary satellite Olympus 1. The observations were separated by 5 minutes, the observation rms was 4".

Unidentified Object, January 3/4, 1995			
Elements	a	i	Ω
circular	42167 km	3.21°	99.26°
precise	42166 km	3.12°	96.60°

Table 2.17: Elements from the circular orbit determination algorithm compared to the precise elements of a geostationary satellite with eccentricity $e = 0.023$. The observations were separated by 7 minutes, the observation rms was 4".

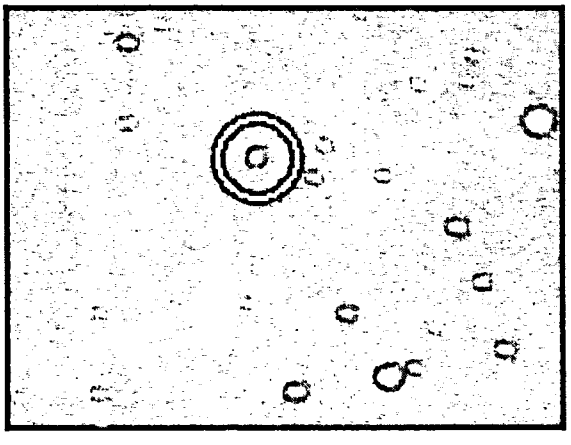

Figure 2.21: Unidentified geostationary satellite observed on January 5, 1995, at Zimmerwald. Integration time was 1 second with fixed telescope. The frame covers 14'x15'.

Of course, the algorithm may also be used for satellites moving on nearly circular non-geostationary orbits: A GPS satellite was observed by chance in the night of January 15/16, 1994. Four observations within 15 seconds (!) were available with an accuracy of 0.5". The determination of a circular orbit provided the elements given in Table 2.18. The object could be easily identified as GPS 29 ($e = 0.005$).

GPS 29, January 15/16, 1994			
Elements	a	i	Ω
circular	26567 km	54.50°	187.13°
precise	26563 km	54.61°	188.76°

Table 2.18: Elements from the circular orbit determination algorithm compared to the precise elements of a GPS satellite. The observations were separated by 15 seconds, the observation rms 0.5".

Elliptic Orbit Determination As opposed to the circular orbit determination the elliptic orbit determination algorithm is relatively fragile. Not only the mean motion and the attitude of the orbital plane have to be determined but also the shape of the orbit which is strongly correlated with all other elements. The observation time interval should neither be too short nor too long, otherwise the algorithm breaks down. For nearly circular orbits it is therefore not recommended to determine an elliptic orbit; the circular elements for GEO objects are good enough as input elements for an orbit improvement algorithm.

For GTO objects for which relatively good observations (rms 0.5" or better) are available within a reasonably long time interval (around 10 minutes) reliable elements are determined: The object remains within a field of view of 0.5° for more than one hour (see Table 2.11). The results under such optimal observation conditions are better than those stemming from the restricted elliptic orbit determination algorithm (with fixed semimajor axis and eccentricity). The algorithm therefore represents — given a suitable set of observations — a valuable tool for determining orbital elements, which may then e.g. be used as input elements for an orbit improvement. We expect that the algorithm is much more powerful for lower (than GEO and GTO) orbits due to the rapidly changing observation geometry.

Restricted Elliptic Orbit Determination Like the circular orbit determination algorithm the elliptic orbit determination algorithm with pre-defined a priori semimajor axis and eccentricity is robust. It provides elements useful for extrapolation over very short observation time intervals. At least two solutions are generated in each case. The correct solution may be selected using the residuals of a third observation.

The elements determined may be biased by up to several degrees in inclination (see Table 2.12) making orbit identification difficult. Nevertheless, the algorithm may be used to test the 'GTO hypothesis' in the case e.g., if implausible elements were generated in the circular orbit determination step.

Starting with an observation time interval of 1 minute the GTO object remains within a field of view of 0.5° for 30 minutes or more. The algorithm may therefore be used to recover a GTO object within half a hour after discovery for determining all elements of

an elliptic orbit using the additionally acquired observations and to invoke eventually an orbit improvement algorithm.

Optimum Observation Scenario Based on the properties of the three algorithms we may now propose an observation scenario which allows it to refine the orbit of a newly detected high orbiting object in order to follow its track for the next few nights. The scenario is slightly different for GEO and GTO objects. For objects thought to be almost geostationary we suggest to proceed as follows:

(1) Take a second exposure immediately after detecting the object (if the object is not already detected on two frames, e.g., for safe elimination of cosmic events).

(2) Determine a circular orbit and compute corresponding ephemerides.

(3) If the circular elements are 'reasonable' for a GEO object, candidate objects with similar inclination and node may be extracted from the data base for identification.

(4) A pair of additional observations should be acquired within the next half an hour to one hour depending on the size of the field of view. The pair of frames may be used as search frame and reference frame for unambiguous identification of the object.

(5) A new circular orbit may be generated together with new ephemerides for the next hours and the object is observed regularly (one pair of frames per hour).

(6) Using the circular elements an orbit improvement algorithm may be invoked allowing it to identify the object or to find the object again the next night.

(7) Eventually a 'high end' orbit improvement algorithm is used to determine elements and radiation pressure coefficient using the observations made during several nights.

For an object for which the first orbit determination (point (2)) indicates a highly eccentric orbit we suggest to proceed as follows:

(3) If the circular elements determined from the two initial observations indicate that the object may move in a GTO a next set of frames should be acquired within about 10 to 20 minutes based on the ephemeris generated from the circular elements.

(4) Using additional observations a restricted elliptic orbit determination algorithm may be used to determine new elements and an ephemeris that should be valid for the following 20 to 40 minutes (depending on the field of view). If it is not possible to decide which of the two solutions of the algorithm is correct two sets of ephemerides have to be computed.

(5) Within 20 to 40 minutes a next set of observations should be acquired. If necessary the two possible fields (depending on the solution of the restricted elliptic orbit determination algorithm) have to be observed.

(6) The elliptic orbit determination algorithm may then be used to determine elements valid for the next hour after which a next observation set is acquired.

(7) Finally, an orbit improvement algorithm is used for refining the orbit using all observations and taking the elliptic elements as a priori elements. If necessary a priori weights have to be put on the eccentricity and the argument of perigee parameters.

(8) Eventually a 'high end' orbit improvement algorithm is used to determine elements and radiation pressure coefficient using the observations stemming from several nights.

3 Orbit Determination

If a considerable number of observations of a satellite is available in a reasonably long time interval an orbit improvement procedure may be invoked. The orbital elements resulting from an initial orbit determination algorithm may be improved, the elements determined with older observations or obtained from an external source may be refined with more recent observations. In addition to the osculating elements a number of parameters may be determined, e.g., radiation pressure coefficients, gravity potential coefficients, or observational offsets.

In the first part of this chapter we introduce the programs used throughout this work together with the methods used for simulation studies. In the second part we put the emphasis on the influence of the distribution of the observations on the formal errors of the elements and of the satellites' extrapolated position.

3.1 Methods and Routines

3.1.1 The Orbit Determination Program

The orbit improvement algorithm implemented into the FORTRAN program ORBDET follows a standard parameter estimation procedure based on the method of least squares. The program consists of three individual programs (see Figure 3.1) which are connected by a command file and which communicate via files:

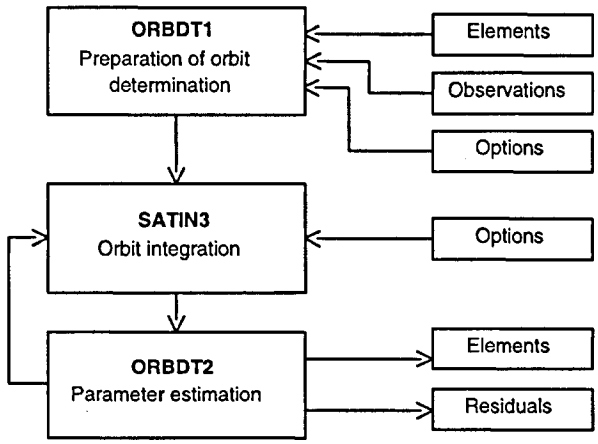

Figure 3.1: Flow diagram of program system ORBDET.

- The program ORBDT1 prepares the orbit determination process. It reads the program input options, the a priori values and weights for the parameters, as well as the observations which are transformed into the apparent system of epoch, if necessary. For each observation epoch the station coordinates and the matrices required for transforming the vectors into the system J2000 are computed.

- The program SATIN3 generates the a priori satellite orbit of the current iteration based on the differential equation system and the initial position and velocity using a numerical integration algorithm. The program is executed in each iteration step. It is separated from the orbit determination program which would allow it to replace the program by other numerical procedures in future.

  The program is based on a program written and documented by Beutler (1990) for the integration of satellite orbits. It uses a Taylor expansion series collocation method with variable step size which is automatically adapted to control the integration error. For more information we refer to Beutler (1990).

  The integration is performed in rectangular coordinates in the inertial system J2000. Position and velocity are transformed to osculating elements and stored at equidistant time intervals or at each observation epoch. Osculating elements are used in order to allow for easy interpolation between epochs. Care is taken to save the elements with a sufficiently high precision in order not to introduce numerical problems degrading the convergence of the orbit improvement for long arcs.

  The program also integrates the *variational equations* (partials of position and velocity with respect to the orbit parameters) for all parameters. The integration of the variational equations may be disabled for the osculating elements. In this case a Keplerian orbit is used as approximation to compute the partial derivatives. The variational equation output is stored for the same epochs as the osculating elements.

  The program SATIN3 may also be used as a stand-alone program for the integration of satellite orbits.

- The actual orbit improvement step is performed by the program ORBDT2. It reads the observations, the station coordinates, the transformation matrices, the program options prepared by the program ORBDT1, the output from the integration program for orbit and variational equations, as well as the values of the parameters from the previous iteration step (current a priori values). Light travel time corrections are applied. The normal equation matrix is set up, inverted, and improved parameter values are computed. The program prepares the input for the integration program or stops the execution if the termination criterium is satisfied.

The programs SATIN3 and ORBDT2 are executed alternatingly by the command file until the termination criterion is satisfied. The current criterion requests that the improvement for each parameter computed in the iteration step is smaller than 1/30 of the rms error of the parameter.

3.1.2 Observation Types and Parameters

Several types of observations may be processed by the program ORBDET:

- astrometric positions (right ascension and declination) of two different categories of accuracy ('high precision' and 'low precision'), see below,
- observations in azimuth and elevation,
- range and range rate observations.

Range and range rate observations from the German FGAN Radar (Mehrholz et al., 1997) were successfully processed with the program (see Chapter 6). For low precision astrometric positions constant observation offsets for all observations may be estimated. The type of the observations as well as the system and equinox of the coordinates are specified in the input observation file. Different kinds of observations may be processed in the same program run.

The program allows the estimation of several types of parameters:

- Keplerian or so-called nonsingular osculating elements (for small eccentricity and low inclination orbits) may be set up for determination. The Keplerian elements are the semimajor axis a, the eccentricity e, the inclination i, the R.A. of the ascending node Ω, the argument of perigee ω, and the mean anomaly σ at the osculation epoch t_{osc}. The implemented nonsingular elements are defined by

$$\begin{aligned} \ell &= \Omega + \omega + \sigma & \varpi &= \Omega + \omega \\ h_1 &= e \cdot \sin \ell & k_1 &= e \cdot \cos \ell \\ h_2 &= \sin i \cdot \sin \varpi & k_2 &= \sin i \cdot \cos \varpi \end{aligned}$$

  where ℓ is the mean longitude at the same epoch, ϖ is the longitude of the perigee. The elements h_1, k_1 and h_2, k_2 may be used for orbits with small eccentricity e and with small inclination i. The user is allowed to select every combination of Keplerian and nonsingular elements. The program tests whether or not a specified combination makes sense. The transformations of derivatives with respect to the different sets of nonsingular elements and Jacobian matrices of the transformations from and to Keplerian elements are given in Appendix A.

- One direct radiation pressure coefficient or three components of a radiation pressure force vector may be determined (see Section 3.1.3 for details).

- Several observation offsets may be estimated in order to calibrate different measurement systems when processing observations from different stations or of different types. The determination of observation offsets is only possible if quasi-simultaneous high precision astrometric observations of the same object are available.

Offsets in azimuth and elevation may be determined when processing 'low precision' observations. In order to calibrate Radar observations to satellites, offsets or scale factors in range and range rate may be set up. In addition, a time bias and system orientation parameters may be determined.

- Geopotential coefficients may be solved for (see Chapter 5).

The actual parameters solved for in the orbit determination process are selected in the input file of the program. If necessary the program user may specify weights for each parameter in the same file. In Figures 3.2 and 3.3 we see an input file for program ORBDET. It is a so-called keyword file in which the user may modify the values in the fields between the angular brackets '> ... <'. The program reads the keyword values and skips comments within the line and entire comment lines (Schildknecht et al., 1995a).

```
------------------------------------------------------------------------------
ORBDET     : DETERMINATION OF SATELLITE ORBIT                    14-OCT-95 HU
------------------------------------------------------------------------------

INTEGRATION:
  Integration of orbit.............................(y/n) >     y <
  Integration of variational equations............(y/n) >     y <
  Integration type: 1: DQNMST..................... >     1 <
  Save osculating elements at observation epochs.(y/n) >     y <
  Save osculating elements at intervals dt......(mins) >    60 <

INTERPOLATION:
  Type: 1: polynomial............................. >     1 <
  Degree for orbital elements..................... >    10 <
  Degree for variation equations.................. >     4 <

ORBIT IMPROVEMENT:
  Output to sysout.................................(y/n) >     y <
  User terminates by keyboard.....................(y/n) >     n <
  Maximum number of iterations.................... >     7 <
  System of elements: 0: apparent, 1; J2000...... >     1 <
  Take elements from panel........................(y/n) >     Y <
  Write output elements to panel..................(y/n) >     n <
  Scaling factor for Q-matrix..................... >     1.D+2 <
  Output of Q-matrix..............................(y/n) >     n <

ORBIT SIMULATION :
  Covariance study................................(y/n) >     n <
  Observation rms error.....................(arcsec) >   0.5 <
```

Figure 3.2: Input file for the program ORBDET (Part I).

```
PARAMETERS TO BE SET UP:

  Locq     Parameter                              solve      a priori sigma

> 1.1   <  Semimajor axis.....................  > X <      >            <(km)
> 1.2   <  Eccentricity.......................  >   <      >            <
> 1.3   <  Inclination........................  >   <      >            <(arcs)
> 1.4   <  Ascending node.....................  >   <      >            <(arcs)
> 1.5   <  Argument of perigee...............  >   <      >            <(arcs)
> 1.6   <  Mean anomaly at tosc..............  >   <      >            <(arcs)

> 2.1   <  Mean longitude at tosc............  > X <      >            <(arcs)
> 2.2   <  Longitude of perigee..............  >   <      >            <(arcs)
> 2.3   <  Small eccentricity: h1, k1........  > X <      >            <
> 2.4   <  Small inclination:  h2, k2........  > X <      >            <

> 3.1   <  Direct radiation pressure.........  > X <      >            <
> 3.2   <  Orthogonal components.............  >   <      >            <

> 4.1.1 <  Offset in Azi......................  >   <      >            <(arcs)
> 4.1.2 <  Offset in Ele......................  >   <      >            <(arcs)
> 4.2.1 <  Offset in range....................  >   <      >            <(m)
> 4.2.2 <  Scale in range.....................  >   <      >            <
> 4.3.1 <  Offset in range rate...............  >   <      >            <(m/s)
> 4.3.2 <  Scale in range rate...............  >   <      >            <
> 4.4   <  Time bias..........................  >   <      >            <(s)
> 4.5.1 <  XY-system bias.....................  >   <      >            <(arcs)
> 4.5.3 <  Z-system bias......................  >   <      >            <(arcs)

> 5.1   <  Potential terms.....>   2,2 <  > X <      >            <
> 5.1   <  Potential terms.....>   3,2 <  >   <      >            <

-------------------------------------------------------------------------------
```

Figure 3.3: Input file for program ORBDET (Part II).

Apart from the selection of the parameters a number of options may be specified in this input file:

- The integration of the orbit and/or of the variational equations may be disabled. In this case a Keplerian orbit will be used to represent the observations. The output mode and the time interval for the integration can be specified. Most of the orbit integration options as well as the force model are specified in the input file of the integration program (next Section).

- If the user decides to write the output of the integration program at equidistant epochs he can specify the degree of the polynomial to be used for interpolation of

the output.

- The user may limit the number of iterations, select the system of the output elements, select the input and output channel for the a priori and the resulting elements, define a scaling factor for the normal equation matrix in order to avoid numerical problems during inversion, and decide whether or not he wants to save the normal equation matrix on file for later use in an orbit combination procedure (see Section 3.1.4).

- It is possible to use the program ORBDET for covariance studies. Using the specified observation rms error together with a file containing a list of observation epochs the formal errors for the parameters are computed (see Section 3.1.5).

The section of the output file of program ORBDET containing the parameter values and the associated rms errors and a priori values is shown in Figure 3.4.

```
ORBIT IMPROVEMENT
-----------------
OBJECT:
 METEOSAT 4          1994

ITERATION:   5
LENGTH OF ARC (DAYS):      49.35999
INTEGRATION OF ORBIT:       1
INTEGRATION OF VAR.EQ.:     1
NUMBER OF OBSERVATIONS:   918
NUMBER OF PARAMETERS:       7
RADIATION PRESSURE:     -0.6900E-07

RMS:       1.371   (     0.584"      0.000"     0.0000d        0.0m     0.0000m/s)

SYSTEM OF ELEMENTS:        J2000
EPOCH OF ELEMENTS:         49645.000000

SEMIMAJOR AXIS              42167815.03 +-          0.48    ( 42167810.66)
ECCENTRICITY              0.00015002858 +-0.00000034813    (0.00014827110)
INCLINATION                  0.6653114  +-    0.0000127     (  0.6653150 )
NODE                        69.3579553  +-    0.0007027     ( 69.3579830 )
PERIGEE                   -229.8140443  +-    0.2808109     (-227.2814980 )
LONGITUDE AT TO             20.22773088 +-    0.00008822    ( 20.22718490)
RADIATION PRESSURE COEF.    -7.1168D-08 +-    5.6054D-10    ( -7.1168D-08)
```

Figure 3.4: Section of the output file of program ORBDET containing the estimated parameters.

3.1.3 The Force Model

The force model used for orbit improvement and the initial conditions are specified in the option file of the integration program SATIN3 (see Figures 3.5 and 3.6).

- Degree and order of the Earth gravity model are specified. It is possible to set a lower limit for the indices in order to study the effect of individual terms on a satellite

```
-------------------------------------------------------------------------------
SATIN3     : INTEGRATION OF SATELLITE ORBIT                      12-OCT-95 HU
-------------------------------------------------------------------------------

Satellite >   METEOSAT 4        1994                                          <

SAVE OPTIONS:
  Output to sysout.............................(y/n) >     Y <
  Saving times from file.......................(y/n) >     N <
  Save osculating elements at intervals dt.....(mins) >  1440.0 <

INTEGRATION SPECIFICATIONS:
  Initial step.................................(secs) >    10 <
  Integration order.............................. >    12 <
  Number of iterations (initialization)..... >    20 <
  Number of iterations (normal step)..... >     2 <
  Threshold for change.........................(%) >    10 <
  Length of integration interval.............(days) >  20.000 <
  Maximum error allowed per step..... >  .0001   <

FORCE FIELD:
  Earth potential degree n, order m, lower limit..... >     0, 0  <
  Earth potential degree n, order m, upper limit..... >    10,10  <
  Include Sun..................................(y/n) >     y <
  Include Moon.................................(y/n) >     y <
  Include Jupiter (only for JPLEPH)............(y/n) >     y <
  Include Venus (only for JPLEPH)..............(y/n) >     y <
  Use JPL ephemerids...........................(y/n) >     y <
  Include tidal potential due to sun and moon....(y/n) >     y <
  Include atmospheric drag.....................(y/n) >     N <
  Include radiation pressure...................(y/n) >     Y <
  Model sunlight/shadow transits...............(y/n) >     N <
  Include relativistic corrections.............(y/n) >     y <

  Precession:    0: P=E, 1: P=P(t0), 2: P=P(t)..... >     2 <
  Nutation:      0: P=E, 1: P=P(t0), 2: P=P(t)..... >     2 <
  Polar wobble:  0: P=E, 1: P=P(t0), 2: P=P(t)..... >     1 <
```

Figure 3.5: Input file for the program SATIN3 (Part I).

```
RADIATION PRESSURE MODEL:
  Model:  1: direct
          2: three components
          3: Meteosat
          4: direct & Y-bias (GPS-Sat.)..... >     1 <
  Coefficients: direct..... > -7.11677696E-08 <
                2-component..... >  3.52388541E-09 <
                3-component..... > -1.59660485E-08 <
                Meteosat..... > -5.58000000E-08 <
                Y-bias (GPS-satellites)..... >       1.d-9     <

CONSTANTS:
  GMS: Gravity constant*solar mass.....(m**3/s**2) >   1.3271250D20  <
  GMM: Gravity constant*lunar mass.....(m**3/s**2) >   4.9027890D12  <
  GMJ: GMsun/GMJupiter..... >  1047.3486D0    <
  GMV: GMsun/GMVenus..... >  408523.71D0    <
  Love number..... >         0.3     <
  Reference height h0 for drag.....(km) >       100.0     <
  Density at h0.....(kg/m**3) >       5.d-7     <
  Scale height h for drag.....(km) >        10.0     <
  C/2*Q/M of Satellite..... >        0.10     <

OSCULATING ELEMENTS OF SATELLITE:
  Osculation epoch Tosc (starting epoch).....(MJD) > 49645.000000000 <
  System.....0:apparent, 1:J2000..... >                1 <
  Revolution period.....P (used if A=0).....(h) >         0D0       <
  Semimajor axis.....A.....(m) > 42167815.026138 <
  Eccentricity.....E..... > 0.0001500285832 <
  Inclination.....I.....(deg) >    0.6653113815 <
  Ascending node.....NODE.....(deg) >   69.3579553306 <
  Perigee.....PER.....(deg) > -229.8140442599 <
  Mean anomaly at Tosc....SIGMA.....(deg) >  180.6838198131 <

INTEGRATION OF VARIATION EQUATIONS:
  Elements (a,e,i,node,per,sigma).....(0/1) >   0,0,0,0,0,0   <
  Radiation pressure .....(0/1) >     0 <
  Number of potential terms..... >     1 <
     degree n, order m..... >  2, 2 <
     degree n, order m..... >  3, 2 <
     degree n, order m..... >   2,0 <
```

Figure 3.6: Input file for the program SATIN3 (Part II).

orbit. The file containing gravity model coefficients may be specified in an input file list. Usually the models JGM3 or GEM-T3 are used.

- The gravitational perturbations from Sun, Moon, Jupiter, and Venus may be switched on or off. For all four bodies the JPL ephemerides can be used (the file can be specified in the input file list). The masses of the perturbing bodies are defined in the option file.

- The tidal potential induced by Sun and Moon is modelled without frequency dependence of the Earth's elasticity. The Love number k is defined in the input file (usually we use $k = 0.3$ (IERS Standards, 1992)).

- Density and scale height of the atmosphere and the drag resistance coefficient of the satellite may be specified to model atmospheric drag.

- Several models are implemented for the direct solar radiation pressure. A direct solar radiation acceleration may be used (which is modulated by the Sun's distance). For the Meteosat satellites a radiation pressure model that takes into account shape and surface properties of the satellite is implemented. The acceleration due to direct solar radiation is varying with the angle of incidence of the radiation onto the cylindrical satellite (see Appendix C). For each type of direct radiation pressure models the coefficient may be determined.

  An additional radiation pressure model involves three components of an acceleration vector. The first component points in the direction Sun–satellite, the second towards the ecliptic pole, and the third is orthogonal to the first two:

$$\boldsymbol{p} = p_1 \cdot \boldsymbol{e}_1 + p_2 \cdot \boldsymbol{e}_2 + p_3 \cdot \boldsymbol{e}_3 \tag{3.1}$$

  with

$$\boldsymbol{e}_1 = \begin{pmatrix} \cos\alpha\cos\delta \\ \sin\alpha\cos\delta \\ \sin\delta \end{pmatrix}, \qquad \boldsymbol{e}_2 = \begin{pmatrix} 0 \\ -\sin\varepsilon \\ \cos\varepsilon \end{pmatrix}, \qquad \boldsymbol{e}_3 = \boldsymbol{e}_1 \times \boldsymbol{e}_2 \tag{3.2}$$

  where α and δ are right ascension and declination of the Sun (as seen from the satellite) and ε is the obliquity of the ecliptic. Because the three components are fixed, the model describes an acceleration vector which points in a fixed direction with respect to the line Sun–satellite. All three components may be determined by the orbit determination program.

  The model (3.1) may be useful for taking into account the effect of solar radiation pressure on a tumbling satellite with extended solar panels. The effect of solar radiation pressure, averaged over one rotation (resp. precession) period, points in a fixed direction which is not necessarily parallel to the direction Sun–satellite. If the object is rotating at a rate which is much higher than the orbital period the model (3.1) may be appropriate to describe the solar radiation pressure effect.

  For GPS satellites the so-called y-bias (see Section 4.3.6) may be included into the force model.

- Shadow transits of the satellites are modelled using a flattened Earth. For testing whether the satellite is inside the shadow all z-coordinates are scaled by the flattening factor (1+1/297) which renders the shape of the Earth spherical with a cylindrical shadow. Penumbra effects are neglected.

  Radiation pressure is switched off, if the satellite is in the Earth's shadow. This may cause problems for long arcs because the variation of the orbital parameters changes also the shadow entry and exit epochs, an effect which is not properly included in the variational equations.

- Relativistic corrections may be included.

- Precession and nutation are modelled according to the IAU 1976 and 1980 resolutions.

- UT1–UTC corrections and polar motion are taken from the IERS Bulletin A.

In the input file of the program SATIN3 the osculating Keplerian elements are specified as initial conditions for the integration. Alternatively to the semimajor axis the revolution period may be given. Some of the input parameters are modified or adapted by programs ORBDT1 and/or ORBDT2 during the iterative orbit determination procedure.

3.1.4 Orbit Combination

Program ORBDET allows the estimation of only one parameter set per observation file. I.e., the elements of only one orbital arc may be determined. In order to have the possibility for combining observations from several arcs or even several satellites, the program ARCOMB was developed. The program combines the normal equation systems stemming from different runs of program ORBDET. The program ORBDET writes the normal equation matrix to a file after removing applied a priori weights, if the corresponding switch is activated in the input file. Program ARCOMB then reads the individual normal equation files and combines them to a combined system of normal equations. In addition to estimating all parameters that may be set up in the program ORBDET the program ARCOMB allows the determination of manœuver parameters (velocity changes) between subsequent arcs.

The approach used for the construction of the combined solution is based on the stacking of the normal equations for the individual arcs. The procedure is discussed in Brockmann (1996) and Beutler et al. (1996b) and shortly outlined in Appendix B. It essentially consists of three steps:

(1) The parameters that shall be determined in the combined solution are set up for each arc (except for the manœuver parameters that will be set up during the combination of the solutions). If necessary, weights are put on the parameters. For each arc an individual solution is computed using program ORBDET.

(2) The normal equations for the individual arcs are added after having removed a priori weights, having set up manœuver parameters, and having transformed all orbital elements of the orbits that shall be connected to one and the same epoch using the continuity conditions. From the combined normal equation corrections to the a priori values of the parameters are determined.

(3) If the termination criterion is not fulfilled, the normal equations for each arc are determined independently by running the orbit determination program with the improved parameters for each arc separately but without iterating. With the new normal equations a next combined solution is computed by repeating step (2).

Steps (2) and (3) are repeated iteratively until the termination criterion is fulfilled. The termination criterion is the same as in program ORBDET. In addition the continuity of the connected orbits may be tested independently.

The big advantage of the described procedure is the possibility to combine independent solutions *a posteriori*. I.e., the existing orbit determination program (which is not capable of processing several orbits at a time or to determine manœuver parameters) can be used to produce more complex solutions than it is designed for. The additional complexity is contained in the independent orbit combination program ARCOMB.

Program ARCOMB was successfully used to combine up to six arcs of Meteosat 4, 5 and 6 with the goal to determine resonance terms of the geopotential (see Chapter 5).

3.1.5 Covariance Studies

The orbit determination problem is a non-linear parameter estimation problem. If there are 'good' approximation for the orbit parameters p available (osculating elements referring to an osculation epoch t_{osc} plus (possibly) dynamical parameters like radiation pressure parameters) the orbit improvement problem must be linearized and solved by conventional least squares algorithms. Let us assume that the orbit improvement problem is governed by the following system of *normal equations*

$$\boldsymbol{A}^{\mathrm{T}}\boldsymbol{P}\boldsymbol{A} \cdot \Delta p = \boldsymbol{A}^{\mathrm{T}}\boldsymbol{P} \cdot \ell$$

where $\boldsymbol{A}$ is the first design matrix (Jacobian of observed functions with respect to the orbit parameters p); $\boldsymbol{P}$ is the weight matrix of the observations (assumed diagonal in our applications, diagonal terms are proportional to σ_i^{-2} with the mean error σ_i of the observation i); $\Delta p = p - p_0$ is the difference between the unknown orbit parameters p and the known a priori values p_0 for the parameters, i.e. the vector of the parameter improvements; l is the array of terms 'observed — computed'.

The variance covariance matrix of the parameter array p is computed as

$$\mathrm{cov}(p) \doteq m_0^2 \cdot \boldsymbol{Q} \doteq m_0^2 \cdot (\boldsymbol{A}^{\mathrm{T}}\boldsymbol{P}\boldsymbol{A})^{-1}$$

where m_0 is the a posteriori rms of unit weight. If we use a plausible value for m_0 we may study the mean error of and the correlations between individual parameters using the matrix $\boldsymbol{Q} = (\boldsymbol{A}^{\mathrm{T}}\boldsymbol{P}\boldsymbol{A})^{-1}$, only. This matrix $\boldsymbol{Q}$ may be computed without actually simulating observations; we only need to define the observation scenario (observation epochs, number of observations, matrix $\boldsymbol{P}$). Such a procedure is called a covariance study. Because the setting up of the normal equation system (i.e., the computation of the observed functions with respect to the parameters) is identical as in the case in which parameters are estimated using observations, it is straightforward to implement an option 'covariance studies' into a parameter estimation program.

The program ORBDET allows to perform covariance studies. In this case no observations are required; output are formal errors of the parameters based on the input rms error of the observations. Program EPOSIM is used for the generation of lists of epochs as input for the covariance studies. It allows to create randomly distributed close encounter series in a given number of nights within a defined time interval. The total number of close encounter series and the minimum number per night may be specified as well as the parameters for the series themselves (number of observations, time gap between the observations). First and last observation times for each night may be specified.

In the following we will use the correlation matrix $\boldsymbol{R}$ which may be computed through

$$\mathrm{corr}(p) \doteq \boldsymbol{R}, \qquad \text{where} \qquad R_{ik} \doteq \frac{Q_{ik}}{\sqrt{Q_{ii}Q_{kk}}}; \qquad i = 1,\ldots,n; k = 1,\ldots,n$$

If, for indices $i \neq k$ the component $R_{ik} = \pm 1$ the parameters i and k are completely correlated, if $R_{ik} \simeq 0$, the estimates are almost independent. The correlation matrix $\boldsymbol{R}$ is part of the output of program ORBDET.

Using the covariance matrix of the orbital elements the rms errors of the satellite's position and velocity at a given time t may be computed. This task is performed by the program ORBDXV. It computes the rms errors of position and velocity in the so-called RSW-system (see Figure 3.7): This system is defined by the 'radial' direction 'R' (first axis), the 'crosstrack' direction 'W' which is perpendicular to the orbital plane (third axis), and

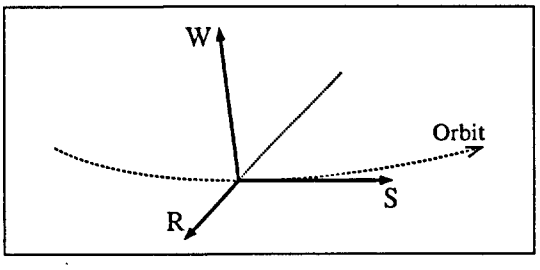

Figure 3.7: Definition of the RSW-system: radial direction 'R', alongtrack direction 'S', and crosstrack direction 'W'.

the 'alongtrack' component 'S' (second axis) pointing in the direction of the motion of the satellite and forming with the other two directions a right handed tripod. For eccentric orbits the 'S' direction is in general not parallel to the satellite's motion.

3.2 Distribution of the Observations

The accuracy of the determined orbital elements depends heavily on the distribution of observations. If the observed arc is too short (shorter than a few hours) it may not be possible to determine the shape of the orbit because in this case the semimajor axis and the eccentricity are strongly correlated. If the observed arc is long (several nights) it is possible to determine the direct radiation pressure coefficient(s) in addition to all osculating elements.

In the following sections we study the optimum distribution of observations for the determination of the orbital elements and radiation pressure coefficients. For simulations the orbit of Meteosat 4 is used as reference orbit. The elements are given in Table 3.1. Throughout the covariance analysis an observation rms error of 0.5″ was assumed.

Elements of Meteosat 4		
Osculation epoch t_{osc}	Oct. 20, 1994,	0:00 UT
Semimajor axis a	42167815 m	
Eccentricity e	0.0001500	
Inclination i	0.6653°	
R.A. of Ascending node Ω	69.3580°	
Argument of perigee ω	130.1860°	
Mean anomaly σ at t_{osc}	180.6838°	

Table 3.1: Elements of Meteosat 4 used for simulations.

3.2.1 Observations within one Night

If all six orbital elements are determined using observations acquired during a single night, strong correlations between the elements — and correspondingly large formal errors — have to be expected. In particular, the semimajor axis a and the eccentricity e will be highly correlated because only one sector of the orbit (in the night hemisphere) may be observed. This correlation between a and e can only be resolved if the length of the observed arc is sufficiently long to allow the determination of the mean motion (and therefore a) with high accuracy. An alternative is to add high accuracy range observations (Laser, transponders).

If the observed orbital arc is short, the eccentricity and (for small e) the argument of perigee must be constrained or even fixed to the a priori value. If only four orbital parameters (a, i, Ω, σ) are determined, the correlation between the elements is of course reduced significantly. In Figure 3.8 the correlation coefficient between a and i is given for a four element solution (+) and a six element solution (×) as a function of the length of the observed arc. The Figure is a result from covariance analyses based on the assumption of 5 close encounter series distributed within the observation interval. Each close encounter series contains 10 individual observations with an observation rms error of 0.5″.

The correlation between the semimajor axis and the inclination (as well as between the other elements) obtained from these analyses (based on realistic observation scenarios) is below 0.5 even for an observed arc length of only 1 hour, if only four elements are estimated (eccentricity and argument of perigee fixed). For an arc length of 6 hours the correlation between semimajor axis and eccentricity is below 0.2. If all six elements are determined without imposing a priori weights the correlation is close to 1 for arc lengths up to 3 hours. With increasing arc length the average correlation decreases, but its value strongly depends on the actual distribution of the observations. Therefore the scatter in Figure 3.8 increases with the length of the arc. For well distributed observation epochs the correlation may become insignificant for arc lengths of about 10 hours (i.e. an entire night). The correlation between semimajor axis and eccentricity, however, remains above 0.99 even for arc lengths as long as 10 hours.

Due to the strong correlation between the elements in the case of determining all six elements from observations acquired within one night, the formal errors of the elements

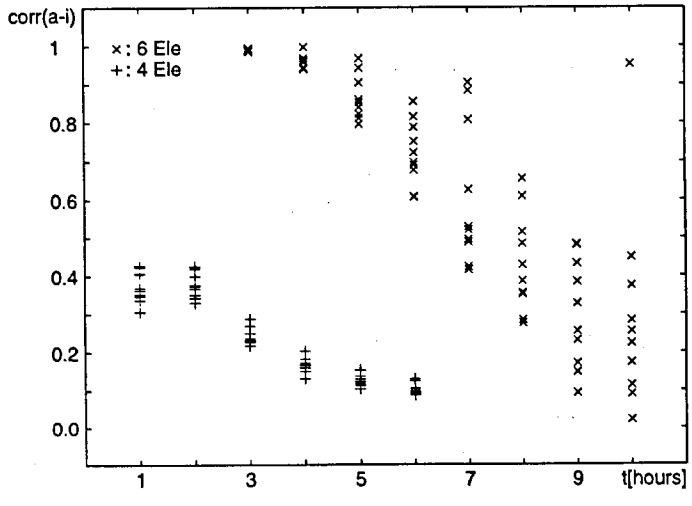

Figure 3.8: Correlation between the semimajor axis and the inclination as a function of the arc length when estimating four osculating elements (+) and six osculating orbital elements (×). Result from covariance analysis assuming five close encounter series with an observation rms error of 0.5″.

are much bigger than the formal errors obtained when estimating only four elements. The covariance analysis gives formal errors of more than 4 km in the semimajor axis for an arc length of 3 hours and about 2 km for an arc length of 10 hours. If eccentricity and argument of perigee are not determined the formal rms errors of the semimajor axis are below 100 m for an arclength of 1 hour. If only four elements are determined, systematic errors have to be expected, however, that may degrade the small formal errors.

The formal errors of the semimajor axis are shown as a function of the length of the observed arc in Figure 3.9. Figure 3.9 (left) corresponds to the case where eccentricity and argument of perigee are fixed, Figure 3.9 (right) to the case when all six elements are determined. The results from the covariance analysis follow more or less a straight line in the double logarithmic plot with a slope of -1 and -2.5, respectively. The formal error in the semimajor axis decreases proportional to Δt^{-1} if the eccentricity and the argument of perigee (i.e. the shape of the orbit) are fixed due to the improvement of the mean motion (where Δt is the length of the observed arc; the number of observations is fixed).

If all six elements are determined the improvement of the formal error of the semimajor axis decreases proportional to about $\Delta t^{-2.5}$ (but starting at a much higher value) because with increasing length of the arc not only the accuracy of the mean motion improves but also the shape of the orbit is established in a much better way. The formal errors of the other elements show a similar behaviour with increasing arc length as those for the semimajor axis.

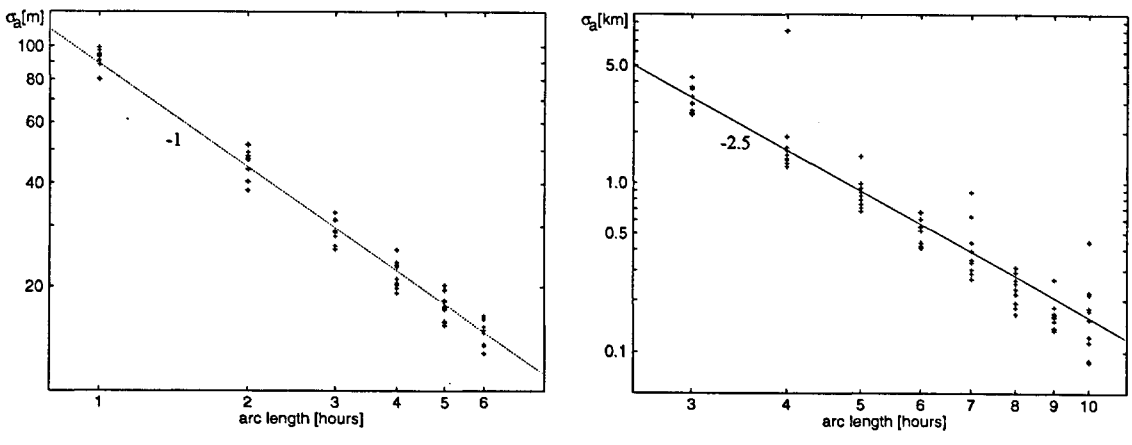

Figure 3.9: Formal errors in semimajor axis as a function of length of arc for four elements (left) and six elements determined (right). The symbols (+) give results from the covariance analysis, the dotted line indicates lines of slope -1 and -2.5, respectively, in the double logarithmic plot.

3.2.2 Observations Distributed over Several Nights

Combining the observations from more than one night for an orbit determination substantially improves the accuracy of the semimajor axis and greatly reduces the correlation between semimajor axis and eccentricity. In Figure 3.10 the formal errors of the semimajor axis (left) and of the orbital inclination are given as a function of the number of successive nights of observation. In the covariance analyses it was assumed that five close encounter series with 10 individual observations for each observation night (lasting from 20 UT to 4 UT) could be observed. The number of observations therefore increases (as opposed to the analyses in the previous section) linearly with time. The adopted observation rms error was again 0.5″.

As expected the formal errors of the elements decrease for each additional night of observation. For the inclination (and the other elements except the semimajor axis) the formal error decreases with the square root of the arc length (i.e. the number of observations) as expected from statistics (line with slope $-1/2$ in the double logarithmic scale of Figure 3.10 (right)). The formal error of the semimajor axis on the other hand decreases with the power $-3/2$ of the number of observation nights. In fact, a factor $t^{-1/2}$ results from the increased number of observations while an additional factor t^{-1} stems from the longer time interval covered by the observations.

The behaviour of the formal errors in Figure 3.10 is expected if the correlation between elements is small. Each element improves in this case as predicted by statistics for the number of observations and geometrical constraints (length of arc). In fact, covariance

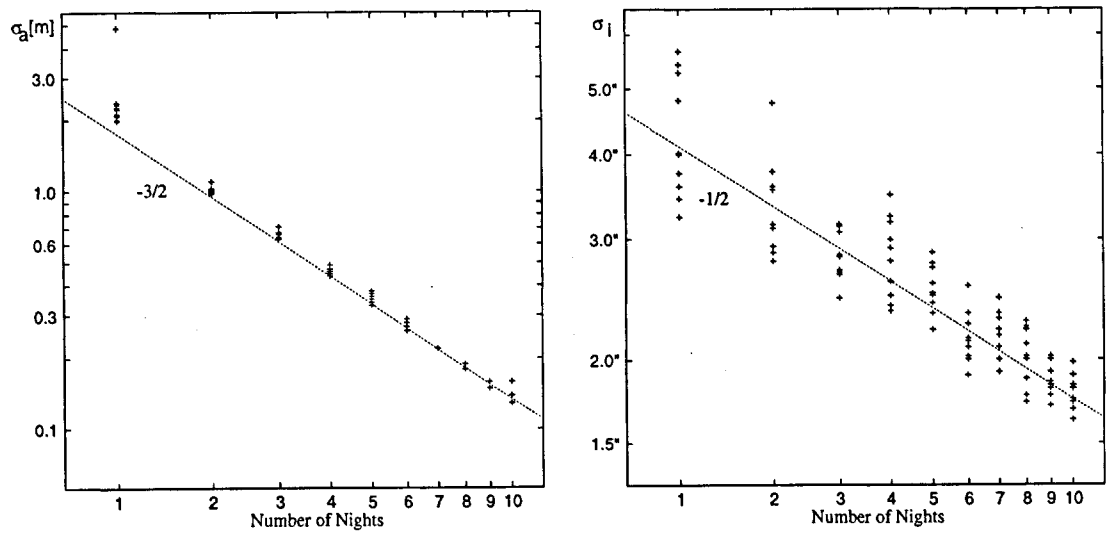

Figure 3.10: Formal errors of semimajor axis (left) and inclination (right) as a function of the arc length. The symbols (+) result from covariance studies, the dotted line indicates the theoretical slope in the double logarithmic plot.

studies give correlations between a and e of about 0.3 for two observation nights and of about 0.2 for ten observation nights.

3.2.3 Errors in the Extrapolated Position of the Satellites

In order to visualize the effect of different observation scenarios, different sets of measurements for Meteosat 4 acquired at the Zimmerwald observatory for the satellite Meteosat 4 in the time period between 3 to 6 of January 1995 were processed. In this time interval the satellite was observed every night (see Table 5.2 in Chapter 5) with an observation rms error of about 0.5" to 0.7" in each coordinate. In this section we deal with real astrometric observations and not with covariance studies.

Different subsets from the entire set of observations were selected for several orbit determinations. Observation epochs, number of close encounter series, and their time distribution within the day are given in Table 3.2 for each of the four experiments carried out. In each experiment all six osculating elements were estimated. From the associated rms errors the time evolution of the formal errors in the satellite position was computed for a time interval of 3 days. The rms errors in the radial (R), the alongtrack (S), and the crosstrack (W) components of the position are given in Figure 3.11 as a function of time for the four experiments carried out. The rms errors for the osculating elements are summarized in Table 3.3 (the osculation epoch is close to the observation epoch).

	Night	Obs. Series	Observ.	Epochs (UT)
Experiment 1	3/4 Jan.	2	18	22:50, 23:01
	4/5 Jan.	1	9	22:48
Experiment 2	3/4 Jan.	2	18	22:50, 23:01
	4/5 Jan.	1	9	22:48
	5/6 Jan.	2	14	20:36, 21:04
Experiment 3	4/5 Jan.	7	59	18:52 — 05:38
Experiment 4	3/4 Jan.	3	28	22:50 — 05:39
	4/5 Jan.	7	59	18:52 — 05:38
	5/6 Jan.	4	20	20:36 — 02:58

Table 3.2: Number, distribution, and coverage of the nights of the observations used for the four orbit determination experiments described in the text.

Two Nights, Few Observations In a first experiment only three close encounter series were selected in two successive nights. They were acquired at nearly the same time of the day (at 22:50 UT and 23:01 UT in the first night, at 22:48 UT in the second night, see Table 3.2). It is obvious that with such a distribution of observations the semimajor

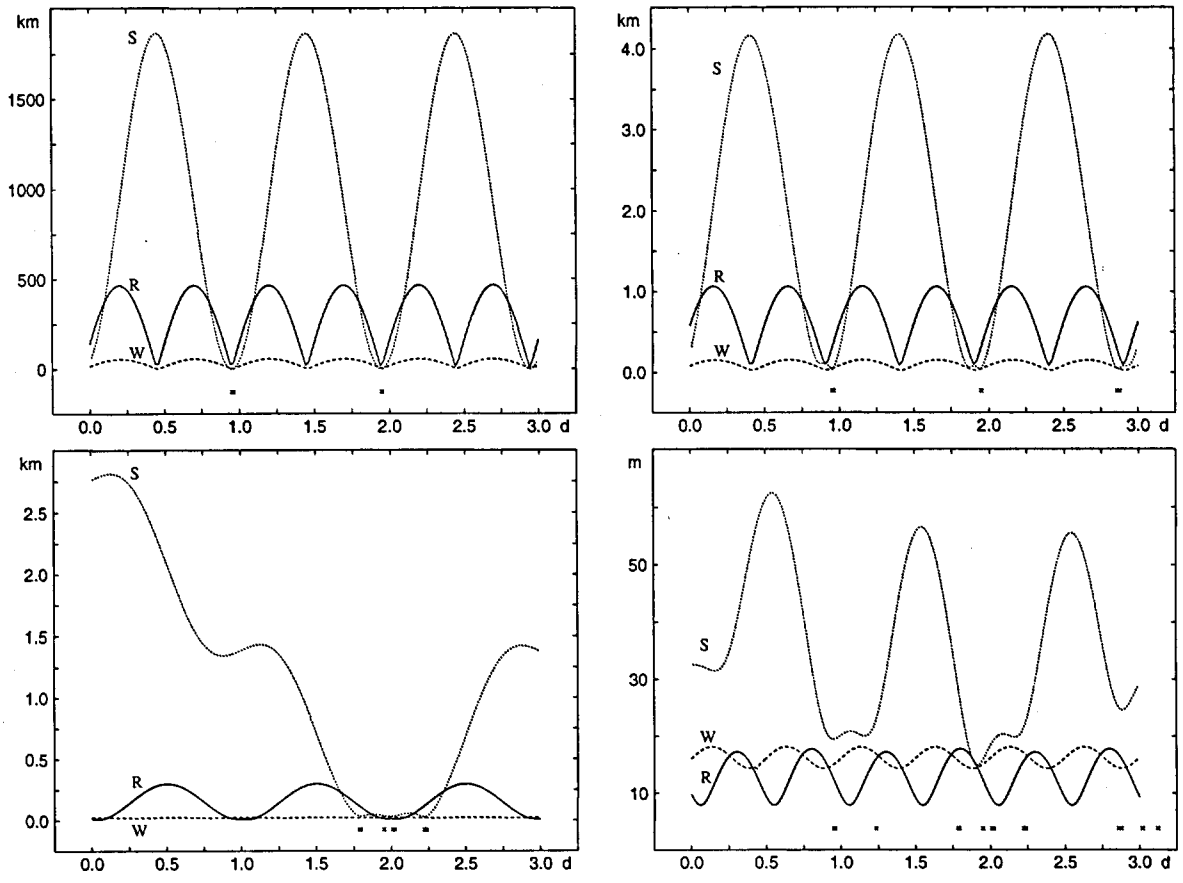

Figure 3.11: RMS errors in the position (R: radial, S: alongtrack, W: crosstrack direction) of Meteosat 4 for different distributions of the observations. Top left: Two observation nights with one close encounter series in each night at nearly the same time of day. Top right: Three observation nights with one close encounter series in each night. Bottom left: Good coverage by observations in only one night. Bottom right: All observations from three nights. The crosses indicate the observation epochs.

axis a is well determined due to the arc length of 24 hours. But the eccentricity is not well determined because the same part of the orbit was observed in both nights. This fact can be seen clearly in Figure 3.11 (top left): The radial (R) and the alongtrack (S) components show large variations which are entirely due to the poorly determined eccentricity (rms error of about 0.01, Table 3.3). (The 'true' value for the eccentricity is 0.00025; the relatively small error in the argument of perigee is only due to the eccentricity for which a value of 0.026 was determined.) Both, the curves for R and S, reach their minima around midnight (the observation epochs) for each night, even when there were no observations acquired. This fact indicates the comparatively good determination of the semimajor axis.

The rms error in the alongtrack component reaches the maximum value of more than 2'000 km around noon of each day; the error in alongtrack position at noon may reach ±3.5° (rms) due to the poorly known eccentricity. In radial direction the rms error reaches values up to 500 km, but this value is reduced to a similarly low value at noon as at midnight. The reason is clear: If we fix the semimajor axis and an arbitrary point P on the ellipse with given distance r to the focal point (center of gravity), the distance r' of the point P' in the opposite direction of point P is also known (up to terms of second order in the eccentricity). The two distances may be computed through

$$r = \frac{p}{1 + e\cos\nu} \qquad r' = \frac{p}{1 - e\cos\nu}$$

with $p = a \cdot (1 - e^2)$, eccentricity e, and true anomaly ν (e and ν unknown). The product of the two radii is

$$r \cdot r' = \frac{a^2(1 - e^2)^2}{1 - e^2\cos^2\nu} = a^2 + O(e^2).$$

Three Nights, Few Observations In a second experiment observations from five close encounter series distributed over three nights were used. The coverage of the orbit within the day by the series is somewhat better than in the previous experiment, the observations span the time interval between 20:36 UT to 23:01 UT. As expected (Figure 3.11 (top right) and Table 3.3) the rms errors in the elements and in the satellite positions are drastically reduced, the general shape of the curves describing the temporal evolution of the formal errors in position looks, however, very similar as in the previous experiment: The uncertainty of the orbit is still dominated by the uncertainty in the eccentricity. The maximum rms error in the alongtrack direction is reduced to below 4.5 km, the error in radial direction to about 1 km. Due to the observation time interval the semimajor axis is determined with a rms error of about 5 m instead of 140 m (previous experiment).

Element	RMS Errors of Elements			
	2 nights few. obs.	3 nights few obs.	1 night all obs.	3 nights all obs.
Semimajor axis [m]	139.2	5.1	147.1	1.8
Eccentricity	0.0111567	0.0000021	0.0000037	0.0000003
Inclination	0.07581°	0.00021°	0.00003°	0.00002°
R.A. of ascending node	1.33657°	0.00244°	0.00206°	0.00130°
Argument of perigee	0.94372°	14.66427°	0.53899°	0.19700°
Mean longitude at t_{osc}	1.27936°	0.00277°	0.00308°	0.00005°

Table 3.3: RMS errors of elements for four different distributions of the observations (see text). Geostationary orbit, observation rms 0.5" to 0.7".

One Night, Good Coverage For comparison we include an experiment containing observations from one night only, but composed of 7 close encounter series covering a time interval of almost 11 hours, i.e., almost half of the entire ellipse. The formal errors in position are shown in Figure 3.11 (bottom left). Maximum rms errors in alongtrack direction are below 3 km within the studied time interval, i.e., below the values obtained in the second experiment which used observations from three nights. In fact, the eccentricity is determined with the same rms error as in that experiment (Table 3.3). The semimajor axis on the other hand is determined with a precision which is more than 25 times worse. This error in the semimajor axis causes the quickly growing rms error in the alongtrack position of the satellite with the time difference to the observation night. That error remains, restricted by the observations, nearly constant at a small value for the entire observation night but starts to grow immediately after (and before) the time span covered by the observations with a rate of about 1.5 km/day.

Three Nights, All Observations As a reference we study in the last experiment the orbit estimation using all observations (a total of 14 close encounter series) within three successive observation nights. The observations cover nearly 11 hours in the second night. The semimajor axis is determined with a rms error of about 2 m, the eccentricity with one of $3 \cdot 10^{-7}$, and the inclination with one of 0.09″. The last value corresponds roughly to the observation error divided by the square root of the number of observations. The rms errors (see Figure 3.11, bottom right) reach about 60 m in the alongtrack component at noon in the three days interval with a slow increase towards the left and right boundaries, rms errors for the radial and crosstrack components both remain below 20 m (although the radial direction is not directly restricted by the observations but transferred through the dynamical equations).

From our few experiments we conclude that, in order to obtain the best possible orbits, the distribution of the observations must be in accordance with the following rules:

Rule 1: For a good determination of the semimajor axis the observations should be distributed over at least two nights. The longer the time base for the orbit determination, the better the mean motion is established (and with it the semimajor axis).

Rule 2: In order to obtain a good estimate for the eccentricity it is necessary to have a good coverage of the orbital curve by the observations. The longer the observation time span within the individual nights, the better the shape of the orbit is established (and with it the eccentricity together with the argument of perigee).

A good coverage of the orbit may also be obtained by, e.g., observations acquired during the second half of the first night and during the first half of the second night.

The two rules optimize the three orbital elements defining size and shape of the orbit and which are most difficult to be determined. The estimation of the other elements describing

the orientation of the orbital plane and the position of the object within the orbit is much less critical. If the two rules stated above are followed, these elements are determined with high precision, as well.

3.2.4 Determination of Radiation Pressure Coefficients

Because radiation pressure coefficients are correlated with the osculating elements, in particular with the semimajor axis, the eccentricity, and the argument of perigee, the observations used when trying to determine radiation pressure parameters must be well distributed. The elements which show the strongest correlation with radiation pressure coefficients depend on the relative position of the Sun (i.e., the direction of the perturbing force) and the apsidal line of the orbit. If, e.g., the perturbing force is parallel to the apsidal line, the correlation between radiation pressure and the semimajor axis is close to one. It is, at first sight, not obvious that radiation pressure correlates strongly with the semimajor axis because the solar radiation (apart from the Pointing-Robertson Effect) does only introduce periodic terms into the variation of the semimajor axis. The reason for the correlation will become clear later in this section.

As is easily seen from the perturbation equations the most prominent perturbation in the semimajor axis due to solar radiation pressure has a period of one revolution: The perturbation equation for the semimajor axis a reads (see e.g. Beutler (1992), p. 33)

$$\frac{da}{dt} = \frac{2}{n}\frac{1}{\sqrt{1-e^2}}\{e\sin\nu \cdot R + (1+e\cos\nu)\cdot S\} \tag{3.3}$$

where n is the mean motion, e the eccentricity, ν the true anomaly, and R and S the perturbing accelerations in the radial direction R, the direction S (perpendicular to R in direction of motion, alongtrack direction for circular motion). These accelerations may be computed with

$$\begin{pmatrix} R \\ S \\ W \end{pmatrix} = \mathrm{R}_3(\omega+\nu)\cdot\mathrm{R}_1(i)\cdot\mathrm{R}_3(\Omega)\cdot \boldsymbol{f} \tag{3.4}$$

where $\boldsymbol{f}$ is the perturbing acceleration in the equatorial coordinate system. Neglecting the motion of the Sun during the time interval considered as well as its parallax due to the finite distance between Sun and satellite, resp. the geocenter, we may write

$$\boldsymbol{f} = p\begin{pmatrix} \cos\alpha\cos\delta \\ \sin\alpha\cos\delta \\ \sin\delta \end{pmatrix} \tag{3.5}$$

where α and δ are the right ascension and declination of the Sun and p is the direct solar radiation pressure coefficient (with a negative value). With eqn. (3.5) the explicit form of

eqn. (3.4) reads

$$\begin{aligned} R &= p[\cos(\nu+\omega)\cos(\Omega-\alpha)\cos\delta \\ &\quad -\sin(\nu+\omega)\sin(\Omega-\alpha)\cos\delta\cos i+\sin(\nu+\omega)\sin\delta\sin i] \\ S &= p[-\sin(\nu+\omega)\cos(\Omega-\alpha)\cos\delta \\ &\quad -\cos(\nu+\omega)\sin(\Omega-\alpha)\cos\delta\cos i+\cos(\nu+\omega)\sin\delta\sin i]. \end{aligned} \tag{3.6}$$

In the following we will assume that the inclination is $i = 0°$. Eqns. (3.6) are then reduced to

$$\begin{aligned} R &= +p\cos(\nu+\Omega+\omega-\alpha)\cos\delta \\ S &= -p\sin(\nu+\Omega+\omega-\alpha)\cos\delta. \end{aligned} \tag{3.7}$$

Inserting these equations into eqn. (3.3) and neglecting terms of the order $O(e)$ we obtain the equation

$$\frac{da}{dt} = -\frac{2p}{n}\cos(\nu+\Omega+\omega-\alpha)\cos\delta + O(e) \tag{3.8}$$

which proves that the first order perturbation effect due to direct solar radiation pressure of the semimajor axis a is periodic with a period of one orbital revolution.

Let us now study the effect of radiation pressure on the eccentricity and the argument of perigee:

$$\frac{de}{dt} = \left\{\sin\nu\cdot R + \frac{2\cos\nu + e(1+\cos^2\nu)}{1+e\cos\nu}\cdot S\right\}. \tag{3.9}$$

Using expressions (3.7) for the perturbing accelerations neglecting terms of order $O(e)$ we obtain

$$\begin{aligned} \frac{de}{dt} &= \frac{1}{an}\{\sin\nu\cdot R + 2\cos\nu\cdot S\} + O(e) \\ &= \frac{p}{2an}\{3\sin(\Omega+\omega-\alpha)+\sin(2\nu+\Omega+\omega-\alpha)\}\cos\delta + O(e). \end{aligned} \tag{3.10}$$

We can see that the eccentricity contains a 'secular' term, namely

$$\left(\frac{de}{dt}\right)_{\text{sec}} = \frac{3p}{2an}\sin(\Omega+\omega-\alpha)\cos\delta + O(e). \tag{3.11}$$

This perturbation changes the eccentricity e at a constant rate. It is maximum if the geocentric angle between Sun and apsidal line is 90° which is why a high correlation between the two parameters (direct radiation pressure and eccentricity) must be expected. If, on the other hand, the Sun lies in the apsidal line, no such drift in the eccentricity is induced by radiation pressure.

For the argument of perigee the perturbation equation reads as

$$\frac{d\omega}{dt} = \frac{1}{e}\frac{\sqrt{1-e^2}}{an}\left\{-\cos\nu\cdot R + \frac{2+e\cos\nu}{1+e\cos\nu}\sin\nu\cdot S\right\} - \cos i\frac{d\Omega}{dt}. \tag{3.12}$$

If we again use eqn. (3.7) and retain only terms of the order $O(1/e)$ we obtain

$$\begin{aligned} e\frac{d\omega}{dt} &= \frac{1}{an}\{-\cos\nu \cdot R + 2\sin\nu \cdot S\} + O(e) \\ &= -\frac{p}{2an}\{3\cos(\Omega+\omega-\alpha) - \cos(2\nu+\Omega+\omega-\alpha)\}\cos\delta + O(e) \end{aligned} \quad (3.13)$$

and again we find a 'secular' term

$$\left(\frac{d\omega}{dt}\right)_{\text{sec}} = -\frac{1}{e}\frac{3p}{2an}\cos(\Omega+\omega-\alpha)\cos\delta + O(1) \quad (3.14)$$

which is maximum if the geocentric direction to the Sun coincides with the apsidal line. For the elements of Meteosat 4 used for the simulations together with a solar radiation pressure coefficient of $-7.1 \cdot 10^{-8}\text{m/s}^2$ a maximum drift of 0.6°/day is expected from the above equation.

If the perturbation by solar radiation on the argument of perigee is maximum a maximum correlation between the two parameters has to be expected. In addition, because the rotation of the orbital ellipse interferes with the motion of the satellite on the orbit, a strong correlation with the semimajor axis a will result, as well!

In Figure 3.12 the correlation coefficients of the semimajor axis with the radiation pressure (left) and of the argument of perigee with the radiation pressure (right) are shown as computed by covariance studies with an adopted observation rms error of 0.5″. The plus signs (+) correspond to the case where the geocentric direction to the Sun is parallel to

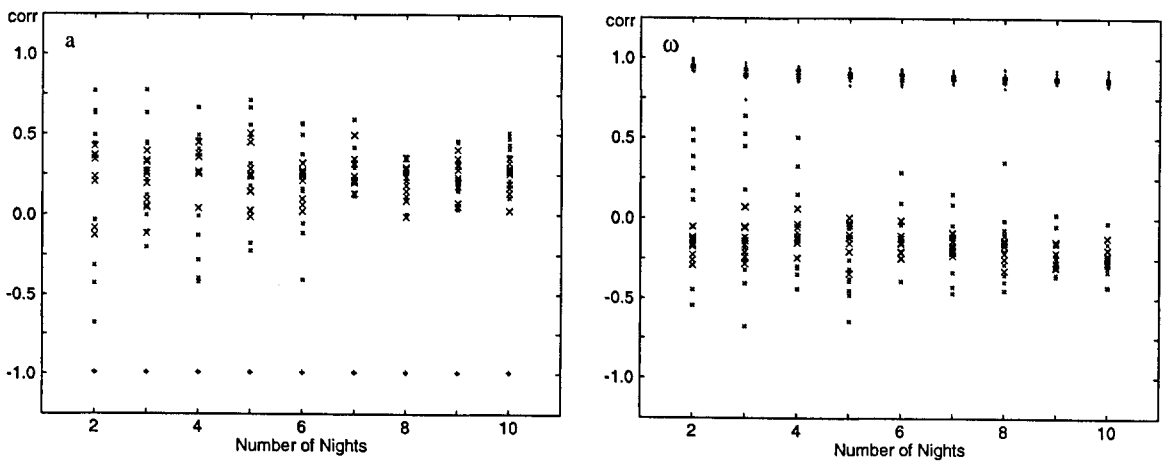

Figure 3.12: Correlation coefficients between direct solar radiation pressure and semimajor axis (left) and argument of perigee (right). Symbols +: direction of Sun parallel to apsidal line. Symbols ×: direction of Sun orthogonal to apsidal line. Results from covariance studies with an adopted observation rms error of 0.5″.

the apsidal line, the crosses (×) to the case where the geocentric direction to the Sun is orthogonal to the apsidal line. In fact, the correlation of the semimajor axis with the radiation pressure is almost perfect (correlation coefficient of −0.99 to −1.00) in the first case but only around 0.25 in the second case. The correlation between the argument of perigee and the radiation pressure is in the first case close to 1, too (0.85 to 0.95), and small in the second case. For the eccentricity, on the other hand, a strong correlation with the radiation pressure (−0.85 to −0.95) occurs in the case in which the perturbing force is normal to the apsidal line. The correlation of the mean longitude of the satellite at t_{osc} with the radiation pressure shows (of course) a similar behaviour as that for the semimajor axis, while the inclination i and the R.A. of the ascending node Ω are nearly uncorrelated with the solar radiation pressure. (The elements i and Ω may only be changed by an out of plane acceleration.)

The variation of the correlations of the radiation pressure with the osculating elements which describe size and shape of the orbit are also seen in the formal errors of these elements. In Table 3.4 the formal errors are given for orbits estimated with and without including radiation pressure coefficients and with different numbers of observations. In all covariance studies 5 close encounter series for each of the 2 resp. 10 successive nights were used with an observation rms error of 0.5″. If the geocentric direction to the Sun coincides with the apsidal line the formal error of the semimajor axis a is about one order of magnitude larger if the radiation pressure coefficient is estimated. If, on the other hand, the geocentric direction to the Sun is orthogonal to the apsidal line the formal errors are only slightly larger. In this case, however, the formal errors of the eccentricity are magnified by more than a factor of two.

In Figure 3.13 we see the improvement of the formal errors in the semimajor axis a (left) and the radiation pressure coefficient p (right) with the number of nights and observations used for the orbit determination. The two 'populations' pertaining to the simulations

Formal Errors for the Semimajor Axis a			
Parameters	Number of Nights	Direction to Sun rel. to apsidal line	Formal error
6 Elements	2	—	2.3 m
	10	—	0.15 m
6 Elements plus rad. press. coef.	2	parallel	17 m
		orthogonal	2.5 m
	10	parallel	1.2 m
		orthogonal	0.18 m

Table 3.4: Formal errors for the semimajor axis a, when radiation pressure coefficients are not estimated (6 parameters) resp. estimated. Result from covariance studies using an observation rms error of 0.5″.

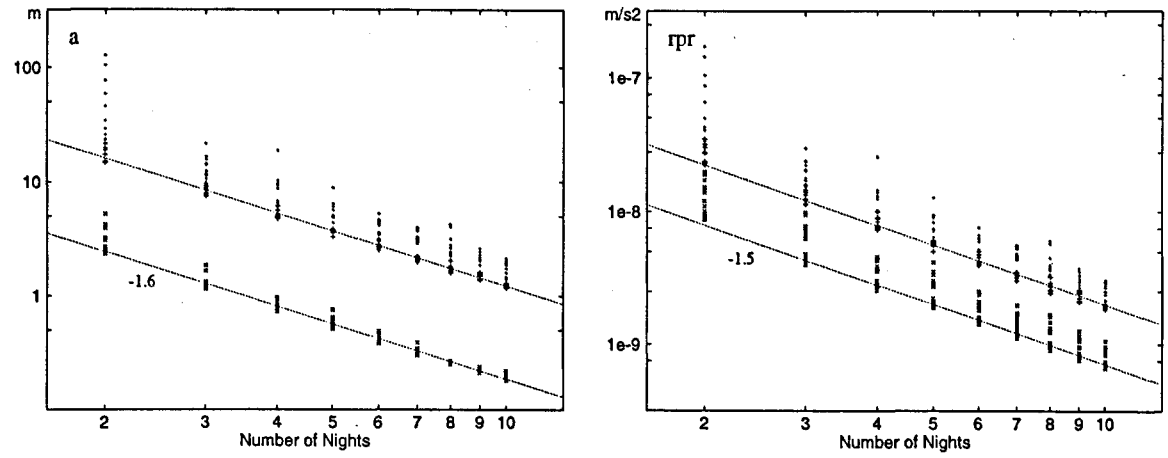

Figure 3.13: Formal errors of the semimajor axis a (left) and the radiation pressure coefficient p (right) as a function of number of successive nights used for the orbit determination process (double logarithmic representation). The two lines correspond to the case where the geocentric direction to the Sun is parallel (upper line) resp. normal (lower line) to the apsidal line. The slopes of the lines are -1.6 (left) and -1.5 (right). (Results from covariance studies with observation rms error of 0.5″.)

with the geocentric direction to the Sun parallel (upper lines) and normal (lower lines) to the apsidal line are clearly visible. The improvement for both parameters is roughly proportional to $\Delta t^{-3/2}$ where Δt is the arc length. For the other elements the formal error improves roughly proportional to $\Delta t^{-1/2}$. This behaviour is expected due to the growing number of observations and due to the increasing length of the observed arc.

We conclude that for a reliable determination of the radiation pressure coefficient(s) the two rules set up in the previous section for planning an observation campaign must be observed, too. In order to get reasonably small rms errors in the elements, in particular for the semimajor axis a which causes the linear growth of the alongtrack uncertainty in position as a function of time, the arc length should be longer than for the determination of the six osculating elements alone. In addition, the distribution of observation nights within the observed arc should be as homogeneous as possible. If the orbit is covered by observations only at the beginning and the end of the arc, the correlations between the elements and the radiation pressure may allow systematic effects (actually caused by radiation pressure) to 'hide' in the osculating elements. We may therefore state a third rule in addition to the two rules already stated above:

Rule 3: In order to get a reliable estimate for all orbital orbital parameters (osculating elements and radiation pressure parameters) the observed arc should have a length of one week or more. The observations should not only be well distributed within the individual nights but the observation nights should also be well distributed within the observation interval.

Rules 1 to 3 should be observed when scheduling observation sequences for an optimum determination of the orbit parameters for (high orbiting) objects selected for precise orbit determination.

4 Resonance of Satellite Motion with the Geopotential

4.1 Introduction

It is well known since the beginning of the space age that the ellipticity of the Earth's equator causes a resonant longitude drift of satellites in geosynchronous orbits (see e.g., Sehnal (1960), Kovalevsky (1961), Blitzer (1962), Morando (1962), Allan (1963)). The dominant terms in the geopotential responsible for this drift are the coefficients C_{22} and S_{22} of the Earth's gravitational potential. Figure 4.1 (left) shows the variations in the semimajor axis of the geostationary satellite Intelsat 4a f-6 over a time interval of 6 years (starting in April 1993). The figure is the result from a numerical integration of the orbit of this abandoned telecommunication satellite based on elements determined from astrometric observations at the Zimmerwald observatory in April 1993. In Figure 4.1 (right) the corresponding eastern longitude of the subsatellite point is given as a function of time. The oscillation with a period of about 1250 days or 3.4 years, amplitudes of about 35 km in the semimajor axis, and about 67° in longitude, is practically entirely due to the C_{22} and S_{22} terms of the Earth's potential.

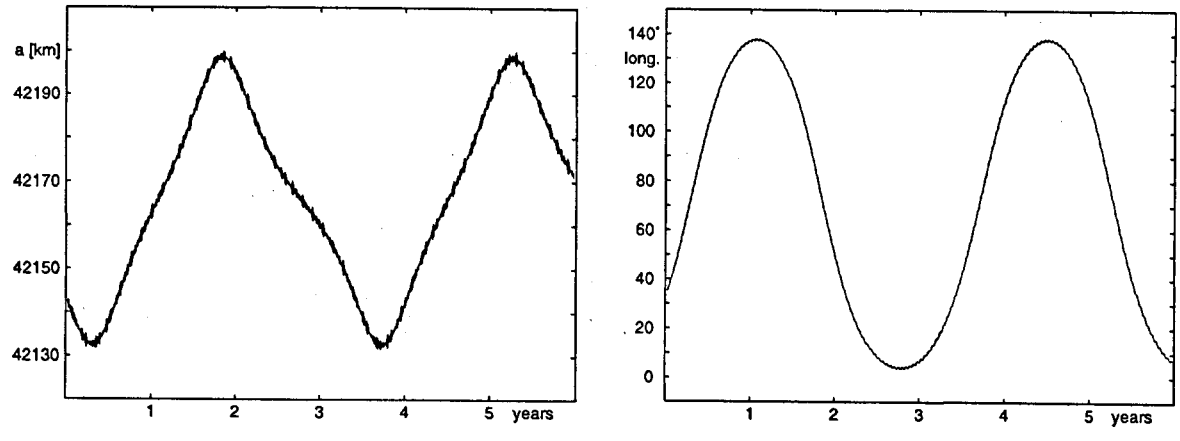

Figure 4.1: Resonant drift in the semimajor axis of the geosynchronous satellite Intelsat 4a f6 (left) and the corresponding oscillation in the geocentric eastern longitude of the satellite (right).

The accelerations due to different perturbations and the resulting longitude drifts are given in Table 1.7 for a geosynchronous satellite. It is obvious from that table that the perturbation caused by the ellipticity of the Earth's equator has different consequences than the other perturbations. Whereas the other perturbations cause a constant alongtrack drift, the perturbation from the ellipticity of the equator results in a constant alongtrack acceleration. After about one month the resulting displacement in longitude is equal to the

displacement caused by the oblateness of the Earth although the perturbing acceleration is three orders of magnitude smaller. The reason for this behaviour is a resonance effect of satellite motion with Earth rotation.

Because geostationary satellites are particularly sensitive to these geopotential terms, observations of their librating motion may be used to determine these coefficients. The first determination of the two geopotential coefficients using observations of geostationary satellites was performed by Wagner (1965) who processed radio-tracking data from the satellite SYNCOM 2. Catalano et al. (1983) proposed the determination of the resonant coefficients and their temporal variation using optical observations of geostationary satellites. Nobili (1987) established the research project COGEOS (International Campaign for Optical Observations of Geosynchronous Satellites).

The COGEOS project was sponsored by the European Community. Research groups from Belgium, Peoples Republic of China, Czech Republic, France, Germany, Hungary, Italy, Poland, Russia, Spain, Switzerland, United Kingdom, Ukraine, and USA participated in COGEOS. Optical observations were made at the Gönnsdorf Observatory of the Technical University of Dresden (Böhme et al., 1995), the Main Astronomical Observatory of the Ukrainian Academy of Science (Duma et al., 1986) (Ivashchenko, 1989), the Royal Greenwich Observatory at Herstmonceux (Appleby et al., 1995), and the Zimmerwald observatory of the Astronomical Institute of the University of Bern (Hugentobler et al., 1995). The first two observatories used sophisticated photographic techniques whereas the latter two applied CCD techniques. In addition, time synchronization methods were used for the position determination of commercial geosynchronous telecommunication satellites (Kardos et al., 1995) in the framework of COGEOS.

Using astrometric observations acquired at the Zimmerwald observatory it was possible to determine the resonant geopotential coefficients (Hugentobler et al., 1996) with an accuracy corresponding to the expectations based on simulations (Rossi, 1988). The observations and results will be discussed in detail in Chapter 5.

In this chapter we will study the 1:1-resonance and the 2:1-resonance. Through covariance studies we assess the accuracy of the determination of the resonant geopotential coefficients from astrometric observations of geostationary satellites. For the satellites of the GPS system we compute the effects of resonance from theory and compare them with measurements.

4.1.1 Commensurability and Resonance

A resonance of satellite motion with terms of the geopotential only occurs if the orbital period is commensurable with the rotation period of the Earth. A satellite in m:n-commensurability orbits the Earth m times while the Earth rotates n times, i.e., in n sidereal days, where m and n are small integers. A satellite in such an orbit may be subject to resonance with some sectorial and/or tesseral terms of the Earth's potential. Such a resonance manifests itself as a longperiodic variation of the orbital elements. Fig. 4.10

shows such a resonance phenomenon in the semimajor axis for a GPS satellite in deep 2:1-resonance. As we will see in Section 4.2, a commensurability must not always cause resonance, however.

Below we will discuss the 1:1-commensurability and the 2:1-commensurability. In the 1:1-commensurability we find the geostationary satellites, in the 2:1-commensurability the GPS satellites. We will study in detail the resonance phenomena in the semimajor axis where they are visible most easily because the Earth's potential produces, as we will see, no longperiodic first order perturbations in this element.

4.1.2 The Earth's Potential

Following usual conventions we expand the Earth's gravitational potential into spherical harmonics:

$$V(\boldsymbol{r}) = -\frac{\mu}{r} + \sum_{l=2}^{\infty} \sum_{m=0}^{l} V_{lm}(\boldsymbol{r}), \qquad \mu = GM \tag{4.1}$$

where V_{lm} is the term of degree l and order m:

$$V_{lm}(\boldsymbol{r}) = -\frac{\mu}{r}\left(\frac{a_e}{r}\right)^l P_{lm}(\sin\beta)\left(C_{lm}\cos m\lambda + S_{lm}\sin m\lambda\right). \tag{4.2}$$

r, λ, β are the spherical coordinates of the vector $\boldsymbol{r}$ in the Earth-fixed system, namely geocentric distance, longitude and latitude respectively. P_{lm} are the associated Legendre functions of degree l and order m, C_{lm} and S_{lm} are the expansion coefficients of the potential, and a_e is the equatorial radius of the Earth. The term V_{20} represents the flattening of the Earth, the term V_{21} is due to the deviation of the principal axis of inertia from the z-axis of the coordinate system in which the potential is expanded, the term V_{22} represents the flattened azimuthal mass distribution, i.e. the ellipticity of the Earth's equator. The latter term will be of particular interest to us.

The expansion usually starts with degree $l = 2$, which assumes that the origin of the coordinate system coincides with the center of mass of the Earth. If this condition is not fulfilled, terms with degree $l = 1$ would occur, as well.

Eqn. (4.2) may be written in the following way

$$V_{lm} = -\frac{\mu}{r}\left(\frac{a_e}{r}\right)^l P_{lm}(\sin\beta) J_{lm}\cos m(\lambda - \lambda_{lm}), \tag{4.3}$$

where

$$\begin{aligned} C_{lm} &= J_{lm}\cos m\lambda_{lm} \\ S_{lm} &= J_{lm}\sin m\lambda_{lm} \end{aligned} \quad .$$

Usually, normalized coefficients are used:

$$\left\{ \begin{array}{c} \bar{C}_{lm} \\ \bar{S}_{lm} \end{array} \right\} = \sqrt{\frac{(l+m)!}{k(2l+1)(l-m)!}} \left\{ \begin{array}{c} C_{lm} \\ S_{lm} \end{array} \right\} \qquad k = \left\{ \begin{array}{lll} 1 & \text{for} & m = 0 \\ 2 & \text{for} & m \neq 0 \end{array} \right. \tag{4.4}$$

which are then associated with the fully normalized Legendre functions.

The first few terms of the JGM3 geopotential model (Tapley et al., 1996) are given in Table 4.1 together with their formal errors. The complete JGM3 model contains all terms up to degree and order 70, i.e. more than 5000 terms.

l	m	$\bar{C}_{lm}$	$\pm$	$\bar{S}_{lm}$	$\pm$
2	0	$-4841.69548 \cdot 10^{-7}$	$4.7 \cdot 10^{-11}$	—	
2	1	$-0.00187 \cdot 10^{-7}$		$0.01195 \cdot 10^{-7}$	
2	2	$24.39263 \cdot 10^{-7}$	$3.7 \cdot 10^{-11}$	$-14.00266 \cdot 10^{-7}$	$3.7 \cdot 10^{-11}$
3	0	$9.57176 \cdot 10^{-7}$	$3.6 \cdot 10^{-11}$	—	
3	1	$20.30137 \cdot 10^{-7}$	$11.5 \cdot 10^{-11}$	$2.48131 \cdot 10^{-7}$	$11.5 \cdot 10^{-11}$
3	2	$9.04706 \cdot 10^{-7}$	$9.4 \cdot 10^{-11}$	$-6.18923 \cdot 10^{-7}$	$9.4 \cdot 10^{-11}$
3	3	$7.21145 \cdot 10^{-7}$	$5.8 \cdot 10^{-11}$	$14.14204 \cdot 10^{-7}$	$5.7 \cdot 10^{-11}$
4	0	$5.39777 \cdot 10^{-7}$	$13.4 \cdot 10^{-11}$	—	
4	1	$-5.36244 \cdot 10^{-7}$	$8.7 \cdot 10^{-11}$	$-4.73772 \cdot 10^{-7}$	$8.7 \cdot 10^{-11}$
4	2	$3.50670 \cdot 10^{-7}$	$15.6 \cdot 10^{-11}$	$6.62571 \cdot 10^{-7}$	$15.6 \cdot 10^{-11}$
4	3	$9.90869 \cdot 10^{-7}$	$7.9 \cdot 10^{-11}$	$-2.00987 \cdot 10^{-7}$	$7.9 \cdot 10^{-11}$
4	4	$-1.88481 \cdot 10^{-7}$	$7.2 \cdot 10^{-11}$	$3.08848 \cdot 10^{-7}$	$7.2 \cdot 10^{-11}$

Table 4.1: Normalized geopotential coefficients from the JGM3 model (Tapley et al., 1996).

4.1.3 The Oscillation Equation for a Geosynchronous Satellite

To get the intersection of the equipotential surface of the Earth with the equatorial plane we consider only the monopole term and the J_{22}-term in eqn. (4.1) and equate it to a 'mean' potential $-\mu/a_e$. Solving for r gives the equipotential shape of the Earth's equator (to first order in $r/a_e - 1$)

$$r \simeq a_e[1 + 3J_{22} \cos 2(\lambda - \lambda_{22})].$$

Obviously the equator is elongated towards $\lambda_{22} \simeq 14.9°$ W (Westafrica) and 165.1° E (Pacific Ocean). The difference between semimajor and the semiminor axes is $6 \cdot a_e J_{22} \simeq$ 69 km.

Let us briefly derive the differential equation for the longitudinal acceleration of a geostationary satellite due to this ellipticity of the equator. For simplicity we assume a circular

orbit with zero inclination ($a = 42164$ km, $e = 0$, $i = 0°$). We insert the potential term J_{22} into the perturbation equation for the semimajor axis (see e.g. Beutler (1992))

$$\dot{a} = -\frac{2}{an}\frac{\partial V}{\partial \lambda} \quad . \tag{4.5}$$

The acceleration $\ddot{\lambda}$ of the longitude of the satellite is equal to the change of the mean motion $\dot{n}$ which in turn is related to the change of the semimajor axis by Kepler's third law

$$\dot{a} = -\frac{2}{3}\frac{a}{n}\dot{n}. \tag{4.6}$$

We therefore may write down the differential equation for λ

$$\ddot{\lambda} = 18n^2\left(\frac{a_e}{a}\right)^2 \cdot J_{22} \cdot \sin 2(\lambda - \lambda_{22}) \quad . \tag{4.7}$$

Substituting $x \equiv 2(\lambda - (\lambda_{22} - \pi/2))$ we get the differential equation

$$\begin{aligned} \ddot{x} - \omega^2 \sin x &= 0 \\ \omega^2 &= 36n^2\left(\frac{a_e}{a}\right)^2 J_{22} \end{aligned} \tag{4.8}$$

which is the equation of the mathematical pendulum. The satellite oscillates around the small axes of the equipotential surface which are at 75.1° E (over the Indian Ocean) and at 104.9° W (near Galapagos). I.e., the stable points of the motion are at the orbit location corresponding to the highest potential whereas the points lowest in the potential are unstable! The reason for this, at first sight, strange behaviour is found in the negative sign in eqn. (4.6) which causes the sign of the longitude acceleration to be opposite to the perturbing alongtrack force.

With the numerical values for a geostationary satellite

$$\begin{aligned} n &= 6.300[\text{rad/day}] \\ a_e/a &= 0.15 \\ J_{22} &= 1.8155 \cdot 10^{-6} \end{aligned}$$

we get from eqn. (4.8) the frequency $\omega = 7.632 \cdot 10^{-3}$ rad/day and for small amplitudes an oscillation period of $T \simeq 823$ days. The solution of the mathematical pendulum involves the complete elliptic integral of the first kind $K(\alpha)$ (Abramowitz et al., 1965)

$$T = \frac{2\pi}{\omega}K(\alpha) = \frac{2\pi}{\omega}\left[1 + \left(\frac{1}{2}\right)^2\alpha + \left(\frac{1\cdot 3}{2\cdot 4}\right)^2\alpha^2 + \left(\frac{1\cdot 3\cdot 5}{2\cdot 4\cdot 6}\right)^2\alpha^3 + \ldots\right] \tag{4.9}$$

with

$$\alpha = \sin^2 \Delta\lambda_{\max}$$

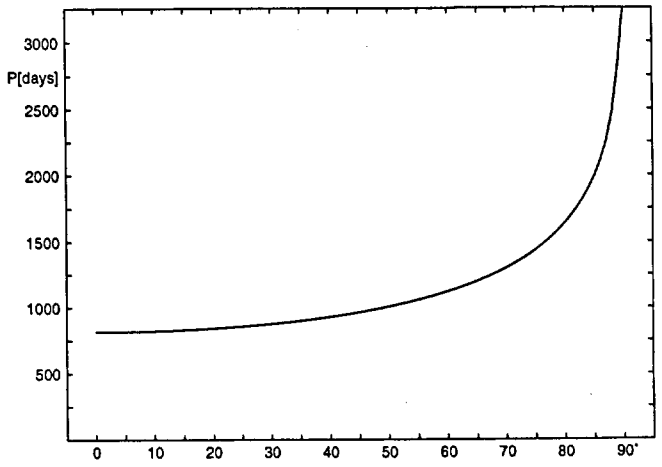

Figure 4.2: Libration period as a function of time for a satellite in 1:1-resonance ($a = 42164$ km, $e = 0$, $i = 0°$) due to the geopotential term J_{22}.

where $\Delta\lambda_{\max}$ is the amplitude of the oscillation in longitude. In Figure 4.2 we see the period of the libration as a function of the amplitude.

From energy conservation follows the maximum change of the semimajor axis during the librational motion

$$\Delta a < 4a_e\sqrt{J_{22}} = 35\text{km} \quad , \tag{4.10}$$

as well as the maximum possible drift in longitude which is equal to $\omega = 0.44°/\text{day}$. The numerical values from numerical integration given for Intelsat 4a f-6 agree fairly well with the numbers deduced from theory.

4.2 The Resonance Terms

4.2.1 The perturbation Equation for the Semimajor Axis

Following Kaula (1966) we expand the Earth's potential into a trigonometric series with the arguments mean anomaly M, longitude of the ascending node Ω, argument of perigee ω, and sidereal time Θ. In a first step we use the potential in the form of eqn. (4.3) and express β and λ by the orbital elements and the true anomaly of a satellite (parametrized by the elements i, Ω, ω and the true anomaly ν) and we obtain

$$\begin{aligned} V_{lm} &= -\frac{\mu}{r}\left(\frac{a_e}{r}\right)^l \sum_{p=0}^{l} F_{lmp}(i) J_{lm} \begin{bmatrix} \cos\Psi_{lmp} \\ \sin\Psi_{lmp} \end{bmatrix}_{l-m}^{l-m} \quad \begin{matrix} \text{even} \\ \text{odd} \end{matrix} \\ \Psi_{lmp} &= (l-2p)(\omega+\nu) + m(\Omega - \Theta - \lambda_{lm}). \end{aligned} \tag{4.11}$$

$F_{lmp}(i)$ is the so-called inclination function, the explicit form of which may be found in Kaula (1966). In a second step we replace r and ν by series in a, e, and M to obtain the potential terms in the form

$$\begin{aligned} V_{lm} &= -\frac{\mu}{a}\left(\frac{a_e}{a}\right)^l \sum_{p=0}^{l}\sum_{q=-\infty}^{\infty} F_{lmp}(i)G_{lmq}(e)J_{lm}\begin{bmatrix}\cos\Psi_{lmpq}\\ \sin\Psi_{lmpq}\end{bmatrix}_{l-m}^{l-m} \quad \begin{matrix}\text{even}\\ \\ \text{odd}\end{matrix} \qquad (4.12)\\ \Psi_{lmpq} &= (l-2p)\omega + (l-2p+q)M + m(\Omega - \Theta - \lambda_{lm}) \quad . \end{aligned}$$

An elegant derivation of the second equation may be found in Tisserand (1888). $G_{lmq}(e)$ is the so-called eccentricity function, given e.g. in Kaula (1966). It is proportional to the eccentricity to the power $|q|$. Therefore only terms with small $|q|$ contribute for small eccentricities.

For studying the effect of the perturbations from geopotential terms on the semimajor axis we introduce the expression of the potential from eqn. (4.13) into the Lagrangian perturbation equation (see e.g. Beutler (1992)).

$$\frac{da}{dt} = -\frac{2}{na}\frac{\partial V}{\partial M}$$

and we get

$$\frac{da}{dt} = 2na\sum_{lmpq}\left(\frac{a_e}{a}\right)^l F_{lmp}(i)G_{lmq}(e)J_{lm}(l-2p+q)\begin{bmatrix}-\sin\Psi_{lmpq}\\ \cos\Psi_{lmpq}\end{bmatrix}_{l-m}^{l-m} \quad \begin{matrix}\text{even}\\ \\ \text{odd}\end{matrix} \quad . \qquad (4.13)$$

In first order perturbation theory the angular argument Ψ_{lmpq} is a linear function of time with the variables M and Θ increasing fastest. The rate of change of Ψ_{lmpq}

$$\dot{\Psi}_{lmpq} = (l-2p)\dot{\omega} + (l-2p+q)\dot{M} + m(\dot{\Omega} - \dot{\Theta}) \qquad (4.14)$$

depends on the values of the indices l, m, p, q and determines what frequencies are contained in the temporal evolution of the semimajor axis and which terms in the geopotential are responsible for the perturbations. For each set of indices the amplitude, period, and phase of the perturbation in the semimajor axis may be computed from eqn. (4.13) for a specific orbit. (For the other elements similar equations as eqn. (4.13) hold, the following discussion might therefore be applied to all elements). In first order perturbation theory perturbations are classified into *short-periodic*, *long-periodic*, *secular*, *m-daily*, and *resonant* perturbations (see Klokocnik (1991)). If the coefficient of M in eqn. (4.13) does not vanish, i.e., if $l-2p+q \neq 0$, short periodic perturbations with periods of multiples of the orbital revolution do occur. Potential terms with $l-2p+q=0$ and $m=0$, on the other hand, generate only longperiodic perturbations since the only time dependent argument left in eqn. (4.13) is ω. For $m \neq 0$ so-called *m-daily* perturbations occur with periods of the m-th fraction of a day, generated by tesseral potential terms because Ψ_{lmpq} contains a term $m\Theta$. If all coefficients in eqn. (4.14) are zero the right hand side of the perturbation equation is constant and a secular perturbation may occur.

From eqn. (4.13) it is obvious that the geopotential cannot induce secular or longperiodic perturbations in the semimajor axis because for all terms with $l-2p+q = 0$ the right hand side of the equation is zero leaving the semimajor axis unperturbed. All other elements may contain longperiodic terms. The elements ω, Ω and M can show secular perturbations, i.e., those elements whose Lagrangian perturbation equations contain derivatives with respect to a, e, or i which are the only partials of eqn. (4.12) that do not vanish in the secular case $\Psi_{lmpq} = 0$.

4.2.2 Resonance

Resonance occurs if eqn. (4.14) is close to zero for $m \neq 0$, (for $m = 0$ the Earth's rotation would not be involved in the perturbations and one would not speak of resonance but of long-periodic or secular perturbations)

$$(l-2p)\dot{\omega} + (l-2p+q)\dot{M} + m(\dot{\Omega} - \dot{\Theta}) \cong 0 \qquad m \neq 0 \quad . \tag{4.15}$$

The potential terms for which the resonance condition (4.15) holds induce only a small variation of da/dt (and the other orbital elements), and a consequently may show a quasi-secular, resonant behaviour. Because M and Θ are the variables that vary fastest with time the resonance condition may be stated in the following form

$$(l-2p+q)n \simeq m\dot{\Theta}, \tag{4.16}$$

where n is the satellite's mean motion. For a given resonance $n/\dot{\Theta} = \beta/\alpha$ the indices l, m, p and q of the terms responsible for the resonance may be extracted from eqn. (4.16):

$$(l-2p+q) = \alpha\gamma \qquad m = \beta\gamma \quad . \tag{4.17}$$

$\gamma = 1, 2, 3, \ldots$ is the so-called resonance level. The lowest resonance indices are given in Tables 4.2 and 4.3 for the 1:1- and the 2:1-resonance respectively. The influence of the resonance terms is reduced by the factor $(a_e/a)^l$ in the perturbation equation. For nearly circular orbits the influence of the terms with $q \neq 0$ is small because the terms are proportional to the eccentricity $e^{|q|}$. The most important terms for resonance are therefore those with low l and with $q = 0$, i.e., the J_{22} term for the 1:1-resonance and the J_{32} term for the 2:1-resonance.

Tables 4.4 and 4.5 contain perturbing terms and the corresponding periods and amplitudes or drift rates of the perturbations in the semimajor axis for an orbit in 1:1-resonance (with elements $a = 42164$ km, $e = 0.001$, $i = 10°$, Table 4.4) and an orbit in 2:1-resonance (with elements $a = 26562$ km, $e = 0.006$, $i = 57°$, Table 4.5) respectively. Terms inducing short periodic perturbations with amplitudes larger than 0.5 m and resonant perturbations with drift rates larger than 5 cm/day are listed. For the the semimajor axis the values for exact resonance are given. The secular changes in Ω and ω due to the oblateness of the Earth were computed using the equations (see e.g. Kaula (1966))

$$\frac{d\Omega}{dt} = \frac{3nC_{20}a_e^2}{2(1-e^2)^2a^2}\cos i, \qquad \frac{d\omega}{dt} = \frac{3nC_{20}a_e^2}{4(1-e^2)^2a^2}(1-5\cos^2 i).$$

l	2	2	**2**	2	3	**3**	3	3	3	**3**	3	4	4	4	4	4	4	4	4
m	1	1	**2**	2	1	**1**	1	2	2	**3**	3	1	1	2	**2**	2	3	3	4	4
p	0	1	**0**	1	0	**1**	2	0	1	**0**	2	1	2	0	**1**	2	0	1	**0**	1
q	-1	1	**0**	2	-2	**0**	2	-1	1	**0**	1	-1	1	-2	**0**	2	-1	1	**0**	2

Table 4.2: Selectors for the 1:1-resonance. All indices with $|q| < 3$ and $l \leq 4$. Terms proportional to the eccentricity $e^0 = 1$ are printed in bold numbers.

l	2	2	3	**3**	3	4	4	4	4	**5**	5	5
m	2	2	2	**2**	2	2	2	4	4	**2**	4	4
p	0	1	0	**1**	2	1	2	0	**1**	**2**	1	2
q	-1	1	-2	**0**	2	-1	1	-2	**0**	**0**	-1	1

Table 4.3: Selectors for the 2:1-resonance. All indices with $|q| < 3$ and $l \leq 5$. Terms proportional to the eccentricity $e^0 = 1$ are printed in bold numbers.

The contribution of different potential terms to the drift rate da/dt are given in Figure 4.3 for the geostationary satellite Intelsat 4a f-6. The dotted lines indicate the maximum

$l\ m\ p\ q$	$2an(a_e/a)^l$ [m/s]	$\bar{J}_{lm}$	$\bar{F}_{lmp}(i)$	$G_{lpq}(e)$	Ampl. [m]	Period [d]	Drift [m/d]	a [km]	γ
2 0 0 0	$1.41 \cdot 10^{+2}$	$4.84 \cdot 10^{-4}$	−0.025	1.000	23.6	.4986			
1-1			−1.067	0.002	1.5	.9972			
1			−1.067	0.002	1.5	.9972			
2 0			−0.025	1.000	23.6	.4986			
2 0 0		$2.81 \cdot 10^{-6}$	1.907	1.000			130.18	42166.15	2
3 1 1 0	$2.13 \cdot 10^{+1}$	$2.04 \cdot 10^{-6}$	−1.487	1.000			5.59	42166.15	1
3 0 0		$1.58 \cdot 10^{-6}$	2.044	1.000			17.78	42166.15	3
4 2 1 0	$3.22 \cdot 10^{+0}$	$7.52 \cdot 10^{-7}$	−1.479	1.000			.62	42166.15	2
4 0 0		$3.57 \cdot 10^{-7}$	2.152	1.000			.85	42166.15	4
5 3 1 0	$4.87 \cdot 10^{-1}$	$5.09 \cdot 10^{-7}$	−1.468	1.000			.09	42166.15	3
5 0 0		$6.78 \cdot 10^{-7}$	2.240	1.000			.32	42166.15	5

Table 4.4: Perturbations in the semimajor axis for the 1:1-resonance ($a = 42164$ km, $e = 0.001$, $i = 10°$) due to different potential terms. All terms causing amplitudes > 0.5 m or drifts > 5 cm/day are listed together with the numerical values of the expressions in eqn. (4.13).

$l\ m\ p\ q$	$2an(a_e/a)^l$ [m/s]	$\bar{J}_{lm}$	$\bar{F}_{lmp}(i)$	$G_{lpq}(e)$	Ampl. [m]	Period [d]	Drift [m/d]	a [km]	γ
2 0 0-1	$4.47 \cdot 10^{+2}$	$4.84 \cdot 10^{-4}$	−0.590	−0.003	2.6	.4986			
0			−0.590	1.000	874.6	.2493			
1			−0.590	0.021	18.4	.1662			
1-1			0.062	0.009	.8	.4986			
1			0.062	0.009	.8	.4986			
2-1			−0.590	0.021	18.4	.1662			
0			−0.590	1.000	874.6	.2493			
1			−0.590	−0.003	2.6	.4986			
2 0-1		$2.81 \cdot 10^{-6}$	1.155	−0.003			.38	26560.67	1
0			1.155	1.000	19.9	.4986			
1 1			0.681	0.009			.66	26559.87	1
2 0			0.100	1.000	.6	.1662			
3 1 0 0	$1.07 \cdot 10^{+2}$	$2.04 \cdot 10^{-6}$	−1.100	1.000	2.0	.1995			
1 0			0.625	1.000	1.9	.9973			
2 0			−0.820	1.000	.8	.3324			
2 0 0		$1.09 \cdot 10^{-6}$	1.282	1.000	1.5	.2493			
1 0			−0.526	1.000			5.31	26560.27	1
3 0 0		$1.58 \cdot 10^{-6}$	0.964	1.000	2.2	.3324			
1 0			0.852	1.000	2.0	.9970			
4 4 1 0	$2.58 \cdot 10^{+1}$	$3.57 \cdot 10^{-7}$	0.931	1.000			1.48	26560.27	2
5 2 2 0	$6.19 \cdot 10^{+0}$	$7.29 \cdot 10^{-7}$	−0.606	1.000			.24	26560.27	1

Table 4.5: Perturbations in the semimajor axis for the 2:1-resonance ($a = 26562$ km, $e = 0.006$, $i = 57°$) due to different potential terms. All terms causing amplitudes > 0.5 m or drifts > 5 cm/day are listed together with the numerical values of the expressions in eqn. (4.13).

possible value (i.e., the the amplitude in eqn.(4.13)) while the solid lines give the values corresponding to the orbital elements of the satellite. The potential term J_{22} with 120 m/day is responsible for more than 80% of the total resonant drift in the semimajor axis of 147 m/day. The elements, determined from astrometric observations at the Zimmerwald observatory from April 19 and 21, 1993, are given in Table 4.6.

4.2.3 The Lumped Coefficients

For perturbations with m and q fixed the indices l and p may be varied in such a way that the combination $l - 2p$ remains constant. According to eqn. (4.13) all these perturbations are caused by different geopotential terms but have exactly the same period. This

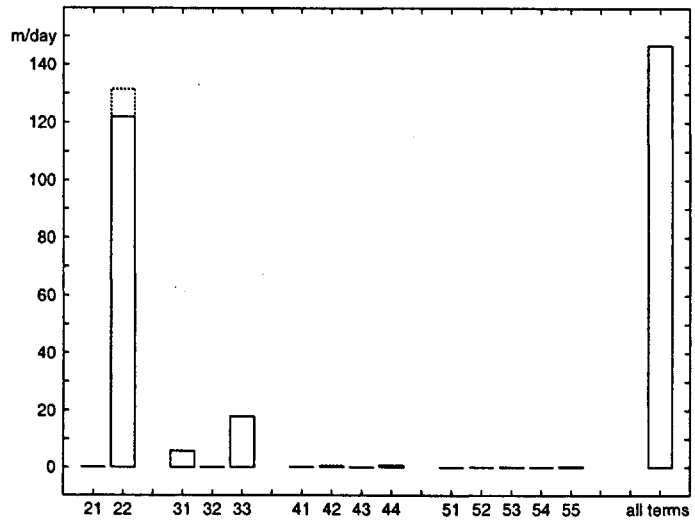

Figure 4.3: Contribution of different geopotential terms to the resonant drift in the semimajor axis of Intelsat 4a f-6 in April 93 (solid lines) and amplitudes of the perturbations (dotted lines).

Satellite	Intelsat 4a f-6
COSPAR designation	78 035A
Size	2.82 m long, 2.39 m diameter
Epoch and system of osculating elements	1993-04-19 00:01 UT, J2000
Semimajor axis	42143.76 km
Eccentricity	0.000846
Inclination	6.67°
Longitude of ascending node	60.9°
Argument of perigee	337°
Mean anomaly at osculation epoch	198.3°
Drift rate in longitude	0.29°/day

Table 4.6: Characteristics of the geostationary satellite Intelsat 4a f-6. The elements are determined from astrometric observations of the object acquired at the Zimmerwald observatory in April 93.

means (because the sum of two harmonic functions with equal period is again a harmonic function with the same period) that a particular satellite 'feels' only a linear combination of these potential terms (with coefficients depending on a, e, and i), the so-called lumped coefficients

$$\tilde{C}_m^{qk}(a,e,i) = \sum_l Q_{lm}^{qk}(a,e,i) C_{lm} \qquad \text{and} \qquad \tilde{S}_m^{qk}(a,e,i) = \sum_l Q_{lm}^{qk}(a,e,i) S_{lm}, \tag{4.18}$$

where

$$k = l - 2p$$

(e.g. Gooding et al. (1989)). The sum in eqn. (4.18) contains only terms with odd or with even degree l. The so-called influence functions Q_{lm}^{qk} are computed from

$$Q_{lm}^{qk} = \left(\frac{a_e}{a}\right)^{l-l_0} \frac{\bar{F}_{lmp}G_{lpq}}{\bar{F}_{l_0mp_0}G_{l_0p_0q}}(-1)^{l-l_0}, \qquad Q_{l_0m}^{qk} \equiv 1,$$

where l_0 is the lowest degree occurring in the series and $k = l_0 - 2p_0$ (sign convention from Kaula (1966)).

All potential terms in a lumped series have the same order m and a degree which is either even or odd. The lumped coefficient with $q = 0$ which contains C_{22} reads

$$\tilde{C}_2^{02} = C_{22} - \left(\frac{a_e}{a}\right)^2 \frac{\bar{F}_{421}}{\bar{F}_{220}}C_{42} + \left(\frac{a_e}{a}\right)^4 \frac{\bar{F}_{622}}{\bar{F}_{220}}C_{62} + \ldots$$

In Tables 4.7 and 4.8 the first few influence coefficients Q_{lm}^{qk} for the most important geopotential terms for the 1:1-resonance and the 2:1-resonance are listed together with the corresponding lumped coefficients $\tilde{C}_m^{qk}$ and $\tilde{S}_m^{qk}$.

Using the lumped coefficients the potential in eqn. (4.1) may be written in the form

$$\begin{aligned} V &= -\frac{\mu}{r} + \sum_{l=2}^{\infty}\sum_{m=0}^{l} \tilde{V}_{lm} \\ \tilde{V}_{lm} &= -\frac{\mu}{a}\sum_{p=0}^{l}\sum_{q=-\infty}^{\infty}\left(\frac{a_e}{a}\right)^l F_{lmp}(i)\,G_{lmq}(e)\,\tilde{S}_m^{ql-2p}(a,e,i) \\ \tilde{S}_m^{qk} &= \left\{\tilde{C}_m^{qk}\begin{bmatrix}\cos\Psi_{kmq}\\ \sin\Psi_{kmq}\end{bmatrix} + \tilde{S}_m^{qk}\begin{bmatrix}\sin\Psi_{kmq}\\ -\cos\Psi_{kmq}\end{bmatrix}\right\}\begin{matrix}l-m & \text{even}\\ l-m & \text{odd}\end{matrix} \\ \Psi_{kmq} &= k\omega + (k+q)M + m(\Omega - \Theta) \quad . \end{aligned} \tag{4.19}$$

$l\ m\ q\ k$	$Q_{l+2,m}^{qk}$	$Q_{l+4,m}^{qk}$	$Q_{l+6,m}^{qk}$	$Q_{l+8,m}^{qk}$	$\tilde{C}_m^{qk}$	$\tilde{S}_m^{qk}$
2 0 0 2	$-7.405\cdot10^{-2}$	$3.367\cdot10^{-3}$	$-1.221\cdot10^{-4}$	$3.854\cdot10^{-6}$	$-4.8421\cdot10^{-4}$	
2 0 0-2	$-7.405\cdot10^{-2}$	$3.367\cdot10^{-3}$	$-1.221\cdot10^{-4}$	$3.854\cdot10^{-6}$	$-4.8421\cdot10^{-4}$	
2 2 0 2	$-1.774\cdot10^{-2}$	$3.275\cdot10^{-4}$	$-5.536\cdot10^{-6}$	$7.891\cdot10^{-8}$	$2.4331\cdot10^{-6}$	$-1.4121\cdot10^{-6}$
3 1 0 1	$-1.954\cdot10^{-2}$	$3.510\cdot10^{-4}$	$-5.516\cdot10^{-6}$	$6.610\cdot10^{-8}$	$2.0315\cdot10^{-6}$	$2.5000\cdot10^{-7}$
3 3 0 3	$-1.643\cdot10^{-2}$	$2.866\cdot10^{-4}$	$-4.522\cdot10^{-6}$	$5.667\cdot10^{-8}$	$7.2861\cdot10^{-7}$	$-1.4177\cdot10^{-6}$
4 4 0 4	$-1.544\cdot10^{-2}$	$2.545\cdot10^{-4}$	$-3.711\cdot10^{-6}$	$3.877\cdot10^{-8}$	$-1.8721\cdot10^{-7}$	$3.1614\cdot10^{-7}$

Table 4.7: Influence coefficients and lumped coefficients for selected indices for a satellite in 1:1-resonance ($a = 42164$ km, $e = 0.001$, $i = 10°$). Compare with potential coefficients given in Table 4.1.

$l\ m\ q\ k$	$Q^{qk}_{l+2,m}$	$Q^{qk}_{l+4,m}$	$Q^{qk}_{l+6,m}$	$Q^{qk}_{l+8,m}$	$\tilde{C}^{qk}_m$	$\tilde{S}^{qk}_m$
2 0-1 2	$3.470 \cdot 10^{-2}$	$6.315 \cdot 10^{-3}$	$-2.225 \cdot 10^{-5}$	$-3.817 \cdot 10^{-5}$	$-4.8415 \cdot 10^{-4}$	
2 0 0 2	$-3.470 \cdot 10^{-2}$	$-2.105 \cdot 10^{-3}$	$4.452 \cdot 10^{-6}$	$5.455 \cdot 10^{-6}$	$-4.8419 \cdot 10^{-4}$	
2 0 1 2	$-4.461 \cdot 10^{-2}$	$-3.308 \cdot 10^{-3}$	$8.265 \cdot 10^{-6}$	$1.168 \cdot 10^{-5}$	$-4.8419 \cdot 10^{-4}$	
2 0-1-2	$-4.461 \cdot 10^{-2}$	$-3.308 \cdot 10^{-3}$	$8.265 \cdot 10^{-6}$	$1.168 \cdot 10^{-5}$	$-4.8419 \cdot 10^{-4}$	
2 0 0-2	$-3.470 \cdot 10^{-2}$	$-2.105 \cdot 10^{-3}$	$4.452 \cdot 10^{-6}$	$5.455 \cdot 10^{-6}$	$-4.8419 \cdot 10^{-4}$	
2 0 1-2	$3.470 \cdot 10^{-2}$	$6.315 \cdot 10^{-3}$	$-2.225 \cdot 10^{-6}$	$-3.817 \cdot 10^{-5}$	$-4.8415 \cdot 10^{-4}$	
2 2-1 2	$-3.676 \cdot 10^{-2}$	$-2.863 \cdot 10^{-3}$	$1.782 \cdot 10^{-4}$	$2.933 \cdot 10^{-5}$	$2.4262 \cdot 10^{-6}$	$-1.4235 \cdot 10^{-6}$
2 2 0 2	$3.676 \cdot 10^{-2}$	$9.544 \cdot 10^{-4}$	$-3.564 \cdot 10^{-5}$	$-4.191 \cdot 10^{-6}$	$2.4522 \cdot 10^{-6}$	$-1.3763 \cdot 10^{-6}$
2 2 1 0	$-6.719 \cdot 10^{-2}$	$-5.870 \cdot 10^{-3}$	$1.612 \cdot 10^{-5}$	$2.426 \cdot 10^{-5}$	$2.4154 \cdot 10^{-6}$	$-1.4426 \cdot 10^{-6}$
3 1 0 1	$-7.734 \cdot 10^{-3}$	$-2.594 \cdot 10^{-3}$	$-9.444 \cdot 10^{-5}$	$2.801 \cdot 10^{-6}$	$2.0299 \cdot 10^{-6}$	$2.4861 \cdot 10^{-7}$
4 4 0 2	$1.734 \cdot 10^{-2}$	$-9.762 \cdot 10^{-4}$	$-9.247 \cdot 10^{-5}$	$-1.887 \cdot 10^{-6}$	$-1.8973 \cdot 10^{-7}$	$3.0061 \cdot 10^{-7}$

Table 4.8: Influence coefficients and lumped coefficients for selected indices for a satellite in 2:1-resonance ($a = 26562$ km, $e = 0.006$, $i = 57°$). Compare with potential coefficients given in Table 4.1.

Because a particular satellite is susceptible only to the lumped coefficients it is *not* possible to determine individual potential terms from the observations of only one satellite. For the determination of potential coefficients observations of satellites with different inclinations, semimajor axes and/or eccentricities are necessary. For satellites with different elements a, e, i the coefficients Q^{qk}_{lm} are different and individual coefficients may therefore be extracted from the lumped values (see e.g. Kostelecky et al. (1982)).

Using the observations of one satellite only it is possible to estimate directly the lumped coefficients within an orbit determination procedure. For the computation of the variation equations the potential (4.19) has to be differentiated with respect to the lumped coefficients. More cumbersome is the computation of the gradient of the potential which is not expressed in terms of cartesian coordinates but in terms of osculating elements of the satellite orbit.

It is easier to determine the lumped coefficients in the following way: Consider e.g., the lumped coefficient containing the potential term C_{22} (leaving out some of the indices)

$$\tilde{C}_2 = Q_2 C_{22} + Q_4 C_{42} + Q_6 C_{62} + \ldots$$

Because the potential terms in this series are perfectly correlated when using observations from only one satellite the orbit determination procedure cannot decide to which term an improvement of the lumped coefficient has to be attributed. It is therefore possible to estimate one potential term in the series (which may be selected arbitrarily) and to attribute the product of the improvement of this term with the corresponding influence function to the improvement of the lumped coefficient as indicated by the following equations (for the term C_{22} estimated):

$$\begin{aligned} \tilde{C}_2 + \Delta\tilde{C}_2 &= Q_2(C_{22} + \Delta C_{22}) + Q_4 C_{42} + Q_6 C_{62} + \ldots \\ &= Q_2(C_{22} + \Delta C'_{22}) + Q_4(C_{42} + \Delta C'_{42}) + Q_6(C_{62} + \Delta C'_{62}) + \ldots \end{aligned}$$

from which follows

$$\Delta\tilde{C}_2 \equiv Q_2\Delta C_{22} \equiv Q_2\Delta C'_{22} + Q_4\Delta C'_{42} + Q_6\Delta C'_{62} + \ldots$$

It is therefore not necessary to modify the orbit determination program, which is only capable to estimate potential coefficients but not lumped coefficients. The transformation of the rms error of the estimated potential coefficient to the corresponding lumped coefficient can be done a posteriori.

4.2.4 Covariance Studies for the Determination of Resonant Geopotential Coefficients

In this section we study, through covariance analyses, the dependence of the formal errors of the resonant geopotential terms C_{22} and S_{22} on the value of the semimajor axis a. It is expected that the formal errors are minimum if the semimajor axis is equal to the radius of the geostationary ring (deep resonance). For our purpose we use an orbit with characteristics similar to that of Meteosat 4; eccentricity and inclination are given in Table 4.9, the semimajor axis is varied systematically.

Eccentricity	0.00026
Inclination	0.82°

Table 4.9: Characteristics of the orbit used for covariance studies.

For each covariance analysis observation epochs distributed over an interval of 42 days are simulated. The observation scenario closely resembles the distribution of the Zimmerwald observations of Meteosat 4 in winter 1995 (Chapter 5): A total of 54 close encounter series containing 8 observations each were distributed over 13 nights. An observation rms of 0.5" was assumed for all simulations.

The formal error in the semimajor axis shows a prominent peak close to the 1:1-resonance (see Figure 4.4): The formal error in the parameter grows by more than one order of magnitude in an interval of only a few hundred meters of the semimajor axis. Obviously, close to the resonance correlations between orbit parameters affect the semimajor axis.

For the resonant geopotential terms, on the other hand, we would expect a dip in the formal errors close to resonance. However, Figure 4.5 reveals that the formal error of both terms, C_{22} and S_{22}, show a peak when the semimajor axis corresponds to resonance. This behaviour is surprising at first sight, but may be understood in the following way: According to eqn. (4.7) the acceleration in longitude of a geostationary satellite on a circular orbit with vanishing inclination is proportional to

$$\ddot{\lambda} \sim C_{22}\sin 2\lambda - S_{22}\cos 2\lambda. \tag{4.20}$$

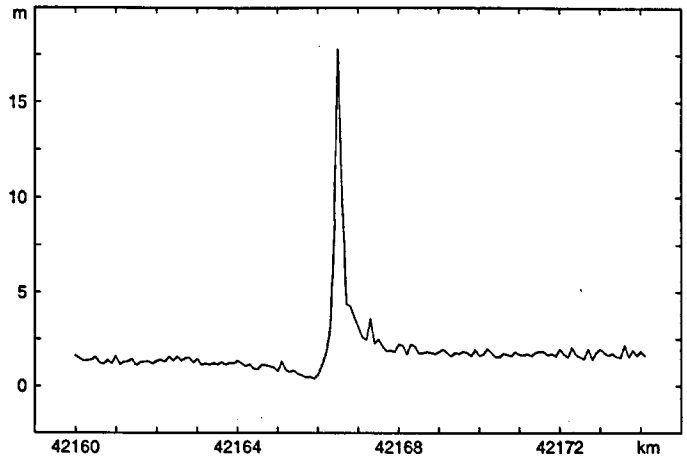

Figure 4.4: Formal error of the semimajor axis as a function of the semimajor axis at the osculation epoch. Arclength is 42 days, observation rms error is 0.5".

Therefore, would a satellite in resonance be observed only at longitude $\lambda = 0°$, only the potential term S_{22} could be determined, while C_{22} would remain undetermined because its coefficient is zero in eqn. 4.20. For an arbitrary longitude λ of the satellite only the combination

$$A \doteq C_{22} \sin 2\lambda - S_{22} \cos 2\lambda \tag{4.21}$$

of the geopotential terms may be determined while the orthogonal combination

$$B \doteq C_{22} \cos 2\lambda + S_{22} \sin 2\lambda \tag{4.22}$$

remains undetermined using the observations of this satellite only.

In our covariance study the satellite was assumed to be stationary at about 8° west at the initial epoch. At resonance the satellite remains close to this longitude during the entire observation interval of 42 days. The potential term C_{22} is thus determined with significantly lower accuracy than the term S_{22}, and both terms have a higher formal error than outside resonance.

If instead of the potential coefficients C_{22} and S_{22} the linear combinations defined in eqns. (4.21) and (4.22) are determined, the picture looks differently: The peak in the formal error of B is even higher than for C_{22} while it vanishes in the formal error of A. In Figure 4.6 formal errors in A and B are shown for a larger range of values for the semimajor axis. (Actually we do not give the formal errors of A and B but the formal errors of that linear combination of C_{22} and S_{22} which diagonalizes the corresponding 2x2-submatrix in the parameter correlation matrix. In the case of resonance the result is identical. Outside resonance the result is the same, too, if the longitude λ in eqns. (4.21) and (4.22) is replaced by the longitude corresponding to the satellite position at the middle

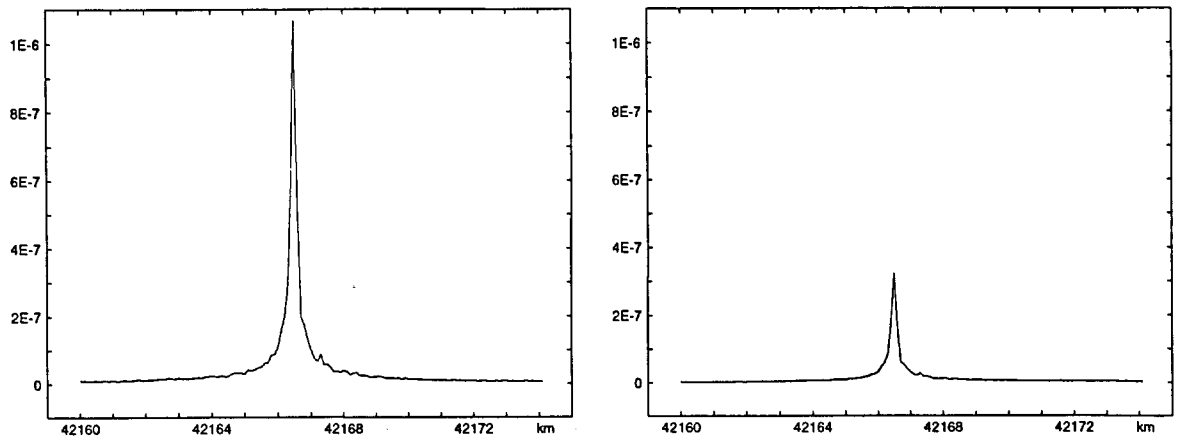

Figure 4.5: Formal error of the geopotential terms C_{22} (left) and S_{22} (right) as a function of the semimajor axis at the osculation epoch. Arclength is 42 days, observation rms error is 0.5″.

of the observed arc.) The large formal error in B also causes — due to the correlation between the parameters — the large formal error of the semimajor axis near resonance.

If the coefficients C_{22} and S_{22} should be determined both with the same precision two satellites which are 90° apart in longitude have to be observed.

Figure 4.6 shows the formal error of the two terms A (left) and B (right) for a range in the semimajor axis covering 3′700 km. The two errors show a similar behaviour — except for the peak in B. The formal errors increase with the difference of the semimajor axis

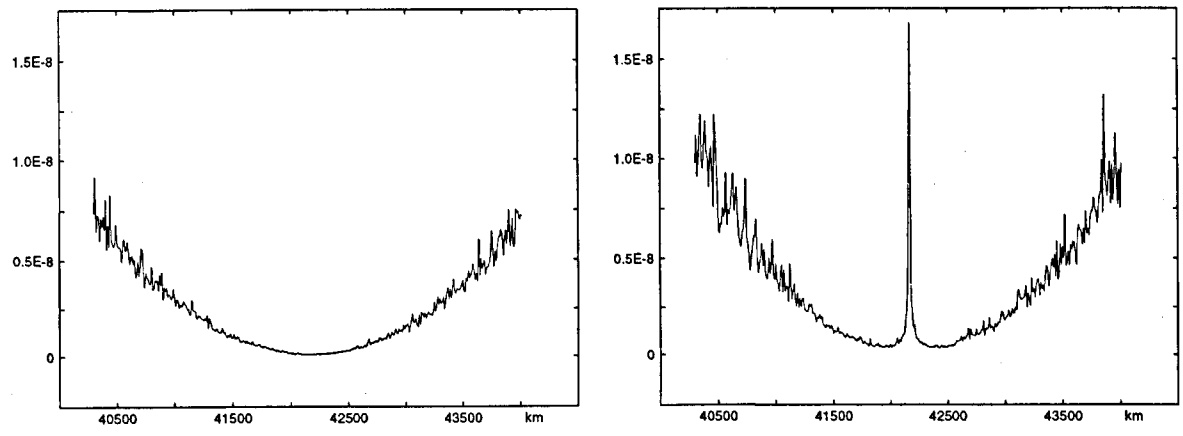

Figure 4.6: Formal error of the linear combinations A (left) and B (right) of the geopotential terms C_{22} and S_{22} as a function of the semimajor axis at the osculation epoch. Arclength is 42 days, observation rms error is 0.5″.

from the resonant value. The parameters remain, however, well determined for a range of semimajor axes several hundred kilometers wide. This means that even graveyard orbits are useful for the determination of resonant terms of the geopotential!

Covariance studies with different arclengths and different numbers of observations show, that outside resonance the formal errors of the resonant geopotential terms improve with the number of observations (inversely proportional to the square root of the number of observations) while an extension of the arclength with constant number of observations does not significantly improve the results. Close to resonance, on the other hand, the formal errors of the resonant geopotential coefficients behave in a different way: They are more sensitive to an extension of the arclength than to the number of observations. The formal errors improve proportional to the arclength in this case.

The two regimes of behaviour of the formal errors of the geopotential coefficients are show in Figure 4.7. Figure 4.7 (left) shows the formal error of A as a function of the semimajor axis of the orbit for semimajor axes between 40'300 km to 44'000 km. The four curves correspond to different numbers of observations and different arclength. The 432 resp. 864 single observations were assumed to be contained in 54 resp. 108 close encounter series distributed over 13 resp. 26 nights within a time interval (arclength) of 42 resp. 84 days. In all cases an observation rms error of 0.5" was assumed. The difference of the two curves determined with different numbers of observations is obvious while the curves for equal number of observations but different arclength are more or less identical.

Figure 4.7 (right) shows the central (resonant) region of Figure 4.7 (left) with the semimajor axis covering the interval between 41'700 km and 42'700 km. Obviously the increase of the number of observations also reduces the formal errors, more pronounced, however, is the reduction of the errors when increasing the arclength. When determining precise

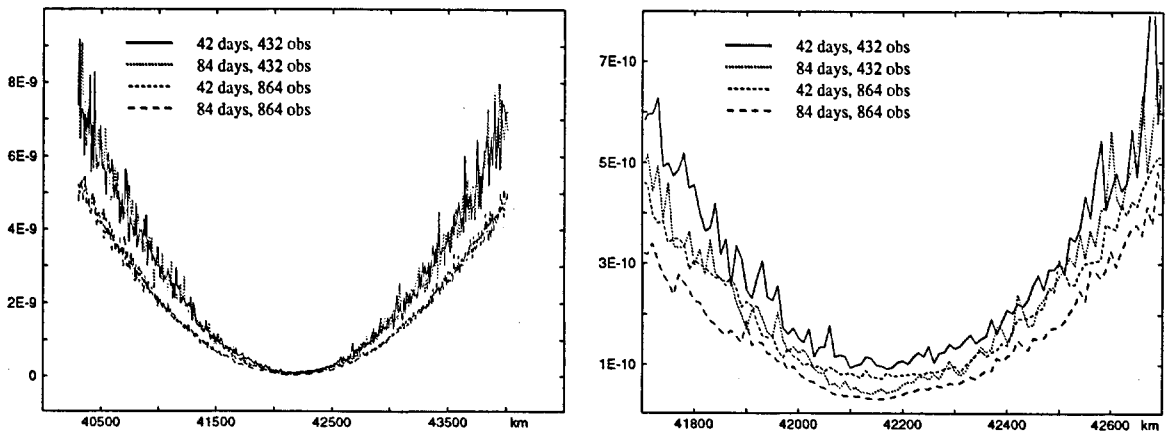

Figure 4.7: Formal error of A determined from different arc lengths (42 and 84 days) and different number of observations (432 and 864) as a function of the initial semimajor axis. Right: Central region of the left Figure. Observation rms error is 0.5".

resonant geopotential coefficients from astrometric measurements of geostationary satellites one should therefore use observations of at least two objects at significantly different longitudes covering a long orbital arc. The observations of the two satellites Meteosat 4 and Meteosat 5 presented in Chapter 5 covering a time interval of 111 days seem to be well suited for that purpose.

4.3 Resonance for GPS Satellites

4.3.1 Heuristic Identification of Resonant Potential Terms

For geostationary satellites it is intuitively clear that resonance with the Earth's rotation may occur and that the ellipticity of the equator (i.e. the geopotential term J_{22}) is the dominant contributor: The satellite is at a fixed position in an Earth-fixed frame and therefore 'senses' always the same perturbing acceleration from the geopotential. For a satellite in 2:1-resonance it is also possible to find the most important geopotential terms responsible for resonance in a heuristic way. In the previous section we found from theory that for the 2:1-resonance the term J_{32} plays the most important role for circular orbits with non-zero inclination.

In order to get an intuitive picture we shade on a map of the world the regions for which a given geopotential term has a positive value; in the other (blank) regions the same term has a negative value (see Figure 4.8). Into the same map we draw the ground track of a satellite in a 12-hour orbit. We now may find the sign of the perturbing acceleration in alongtrack direction caused by the particular potential term (arrows in Figure 4.8).

For the term V_{32} (Figure 4.8, top right) we recognize that (for the selected longitude of the node) the acceleration at the same locations along the orbit have the same sign in the northern and the southern hemisphere. A net effect of the accumulated acceleration along a revolution may therefore cause resonance.

The case is different for the term V_{22} (Figure 4.8, top left): At the same locations along the orbit in the northern and in the southern hemisphere the sign of the perturbing acceleration has different signs. The effect of the potential term from the two hemispheres therefore cancels out as long as the orbit is circular. Resonance may occur if the eccentricity of the orbit is non-zero: If due to the eccentricity the orbit is e.g. closer to the Earth in the northern than in the southern hemisphere the accelerations at the same locations thus may have different values and a net effect of the perturbations may occur. In fact, as we found in the last section, the resonance effect caused by the term V_{22} is proportional to the eccentricity. We find the same behaviour for the term V_{42} (Figure 4.8, bottom left), whereas the term V_{44} may cause resonance effects for circular orbits (Figure 4.8, bottom right) as does the term V_{32}.

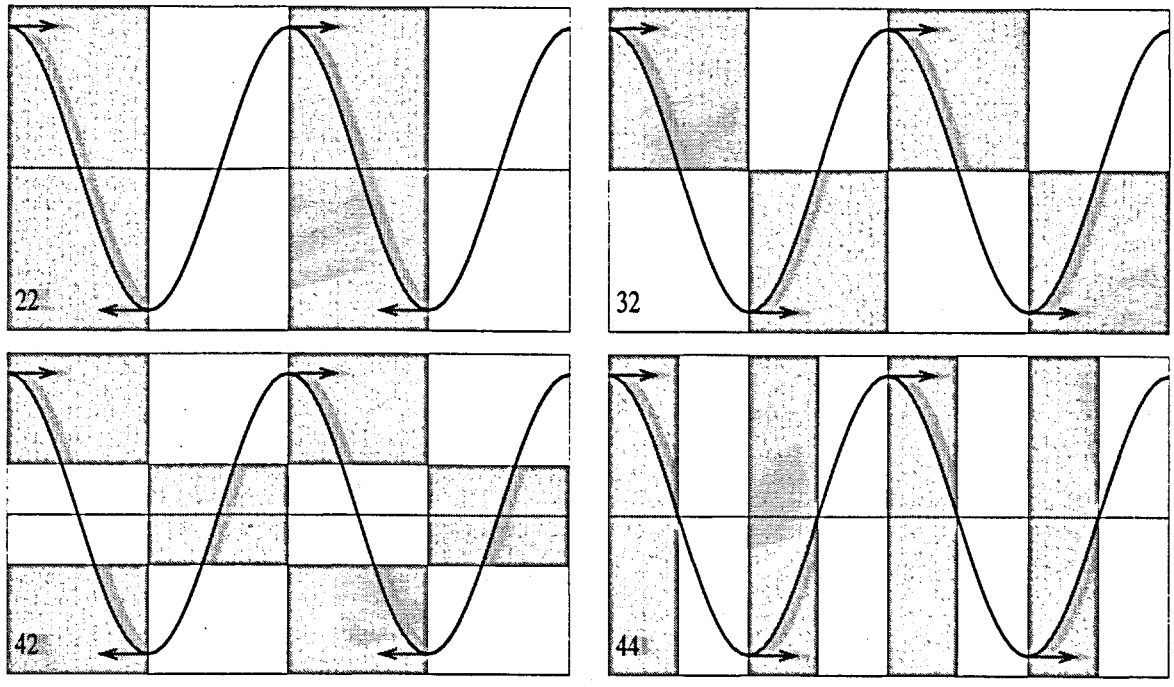

Figure 4.8: Heuristic identification of resonant geopotential terms for satellites in 2:1-commensurability (GPS-type orbits). Top left: Term J_{22}; top right: J_{32}; bottom left: J_{42}; bottom right: J_{44}. Shaded areas: Positive values of corresponding potential term.

4.3.2 Dependence on the Inclination

The dependence of the resonance effect on the inclination is described by the inclination function $\bar{F}_{lmp}(i)$ (see eqn. (4.13)). Normalized inclination functions are given in Figure 4.9 as a function of the inclination i for the indices l, m, p corresponding to the most important resonant perturbations of a satellite in 2:1-resonance. The dotted lines correspond to perturbations which are proportional to the eccentricity, the solid line to terms which are to first order independent on the eccentricity.

The function $\bar{F}_{321}$ which is contained in the expression for the dominant resonant perturbation has its maximum absolute value at $i \simeq 35°$ and changes its sign for $i \simeq 70°$. Therefore for satellites with an orbital inclination around 35° the resonance effect is largest whereas the resonance effect from the potential term J_{32} may vanish for nearly circular orbits for satellites with an inclination around 70°.

For GPS Block II satellites with inclinations of about 55° the resonant perturbation caused by the 32-term is about 60% of its maximum value. For the Block I satellites with inclinations of about 63° the resonance effect is about two times smaller than for Block II satellites.

For all resonant perturbations which do not contain the eccentricity to first order, the

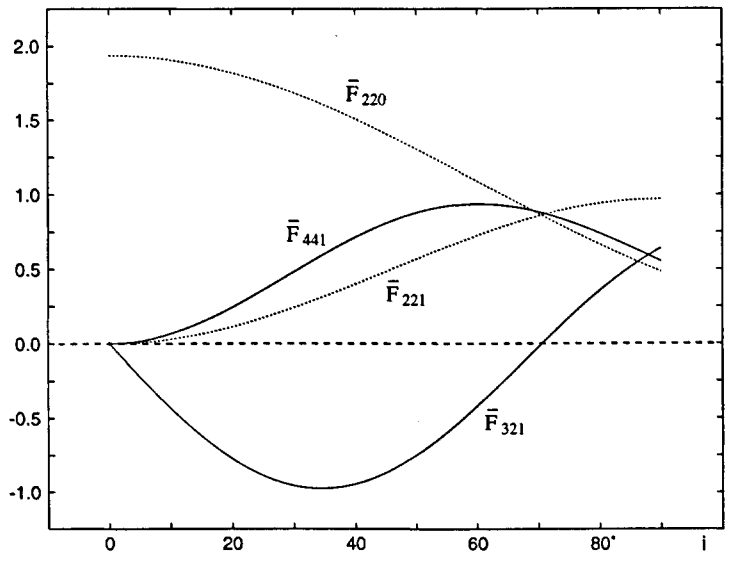

Figure 4.9: Normalized inclination functions for 2:1-resonance as a function of inclination. Solid lines: functions appearing in dominant perturbations, dotted lines: functions appearing in perturbations which are proportional to the eccentricity.

inclination functions have a root for $i = 0°$. This means that a circular orbit in the equatorial plane which is in the 2:1-commensurability does not show a resonant behaviour. It is therefore important to distinguish between the two terms 'commensurability' and 'resonance'.

4.3.3 Derivation of the Oscillation Equation for a GPS Satellite

The time evolution of the semimajor axis of a GPS satellite in resonance is given in Figure 4.10. On top of the short periodic perturbation due to the flattening (term J_{20}, see Table 4.5) with an amplitude of about 2 km we see the longperiodic resonant perturbation with a period of about 12 years and an amplitude of about 4.5 km.

To get an equation for the resonant satellite motion we use eqn. (4.13) for eccentricity $e = 0$ and consider only the potential term J_{32}. Eqn. (4.13) then reads for the resonant index combination $lmpq = 3210$ as

$$\left(\frac{da}{dt}\right)_{3210} = +2na\left(\frac{a_e}{a}\right)^3 \bar{J}_{32}\,\bar{F}_{321}(i)\,\cos\Psi_{3210} \tag{4.23}$$

with

$$\Psi_{3210} = \omega + M + 2\,(\Omega - \Theta - \lambda_{32}). \tag{4.24}$$

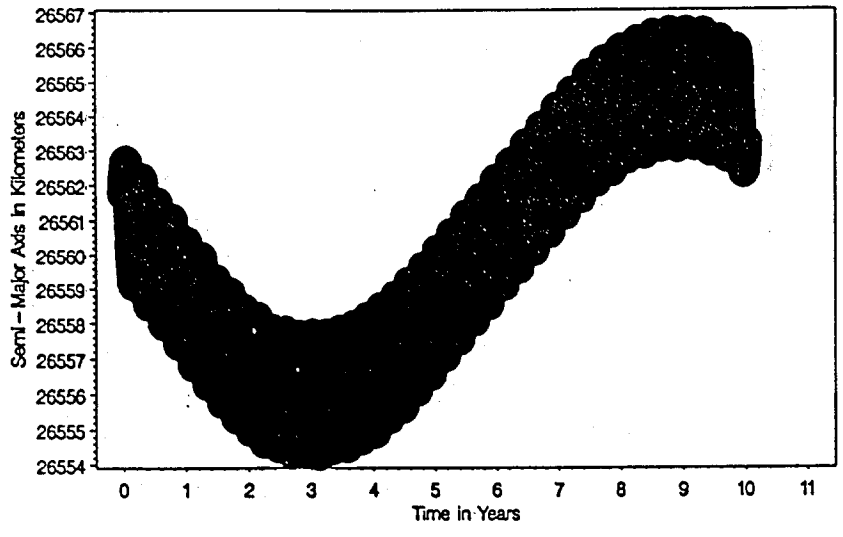

Figure 4.10: Perturbations in the semimajor axis for a GPS satellite (from Rothacher (1992)).

We obtain a differential equation for Ψ (omitting the indices) by replacing $\dot{a}$ in eqn. (4.23) by $\dot{n}$ which is in turn replaced by $\ddot{\Psi}$ obtained by taking the second derivative of eqn. (4.24):

$$\ddot{\Psi} = -3n^2 \left(\frac{a_e}{a}\right)^3 \bar{J}_{32}\, \bar{F}_{321}(i)\, \cos\Psi \tag{4.25}$$

This is the equation of a mathematical pendulum around the stable point $\Psi = +90°$. This means that the resonant oscillation of a satellite in 2:1-resonance is at its stable equilibrium point if the nodes of its orbit are arranged in such a way that the satellite in its orbit always is above those parts of the world where V_{32} is negative (see Figure 4.11, left). In the opposite case (Figure 4.11, right), it is at the unstable equilibrium point of the oscillation.

The frequency of the oscillation for small amplitudes is

$$\omega^2 = -3n^2 \left(\frac{a_e}{a}\right)^3 \bar{J}_{32}\, \bar{F}_{321}(i)$$

and the period is

$$T = \frac{2\pi}{\omega} K(\alpha) \qquad \text{with} \qquad \alpha = \sin^2 \Delta\Psi_{\max}/2$$

where $\Delta\Psi_{\max}$ is the amplitude of the oscillation in Ψ and $K(\alpha)$ is the complete elliptic integral of the first kind. For an inclination $i = 55°$ we get

$$\begin{aligned} \omega &= 2.07 \cdot 10^{-3} \text{ rad/day} \\ T &= 8.3 \cdot K(\alpha) \text{ years.} \end{aligned}$$

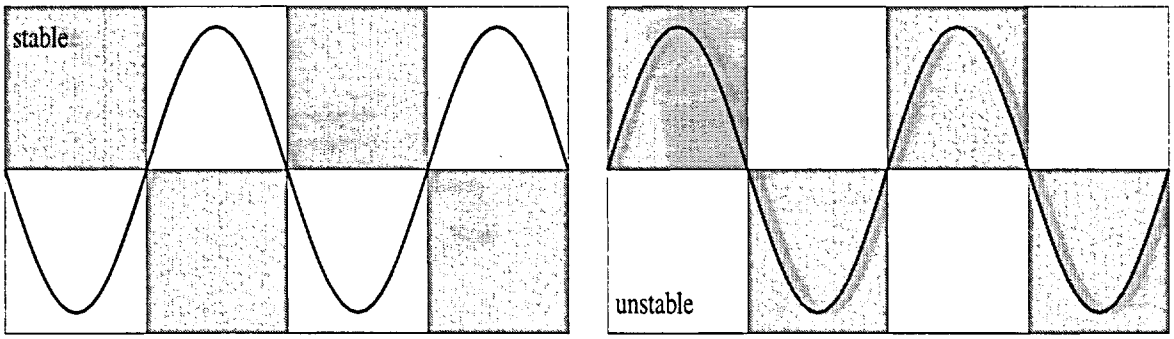

Figure 4.11: Stable (left) and unstable (right) orbit configuration for a satellite in 2:1-resonance due to the geopotential term V_{32}.

From energy conservation an upper limit for the amplitude in the semimajor axis of

$$\Delta a < \frac{4\omega}{3n} a \simeq 5.8\text{km}$$

results. Similar results are obtained by Vilhena de Moraes et al. (1995).

4.3.4 Mean Elements

The International GPS Service for Geodynamics (IGS, see e.g. Beutler et al. (1996a)) generates high precision orbits for the GPS satellites for every day since June 21, 1992. Daily 'mean' elements may be computed from the IGS results since that time. Figures 4.12 show the drift in the mean semimajor axis induced by resonance for satellites 14 (left) and 24 (right) for a time interval of about 200 days (Beutler, 1996).

In order to avoid satellite manœuvers and in order to remove lunar perturbations the drift in the daily mean elements were averaged over 27 days within December 13, 1992 to January 13, 1993, a time interval in which no manœuver occurred. In Figure 4.13 the averaged drift rates in the semimajor axis computed numerically from the IGS observations by this procedure are given for each observed GPS satellite. The largest drift exceeds 7 m/day (satellite PRN 16).

4.3.5 Resonant Drift Rates Computed from Theory

In order to compare the observed drift rates in the semimajor axis with the values expected from theory the influence of the resonant geopotential coefficients on the different GPS satellite orbits was computed using eqn. (4.13) and the IGS orbital elements of the satellites on Dec. 31, 1992. The drift rates in the semimajor axis (shaded columns) and

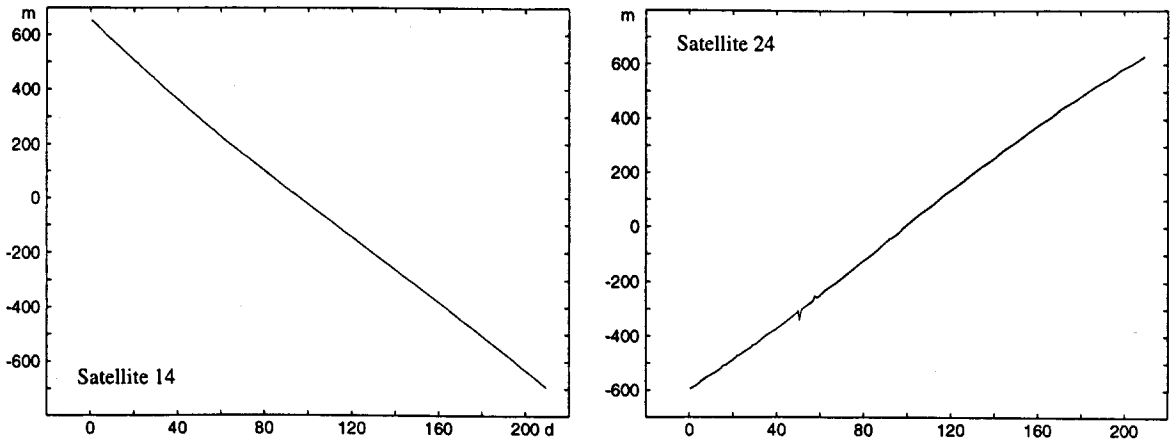

Figure 4.12: Resonant drift in the mean semimajor axis of the GPS satellites 14 (left) and 24 (right). The offset in the semimajor axis is 26560 km, the left time interval boundary corresponds to July 25, 1992 (from Beutler (1996)).

the amplitudes of the perturbations (dotted columns) are shown in Figure 4.14 for all GPS satellites for the most important resonant geopotential terms. In Figure 4.14 (top left) we see the resonant effect of the potential term J_{32}, in Figure 4.14 (top right) the effect of J_{22} and in Figure 4.14 (bottom left) the effect of the term J_{44}. All figures are to the same scale.

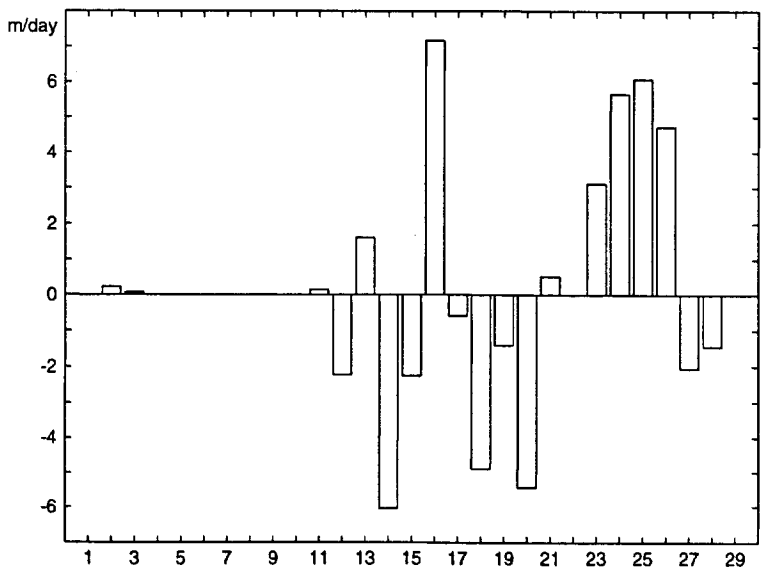

Figure 4.13: Mean resonant drift rates in the mean semimajor axis for all observed GPS satellites.

As expected the term J_{32} gives the largest contribution. In Figure 4.14 (top left) two classes of amplitudes are distinguished: amplitudes of about 6 m/s and amplitudes of about 3 m/s. The difference is due to the different orbital inclinations for the Block I (63°) and the Block II satellites (55°). For Block I satellites the value of the inclination function $F_{321}(i)$ is about 2 times smaller than for the Block II satellites (see section 4.3.2).

The perturbation amplitudes induced by the term J_{22} (Figure 4.14, top right) is 2.5 m/s or smaller. The highest values are observed for the satellites with largest orbital eccentricity ($e = 0.0136$ for satellite 11, but $e = 0.0010$ for satellite 16) because the eccentricity functions $G_{211}(e)$ and $G_{20\text{-}1}(e)$ are proportional to the eccentricity e. The term J_{44} (Figure 4.14, bottom left) for most satellites is more important than the term J_{22}. The amplitude for all satellites is about 1.5 m/s because the perturbation is not proportional to the eccent-

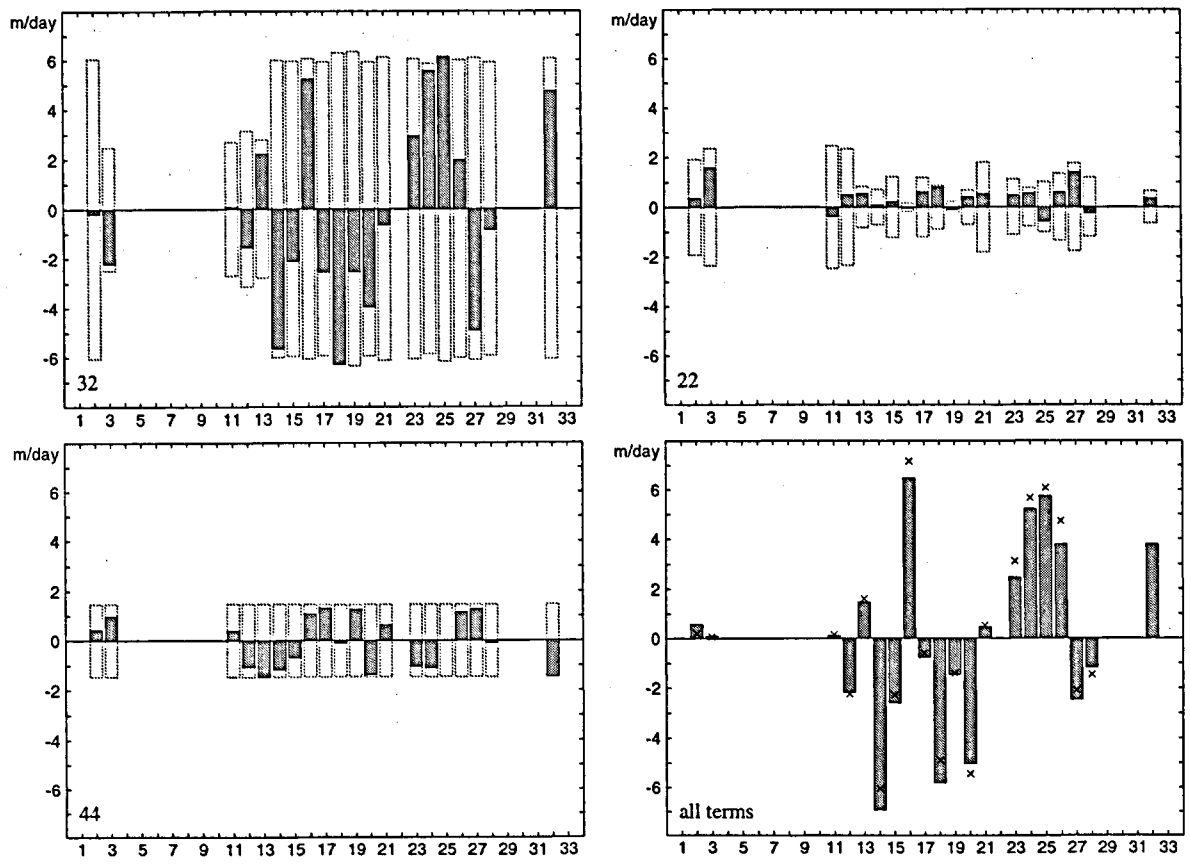

Figure 4.14: Resonant drifts in a (m/day) (solid lines) and perturbation amplitudes (dotted lines) in the mean semimajor axis for GPS satellites due to the geopotential terms J_{32} (top left), J_{22} (top right), J_{44} (bottom left). Bottom right: Combined effect due to all resonant terms up to degree $l = 6$ compared to the observations (crosses). All Figures are to the same scale. Epoch of the satellite elements: Dec. 31, 1992.

ricity and the inclination function $F_{441}(i)$ has similar values for Block I ($i \sim 63°$) and for Block II satellites ($i \sim 55°$).

The sum of all resonant perturbing potential terms with degree $l \leq 6$ is given in Figure 4.14 (bottom right) for all satellites for which orbital elements were available (shaded columns). The crosses indicate the values of the drifts actually observed in the semimajor axis (see Figure 4.13). The correspondence between observed and computed values is obvious but not perfect. Differences up to almost 1 m/s are observed. The differences are mainly due to radiation pressure effects which will be discussed below.

4.3.6 Contribution of the Y-Bias to the Drift in the Semimajor Axis

GPS satellites are large structures with extended solar panels. The cross section area for the Block II satellites, as seen from the Sun, is larger than 13 m^2 (Fliegel et al., 1992). While direct radiation pressure does not induce longperiodic or secular variations of the semimajor axis (apart from the negligible Pointing-Robertson effect), induced forces acting perpendicular to the direction to the Sun may produce longperiodic drifts in the semimajor axis.

The so-called *y-bias* is a force acting along the axis of the solar panels (y-axis of the satellites, Fliegel et al. (1992)). It may be due to a misalignment of the solar panels or to thermal emissions of the satellites. The acceleration p_y is of the order of $10^{-9}m/s^2$ and it is different for each satellite.

The goal of the satellite's attitude control is to point the antenna array (z-axis in the satellite coordinate system) at any time towards the Earth's center and the solar panel axis (y-axis) perpendicular to the direction Sun–satellite, in order to optimally cover the Earth with the microwave beacon and to maximize the solar irradiance onto the solar panel arrays (which may rotate around the y-axis). Adopting this optimal attitude control scenario the direction of the satellite's y-axis may be computed from the geocentric position vector $\boldsymbol{r}$ of the satellite and the unit vector satellite–Sun $\boldsymbol{s}$:

$$\boldsymbol{e}_y = \frac{\boldsymbol{s} \times \boldsymbol{r}}{|\boldsymbol{s} \times \boldsymbol{r}|}. \tag{4.26}$$

The perturbing y-bias acceleration may thus be written as $\boldsymbol{p}_y = p_y \boldsymbol{e}_y$. In Figure 4.15 (left) the alongtrack component of the perturbation is shown for three angles ψ of the Sun above the orbital plane. Obviously a net effect over one revolution must be expected affecting the semimajor axis. The effect increases with the angle ψ of the Sun above the orbital plane. Using the Lagrangian perturbation equation

$$\frac{da}{dt} = \frac{2}{n^2 a}\, \dot{\boldsymbol{r}} \cdot \boldsymbol{p}_y \tag{4.27}$$

the effect on the semimajor axis a may be computed. For simplicity we assume a circular orbit $\boldsymbol{r} = a(\cos\varphi, \sin\varphi, 0)$ and $\boldsymbol{s} = (\cos\psi, 0, \sin\psi)$, where φ is the angle between the satellite and the Sun projected onto the orbital plane, ψ is the elevation angle of the Sun above the orbital plane

$$\sin\psi = \cos i \sin\delta + \sin i \cos\delta \sin(\Omega - \alpha),$$

and α, δ are the right ascension and declination of the Sun, i and Ω are the inclination and longitude of the ascending node of the satellite orbit in the equatorial system. $\varphi \equiv u$ may be interpreted as the argument of latitude. Eqns. (4.26) and (4.27) then give

$$\frac{da}{dt} = \frac{2p_y}{n} \frac{\sin\psi}{\sqrt{\sin^2\psi + \cos^2\psi \sin^2\varphi}}. \tag{4.28}$$

Averaging the variation in a over one orbital revolution gives the net effect of the y-bias inducing longperiodic variations of the semimajor axis

$$\begin{aligned}\left(\frac{da}{dt}\right)_{\text{sec}} &= \frac{2p_y}{n}\frac{1}{2\pi}\int_0^{2\pi} \frac{\sin\psi d\varphi}{\sqrt{1-\cos^2\psi\cos^2\varphi}} = \frac{2p_y}{n}\frac{2}{\pi}\int_0^{\pi/2} \frac{\sin\psi d\varphi}{\sqrt{1-\cos^2\psi\sin^2\varphi}} \\ &= \frac{4p_y}{\pi n} K(\cos^2\psi)\sin\psi \quad . \end{aligned} \tag{4.29}$$

where $K(z)$ is the complete elliptic integral of the first kind (Abramowitz et al., 1965). The drift rate in the semimajor axis induced by the y-bias, computed from eqn. (4.29), is shown in Figure 4.15 (right) for a satellite with $\Omega = 180°$ and $p_y = 10^{-9}\text{m/s}^2$ in a time interval of two years. The drift in the semimajor axis reaches values up to 1.2 m/day.

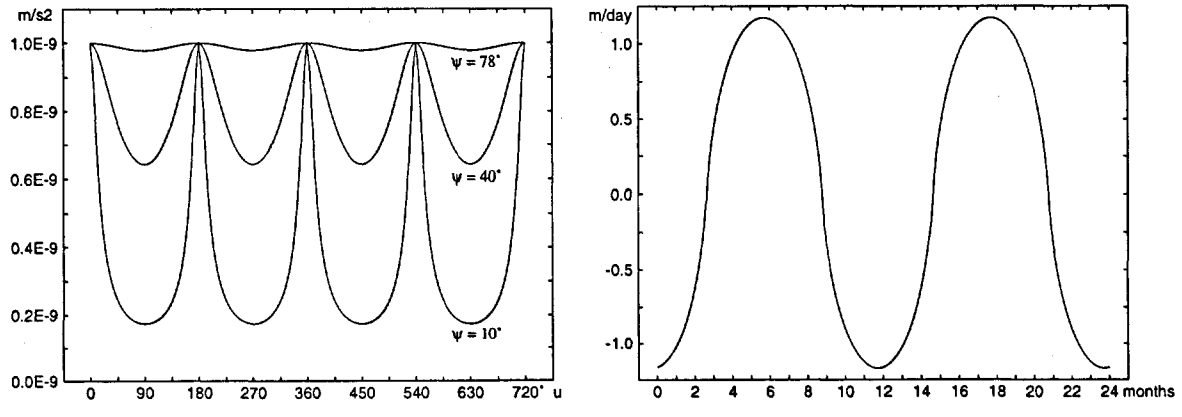

Figure 4.15: Left: Alongtrack acceleration of a GPS satellite due to a y-bias of $p_y = 10^{-9}\text{m/s}^2$ over two revolutions with the Sun 10°, 40° and 78° above the orbital plane. Right: Drift rate in the semimajor axis due to the y-bias for a GPS satellite with $\Omega = 180°$ and $p_y = 10^{-9}\text{m/s}^2$ for a time interval of 2 years.

The theoretical drift rate for the individual GPS satellites are given in Figure 4.16 (left), and in Figure 4.16 (right) we see the sum of the drift rates in the semimajor axes from the resonant geopotential terms (with $l \leq 6$) and the y-bias. A comparison with Figure 4.14 shows that the difference to the observed drift rates is greatly reduced. The maximum value which is 1 m/s if only geopotential terms are considered is reduced to 0.25 m/s if the effect of the y-bias is included.

We have seen that the y-bias induces a drift rate in the semimajor axis with an amplitude up to nearly 20% of the effect stemming from the resonant geopotential terms. The determination of resonant geopotential coefficients is therefore strongly correlated with the y-bias. On the other hand such determinations would not rely on one single satellite but on an entire satellite system well observed without interruption since June 92. The fact that the drift rate from the y-bias has an annual period and shows a characteristic signature within the individual revolutions may help to decorrelate different effects, in particular the y-bias and resonance effects due to the geopotential.

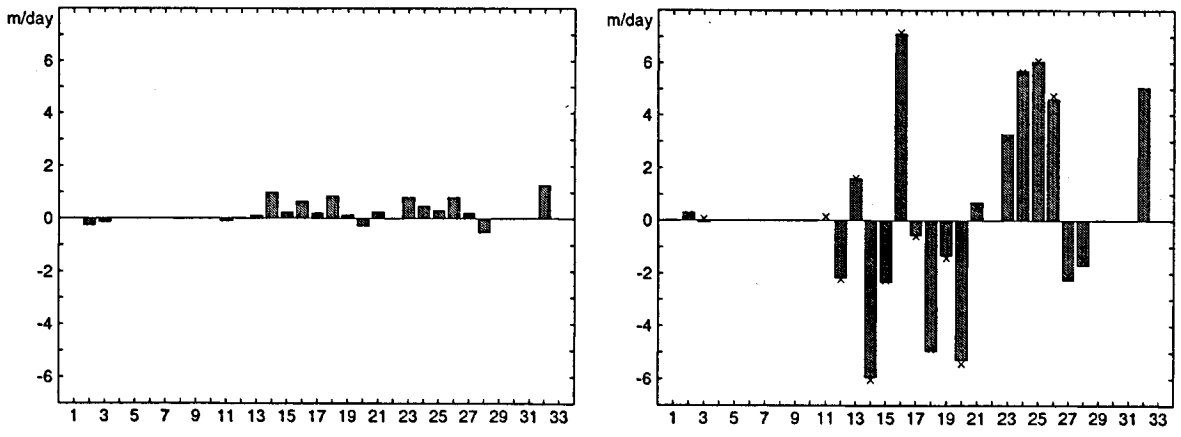

Figure 4.16: Left: Theoretical drift rates due to satellite specific y-biases for all GPS satellites with elements available. Right: Sum of drift rates in the semimajor axis from the resonant geopotential terms with $l \leq 6$ and from the y-bias (shaded columns) and observed drifts (crosses).

5 Meteosat: Observations and Results

5.1 Observation Campaign of Meteosat 4 and 5

5.1.1 Background

In winter 1994/95 astrometric observations of the two geostationary satellites Meteosat 4 and Meteosat 5 were acquired in the context of the COGEOS (International Campaign for Optical Observations of Geosynchronous Satellites) research project (see Nobili (1987)). The aim of COGEOS is the determination of the resonant coefficients C_{22} and S_{22} of the geopotential. The Meteosat satellites were selected as observation targets: Due to their relatively small size, their cylindrical shape, and the fact, that they have no outside despun antenna but an antenna system that is embedded in the satellite body, the effects due to solar radiation pressure are relatively easy to model. Moreover the two satellites are manœuvered only every few months. The essential characteristics of the satellites Meteosat 4 and 5 are summarized in Table 5.1.

	Meteosat 4	*Meteosat 5*
COSPAR designation	89 020B	91 015B
Size	3.10 m long, 2.10 m diameter	
Epoch of osc. elements	1994-11-29	1994-11-29
Semimajor axis	42165.90 km	42162.08 km
Eccentricity	0.00023	0.00025
Inclination	0.80°	0.13°
Ascending node	69°	259°
Argument of perigee	140°	312°
Geographic longitude	8.22°west	0.88°east
Drift	-0.01°/day	0.04°/day

Table 5.1: Characteristics of the geostationary satellites Meteosat 4 and 5 according to the ESA log of objects near the geostationary ring, Dec. 94 (Janin, 1996).

An observation campaign for Meteosat 4 and 5 was initiated at the Sixth COGEOS Workshop in Walferdange, Luxembourg, 1994. The campaign was timed such that neither of the two satellites crossed the Earth's or Moon's shadow during the observation period. The campaign was coordinated by G. Appleby from the Royal Greenwich Observatory who distributed state vectors for Meteosat 4 and (for the second half of the campaign) for Meteosat 5. The Royal Greenwich Observatory (RGO) in Herstmonceux (G. Appleby, P. Gibbs), the Observatoire de la Côte d'Azur (OCA, C. Veillet), the Main Astronomical

Observatory in Kiev (Y. Ivashchenko), and the Zimmerwald observatory of the AIUB (T. Schildknecht and U. Hugentobler) were participating in the campaign. In this chapter the Zimmerwald observations of the two satellites are analyzed.

5.1.2 The Zimmerwald Observations

The amount and distribution of the astrometric observations acquired in Zimmerwald are listed in Table 5.2 . For each observation night the date, the number of close encounter series, the number of single observations, and the time of the first and last observation are given. Meteosat 4 was observed in 20 nights spanning a time interval of 111 days from October 26, 1994 to February 14, 1995. A total of 108 close encounter series were measured containing 903 single observations. Meteosat 5 was observed during 11 nights spanning 42 days. The observations contain 49 close encounter series and 405 single observations. The measurement technique is discussed in Chapter 1.

Figure 5.1 shows the distribution of the observation epochs. The shaded area indicates the eclipsing periods around the equinoxes. The arrow gives the epoch of the manœuver of Meteosat 4 within the observation period. Meteosat 5 was not manœuvered during the time interval of interest. The epochs of the manœuvers for Meteosat 4 from October 1994 to February 1995 are given in Table 5.3.

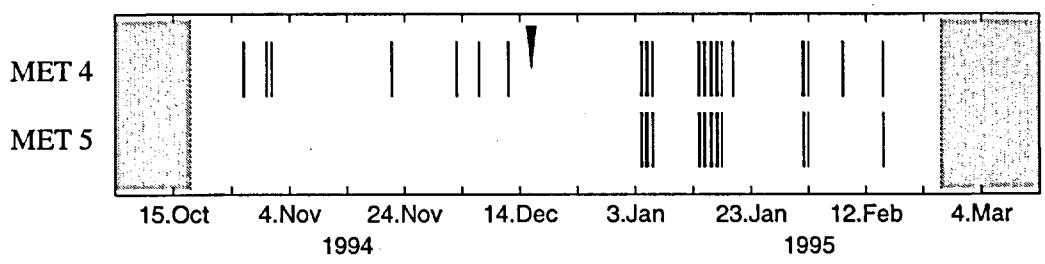

Figure 5.1: Epochs of the Zimmerwald observations of Meteosat 4 and 5 in winter 1994/95. The shaded areas indicate the eclipsing periods. The arrow indicates the epoch of the manœuver of Meteosat 4.

The two European weather satellites were observed during 20 nights. For each observation night the satellite ephemerides were computed and reference stars were selected along the orbit within a stripe with a width of 10 arcmin centered around the orbit. The PPM catalogue was used for 197 stars, 15 stars were selected from the CMC catalogue (see Section 1.1.3).

In Figure 5.2 we see Meteosat 4 on a frame taken with fixed telescope and an exposure time of 4 seconds. The frames used for measuring the positions of satellite and reference star were exposed for only one second, however. For each close encounter series the frames were processed immediately after their acquisition. It was therefore not necessary to store them

on disk. After terminating the observations at the end of the night the CCD coordinates for the satellites and reference stars were already available. They were astrometrically reduced the following morning. Usually, all frames from one night could be reduced within the same run (together with observations of other satellites) if the camera was not removed from

Date	Meteosat 4 Series	Observations	(UT)	Meteosat 5 Series	Observations	(UT)
26. Oct. 94	7	61	00:20 - 04:58			
30. Oct.	6	53	23:26 - 03:00			
31. Oct.	6	54	21:24 - 23:13			
21. Nov.	3	26	18:43 - 22:04			
2. Dec.	6	45	00:59 - 04:53			
6. Dec.	10	88	21:33 - 23:10			
11. Dec.	16	132	23:16 - 02:29			
3. Jan. 95	3	28	22:50 - 05:39	4	35	23:04 - 05:40
4. Jan.	7	60	18:52 - 05:39	8	56	18:09 - 05:51
5. Jan.	3	20	20:37 - 00:28	3	27	20:42 - 03:10
13. Jan.	6	56	19:48 - 03:02	6	55	21:31 - 04:39
14. Jan.	7	48	18:13 - 03:07	6	39	18:10 - 03:15
15. Jan.	4	32	21:40 - 04:51	4	32	21:53 - 05:04
16. Jan.	7	63	22:18 - 05:36	7	59	22:26 - 05:30
17. Jan.	1	6	20:47 - 20:48	1	6	22:22 - 22:23
19. Jan.	1	10	19:54 - 19:55			
31. Jan.	5	45	20:59 - 04:08	5	47	00:07 - 04:16
1. Feb.	4	30	21:38 - 23:02	4	33	21:32 - 23:12
7. Feb.	4	32	21:12 - 00:48			
14. Feb.	2	12	21:49 - 21:57	1	10	01:00 - 01:01
Total	108	901		49	399	

Table 5.2: Astrometric observations (number of series, number of single observations, times of first and last observation) of Meteosat 4 and 5 performed at Zimmerwald in the context of the COGEOS project.

Manœuvers of Meteosat 4	
6. Oct. 1994	22:51 UT
16. Dec. 1994	08:58
22. Feb. 1995	02:24

Table 5.3: Date and time for the manœuvers of Meteosat 4 in the time period from October 1994 to February 1995, from Appleby (1995).

the telescope, the focus was not changed, and the environmental temperature did not change much during the night. The astrometric reduction gave values for the rms of single observations between 0.3″ and 0.7″. The histogram for the rms errors of all determined satellite positions in right ascension are shown in Figure 5.3. (The corresponding diagram for the rms errors in declination looks similar.) The mean positioning error is 0.5″, it may however be as small as 0.3″ or as large as 0.8″.

Figure 5.2: Meteosat 4 on a frame exposed for 4 seconds with fixed telescope on Dec. 11, 1994, in Zimmerwald. Frame size is 17' x 11'.

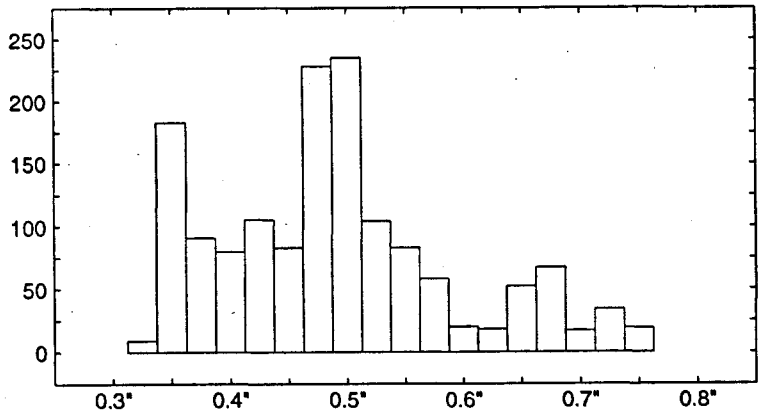

Figure 5.3: Histogram of rms errors in right ascension for all observations from Meteosat 4 and Meteosat 5 as provided by the astrometric reduction.

Finally the measurements were screened for outliers by fitting an orbit through the observations. From a total of 1494 single observations (1004 for Meteosat 4, 490 for Meteosat 5) 186 showed exceedingly large residuals after fitting an orbit. Most of them could be attributed to a superposition of the satellite image with the image of a background star. In

most cases this was already indicated by an anomalous shape (given by the moments of inertia of the image) and intensity determined by the object recognition algorithm.

In Figure 5.4 Meteosat 5 is shown on a series of frames during a close encounter with a reference star. In the same field of view covering only 14' x 10' there are two other geostationary objects that are much brighter than Meteosat 5, which could not be identified. One of them might be Intelsat 7 F2 or TV Sat-2. The inclination of its orbit is 0.06°, but identification is difficult due to the fact that these large telecommunication satellites are often manœuvered. The other object is drifting on an orbit with an inclination of about 1°(result from a circular orbit determination).

Figure 5.4: Meteosat 5 (bottom right) together with two other geostationary satellites in front of the moving stellar background. Series of Zimmerwald frames taken on January 31, 1995, spaced by 8 seconds. Integration time was 1 second. The field covers 14' x 10'.

5.2 Orbit Determination for Four Days and the Precision of the Observations

5.2.1 Orbit Determination with and without Radiation Pressure

To get a first impression for the quality of the acquired data the measurements of Meteosat 4 from four successive nights from January 13 to January 16, 1995, were used for an orbit determination. They contain 24 close encounter series with a total of 199 observations.

The force model used for the orbit determination consists of

- the Earth potential model JGM3 up to terms of degree and order 10,
- the gravity from Sun and Moon, using the JPL DE200 ephemerides,
- the direct radiation pressure,
- the tidal potential due to Sun and Moon,
- precession and nutation according to the IAU 1976 and 1980 resolutions,
- UT1–UTC correction and polar wobble from the IERS.

Because the coefficient for direct solar radiation pressure is not known a priori, three orbits were determined:

(a) No radiation pressure included in the force model.

(b) An a priori direct solar radiation pressure coefficient of

$$\frac{A}{M}\frac{S_\odot}{c} = 5.58 \cdot 10^{-8}\mathrm{m/s^2} \tag{5.1}$$

was adopted assuming an area-to-mass ratio $A/M = 0.123$ m^2/kg, based on an area of 4 m^2 and a mass of about 325 kg (Veillet et al., 1990). $S_\odot = 1.36 \cdot 10^3$W/m^2 is the solar constant, c the velocity of light.

(c) The direct solar radiation pressure coefficient was determined together with the orbital elements.

The results for the three cases are given in Table 5.4. The differences between cases (a) and (b) are obvious: The representation of the observations is significantly improved by using a reasonable radiation pressure coefficient. The rms of unit weight is reduced from 1.52 to 1.43 (corresponding to mean observation errors of 0.79″ and 0.74″ respectively). Whereas the elements characterizing the orbital plane (i and Ω) remain unchanged as expected, the elements describing the shape and orientation of the orbit within the orbital plane are changed significantly.

Compared to the solution with fixed radiation pressure coefficient (case (b)) the determination of the direct radiation pressure coefficient (case (c)) does, for the short arc considered, not significantly improve the representation of the observations: The rms of unit weight remains nearly unchanged. The determined elements are not significantly different, i.e., the differences are in all cases lower than about 1.3 σ. The radiation pressure coefficient determined is about 25% larger than the a priori value specified in eq. (5.1). Its relative rms error is with 14% relatively large, however, the difference relative to the a priori value is only about 1.4 σ.

Whereas the determination of the radiation pressure coefficient does not improve the representation of the orbit, it increases the rms errors of the orbital parameters describing the shape of the orbit, i.e., of a, e, ω and (as a consequence) of the mean longitude ℓ by as much as a factor of 6.7 e.g., for the semimajor axis. This is caused by the strong correlation of the radiation pressure coefficient with the elements a and e for short arcs (see Chapter 3). This result is also observed in the rms errors in the satellite position. In Figure 5.5 the rms errors in position are given as a function of time for the three solutions, separately for the radial (R), the alongtrack (S), and the crosstrack (W) direction.

The figures corresponding to cases (a) and (b) are very similar, reflecting the fact that the rms errors of the orbital elements are nearly the same for both cases, i.e., when no radiation pressure coefficient is determined. The largest rms errors (up to 70 m in the time

interval considered) occur, as expected, in the alongtrack direction. The daily oscillations are a consequence of the uncertainty in the eccentricity and in the location of the perigee whereas the increase of the rms error towards both time interval boundaries is caused by the uncertainty in the semimajor axis.

For solution (c), in which the radiation pressure coefficient was estimated, the rms errors in position are larger by a factor of about four in both, the radial and the transverse directions as a consequence of the increased errors in a, e, and ω. The rms error in the alongtrack direction may reach values up to 350 m (corresponding to 2″ in the geostationary distance). At the observation epochs, however, the rms errors are below 135 m (corresponding to

(a) No Radiation Pressure	
Observation rms of unit weight	1.521 (0.787″)
Semimajor axis	42165155.09 ± 0.94 m
Eccentricity	.00012830 ± .00000022
Inclination	0.888344 ± 0.000019°
R.A. of ascending node	69.372641 ± 0.001264°
Argument of perigee	198.687423 ± 0.187342°
Mean longitude at T_{osc}	101.978601 ± 0.000063°

(b) Radiation Pressure Fixed, $5.58 \cdot 10^{-8} m/s^2$	
Observation rms of unit weight	1.427 (0.741″)
Semimajor axis	42165190.47 ± 0.88 m
Eccentricity	.00013141 ± .00000022
Inclination	0.888343 ± 0.000018°
R.A. of ascending node	69.372766 ± 0.001186°
Argument of perigee	194.655674 ± 0.168568°
Mean longitude at T_{osc}	101.979430 ± 0.000059°

(c) Radiation Pressure Determined	
Observation rms of unit weight	1.426 (0.741″)
Semimajor axis	42165198.46 ± 5.92 m
Eccentricity	.00013220 ± .00000063
Inclination	0.888343 ± 0.000018°
R.A. of ascending node	69.372794 ± 0.001185°
Argument of perigee	193.772729 ± 0.663043°
Mean longitude at T_{osc}	101.979617 ± 0.000149°
Radiation pressure coefficient	$6.84 \pm 0.92 \cdot 10^{-8} m/s^2$

Table 5.4: Orbital elements of Meteosat 4 based on observations from four nights, (a) without radiation pressure in the force model, (b) with a 'reasonable' direct radiation pressure coefficient, (c) with the direct radiation pressure coefficient determined from the observations. Osculation epoch of the elements: January 11., 1995, system J2000.

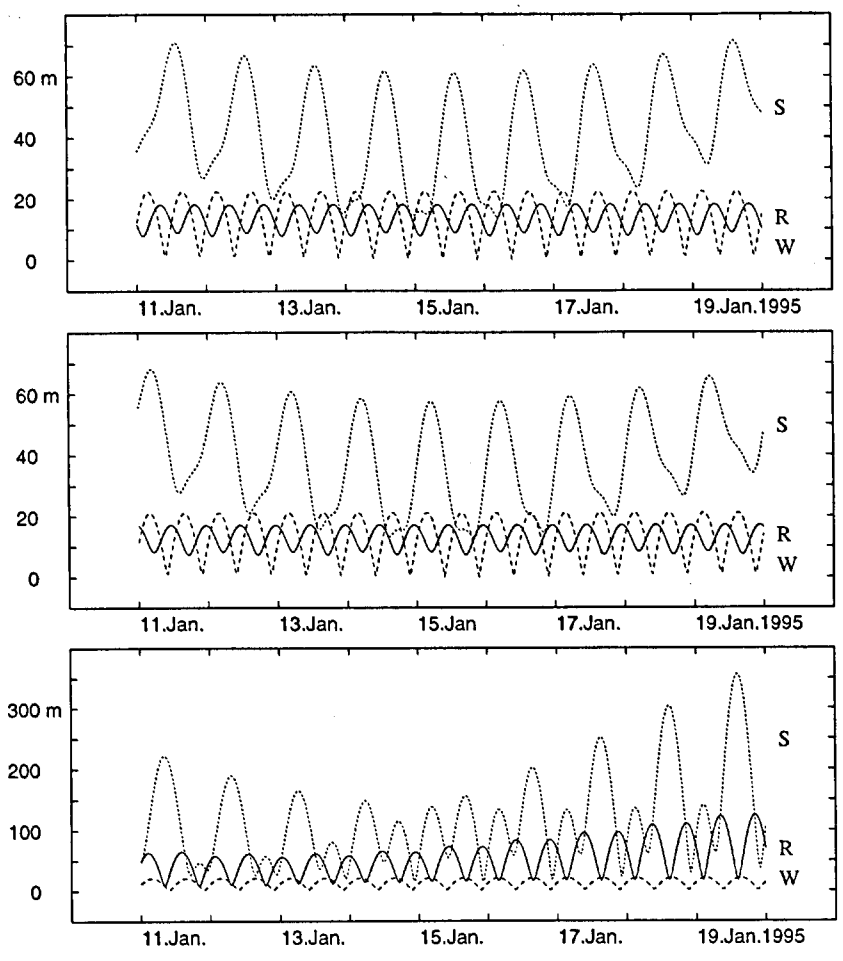

Figure 5.5: RMS errors in radial (R), alongtrack (S), and crosstrack (W) direction as a function of time for the orbit determination of Meteosat 4 without radiation pressure (top), with fixed a priori radiation pressure coefficient (center), and with radiation pressure coefficient determined.

0.8″), because the alongtrack position is restricted by the observations.

In the crosstrack direction the rms error is about the same in all three considered cases, because it is only determined by the rms errors in the elements determining the orientation of the orbit (i.e. i and Ω) which are not affected by the radiation pressure on short arcs.

5.2.2 Precision of the Observations

One question remains to be answered: Why is the rms of unit weight for all three cases significantly larger than one? This fact implies that either the a priori weights of the observations introduced into the orbit determination procedure are too optimistic, or that significant systematic errors are present. An inspection of the residuals seems to

indicate that the first cause is dominant. Figure 5.6 shows the residuals in right ascension (top) and declination (bottom). For each close encounter the average together with the standard deviation of the corresponding residuals is plotted. In fact, no systematics are observed.

The rms errors of the satellite's astrometric positions used for weighting the observations for the orbit determination contain only those errors that are introduced by the astrometric reduction process, i.e., those caused by the errors in the mapping scale, the camera orientation, and the pointing direction. They contain neither the errors from the centroiding of the satellite images on the CCD frame nor those from the reference star coordinates. For the former error source about one tenth of a pixel has to be expected, i.e., about 0.4″. For the PPM stars errors of 0.3″ are claimed (Röser et al., 1991). The sum of the two contributions indicates that a rms of unit weight of the order of 1.4 is realistic.

The mean residuals averaged for each close encounter series in Figure 5.6 contain all errors that are common for each close encounter, i.e. the errors in the pointing directions and those in the catalogue star positions. The pointing errors are given by the astrometric reduction and are in the range between 0.2″ and 0.3″. The observed scatter of the mean residuals is 0.33″, i.e. it is somewhat smaller than the quadratic sum of the two sources (pointing errors and reference star errors) implying that the positions of the reference stars used are in fact better than the quoted accuracy.

The standard deviation of the residuals within the close encounter series is due to the centroiding errors (that are of the order of a tenth of a pixel, i.e. about 0.4″), due to errors introduced by the astrometry, and possibly due to refraction effects (affecting the mapping scale). The observed value is about 0.7″.

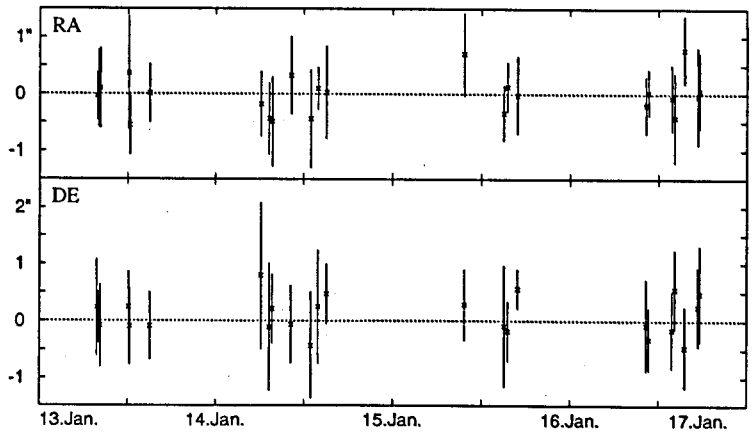

Figure 5.6: Residuals in right ascension and declination for Meteosat 4 for the orbit solution (c). Mean values together with the standard deviation for each close encounter series.

5.3 Orbit Determination for the Three Arcs and the Radiation Pressure

5.3.1 The Solutions for the Three Arcs

Meteosat 4 was observed during a time interval of 111 days in the center of which a manœuver occurred (see Table 5.3). The satellite orbit was therefore divided into two arcs with a length of 46 days and 42 days. Meteosat 5 was observed during the second half of the campaign over a time interval of 42 days during which the satellite was not manœuvered. Its observations were thus analyzed using a single arc. Table 5.5 lists the three arcs that were processed.

	Satellite	*Time span*	*Length*	*Obs.*
Arc 1:	Meteosat 4	26. Oct. – 11. Dec 1994	46 days	459
Arc 2:	Meteosat 4	3. Jan. – 14. Feb 1995	42 days	442
Arc 3:	Meteosat 5	3. Jan. – 14. Feb 1995	42 days	399

Table 5.5: List of arcs into which the observations of the two satellites were split.

The three arcs were processed independently using the force model given in Section 5.2. The resulting orbital elements and the direct radiation pressure coefficient are given in Table 5.6. Residuals may be found in Figures 5.7 to 5.9.

The rms of unit weight is of the order of 1.4 for all three arcs as it is for the short arc discussed in Section 5.2. This fact, as well as the inspection of the residuals give confidence that no large systematics are present even for these relatively long arcs. The residuals for arc 2 and arc 3 seem, however, to indicate some systematic deviation for the last data points. This might be due to a modelling problem or bad catalogue stars. In fact, only two (arc 2) and one (arc 3) close encounter series was measured during the last night of observation, thus reducing the statistical significance of these residuals. It has to be pointed out again, that the residuals from one close encounter series always contain the bias introduced by the reference star used.

Averaging the residuals for the last close encounter series shows, that for arc 3 the mean value for the residuals from the last night is close to zero in both coordinates, however with a large standard deviation ($-0.15'' \pm 1.03''$ and $0.06'' \pm 0.67''$ respectively). A deviation of the residuals from zero is thus not significant. For arc 2 the averaging of the residuals for the last two close encounter series reveals that only the second of the two series shows in right ascension a large average. The average residual are for the first series $-0.24'' \pm 0.55''$ and $-0.37'' \pm 0.70''$ in right ascension and declination respectively, and for the second series $-0.80'' \pm 0.54''$ resp. $0.08'' \pm 0.32''$. It is therefore plausible that the reference star used for the second close encounter series has either bad coordinates, or is a double star unresolved with the mapping scale of $4''$/pixel.

The rms errors for the orbital elements given in Table 5.6 may be compared with those from the 4-days-solution for Meteosat 4 discussed in Section 5.2 (see Table 5.4, case (c)). As expected the improvement is most significant for the semimajor axis (due to the much longer arc). In fact, the improvement of more than a factor of ten in the rms error for this elements corresponds about to the ratio of the arc lengths. The rms errors for all other elements are reduced more or less by the square root of the ratio of the

Arc 1: Meteosat 4, 1994	
RMS of unit weight	1.371 (0.584")
Arc length, number of obs.	46 days, 459 Obs.
Semimajor axis	42165763.30 ± 0.13 m
Eccentricity	.00025505 ± .00000013
Inclination	0.816024 ± 0.000013°
R.A. of ascending node	68.173583 ± 0.000571°
Argument of perigee	177.579207 ± 0.144387°
Mean longitude at T_{osc}	211.101080 ± 0.000073°
Radiation pressure coefficient	$7.117 \pm 0.056 \cdot 10^{-8}$m/s^2

Arc 2: Meteosat 4, 1995	
RMS of unit weight	1.413 (0.703")
Arc length, number of obs.	42 days, 442 Obs.
Semimajor axis	42165758.75 ± 0.16 m
Eccentricity	.00025615 ± .00000050
Inclination	0.819155 ± 0.000012°
R.A. of ascending node	68.008243 ± 0.000784°
Argument of perigee	177.368759 ± 0.160552°
Mean longitude at T_{osc}	211.101306 ± 0.000086°
Radiation pressure coefficient	$7.281 \pm 0.079 \cdot 10^{-8}$m/s^2

Arc 3: Meteosat 5, 1995	
RMS of unit weight	1.464 (0.725")
Arc length, number of obs.	42 days, 399 Obs.
Semimajor axis	42168881.77 ± 0.44 m
Eccentricity	.00009860 ± .00000016
Inclination	0.064628 ± 0.000012°
R.A. of ascending node	259.283729 ± 0.012089°
Argument of perigee	197.679585 ± 0.199748°
Mean longitude at T_{osc}	101.714724 ± 0.000029°
Radiation pressure coefficient	$7.028 \pm 0.070 \cdot 10^{-8}$m/s^2

Table 5.6: Orbital elements of Meteosat 4 and 5 determined for the three arcs defined in Table 5.5. The osculation epochs for the elements are for arc 1 and arc 2: Dec. 16, 1994, 08:58 UT, and for arc 3: Jan. 3, 1995, 00:00 UT. The system is J2000 for all elements.

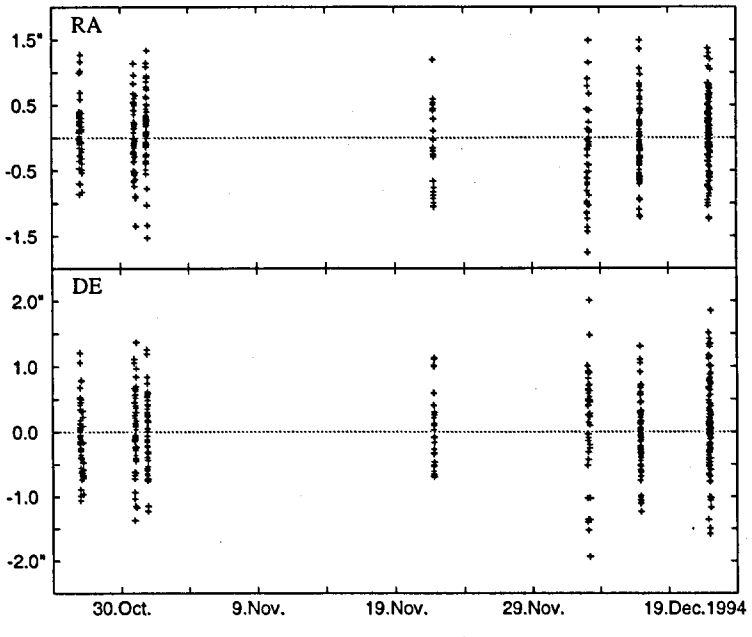

Figure 5.7: Residuals in right ascension (top) and declination (bottom) for arc 1 (Meteosat 4, 1994).

number of observations. The large rms error of the ascending node in arc 3 is due to the orbital inclination of Meteosat 5 which is about ten times smaller than the inclination of Meteosat 4.

5.3.2 The Radiation Pressure

The direct radiation pressure coefficient is determined to a precision of about 1%. In fact, due to the long arcs the radiation pressure coefficient and the semimajor axis and eccentricity are decorrelated. The determined values for direct radiation pressure coefficients for all three arcs are significantly larger than the value of $5.58 \cdot 10^{-8} \mathrm{m/s^2}$ given in eqn. (5.1). Eqn. (5.1) was derived assuming a perfectly absorbing satellite surface. If the surface reflects and diffuses a certain portion of the light, the radiation pressure is increased by a factor depending on the specular and diffuse reflection coefficient of the surface. For a cylinder the acceleration due to radiation pressure may increase by as much as 50% (see equations in Appendix C). Values larger by 25% to 30% than the one given by eq. (5.1) are therefore realistic. The coefficients determined for the three arcs are consistent within the rms errors.

Apart from the simplest model for the direct solar radiation pressure with the accelerating force parallel to the incident radiation (i.e. assuming a spherical satellite) a more sophisticated radiation pressure model for the Meteosat satellites was used. The model,

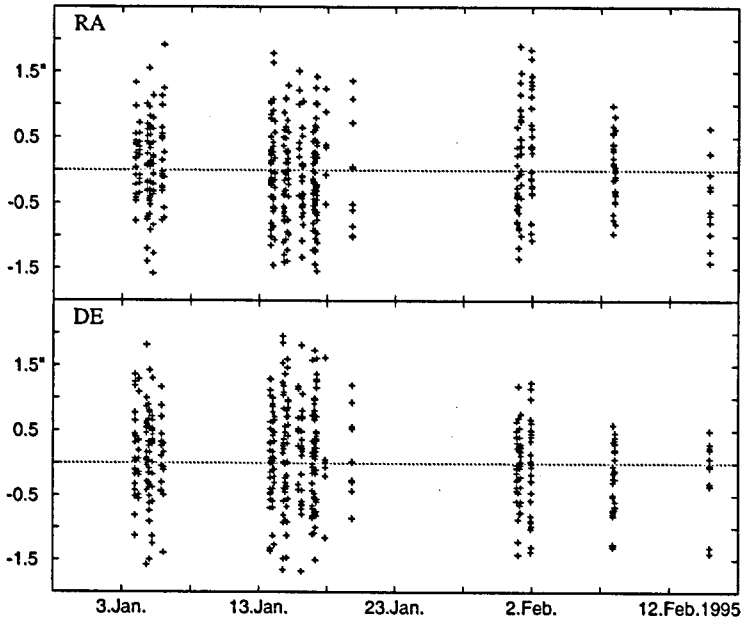

Figure 5.8: Residuals in right ascension (top) and declination (bottom) for arc 2 (Meteosat 4, 1995).

proposed by Veillet et al. (1990), describes the satellites as three concentric cylinders with specified optical properties of the surfaces. It is described in more detail in Appendix C.

According to this model, the magnitude of the acceleration induced by direct radiation pressure is dependent on the angle of the incident light to the axis of symmetry. In addition, the acceleration is no longer exactly parallel to the direction Sun–satellite. Because the spin axis of the controlled Meteosat satellites, which coincides with the cylinder axis, is perpendicular to the orbital plane, the value and direction of the direct radiation pressure may be computed for any position of the Sun. In order to allow for insufficiencies of the model, only the direction and functional dependency of the acceleration on the declination of the Sun was taken from the model whereas the factor corresponding to $AS_\odot/Mc$ was determined from observations. (This factor is called below 'Meteosat radiation pressure coefficient'.)

The direct radiation pressure coefficients and the Meteosat coefficients are given for all three arcs in Table 5.7. The relative rms errors of the Meteosat coefficients are of the order of 1% as for the direct radiation pressure coefficients. They are closer to the theoretical value of $5.58 \cdot 10^{-8}\mathrm{m/s^2}$ but still significantly larger. This difference may be due to the imperfections of the model, in particular due to the not accurately enough known optical properties of the surfaces.

In addition to the Meteosat radiation pressure coefficient three components of a radiation pressure acceleration vector were determined in a separate orbit determination run (see

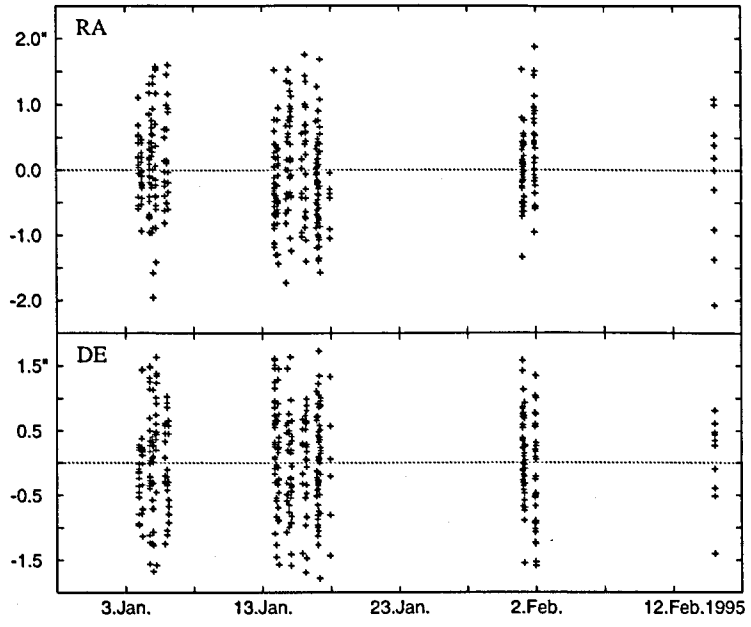

Figure 5.9: Residuals in right ascension (top) and declination (bottom) for arc 3 (Meteosat 5, 1995).

		Radiation Pressure Coefficients			
		arc 1	arc 2	arc 3	
Direct rpr. coef.		7.12±.06	7.28±.08	7.03±.07	$\cdot 10^{-8}$m/s^2
Meteosat rpr. coef.		6.79±.06	6.95±.08	6.71±.07	$\cdot 10^{-8}$m/s^2
Three rpr. coef.	1	6.57±.19	7.71±.22	7.04±.21	$\cdot 10^{-8}$m/s^2
	2	0.35±.12	0.24±.14	0.09±.10	$\cdot 10^{-8}$m/s^2
	3	-1.60±.48	1.26±.62	0.18±.49	$\cdot 10^{-8}$m/s^2

Table 5.7: Different radiation pressure coefficients determined for the three arcs.

Table 5.7). The coordinate system decomposing the vector has its 1-axis in the direction Sun–satellite, the 3-axis towards the ecliptic pole, and the 2-axis perpendicular to the other two in the direction of the orbital motion. It rotates in a Sun-fixed frame. Only the 1-component is determined with sufficient significance whereas the other two have large rms errors and are only marginally significant or even consistent with a value of zero.

The determination of the coefficients of the different radiation pressure models have no significant influence on the osculating orbital elements: The orbital elements of the solutions are all consistent. Table 5.8 shows the rms of unit weight and the rms for the single observations for the different solutions. As long as a radiation pressure coefficient is determined the values are nearly the same. If the Meteosat radiation pressure coefficient is

fixed to $5.58 \cdot 10^{-8} m/s^2$ the rms of unit weight are slightly larger, and significantly larger, if the direct radiation pressure is fixed at the same value. In the latter case systematic variations of up to 2" occur in the residuals . If the radiation pressure is not modelled at all, the rms is 2.5" or more, and systematic variations of the residuals in right ascension up to 10" are observed.

	RMS of unit weight		
	arc 1	arc 2	arc 3
No radiation pressure	5.96 (2.82")	5.04 (2.48")	5.66 (2.72")
Direct rpr. coef. fixed at $5.58 \cdot 10^{-8} m/s^2$	1.86 (0.83")	1.80 (0.90")	1.85 (0.91")
Meteosat rpr. coef. fixed at $5.58 \cdot 10^{-8} m/s^2$	1.41 (0.60")	1.48 (0.74")	1.50 (0.74")
Direct rpr. coef. determined	1.37 (0.58")	1.41 (0.70")	1.46 (0.73")
Meteosat rpr. coef. determined	1.37 (0.58")	1.41 (0.71")	1.46 (0.73")
Three rpr. coef. determined	1.72 (0.76")	1.70 (0.84")	1.73 (0.85")

Table 5.8: RMS of unit weight given by the orbit determination for the three arcs with six different radiation pressure options.

5.4 Combination of Arcs and Determination of Resonance Terms of the Earth's Potential

5.4.1 Combination of Two Arcs of Meteosat 4

After having processed the observations pertaining to the three arcs of Meteosat 4 and Meteosat 5 separately (see previous section) all observations were processed together using the program ARCOMB discussed in Chapter 3. Parameters that are common for several arcs may then be determined rigorously, e.g., a single radiation pressure parameter for the two arcs of Meteosat 4, or geopotential term parameters using all arcs in Table 5.5. In addition, parameters describing manœuvers between subsequent arcs may be set up and determined. The iterative procedure used for the combination of satellite orbits is described in Section 3.1.4. The equations for setting up manœuvre parameters are given in Appendix B and a more detailed discussion may be found in Beutler et al. (1996b).

To combine arcs 1 and 2 of Meteosat 4 the manœuver occurring on Dec. 16., 1994 at 08:58 UT had to be modelled. The osculating elements for the two arcs are given in Table 5.9 for the manœuver epoch. The semimajor axis is changed by only 4.5 m corresponding to a change of 0.21 arcsec/day in the mean motion or 43 m/day in the alongtrack direction. In the mean longitude a jump of 0.7" is observed which is roughly within the observation rms error. Part of this jump may be due to the change in the eccentricity. The changes in right ascension of the node of 1' and in inclination of 11" are clearly visible.

	before	*after*	*difference*
Semimajor axis	42165763.3m	42165758.8m	−4.5 m
Eccentricity	.00025505	.00025615	$1.1 \cdot 10^{-6}$
Inclination	0.816024°	0.819155°	.0031°
R.A. of ascending node	68.173583°	68.008243°	−.1653°
Argument of perigee	177.579207°	177.368759°	−.2104°
Mean longitude at $T_{manœuver}$	211.101080°	211.101306°	.00023°

Table 5.9: Orbital elements of Meteosat 4 before and after the manœuver on Dec. 16, 1995, taken from separate processing of arc 1 and 2 (see Table 5.6).

The resulting differences in position and velocity and the associated rms errors at the epoch of the manœuver , when processing arcs 1 and 2 of Meteosat 4 separately, are given in Table 5.10 in radial (R), alongtrack (S), and out of plane (W) directions. A jump of 238 m in alongtrack direction (corresponding to 1.4" in geostationary distance) and of 82 m in radial direction is observed. The position differences are barely significant, however.

The crosstrack component of the velocity change on the other hand shows a value that significantly differs from zero: The manœuver performed was obviously an inclination manœuver, required to prevent the orbital plane to precess due to lunisolar and Earth oblateness perturbations. The boost was directed towards the southern celestial pole. The observed velocity change of −.21m/s is unusually small for an inclination manœuver. For Meteosat such a manœuver usually results in a velocity change that is about hundred times larger leading to an inclination change of the order of a few tenths of a degree (Soop, 1994). The reason for this particular manœuver is unclear.

		R	*S*	*W*
Difference in position		−82.21 m	237.82 m	0.29 m
Difference in velocity		−0.0151 m/s	0.0058 m/s	−0.2104 m/s
RMS errors in position	arc 1	49.05 m	122.05 m	6.29 m
	arc 2	33.29 m	92.82 m	7.90 m
RMS errors in velocity	arc 1	0.0063 m/s	0.0036 m/s	0.0006 m/s
	arc 2	0.0057 m/s	0.0024 m/s	0.0008 m/s

Table 5.10: Differences of in position and velocity in radial (R), alongtrack (S), and crosstrack (W) direction at the epoch of the manœuver and the corresponding rms errors as computed from separate analyses of arcs 1 and 2.

In a first step the two arcs for Meteosat 4 are combined. A common radiation pressure coefficient is determined. At the manœuver epoch t_c continuity in position of the two arcs is enforced ($\boldsymbol{r}_2 = \boldsymbol{r}_1$) and the components of a velocity change $\Delta\boldsymbol{v}$, the so-called manœuver

parameters, are estimated ($\boldsymbol{v}_2 = \boldsymbol{v}_1 + \Delta\boldsymbol{v}$). In this way the 901 observations of Meteosat 4 covering a time interval of 111 days are represented by one arc which is described by 10 parameters (6 initial conditions, 3 manœuver parameters, 1 radiation pressure coefficient) instead of 14 parameters, when processing arcs 1 and 2 separately.

The manœuver epoch t_c is used as osculation epoch in both arcs. The first arc is integrated backwards and the second arc forwards. Nonsingular elements are used in the estimation process because for Keplerian elements the convergence is bad due to numerical problems. The results were then transformed to the standard Keplerian elements (Table 5.11)

The observations used for the combined solution cover a time interval of 111 days which is more than twice as long as the time intervals of the two original arcs. The rms of unit weight for the combined adjustment is 1.39, i.e., about the same as for arcs 1 and 2 (see Table 5.6). For the two arcs rms values for the single observations of 0.59" and 0.71", respectively, are given after combination, i.e., the same values as obtained from independent orbit determination for the two arcs.

The new orbital elements are within the rms errors of the elements of arc 1 in Table 5.6. The rms errors of the combined arc are significantly reduced thanks to the increased number of observations and thanks to the longer arc. For the semimajor axis the rms error is only 5 cm which corresponds to an alongtrack error of 3 mas/day or 0.5 m/day.

The direct radiation pressure coefficient for the combined solution is determined with a relative precision of $2.5 \cdot 10^{-3}$. The value is within the 1-sigma boundary of the parameter for arc 1 and within the 2-sigma boundary of the value for arc 2. Using the enhanced Meteosat radiation pressure model does not significantly alter the osculating elements.

Combined solution for Meteosat 4				
RMS of unit weight		1.393		
Semimajor axis		42165763.28 ±	0.05	m
Eccentricity		.00025503 ±	.00000010	
Inclination		0.816025 ±	0.000012	deg
R.A. of ascending node		68.173579 ±	0.000548	deg
Argument of perigee		177.512263 ±	0.039611	deg
Mean longitude at T_{osc}		211.101111 ±	0.000021	deg
Radiation pressure coefficient		$(7.104 \pm 0.018) \cdot 10^{-8}$		m/s^2
Manœuver parameter	radial	$(-6.6 \pm 4.3) \cdot 10^{-4}$		m/s
	alongtrack	$(-1.78 \pm 0.05) \cdot 10^{-4}$		m/s
	crosstrack	−0.2103 ±	0.0009	m/s

Table 5.11: Elements, direct radiation pressure coefficient, and manœuver parameters determined by combining the two arcs of Meteosat 4. The osculation epoch corresponds to the manœuver epoch: Dec. 16., 1994, 08:58 UT. The elements are those prior to the manœuvre. The system for the elements is J2000.

The value for the Meteosat radiation pressure coefficient is $(6.784 \pm .018) \cdot 10^{-8}\mathrm{m/s^2}$, again close to the value determined for arc 1.

The alongtrack and the crosstrack manœuver parameters are highly significant. It is evident that the manœuver consisted of a velocity change pointing out of the orbital plane. The corresponding parameter is determined with a relative precision of about 0.4%. The velocity change in radial direction is almost zero. The change in the transverse direction (almost alongtrack), although smaller than the corresponding value in radial direction, is significant.

5.4.2 Determination of the Resonant Geopotential Terms

Before actually combining all observations for determining the resonant terms of the Earth's potential these terms were determined separately for each arc. For each arc the elements, the direct radiation pressure coefficient, and the resonant coefficients C_{22} and S_{22} were computed. The latter are given in Table 5.12. A comparison of the estimations and of the 'true' values taken from the JGM3 potential model shows, that the determined values are not of good quality. Obviously these terms are biased.

	Arc 1	*Arc 2*	*Arc 3*	JGM3
C_{22}	$(2.505 \pm .276) \cdot 10^{-6}$	$(1.804 \pm .095) \cdot 10^{-6}$	$(2.728 \pm .082) \cdot 10^{-6}$	$2.439 \cdot 10^{-6}$
S_{22}	$(-1.421 \pm .082) \cdot 10^{-6}$	$(-1.218 \pm .027) \cdot 10^{-6}$	$(-1.409 \pm .024) \cdot 10^{-6}$	$-1.400 \cdot 10^{-6}$

Table 5.12: Independent determination of resonant geopotential terms C_{22} and S_{22} for all three arcs. Comparison with the 'true' value from the potential model JGM3 shows that the values are not reliable.

Table 5.13 documents that the results are much better for the combined analysis. It is clear that the use of two satellites, the significantly increased number of observations, the increased arclength as well as the reduced number of parameters are responsible for this 'quantum jump' in quality. In the combined estimation procedure a total of 19 parameters were determined. The rms of unit weight of the combined analysis is 1.4, i.e., the observations are still well represented. This is underlined by Figure 5.10 where no systematics are observed. The rms values for the observations in the three arcs are 0.58″, 0.71″, and 0.73″, respectively.

The orbital elements and radiation pressure coefficients are consistent with the values in Table 5.11 for Meteosat 4 and in Table 5.6 for Meteosat 5. Determining the Meteosat radiation pressure coefficients does not significantly change any of the parameters, and the rms errors remain roughly the same. The representation of the orbit is thus not improved by using the Meteosat radiation pressure model.

	Combined Solution	JGM3
C_{22}	$(2.43825 \pm 0.00069) \cdot 10^{-6}$	$(2.439263 \pm 0.000037) \cdot 10^{-6}$
S_{22}	$(-1.40056 \pm 0.00016) \cdot 10^{-6}$	$(-1.400266 \pm 0.000037) \cdot 10^{-6}$

Table 5.13: Resonant geopotential terms C_{22} and S_{22} when using all observations from Meteosat 4 and Meteosat 5 in a common adjustment. The relative rms errors for the two terms are $2.8 \cdot 10^{-4}$ and $1.1 \cdot 10^{-4}$, respectively.

The resonance coefficients C_{22} and S_{22} are determined with relative rms errors of (Hugentobler et al., 1996)

$$\frac{\sigma(C_{22})}{C_{22}} = 2.8 \cdot 10^{-4} \quad \text{and} \quad \frac{\sigma(S_{22})}{S_{22}} = 1.1 \cdot 10^{-4} \tag{5.2}$$

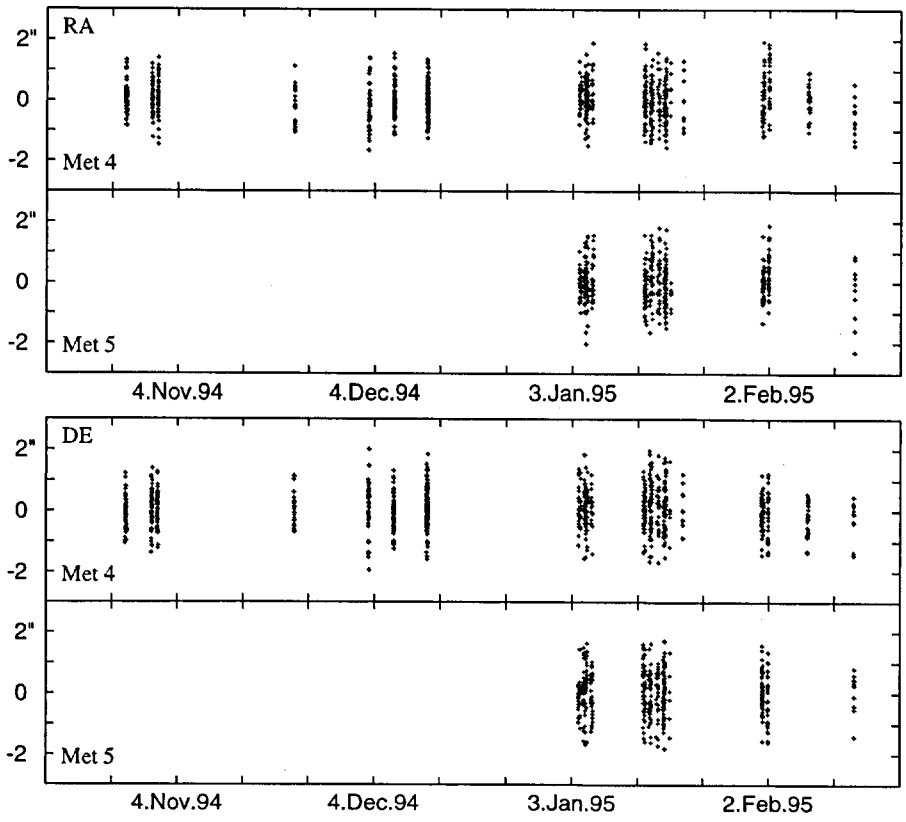

Figure 5.10: Residuals in right ascension (top) and declination (bottom) for Meteosat 4 and Meteosat 5 from combined orbit determination with estimation of manœuver parameters and potential terms C_{22} and S_{22}.

which is about one order of magnitude larger than the relative rms errors of $1.5 \cdot 10^{-5}$ and $2.6 \cdot 10^{-5}$ for C_{22} and S_{22} respectively in the JGM3 model. It has to be pointed out, however, that the results presented here were obtained with a relatively small effort, the observations being acquired during a short campaign with a telescope of modest optical quality. The accuracy corresponds to simulations performed by Rossi (1988).

Covariance studies based on a similar configuration of observations as in the COGEOS campaign show, that an improvement of the astrometric accuracy to 0.1″ — which is what we expect when using the new Zimmerwald 1 m ZIMLAT telescope and the Hipparcos catalogue — leads to an improvement of the rms errors for C_{22} and S_{22} by a factor of 10. In other words, astrometric methods are competitive with other methods for the determination of the geopotential terms C_{22} and S_{22}, provided one has access to a high quality telescope and high precision astrometric catalogues. In addition many different satellites should be analyzed.

5.4.3 Combination of Astrometric Observations from Zimmerwald and Graz

Dr. M. Ploner from the Technical University of Vienna acquired astrometric observations to Meteosat 5 and Meteosat 6 using the BMK camera of the geodetic observatory in Graz-Lustbühel, which was recently equipped with a CCD camera (Ploner, 1996). The BMK camera from Carl Zeiss, Oberkochen, has a focal length of 750 mm and a maximum aperture of 300 mm. A CCD camera of type SITe 1024B from Photometrics was mounted in the focal plane. The 1024 x 1024 pixels with a size of 24.6 x24.6 μm give a field of view of 1°53′ x 1°53′ (instead of the 13.6° x13.6° of the original camera) with a mapping scale of 6.6″/pixel. Due to a fine tuned image processing procedure and due to the fact that for the astrometric reduction always several PPM stars were available in the field of view, the rms of the measured satellite positions was about 0.5″ despite a rather modest mapping scale.

The observations were acquired in 14 nights between April 17, 1996, and June 17, 1996 (arc length of 61 days for both satellites). The information concerning the Graz observation campaign is summarized in Table 5.14.

All observations of Meteosat 4, 5, and 6 from Zimmerwald and Graz were combined (using the program ORBDET for orbit improvement and the program ARCOMB for combining the three arcs from Zimmerwald and the two arcs from Graz) in order to compute the resonant geopotential terms (see Chapter 3). A total of 32 parameters was estimated (24 orbital parameters, 3 manœuvre parameters, 3 radiation pressure coefficients, and 2 geopotential terms), a total of 1′783 observations was available.

The resulting values for the resonant geopotential terms are given in Table 5.15 (see Ploner (1996)). Relative rms errors of the coefficients are

$$\frac{\sigma(C_{22})}{C_{22}} = 1.6 \cdot 10^{-4} \quad \text{and} \quad \frac{\sigma(S_{22})}{S_{22}} = 0.7 \cdot 10^{-4}, \tag{5.3}$$

	Meteosat 5	*Meteosat 6*
Observation period	April 17 — June 17, 1996	April 17 — June 17, 1996
Arc length (days)	61	61
Number of nights	14	14
Number of observations	234	249

Table 5.14: Observations of Meteosat 5 and Meteosat 6 acquired from Graz-Lustbühel (Ploner, 1996).

an improvement of about a factor of 1.7 with respect to the precision of the coefficients determined with the Zimmerwald observations alone. The error for the term S_{22} is only a factor of 2.7 above that of the JGM3 model. The excellent agreement of the coefficients with the JGM3 model is remarkable.

	Combined Solution	JGM3
C_{22}	$(2.43923 \pm 0.00039) \cdot 10^{-6}$	$(2.439263 \pm 0.000037) \cdot 10^{-6}$
S_{22}	$(-1.40031 \pm 0.00010) \cdot 10^{-6}$	$(-1.400266 \pm 0.000037) \cdot 10^{-6}$

Table 5.15: Resonant terms C_{22} and S_{22} of the geopotential determined using all observations from Zimmerwald and Graz for the satellites Meteosat 4, Meteosat 5, and Meteosat 6. The relative rms errors for the two terms are $1.6 \cdot 10^{-4}$ and $0.7 \cdot 10^{-4}$, respectively.

We conclude that optical astrometric observations of geostationary satellites are useful for the determination of the resonant geopotential terms C_{22} and S_{22}. An astrometric accuracy of 0.1″ as expected for the Zimmerwald 1 m telescope and the combination with astrometric observations from other observatories to satellites at different longitudes makes the precision of the coefficients competitive with the best geopotential models available today. With short campaigns and with a limited effort for both, observing and processing, the resonant low order coefficients can be monitored in order to detect temporal variations or in order to establish upper limits for these variations.

6 Combination of Radar and Astrometric Measurements

High precision astrometric observations may be used as an independent calibration tool for other observation techniques. In this chapter the combination of Radar measurements and optical observations of geostationary satellites is studied. Astrometric observations were successfully used for the assessment of the accuracy and the determination of possible offsets in the Radar observables 'range' and 'range rate' as well as 'azimuth' and 'elevation' of the 34-m-Radar of the Research Establishment for Applied Science (FGAN) at Wachtberg-Werthhoven, Germany.

In a joint experiment (see Mehrholz et al. (1997)) of FGAN and the Astronomical Institute of the University of Berne (AIUB) quasi-simultaneous observations of geostationary satellites were acquired in Wachtberg-Werthhoven and in Zimmerwald. The experiment was carried out in the context of a study for DASA Jena-Optronik GmbH (Deutsche Aerospace AG) for the development of an experimental servicing satellite operating in GEO. It is planned that the approach of this satellite to a target satellite would be controlled with the help of an Earth-based Radar until the target is in the range of the on-board optical sensors. The goal of the experiment was the assessment of the accuracy of the Radar based positions and of the corresponding relative distances of geostationary objects.

6.1 Observation of Geostationary Objects by the FGAN Radar

6.1.1 The FGAN Radar

At Wachtberg-Werthhoven, about 20 km south of Bonn, the Research Institute for High Frequency Physics (FHP) of the German Defense Research Organization FGAN (Forschungsgesellschaft für Angewandte Naturwissenschaften) operates a High Power Radar System which is capable of tracking and imaging satellites, aircraft, and space debris. The Radar system TIRA (Tracking and Imaging Radar) consists of a 34 m diameter parabolic dish antenna inside a radome with 49 m diameter (see Figure 6.1), a L-band tracking Radar (1.333 GHz, 22.5 cm wavelength, typical peak power of 1 MW at 1 msec pulse length) and a Ku imaging Radar (16.7 GHz, 17.96 mm wavelength, 13 kW peak power). The field of view of the Radar is 0.5° (3-dB beamwidth in the terminology of the Radar community, i.e., FWHM of the beam power).

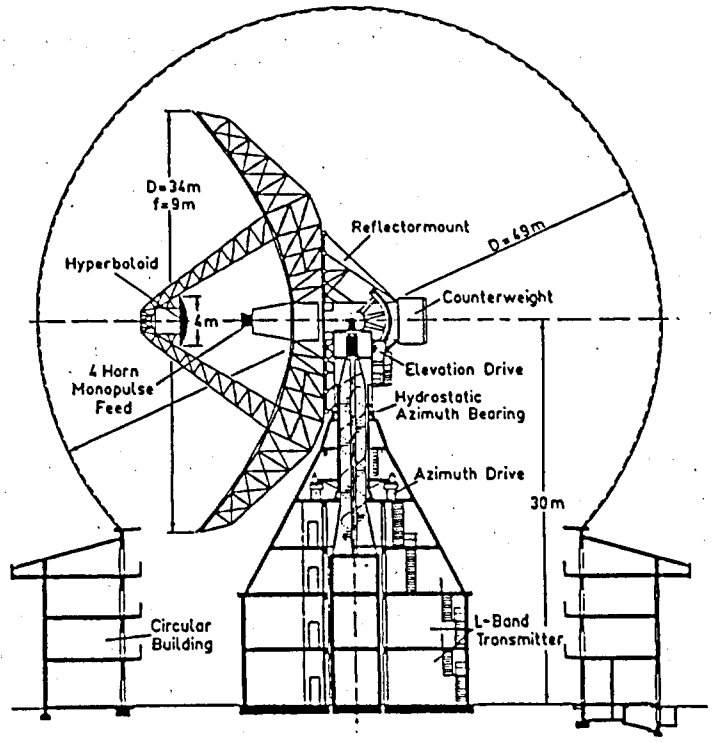

Figure 6.1: The 34-m dish antenna of the TIRA system at FGAN, Wachtberg-Werthhoven, Germany.

6.1.2 The FGAN Observations

The imaging Radar usually is operated simultaneously with the tracking Radar. For the observation of satellites in GEO only the L-band tracking Radar was used because of its much higher power than the imaging Radar. In order to detect an object in GEO with a signal-to-noise ratio of 2 (i.e. 3 dB) using single pulse signal processing technique the object must have a Radar cross-section (RCS) of more than 28 dBm^2 corresponding to 630 m^2. The transformation from Radar cross-section to geometrical cross-section is not trivial. It depends essentially on the conductivity of the reflecting material and on the complexity of the mechanical structure as well as on the wavelength of the Radar signal. Stabilized satellites with extended solar panels reach the required Radar cross-section.

The multi-pulse signal processing applied in the context of the presented study to the observations of the geostationary satellites allows it to increase the detectability by coherent integration of N single pulses. Usually $N = 128$ single pulses were integrated.

The main observable of Radar measurements is the *range rate* of the observed target, measured by the Doppler shift of the reflected Radar signal. In multi-pulse signal processing technique the received signal of N pulses is Fourier-transformed in order to get

the Doppler signal averaged over the N pulses. The expected precision is of the order of 5 – 15 cm/s depending somewhat on the signal-to-noise ratio of the signal. Precise *ranges* may be measured by modulating the Radar signal. This technique, requiring sophisticated processing of the registered signal, was *not* applied in the study. Therefore, the range resolution of about 150 km for single pulses is given by the pulse length of 1 msec. For multipulse processing the expected precision lies in the range between 20 and 70 km, depending on the signal-to-noise ratio.

In addition to range rate and range information the direction to the observed object can be measured: The Radar signal is detected using the 4-horn monopulse feed (which is used for emission of the Radar pulse, too). The four horns are arranged in the focal plane of the Cassegrain-type Radar system in the corners of a square which is aligned with the azimuth and elevation directions. By registering not only the sum of the signal detected in the four receiver horns but also the difference of the signals, information about the position of the reflecting object within the Radar beam may be extracted (the principle of this direction observation is similar to that of a four-quadrant diode). The precision of the angle measurement relative to the axis of the antenna is of the order of 0.05° to 0.2° depending on the signal-to-noise ratio of the signal. The resolution of the angular encoders of the Radar axes was 5″ at the time of the observation campaign presented below and 1.2″ after the upgrade of the gear units of the antenna in 1995. The repeatability of the pointing, as tested by an external target, is 2.5″.

The variations of the detected signal with time and in some cases also the width of the Doppler signal in conjunction with the known linear dimension of the observed satellite allow a characterization of the rotational motion (attitude) of the object.

Satellite	COSPAR	First Observation	Last Observation	Total Obs. Time	Stored Data Amount
TV Sat 1	87095A	1994 Apr. 12 13:40	Jun. 18 21:10	4.09 hours	31.27 MBytes
Olympus 1	89053A	1995 Feb. 15 14:07	Feb. 20 21:00	4.90	38.49
Gorizont 15	88028A	1995 Jan. 17 12:32	Jan. 25 12:58	4.24	33.66
Astra 1A	88109A	1994 Apr. 12 09:42	Mar. 1 10:52	2.94 hours	22.20 Mbytes
Gorizont 4	80049A	1995 Feb. 15 12:13	Feb. 16 12:53	0.97	7.32
Gorizont 5	82020A	1995 Feb. 15 12:45	Feb. 16 12:09	1.36	10.51
Gorizont 7	83066A	1995 Jan. 9 14:40	Feb. 15 13:32	0.85	6.80
Gorizont 8	83118A	1995 Feb. 16 10:10	Feb. 16 11:12	1.01	8.26
Gorizont 13	86090A	1995 Jan. 9 12:25	Jan. 9 13:28	1.03	7.59
Gorizont 14	87040A	1995 Jan. 09 13:31	Feb. 16 10:05	3.03	23.30
Gorizont 23	91046A	1995 Feb. 15.13:34	Feb. 16 09:06	1.45	11.26

Table 6.1: Overview of the FGAN Radar observations of geostationary satellites (from Mehrholz et al. (1997)).

All in all 11 geostationary satellites were observed with the FGAN Radar once or several times in the context of the study. The total observation time was 25.88 hours and the total amount of data collected was more than 200 Mbytes. For preparing the observation parameters of the Radar (tracking ephemeris, range rate and range gates) the Two Line Elements (TLE) of the satellites were used. Table 6.1 summarizes the observations, the total observation time for each satellite, and the amount of raw data (Mehrholz et al., 1997).

The observations of the three satellites TV Sat 1, Olympus 1, and Gorizont 15 were combined with optical observations (see below). The observations of these satellites were made available to the AIUB by Dr. D. Mehrholz from FGAN. In addition to azimuth, elevation, range and range rate measurements the data files contained for each observation epoch the rms errors of each observable estimated from the signal-to-noise ratio, the signal-to-noise ratio for each observed signal, and the number of pulses used for coherent integration.

6.2 Quasi-Simultaneous Radar and Optical Observations

6.2.1 The Observations

In Zimmerwald the satellites TV Sat 1, Olympus 1, and the Gorizont satellites 7, 13, 14, and 15 were observed optically in the context of the joint experiment. The observations of TV Sat 1, Olympus 1, and Gorizont 15 were finally used for the combined experiment. These satellites are no longer operational. They drift in longitude and they are tumbling in an uncontrolled way. Table 6.2 lists the amount of observations and their distribution in time for three satellites as acquired at Wachtberg-Werthhoven and Zimmerwald. The observations of Olympus 1 from Feb. 20, 1995, are truly simultaneous, the other observations are quasi simultaneous, i.e., acquired within overlapping time intervals. The rms error for the astrometric positions, as determined by the astrometric reduction, lies between 0.5″ and 0.7″.

6.2.2 Combination of Different Observation Types

The range rate may be computed from the scalar product $\boldsymbol{e} \cdot \boldsymbol{v}$, where $\boldsymbol{e}$ is the observation unit vector (observer – satellite) and $\boldsymbol{v}$ is the velocity vector of the satellite relative to the observer. Even for a geostationary satellite the range rate is only partly due to the radial displacement of the satellite. Other contributions stem from the satellite's velocity perpendicular to the equatorial plane due to the orbital inclination and from the alongtrack velocity (relative to an exact geostationary position) together with the parallax (observations not in the geocenter). For elements as those of the satellite Olympus 1 given

Satellite	Date	Radar		Optical		
		Observations (UT)		Series	Observations (UT)	
TV Sat 1	94 Jul. 5	43	07:57 – 08:06			
	94 Jul. 7			3	26	00:53 – 01:02
	94 Jul. 12	103	09:11 – 09:45			
	94 Jul. 15	290	11:03 – 12:13	3	30	23:13 – 23:30
	94 Jul. 18	280	19:34 – 21:09			
Olympus 1	95 Feb. 15	266	14:10 – 15:29			
	95 Feb. 16	448	13:21 – 15:23			
	95 Feb. 20	96	20:53 – 21:40	13	106	18:19 – 22:29
	95 Feb. 27			4	35	21:17 – 01:23
	95 Feb. 28			4	37	23:25 – 01:36
Gorizont 15	95 Jan. 14			2	19	01:45 – 02:27
	95 Jan. 15			4	32	21:55 – 03:50
	95 Jan. 16			5	47	23:54 – 04:04
	95 Jan. 17	93	12:32 – 13:35	3	29	22:32 – 23:00
	95 Jan. 19	203	22:56 – 23:35	5	44	18:18 – 20:12
	95 Jan. 25	60	09:03 – 10:03			

Table 6.2: Distribution of the observations of the geostationary satellites TV Sat 1, Olympus 1, and Gorizont 15 acquired with the FGAN Radar at Wachtberg-Werthhoven and the SLR telescope in Zimmerwald.

in Table 6.6 ($e = 0.023$, $i = 2.26°$) the radial velocity may reach (to the first order in eccentricity) a value of

$$\dot{r} = ane \simeq 7\text{m/s}$$

where a is the semimajor axis, n the mean motion, and e the eccentricity. The velocity of the satellite perpendicular to the equatorial plane gives rise to a range rate which may reach

$$v \sin i \sin p_\delta \simeq 122\text{m/s} \cdot \sin p_\delta \simeq 16\text{m/s}$$

where $v \simeq 3.1$ km/s is the mean orbital velocity of the satellite, i is the orbital inclination, and p_δ is the parallax of the satellite in declination which amounts for the FGAN Radar to about 7.5°. The alongtrack velocity variations have an amplitude of (to the first order in the eccentricity) ve. This causes a variation in the range rate with an amplitude of up to

$$ve \sin p_\alpha \simeq 7\text{m/s} \cdot \sin p_\alpha \simeq 0.7\text{m/s}$$

where p_α is the parallax of the satellite in right ascension reaching 5.5° for the FGAN Radar for a satellite just above the horizon. A maximum range rate of the geostationary satellite Olympus 1 of about 23 m/s may therefore be expected. Because Radar 'observes' the eccentricity of an orbit in a relatively direct way through the range rate measurement, Radar observations are particularly well suited for determining the shape of an orbit.

The orientation of the orbital plane, on the other hand, is not so well accessible to range rate measurements. The orientation angles are essentially determined by the azimuth and elevation measurements. The range rate measurements with an accuracy of the order of 5 to 10 cm/s for measuring velocities of the order of 20 to 30 m/s have a similar relative precision as the measurements of azimuth and elevation.

The observations for the three satellites listed in Table 6.2 were used for estimating orbital parameters with the program ORBDET (see Chapter 3). In order to compare the two observation techniques and to assess the improvement of the parameters by combining the observations, three types of solutions were generated for each satellite: The first using only the optical observations from Zimmerwald, the second one using only the FGAN Radar measurements, and the third one using both observation types together. The rms errors given by the astrometric reduction and by the Radar data processing were used to define the weighting of observation types in the combined solution.

The resulting orbital elements and rms observation errors are listed in Table 6.3. Radiation pressure coefficients were estimated for the combined solution and for the solution from the optical observations except for TV Sat 1, which was observed in Zimmerwald only in two nights. In the cases where the radiation pressure coefficient was not determined a 'reasonable' a priori value of $1 \cdot 10^{-7} m/s^2$ was adopted.

The rms errors of the orbital parameters based on astrometric observations are in most cases smaller than the rms errors when using only Radar observations. Eccentricity and argument of perigee for TV Sat 1, which was observed optically only in two nights, are the exceptions. In this case the Radar technique due to its potential for determining the shape of the orbit is superior to the astrometric measurements.

Except for the eccentricity and the argument of perigee the rms errors of the osculating elements are one to several orders of magnitude smaller if optical observations are included because astrometric observations are two to three orders of magnitude more precise than Radar angle measurements. Adding Radar observations therefore 'only' significantly improves the precision of eccentricity and argument of perigee. In the case of a bad coverage of the orbit by astrometric observations (TV Sat 1 in Table 6.3) the rms errors for all osculating elements are significantly better than those stemming from astrometry only and from Radar only.

The a posteriori observation rms error for the Radar observables are $30 - 40$ km in range, $2.5 - 10$ cm/s in range rate, and $0.03 - 0.1°$ in the angular measurements. These values are even somewhat better than expected.

In Figure 6.2 we see the rms errors in position as a function of time for the satellite TV Sat 1 with parameters determined from astrometric observations alone (top), from Radar observations alone (center), and from combined observations (bottom). The figures correspond to orbit determinations not including offsets in the Radar observables. The osculating elements are listed in Table 6.3.

In all three cases — astrometry, Radar, combined observations — the errors in alongtrack direction are largest. Due to the fact that TV Sat 1 was observed in Zimmerwald only

in two nights and because consequently the error of the estimated eccentricity is large, the alongtrack error of the orbit determined using astrometric measurements only shows large variations with a daily period and maximum values around noon. The Radar observations, on the other hand, were fairly well distributed, and the eccentricity is determined

	Astrometry	*Radar*	*Combined*
TV Sat 1			
RMS in R.A., decl.	0.56″	—	0.59″
in range	—	34.5 km	36.2 km
in range rate	—	2.6 cm/s	2.8 cm/s
in azi., ele.	—	0.099°	0.084°
Semimajor axis (m)	42485547.2 ± 9.8	42486491.6 ± 85.9	42485646.0 ± 1.8
Eccentricity	.0011095 ± .0000242	.0010661 ± .0000082	.0010716 ± .0000009
Inclination	4.84771 ± 0.00016	4.78322 ± 0.00325	4.84812 ± 0.00002
R.A. of asc. node	61.99902 ± 0.00129	63.09676 ± 0.03463	62.00288 ± 0.00029
Argument of perigee	−60.72676 ± 0.41090	−48.31735 ± 0.25684	−60.40999 ± 0.01939
Mean long. at t_{osc}	309.81553 ± 0.00199	309.91366 ± 0.01183	309.81375 ± 0.00011
Rad. press. (m/s^2)	—	—	$(223.8 \pm 2.7) \cdot 10^{-9}$
Olympus 1			
RMS in R.A., decl.	0.56″	—	0.70″
in range	—	39.0 km	41.1 km
in range rate	—	7.2 cm/s	9.9 cm/s
in azi., ele.	—	0.030°	0.026°
Semimajor axis (m)	41862871.5 ± 4.5	41863330.3 ± 127.7	41862808.1 ± 2.1
Eccentricity	.0019027 ± .0000008	.0018849 ± .0000159	.0019151 ± .0000004
Inclination	2.35036 ± 0.00001	2.34563 ± 0.00295	2.35036 ± 0.00001
R.A. of asc. node	73.79617 ± 0.00038	72.68431 ± 0.20461	73.79632 ± 0.00027
Argument of perigee	33.99692 ± 0.05558	37.69618 ± 0.58495	33.17120 ± 0.02499
Mean long. at t_{osc}	124.10326 ± 0.00029	124.20337 ± 0.00489	124.09920 ± 0.00014
Rad. press. (m/s^2)	$(146.4 \pm 5.4) \cdot 10^{-9}$	—	$(64.8 \pm 2.5) \cdot 10^{-9}$
Gorizont 15			
RMS in R.A., decl.	0.65″	—	0.97″
in range	—	32.5 km	35.4 km
in range rate	—	4.9 cm/s	9.8 cm/s
in azi., ele.	—	0.081°	0.039°
Semimajor axis (m)	42864708.2 ± 4.7	42866320.8 ± 155.8	42864635.8 ± 4.2
Eccentricity	.0032717 ± .0000005	.0029974 ± .0000086	.0032794 ± .0000005
Inclination	4.62637 ± 0.00002	4.47629 ± 0.00427	4.62637 ± 0.00002
R.A. of asc. node	66.75466 ± 0.00025	65.80408 ± 0.05724	66.75503 ± 0.00026
Argument of perigee	259.14985 ± 0.02264	255.18644 ± 0.13358	259.47805 ± 0.02074
Mean long. at t_{osc}	157.50732 ± 0.00014	157.65565 ± 0.01228	157.50587 ± 0.00013
Rad. press. (m/s^2)	$(81.2 \pm 8.0) \cdot 10^{-9}$	—	$(-56.4 \pm 6.9) \cdot 10^{-9}$

Table 6.3: Results from orbit determinations using optical (AIUB) and/or Radar (FGAN) observations.

with high precision. No large oscillations of the rms errors in position are therefore observed. However, due to the relatively low precision of the determined semimajor axis the

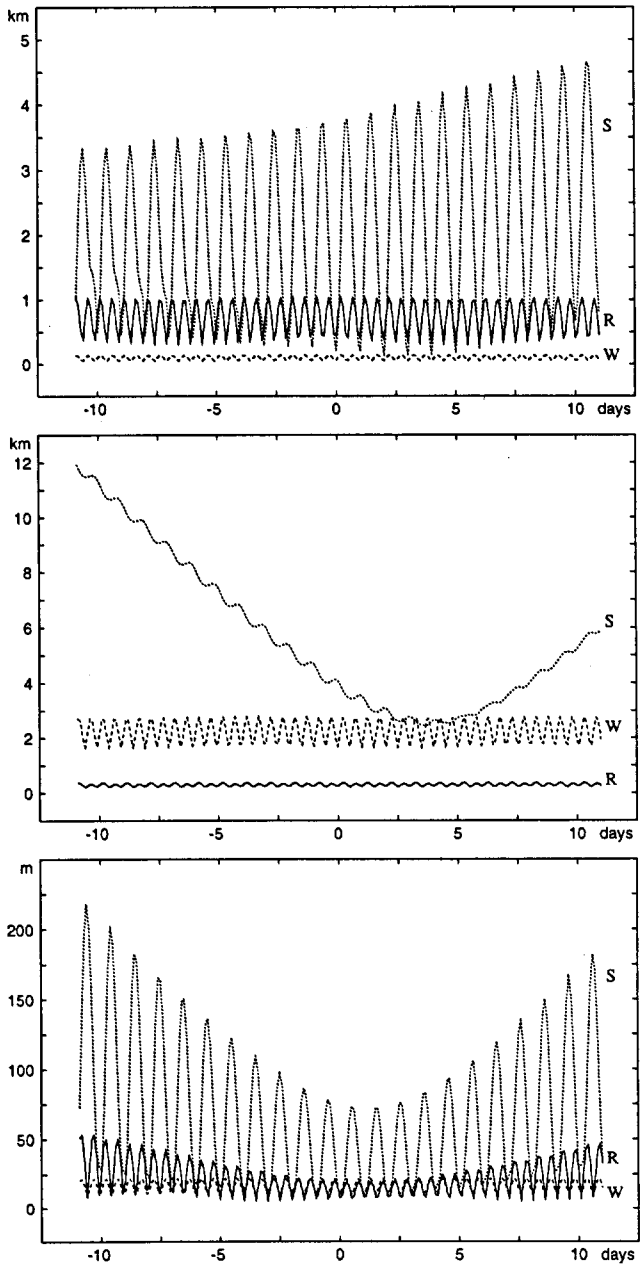

Figure 6.2: RMS errors in position in radial (R), alongtrack (S), and crosstrack (W) direction for the satellite TV Sat 1 from astrometric observations (top), Radar observations (center), and combined observations (bottom) within a time interval of 22 days centered at the observation epochs. Observe the differences in scales!

alongtrack error grows rapidly with the length of the orbital arc.

Not surprisingly, the rms errors in radial direction for orbit determined using only Radar observations are much smaller than the errors in crosstrack direction. In the case when the orbit is determined using only astrometric observations the situation is reversed: The errors in the crosstrack direction are always smaller than those in the radial direction.

Combining the two sets of observations leads to a significant improvement of the rms errors in position. The rms error in alongtrack direction is below 200 m in a time interval of 20 days centered around the observation epochs, whereas the corresponding error reaches 4 km for an orbit determined from astrometric observations and even 12 km for an orbit determined from Radar observations only. Similar improvements in the rms errors are observed in the radial and the crosstrack direction. If, however, the astrometric observations are well distributed the rms errors in position may already be below 100 m (see Figure 3.11, bottom right) and the improvement by using in addition Radar observations is less pronounced.

The osculating elements determined from the Radar observations significantly differ from the elements determined from astrometric observations. This fact indicates the presence of systematic errors. It is not clear a priori whether these systematics are due to the astrometric or the Radar observations. To further study this problem offsets in the Radar observables were estimated. The offsets, to be understood in the sense 'observed – computed', are given in Tables 6.4 and 6.5.

When processing combined observations, offsets in range and range rate as well as offsets in azimuth and elevation (for the Radar measurements) were estimated. For solutions based only on Radar observations only offsets in range and range rate were determined because offsets in the angles are not well determined (these can be absorbed by the osculating elements). An offset in the azimuth is almost perfectly correlated with the longitude of the satellite.

In all cases, the offsets in range and range rate are significant. An offset in range had to be expected because the range was only measured with low precision and without highly sophisticated signal processing techniques. In range rate ambiguities introduced by the signal processing may cause an offset. The actual reason for the measured offset could not yet be identified, however.

We are, however, quite sure that the reasons for the (relatively small) differences between the results using the two measurement techniques are due to the Radar observations. In Tables 6.4 and 6.5 we see, e.g., that the osculating elements determined from Radar observations are getting closer to those determined with astrometric observations, if offsets in range and range rate are determined, and that the observation rms errors in the Radar observables are reduced. Not estimating offsets may even, as in the example of Gorizont 15 (Table 6.3), result in a negative (i.e. attractive) solar radiation pressure coefficient (!).

Residuals of the range rate measurements for two of the measurement sessions of satellite Gorizont 15 are given in Figure 6.3. In the second session the threshold in the signal-to-

noise ratio used for accepting the observations was higher than in the first session. The scatter of the data is therefore reduced. An offset of about −10 cm/s is clearly visible.

The offsets in azimuth and elevation do not show a clear time dependence, although an indication for a time variation of the offset in elevation may be seen in Figure 6.4, where the offsets and the corresponding rms errors in azimuth and elevation for all observation sessions are shown. It would indeed be almost unbelievable if a large and complex structure like the 34 m dish antenna would not show systematic variations in the ele-

	Astrometry	*Radar*	*Combined*
TV Sat 1			
RMS in R.A., decl.	0.56″	—	0.62″
in range	—	19.3 km	19.5 km
in range rate	—	2.6 cm/s	2.1 cm/s
in azi., ele.	—	0.099°	0.080°
Semimajor axis (m)	42485547.2 ± 9.8	42486279.7 ± 82.2	42485712.7 ± 2.0
Eccentricity	.0011095 ± .0000242	.0010712 ± .0000076	.0011274 ± .0000014
Inclination	4.84771 ± 0.00016	4.78627 ± 0.00311	4.84802 ± 0.00002
R.A. of asc. node	61.99902 ± 0.00129	63.12198 ± 0.03337	61.99785 ± 0.00023
Argument of perigee	−60.72676 ± 0.41090	−48.55416 ± 0.24141	−57.80098 ± 0.05524
Mean long. at t_{osc}	309.81553 ± 0.00199	309.89134 ± 0.01118	309.82352 ± 0.00023
Rad. press. (m/s^2)	—	—	$(279.3 \pm 2.2) \cdot 10^{-9}$
Offset in range	—	27.1 ± 1.1 km	29.4 ± 0.9 km
in range rate	—	0.4 ± 0.2 cm/s	−8.2 ± 0.2 cm/s
in azimuth	—	—	0.007 ± 0.003 deg
in elevation	—	—	−0.031 ± 0.003 deg
Olympus 1			
RMS in R.A., decl.	0.56″	—	0.56″
in range	—	19.3 km	19.2 km
in range rate	—	6.6 cm/s	6.7 cm/s
in azi., ele.	—	0.025°	0.025°
Semimajor axis (m)	41862871.5 ± 4.5	41862882.2 ± 89.2	41862871.1 ± 1.9
Eccentricity	.0019027 ± .0000008	.0018768 ± .0000114	.0019027 ± .0000003
Inclination	2.35036 ± 0.00001	2.34360 ± 0.00204	2.35036 ± 0.00001
R.A. of asc. node	73.79617 ± 0.00038	73.60990 ± 0.14975	73.79614 ± 0.00018
Argument of perigee	33.99692 ± 0.05558	34.32422 ± 0.42568	33.98954 ± 0.02320
Mean long. at t_{osc}	124.10326 ± 0.00029	124.10174 ± 0.00341	124.10323 ± 0.00012
Rad. press. (m/s^2)	$(146.4 \pm 5.4) \cdot 10^{-9}$	—	$(145.5 \pm 2.3) \cdot 10^{-9}$
Offset in range	—	36.5 ± 0.7 km	35.7 ± 0.8 km
in range rate	—	−14.5 ± 0.6 cm/s	−11.2 ± 0.2 cm/s
in azimuth	—	—	0.002 ± 0.003 deg
in elevation	—	—	0.007 ± 0.003 deg

Table 6.4: Results from orbit determinations including estimation of Radar observation offsets using optical (AIUB) and Radar (FGAN) observations (Part I).

	Astrometry	*Radar*	*Combined*
Gorizont 15			
RMS in R.A., decl.	0.65″	—	0.66″
in range	—	16.3 km	16.4 km
in range rate	—	4.5 cm/s	6.0 cm/s
in azi., ele.	—	0.036°	0.039°
Semimajor axis (m)	42864708.2 ± 4.7	42864830.7 ± 106.9	42864714.1 ± 2.9
Eccentricity	.0032717 ± .0000005	0.003268 ± .0000107	.0032718 ± .0000003
Inclination	4.62637 ± 0.00002	4.61555 ± 0.00534	4.62636 ± 0.00001
R.A. of asc. node	66.75466 ± 0.00025	66.83221 ± 0.04868	66.75476 ± 0.00016
Argument of perigee	259.14985 ± 0.02264	258.87601 ± 0.13346	259.12526 ± 0.01408
Mean long. at t_{osc}	157.50732 ± 0.00014	157.51294 ± 0.00870	157.50755 ± 0.00008
Rad. press. (m/s^2)	$(81.2 \pm 8.0) \cdot 10^{-9}$	—	$(86.6 \pm 4.9) \cdot 10^{-9}$
Offset in range	—	29.9 ± 0.9 km	31.0 ± 1.4 km
in range rate	—	−11.7 ± 0.4 cm/s	−10.6 ± 0.2 cm/s
in azimuth	—	—	0.000 ± 0.005 deg
in elevation	—	—	−0.008 ± 0.005 deg

Table 6.5: Results from orbit determinations including estimation of Radar observation offsets using optical (AIUB) and Radar (FGAN) observations (Part II).

vation. Nevertheless the estimated offsets in the two angles are consistent with the zero hypothesis.

Despite the few problems encountered in the comparison of the Radar observations with

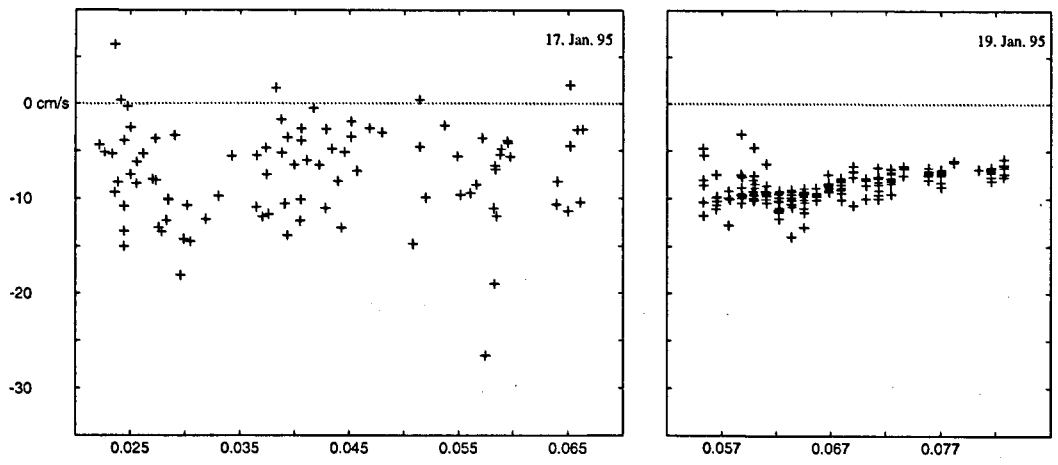

Figure 6.3: Residuals in range rate for Gorizont 15 for two observation sessions as a function of time (fractions of observation day). For the second session the signal-to-noise threshold was set to a higher value. The residuals stem from an orbit determination combining different observation techniques. Six osculating elements and offsets in range, azimuth, and elevation were estimated. Abscissa: time in fractions of observation day.

astrometric measurements it has to be underlined, that the FGAN Radar observations of geostationary satellites are of high quality. Using appropriate signal processing techniques, such as those applied by the FGAN staff, observations allowing the determination of precise orbits for distant objects like geostationary satellites is possible independent on bad weather periods.

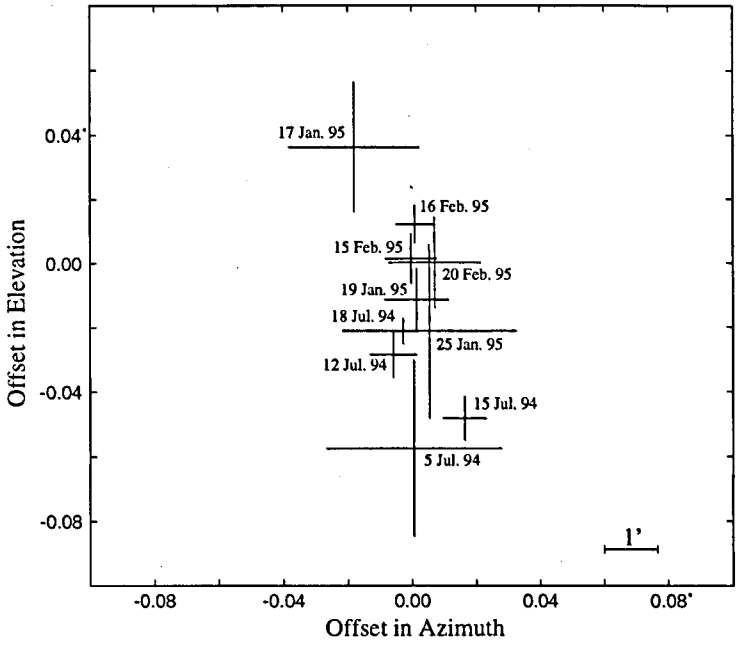

Figure 6.4: Offsets and associated rms errors in azimuth and elevation for Radar observation sessions.

6.3 Covariance Studies

6.3.1 Orbit Determination from Radar Observations

Observing geostationary satellites using Radar is much more expensive than using optical telescopes: A powerful antenna as well as complicated signal processing procedures are required. On the other hand Radar has the obvious advantage of time and weather independence: measurements may be carried out at any time, day and night. The technique is therefore being well suited for time critical events such as the approaching phase of a servicing satellite to an uncontrolled object. In this section we are interested in the accuracy of orbital parameters for geostationary satellites determined from Radar observations. The question of formal precision of the parameters is studied through covariance analyses.

Semimajor axis	41857565 m
Eccentricity	0.00230477
Inclination	2.260°
R.A. of ascending node	66.366°
Argument of perigee	55.923°
Mean longitude a t_{osc}	17.092°
Radiation pressure coefficient	$1.43 \cdot 10^{-6} m/s^2$

Table 6.6: Orbital parameters used for the covariance analysis. They correspond to those of the geostationary satellite Olympus 1. Osculation epoch is May 2, 1995, 23:37 UT.

The simulated observations are based on an orbit similar to that of the satellite Olympus 1. The parameters of the orbit are given in Table 6.6. The Radar observables range rate, azimuth and elevation were used for orbit determination.

Distribution of the Observations. In a first step the accuracy of the osculating elements was studied as a function of the distribution of the observations. The observations were assumed to be concentrated in three session containing 205 measurements each and lasting for one hour. The three observation sessions were assumed to lie in a time interval of 12 to 48 hours. The last session was assumed to take place in all cases at the culmination point of the satellite. The epochs of the sessions for the six studied configurations are given in Table 6.7. Each configuration contains 615 observation epochs. The adopted rms observation errors are given in Table 6.8.

Observation epochs:	0 h	6 h	12 h	18 h	24 h	32 h	36 h	42 h	48 h
Configuration 1:							x	x	x
Configuration 2:						x		x	x
Configuration 3:					x			x	x
Configuration 4:					x		x		x
Configuration 5:				x				x	x
Configuration 6:	x							x	x

Table 6.7: Distribution of the observation sessions for the covariance studies. Each symbol corresponds to 205 observations carried out within one hour.

Formal errors of the osculating elements for the six artificial observation campaigns are given in Table 6.9. It is obvious that the error of the semimajor axis a decreases with increasing arc length. For an observed arc length of 12 hours the formal error in a is about 1 km, for an arc length of 48 hours it is 0.28 km. The formal errors of the inclination i and of the R.A. of the ascending node Ω are of the same order of magnitude (as expected) as

Measurement rms error in range rate	10 cm/s
Measurement rms error in azimuth and elevation	0.1°

Table 6.8: Adopted rms observation errors for the Radar observations.

the formal errors of the angle observations (azimuth and elevation) divided by the square root of the number of observations. Only for configuration 4 the formal error of Ω is larger because the orbit is observed at positions separated by 180° in longitude. Only the R.A. of the ascending node (and not the inclination) is affected by this fact because the observations are assumed to be acquired close to the upper and lower culmination points of the orbit. If the observation epochs are close to the node passing times the formal error of the inclination would be larger.

If the observation sessions are separated by an integer multiple of 12 hours, the determination of the eccentricity and of the argument of perigee is less accurate than in the case when two of the sessions are separated by 6 hours. This is due to the fact that the radial velocity — which is for high orbiting objects close to the geocentric radius changes — measured at two positions in the orbit separated by 90°, the eccentricity e and the argument of perigee ω may be determined using the relations

$$\begin{aligned} \dot{r}_1 &= \frac{ane\sin E}{1-e\cos E} = ane\sin E + O(e^2) \\ \dot{r}_2 &= \frac{ane\sin(E+\pi/2)}{1-e\cos(E+\pi/2)} = -ane\cos E + O(e^2). \end{aligned}$$

Therefore, we may conclude that

$$\dot{r}_1/\dot{r}_2 = -\tan E + O(e) \qquad \sqrt{\dot{r}_1^2+\dot{r}_2^2} = ane + O(e^2),$$

	Formal Errors in Osculating Elements					
Configuration:	1	2	3	4	5	6
Semimajor axis (m)	1016	743	579	581	461	280
Eccentricity	.0000116	.0000131	.0000111	.0000178	.0000137	.0000108
Inclination	0.0046°	0.0058°	0.0047°	0.0046°	0.0060°	0.0048°
R.A. of asc. node	0.153°	0.110°	0.146°	0.233°	0.115°	0.145°
Argument of perigee	0.545°	0.397°	0.551°	0.888°	0.411°	0.556°
Mean long at t_{osc}	0.0695°	0.0502°	0.0388°	0.0379°	0.0305°	0.0305°

Table 6.9: Formal errors of osculating elements determined from six different observation configurations (see Table 6.7) with 615 Radar measurements each. Results from covariance studies with rms errors of the observables as given in Table 6.8.

where n is the mean motion and E is the eccentric anomaly. If the semimajor axis a, the longitude at t_{osc}, and the R.A. of the ascending node are known (i.e. determined using additional observations), the eccentricity e and argument of perigee ω can be computed using the above formulae. If, on the other hand, the two observations are separated by 180° the radial velocities have (to first order in e) the same absolute values and the above equations are linearly dependent.

The formal errors in the position in radial, alongtrack, and crosstrack direction are given in Table 6.10 for different time intervals after the last observation. Due to the less accurately determined R.A. of the ascending node for the observation configuration 4 the formal error in the crosstrack direction shows large variations.

		Formal Errors in Position (km) for configuration					
Error after		1	2	3	4	5	6
0 hours	R	1.14	1.02	0.73	1.00	0.67	0.54
	S	3.40	3.55	3.42	3.81	3.32	3.18
	W	3.26	4.30	3.33	2.97	4.48	3.40
6 hours	R	1.43	0.88	0.81	1.21	0.70	0.63
	S	5.93	5.27	4.67	5.46	4.30	3.90
	W	4.61	3.30	4.42	7.17	3.34	4.38
12 hours	R	1.05	0.83	0.74	0.86	0.81	0.54
	S	8.65	6.67	5.91	6.99	3.25	4.43
	W	3.28	4.27	3.36	3.12	4.44	3.44
18 hours	R	0.88	0.86	0.84	1.00	0.59	0.65
	S	10.28	8.11	6.96	7.48	6.20	4.65
	W	4.60	3.34	4.40	7.12	3.39	4.36
24 hours	R	1.18	1.02	0.74	1.02	0.66	0.55
	S	12.21	10.00	8.30	8.65	6.97	5.31
	W	3.32	4.26	3.40	3.12	4.43	3.49

Table 6.10: Formal errors of the satellite position in R, S, and W direction 0, 6, 12, 18, and 24 hours after the last observation epoch.

Uninterrupted Radar Observation. Here we assume that observations are acquired every minute without interruption over time intervals of 1 to 7 days. A opposed to the minimum observation scenario discussed above this is the maximum observation scenario. The same observation rms errors were used as above (see Table 6.8).

The formal errors for the osculating elements as determined by covariance analyses are given in Table 6.11. As expected for observations perfectly covering the orbit, the formal error of the semimajor axis a is reduced as $\Delta t^{-3/2}$, the formal errors of the other elements are reduced as $\Delta t^{-1/2}$ (Δt is the observation time interval).

Element	*Formal Errors in Osculating Elements for Arc Length (days)* 1	2	4	7
Semimajor axis (m)	245	146	69	32
Eccentricity	.0000072	.0000051	.0000036	.0000027
Inclination	0.0034°	0.0024°	0.0017°	0.0012°
R.A. of asc. node	0.084°	0.059°	0.042°	0.031°
Argument of perigee	0.255°	0.180°	0.126°	0.094°
Mean long at t_{osc}	0.0201°	0.0130°	0.0071°	0.0040°

Table 6.11: Formal errors of osculating elements determined from Radar observations acquired every minute in intervals between 1 and 7 days. (Covariance studies using rms errors of the observables as given in Table 6.8.)

The formal errors in position are shown as a function of time in Figure 6.5 for the seven observation campaigns. The time interval of 13 days starts with the first observation. The symbols (□) mark the last epoch for each campaign. The formal errors decrease with the square root of the number of observations. The smallest errors are found in radial direction (R). Even for observations covering only one day this error is below 0.5 km for the 13 days interval considered. In alongtrack direction (S) the formal error grows linearly with time due to the uncertainty in the mean motion. Shortly after the last measurement it exceeds 2 km. In crosstrack direction (W) the formal errors are below 2.5 km. They are nearly entirely determined by the angular measurements.

Dependence on the Observation RMS Errors. In order to study the dependence of the formal errors of the parameters on the precision of the observations the adopted rms error of the Radar observables was varied. The values used are listed in Table 6.12. The observation epochs assumed for the covariance studies were equal to the configuration 6 used in the first experiment, i.e., three observation sessions of 1 hour, each at epochs $t - 24$ h, $t - 6$ h, and t.

RMS error in range rate	10 cm/s	5 cm/s	1 cm/s	10 cm/s	10 cm/s
RMS error in azimuth and elevation	0.1°	0.1°	0.1°	0.05°	0.02°

Table 6.12: Varied rms observation errors for the Radar observations.

The formal errors of the osculating elements for the five campaigns are given in Table 6.13. It is interesting that the errors are reduced most efficiently when reducing the observation rms error in the angular measurements. The effect when reducing the rms error of the range rate is smaller because the relative precision of the range rate measurement is lower

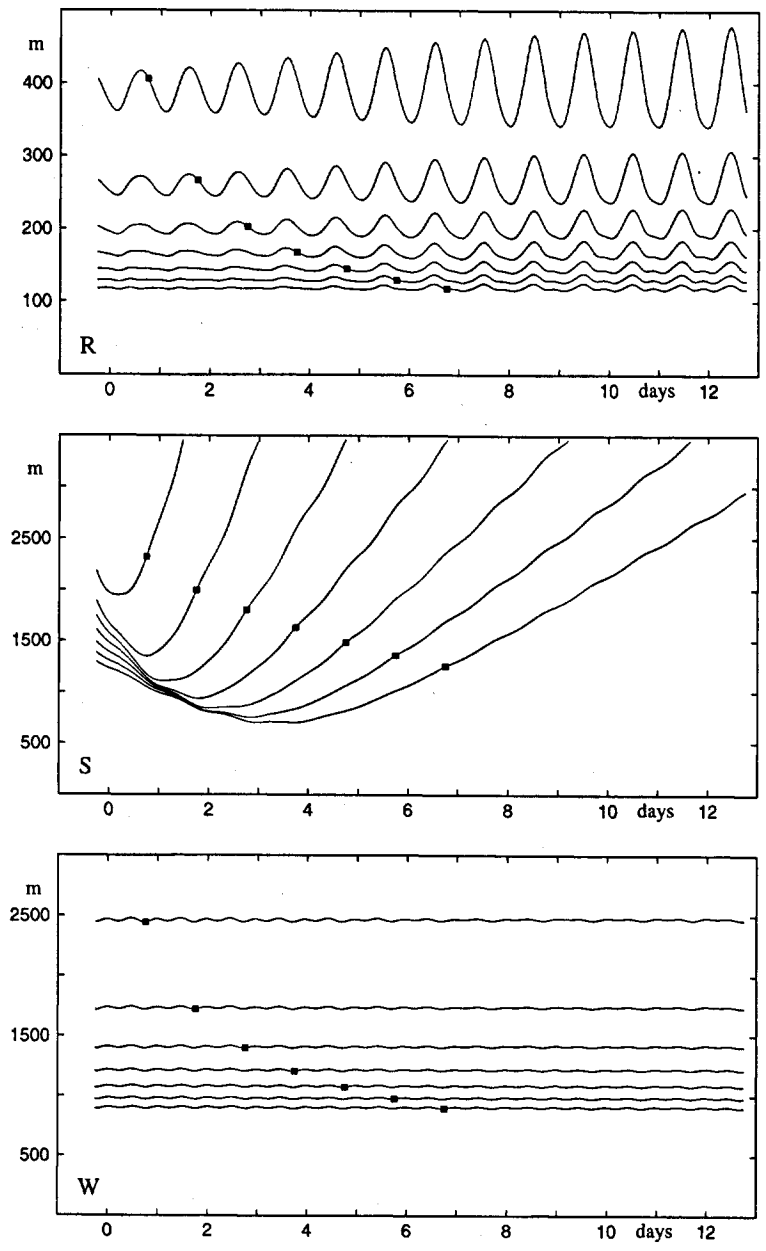

Figure 6.5: Formal errors in radial (top), alongtrack (center), and crosstrack (bottom) position as a function of time for observation campaigns lasting from 1 day (top curve in each diagram) to 7 days (bottom curve). The symbols □ indicate the epoch of the last observation.

than the precision of the angle measurements (although of the same order of magnitude): For the studied orbit the maximum range rate is 22 m/s, the relative precision in the range rate measurement is therefore $4.5 \cdot 10^{-3}$ for an observation rms error of 10 cm/s

	Formal Errors in Osculating Elements				
RMS Error in Range Rate:	10 cm/s	5 cm/s	1 cm/s	10 cm/s	10 cm/s
RMS Error in Azi, Ele:	0.1°	0.1°	0.1°	0.05°	0.02°
Semimajor axis (m)	280	265	132	142	57
Eccentricity	.0000108	.0000105	.0000099	.0000056	.0000029
Inclination	0.0048°	0.0048°	0.0047°	0.0024°	0.0010°
R.A. of asc. node	0.145°	0.144°	0.138°	0.072°	0.029°
Argument of perigee	0.556°	0.557°	0.542°	0.284°	0.123°
Mean long at t_{osc}	0.0305°	0.0170°	0.0086°	0.0091°	0.0037°

Table 6.13: Formal errors of osculating elements determined from five artificial observation campaigns with different observation rms errors. Results from covariance studies.

while the relative precision of the angle measurements is $1.7 \cdot 10^{-3}$ for an observation rms error of 0.1°.

6.3.2 Effects of Offsets in the Radar Observables

Systematic Offsets in the Observations. To study the propagation of systematic offsets in the observations into the estimated orbital elements, error-free observations were generated based on a reference orbit. Subsequently constant offsets were adopted and applied in the range rate, the azimuth, or the elevation measurements. The adopted offsets of −2.5 cm/s in range rate, of 0.01° in azimuth, and of 0.02° in elevation correspond roughly to the values determined for the FGAN Radar. The observations cover 1 to 7 days with a spacing of one minute between epochs. For the sets of observations containing no random errors but affected by constant offsets, osculating elements were determined. The difference of these elements with respect to the true elements of the reference orbit reflect the influence of the systematic observation errors on the results given in Table 6.14. In Figures 6.6 to 6.8 we give the differences in position of the generated orbits to the reference orbit in radial (top), alongtrack (center), and crosstrack (bottom) direction. Each curve corresponds to one of the seven simulations. The solid part of the curves correspond to that part of the orbit which is covered by observations, the dotted parts of correspond to the extrapolations.

Offset in the Range Rate. The semimajor axis determined with observations contaminated by an offset in the range rate show a significant bias relative to the reference orbit (see Table 6.14). The eccentricity is not so much affected by the range rate offset due to a good coverage of the orbit with observations.

The bias in the semimajor axis produces a drift of the satellite relative to its nominal position as can be seen in Figure 6.6 (center). Correspondingly, large systematic residuals

	Reference Orbit	Offset in		
		Range Rate −2.5 cm/s	Azimuth 0.01°	Elevation 0.02°
Semimajor axis (m)	41857565	41856934	41857576	41857597
Eccentricity	.00230477	.00230907	.00230438	.00230403
Inclination	2.2603°	2.2576°	2.2605°	2.2605°
R.A. of asc. node	66.3661°	66.3319°	66.3574°	66.3662°
Argument of perigee	55.9227°	56.0817°	55.9196°	55.9481°
Mean long at t_{osc}	139.3803°	139.3153°	139.3735°	139.3932°

Table 6.14: Osculating elements computed from observations with a systematic bias in range rate, azimuth, or elevation for a nonstop 4 day measurement campaign.

in the angular measurements have to be expected. The shorter the observation time interval, the better the systematic error in the observations can be absorbed by the semimajor axis. For a 4-day observation campaign the drift in alongtrack direction reaches values up to 6 km per day. At the end of the observation interval the satellite is off by 12 km from its nominal position (corresponding to about 0.02°). Also, in the range rate systematics up to −2 cm/s are observed in the residuals for a 4-day observation campaign.

In radial direction (Figure 6.6, top) the systematic offset decreases with increasing observation time; for a 4-day interval the error remains below 1 km. In crosstrack direction (Figure 6.6, bottom) the systematic error shows oscillations with an initial amplitude of about 2.5 km.

Offset in the Azimuth. If the Radar observations are biased by an offset in the azimuth essentially only the longitude of the satellite is changed. Table 6.14 shows that nearly the total offset of 0.01° in the azimuth is absorbed by the satellites's longitude. In fact, would the satellite be observed in the meridian (where its motion in longitude is parallel to the horizon), an offset in the azimuth can be entirely absorbed by the longitude and the residuals do not show any systematic behaviour. Obviously a systematic bias in the azimuth observation cannot be determined from Radar observations alone. Calibrations by astrometric measurements of the same satellite are required (see next section).

The systematic errors relative to the reference orbit in both, the radial and the crosstrack directions (see Figure 6.7, top and bottom respectively), are small. In radial direction the difference is a few ten meters. In crosstrack direction the difference oscillates between −150 m and +150 m because the topocentric satellite positions were not assumed to be in the south and therefore a part of the azimuth offset was absorbed in the orbit orientation angles.

In alongtrack direction (Figure 6.7, center), however, an offset of 6 km is observed for all arcs. These 6 km correspond in the geocentric distance of 36'000 km to the adopted

observation offset of 0.01° in the azimuth. In addition we see a drift of the satellite depending on the precision of the semimajor axis and thus on the arclength.

Offset in the Elevation. The adopted offset in the elevation of 0.02° is partially absorbed in the longitude of the satellite: The longitude is changed with respect to that of the reference orbit by about 0.01°. The rest of the offset is absorbed by the other osculating elements. None of them was, however, changed by more than the associated rms error (Table 6.11). Accordingly, the systematic differences in the position of the satellite are small (see Figure 6.8). In radial direction the offset is below 100 m, in crosstrack direction it is in the range of ±400 m. In alongtrack direction the offset in the mean longitude at the osculation epoch of 0.01° shows up as an offset of about 7.5 km.

Half of the offset in elevation could be absorbed in the longitude because the satellite was assumed to be observed at a place in the sky where its motion is not parallel to the horizon.

It is worth mentioning that the systematic errors in position get larger with increasing observed arc length. In the crosstrack component the curve with the largest amplitude in Figure 6.8 (bottom) corresponds to the 7-day observation interval, in radial direction (Figure 6.8, top) it is the curve with the largest offset, and in alongtrack direction (Figure 6.8, center) the curve with the largest drift. Obviously, with increasing arc length the possibility of the algorithm for 'hiding' an offset in the elevation in the osculating elements is reduced. Consequently we find a systematic behaviour of the residuals in the angular measurements. For a 4-day observation interval a constant offset of about 0.009° is observed in the residuals of the azimuth and an offset of 0.015° in the residuals of the elevation. The signal for an offset in the elevation measurement may therefore be seen in the Radar observations themselves. Nevertheless, a calibration with astrometric measurements is much more accurate and reliable.

6.3.3 Determination of Radar Offsets using Astrometric Observations

In the previous section we found that calibration of the Radar observations is essential for the determination of precise orbits from Radar observations alone. A precise calibration of the instrumental zero-point in the azimuth is required in particular. Astrometric measurements are an ideal (and probably the only) tool for such a calibration. In this section we study the formal errors of the offsets of the Radar observables determined from combined Radar and astrometric observations of the same satellite.

We used the observation rms errors given in Table 6.15 for the covariance study. Four 'non-stop' Radar observation campaigns (one measurement per minute) were simulated with a duration of 1, 2, 4, and 7 days respectively. Three different astrometric campaigns

RMS error in range rate observable	10 cm/s
RMS error in azimuth and elevation Radar observable	0.1°
RMS error in the astrometric observables	0.5″

Table 6.15: Adopted observation rms errors for the Radar and the astrometric measurements.

were simulated: The first with observations from only one night, the second with observations from two successive nights, and the third with observations from three nights. In the latter case it was assumed that the observations were made in the first two and in the fourth observation night (with a gap of one night, e.g., due to bad weather). In each night 5 close encounter series were simulated between 20 UT and 4 UT, each containing 10 individual observations. I.e., from each observation night 50 single direction measurements were acquired. The first day of Radar observations and the first night of astrometric measurements were assumed to coincide. This is realistic because a coordinated campaign would start only if the weather as well as the weather forecast at the astronomical observatory are good, in which case both observatories would start to observe immediately.

From the results given in Chapter 3 for the rms errors of osculating elements determined with astrometric measurements (Table 3.3) and for the rms errors in position (Figure 3.11) and from the corresponding results from Radar observations (Table 6.11 and Figure 6.5) we conclude that the precision of the determination of the offsets in the Radar observables is limited almost entirely by the precision and duration of the Radar observations. The accuracy of the offset in the azimuth essentially is governed by the accuracy of the determination of the alongtrack position of the satellite by the two observation methods. For 3 days of astrometric observations this error is below 100 m (corresponding to 0.6″ in GEO) within a time interval of 7 days whereas for Radar observation the rms error is of the order of 1 km.

In Table 6.16 we see that, in fact, the formal errors of the elements, in particular of the semimajor axis and of the elements i and Ω are determined by the optical observations while the precision of the Radar offsets is limited by the accuracy of the Radar measurements: Changing the length of the arc observed by Radar does not change the formal error of the semimajor axis and the inclination, if the optical observations cover more than a single night. The formal error of the eccentricity slightly improves with increased length of the Radar observation session due to the contribution of the range rate observations for orbit determination.

The formal errors of the offsets in the Radar observables, on the other hand, are independent on the number of nights with astrometric observations but they are reduced with the square root of the number of Radar observations. Only the offset in the azimuth is slightly worse if astrometric observations from only one night are available, because the semimajor axis and thus the alongtrack position of the satellite is determined with lesser

accuracy from astrometric observations from one night only.

With the assumptions made for the covariance study the offsets in the Radar angle measurements are determined with a precision between 7″ and 4″ and the offset in range rate with a precision of 0.3 cm/s to 0.1 cm/s. If the rms errors of the Radar observations are better than the values given in Table 6.15, the formal errors in the offsets are improved accordingly. The quality of the astrometric measurements starts only playing a role for the precision of the offset determination if the rms errors of the Radar observations are more than ten times smaller than the values in Table 6.15. In fact, the astrometic observations

	Formal Errors in Elements and Offsets with Radar Arc Length (days)			
	1	2	4	7
1 astrometric observation night				
Semimajor axis (m)	55.4	38.4	24.8	16.0
Eccentricity	.00000071	.00000060	.00000048	.00000039
Inclination	0.000024°	0.000024°	0.000023°	0.000023°
Offset in azimuth	0.0027°	0.0019°	0.0015°	0.0013°
elevation	0.0026°	0.0019°	0.0013°	0.0010°
range rate (cm/s)	0.26	0.19	0.13	0.10
2 astrometric observation nights				
Semimajor axis (m)	2.1	2.0	2.0	2.0
Eccentricity	.00000043	.00000040	.00000036	.00000032
Inclination	0.000018°	0.000018°	0.000018°	0.000018°
Offset in azimuth	0.0026°	0.0019°	0.0013°	0.0010°
elevation	0.0026°	0.0019°	0.0013°	0.0010°
range rate (cm/s)	0.26	0.19	0.13	0.10
3 astrometric observation nights				
Semimajor axis (m)	0.7	0.7	0.7	0.7
Eccentricity	.00000034	.00000032	.00000030	.00000027
Inclination	0.000015°	0.000015°	0.000015°	0.000015°
Offset in azimuth	0.0026°	0.0019°	0.0013°	0.0010°
elevation	0.0026°	0.0019°	0.0013°	0.0010°
range rate (cm/s)	0.26	0.19	0.13	0.10

Table 6.16: Formal errors in the semimajor axis, the eccentricity, the inclination and the offsets in the Radar observables using astrometric and Radar observations. The Radar observations cover intervals of 1, 2, 4 or 7 days, one Radar observation was made per minute. The astrometric observations are acquired within 1, 2 or 3 nights in 5 close encounters per night, each containing 10 observations. Adopted rms observation errors: 0.1° in azimuth and elevation, 0.1 m/s in range rate, 0.5″ for astrometry.

nearly entirely determine the satellite orbit and the Radar observations are only 'used' to determine the Radar offsets. Osculating elements and Radar offsets are nearly uncorrelated and the determination of the orbit and the determination of the Radar offsets may even be carried out independently without significant loss of accuracy.

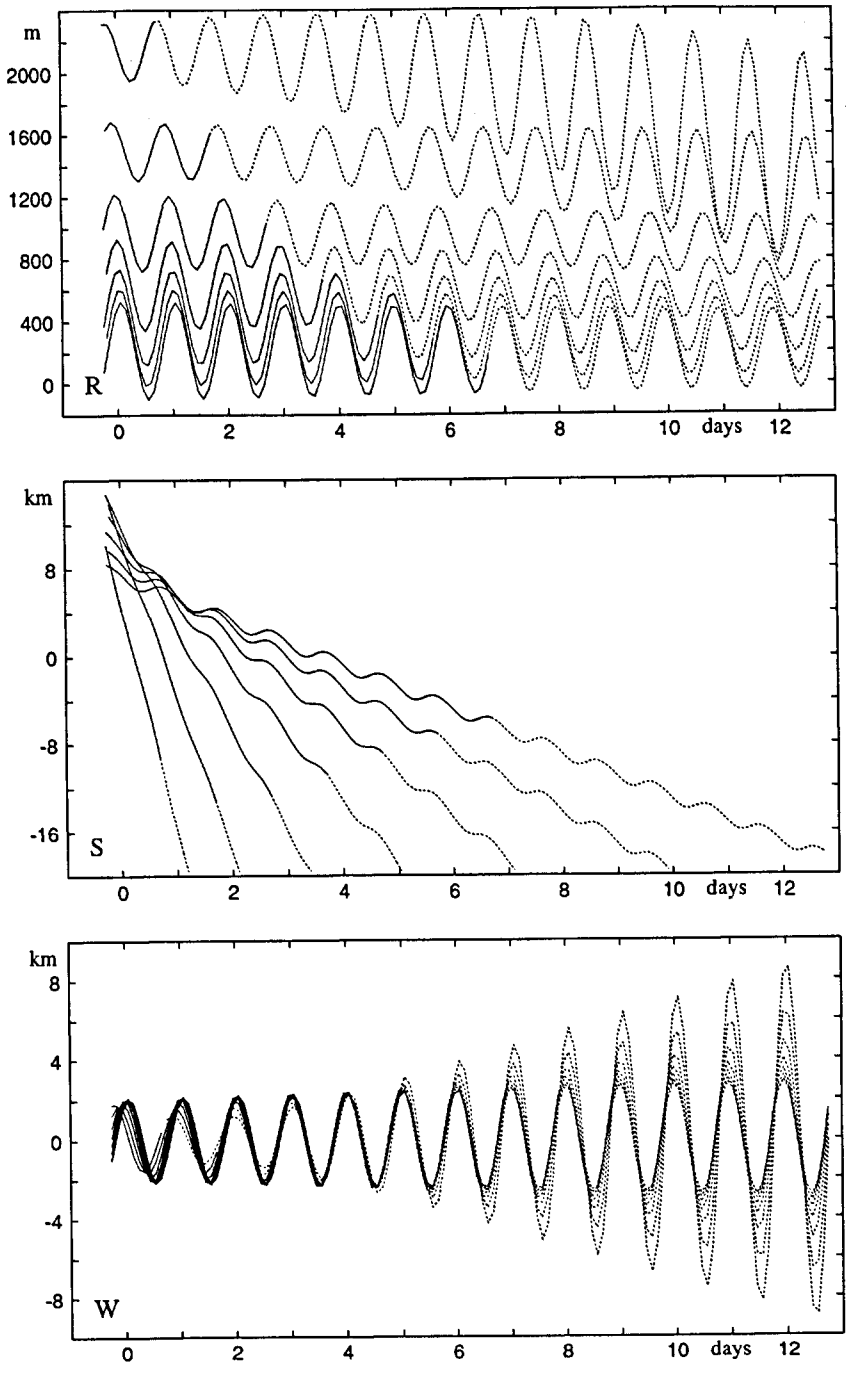

Figure 6.6: Systematic difference of orbits determined from observations with a range rate offset of -2.5 cm/s, in radial (top), alongtrack (center), and crosstrack (bottom) direction as a function of time. The curves correspond to observation time intervals of 1 to 7 days; the solid part of the lines corresponds to the observation interval, the dotted part to the extrapolation in the 13-day interval.

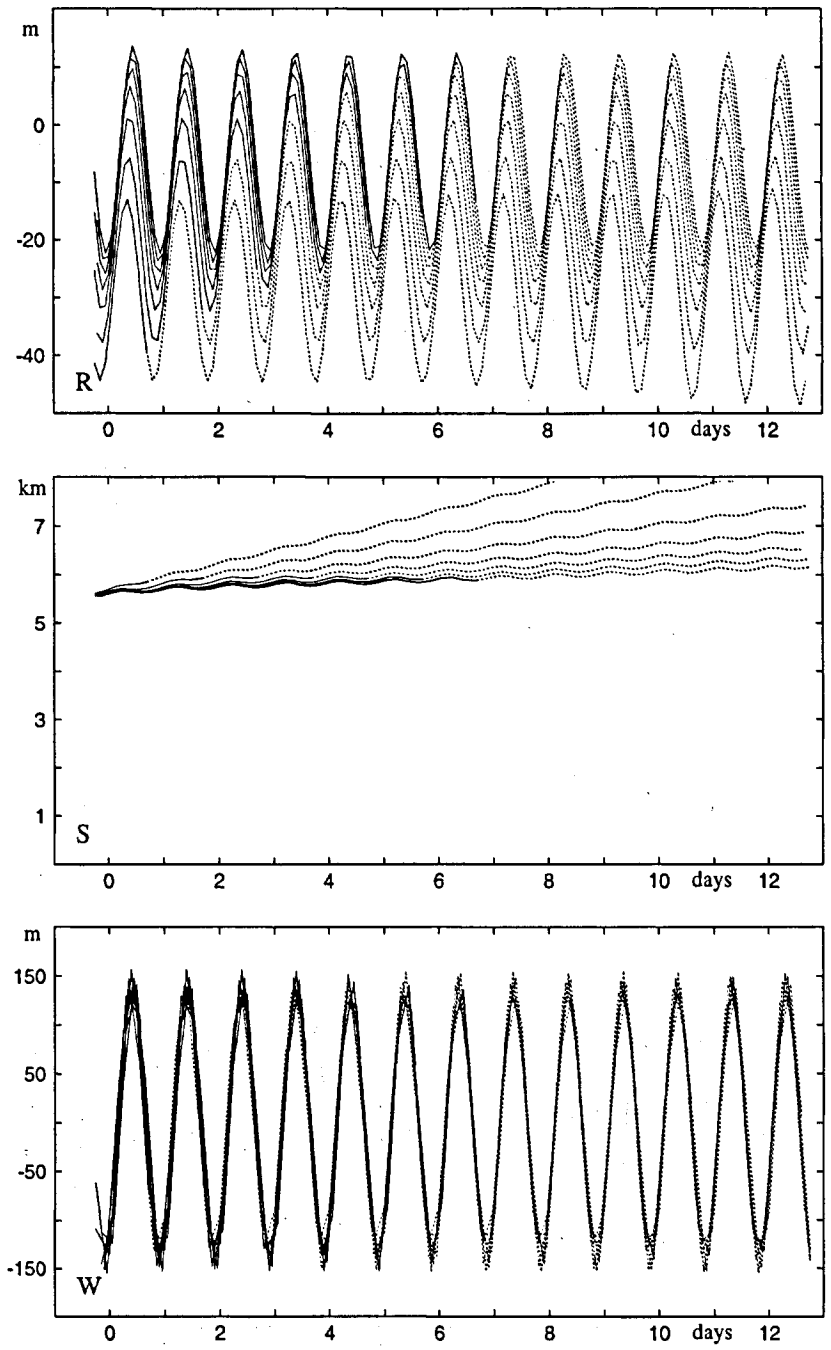

Figure 6.7: Systematic difference of orbits determined from observations with an azimuth offset of 0.01°, in radial (top), alongtrack (center), and crosstrack (bottom) direction as a function of time. The curves correspond to observation time intervals of 1 to 7 days; the solid part of the lines corresponds to the observation interval, the dotted part to the extrapolation in the 13-day interval.

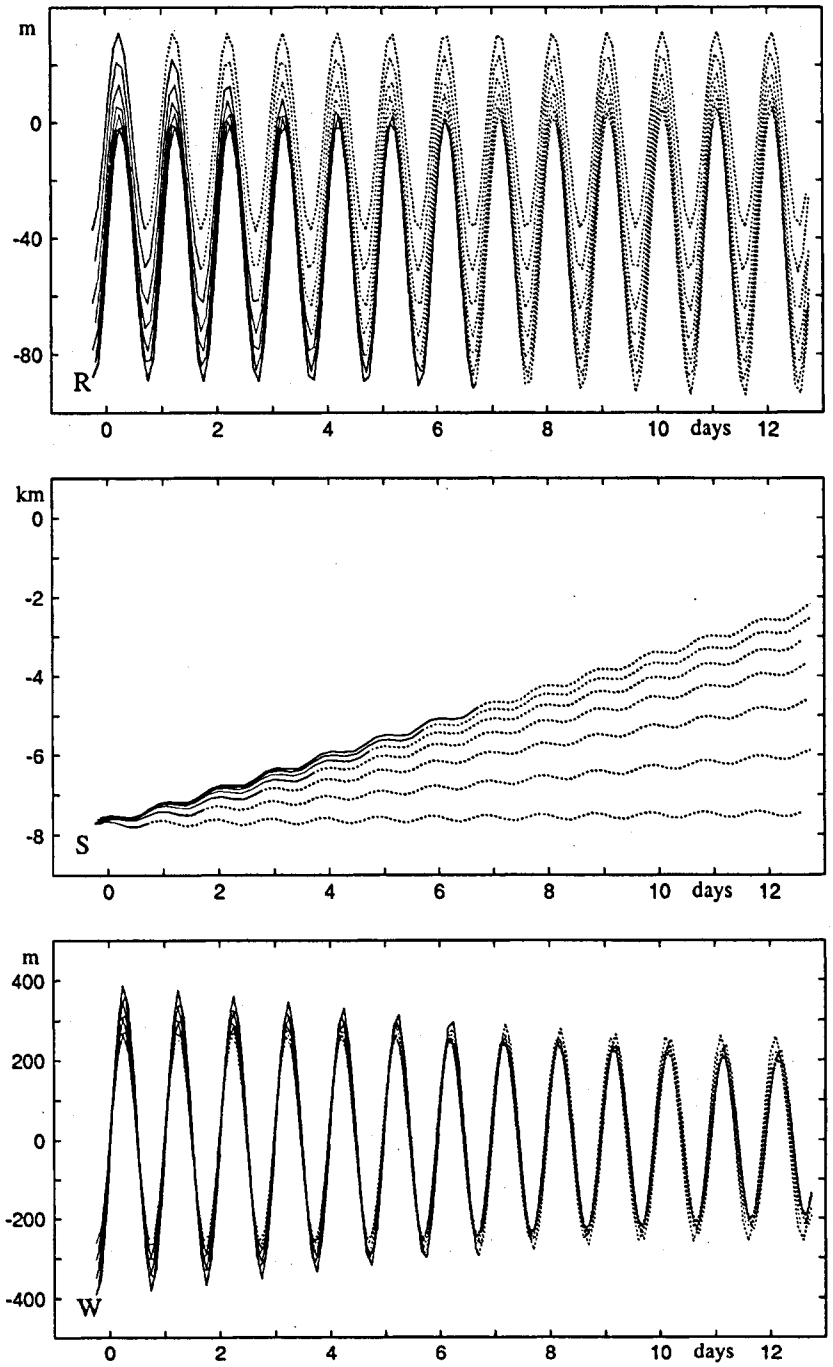

Figure 6.8: Systematic difference of orbits determined from observations with an elevation offset of 0.02°, in radial (top), alongtrack (center), and crosstrack (bottom) direction as a function of time. The curves correspond to observation time intervals of 1 to 7 days; the solid part of the lines corresponds to the observation interval, the dotted part to the extrapolation in the 13-day interval.

A Transformation Formulae

A.1 Different Sets of Orbital Elements and Transformation of Derivatives

The orbit determination program allows it to use Keplerian orbital elements as well as so-called nonsingular elements as orbit parameters for orbits with small eccentricites and/or small inclinations. Several types of nonsingular elements are defined in the literature. The nonsingular element set used in our programs are

$$\begin{aligned} \ell &= \Omega + \omega + \sigma & \varpi &= \Omega + \omega \\ h_1 &= e \cdot \sin \varpi & k_1 &= e \cdot \cos \varpi \\ h_2 &= \sin i \cdot \sin \Omega & k_2 &= \sin i \cdot \cos \Omega \end{aligned}$$

where i is the orbital inclination, Ω is the R.A. of the ascending node, ω the argument of perigee, and σ the mean anomaly at the osculation epoch. ℓ is the mean longitude at the same epoch and ϖ is the longitude of the perigee. Keplerian and nonsingular elements may be 'mixed', the combinations which may be used in the programs are

Element set 1:	a,	e,	i,	Ω,	ω,	σ,
Element set 2:	a,	e,	i,	Ω,	ω,	ℓ,
Element set 3:	a,	e,	i,	Ω,	ϖ,	ℓ,
Element set 4:	a,	h_1,	k_1,	i,	Ω,	ℓ,
Element set 5:	a,	e,	ϖ,	h_2,	k_2,	ℓ,
Element set 6:	a,	h_1,	k_1,	h_2,	k_2,	ℓ.

When setting up the first design matrix in the orbit determination process the partial derivatives of the observations with respect to the parameters have to be computed. I.e., the partial derivatives of satellite position and velocity with respect to the elements of the selected element set are required. Below, the transformation of the partial derivatives of a vector with respect to the Keplerian elements to the partials with respect to the five other element (and vice versa) sets are given.

- Transformation of partials from $(a, e, i, \Omega, \omega, \sigma) \longrightarrow (a', e', i', \Omega', \omega', \ell)$

$$\begin{aligned}
\frac{\partial}{\partial a'} &= \frac{\partial}{\partial a} & \frac{\partial}{\partial a} &= \frac{\partial}{\partial a'} \\
\frac{\partial}{\partial e'} &= \frac{\partial}{\partial e} & \frac{\partial}{\partial e} &= \frac{\partial}{\partial e'} \\
\frac{\partial}{\partial i'} &= \frac{\partial}{\partial i} & \frac{\partial}{\partial i} &= \frac{\partial}{\partial i'} \\
\frac{\partial}{\partial \Omega'} &= \frac{\partial}{\partial \Omega} - \frac{\partial}{\partial \sigma} & \frac{\partial}{\partial \Omega} &= \frac{\partial}{\partial \Omega'} + \frac{\partial}{\partial \ell} \\
\frac{\partial}{\partial \omega'} &= \frac{\partial}{\partial \omega} - \frac{\partial}{\partial \sigma} & \frac{\partial}{\partial \omega} &= \frac{\partial}{\partial \omega'} + \frac{\partial}{\partial \ell} \\
\frac{\partial}{\partial \ell} &= \frac{\partial}{\partial \sigma} & \frac{\partial}{\partial \sigma} &= \frac{\partial}{\partial \ell}
\end{aligned}$$

- Transformation of partials from $(a, e, i, \Omega, \omega, \sigma) \longrightarrow (a', e', i', \Omega', \varpi, \ell)$

$$\begin{aligned}
\frac{\partial}{\partial a'} &= \frac{\partial}{\partial a} & \frac{\partial}{\partial a} &= \frac{\partial}{\partial a'} \\
\frac{\partial}{\partial e'} &= \frac{\partial}{\partial e} & \frac{\partial}{\partial e} &= \frac{\partial}{\partial e'} \\
\frac{\partial}{\partial i'} &= \frac{\partial}{\partial i} & \frac{\partial}{\partial i} &= \frac{\partial}{\partial i'} \\
\frac{\partial}{\partial \Omega'} &= \frac{\partial}{\partial \Omega} - \frac{\partial}{\partial \omega} & \frac{\partial}{\partial \Omega} &= \frac{\partial}{\partial \Omega'} + \frac{\partial}{\partial \varpi} + \frac{\partial}{\partial \ell} \\
\frac{\partial}{\partial \varpi} &= \frac{\partial}{\partial \omega} - \frac{\partial}{\partial \sigma} & \frac{\partial}{\partial \omega} &= \frac{\partial}{\partial \varpi} + \frac{\partial}{\partial \ell} \\
\frac{\partial}{\partial \ell} &= \frac{\partial}{\partial \sigma} & \frac{\partial}{\partial \sigma} &= \frac{\partial}{\partial \ell}
\end{aligned}$$

- Transformation of partials from $(a, e, i, \Omega, \omega, \sigma) \longrightarrow (a', h_1, i', \Omega', k_1, \ell)$

$$\begin{aligned}
\frac{\partial}{\partial a'} &= \frac{\partial}{\partial a} & \frac{\partial}{\partial a} &= \frac{\partial}{\partial a'} \\
\frac{\partial}{\partial h_1} &= \sin\varpi \frac{\partial}{\partial e} + \frac{1}{e}\cos\varpi\left(\frac{\partial}{\partial \omega} - \frac{\partial}{\partial \sigma}\right) & \frac{\partial}{\partial e} &= \sin\varpi \frac{\partial}{\partial h_1} + \cos\varpi \frac{\partial}{\partial k_1} \\
\frac{\partial}{\partial i'} &= \frac{\partial}{\partial i} & \frac{\partial}{\partial i} &= \frac{\partial}{\partial i'} \\
\frac{\partial}{\partial \Omega'} &= \frac{\partial}{\partial \Omega} - \frac{\partial}{\partial \omega} & \frac{\partial}{\partial \Omega} &= \frac{\partial}{\partial \Omega'} + e\cos\varpi \frac{\partial}{\partial h_1} - e\sin\varpi \frac{\partial}{\partial k_1} + \frac{\partial}{\partial \ell} \\
\frac{\partial}{\partial k_1} &= \cos\varpi \frac{\partial}{\partial e} - \frac{1}{e}\sin\varpi\left(\frac{\partial}{\partial \omega} - \frac{\partial}{\partial \sigma}\right) & \frac{\partial}{\partial \omega} &= e\cos\varpi \frac{\partial}{\partial h_1} - e\sin\varpi \frac{\partial}{\partial k_1} + \frac{\partial}{\partial \ell} \\
\frac{\partial}{\partial \ell} &= \frac{\partial}{\partial \sigma} & \frac{\partial}{\partial \sigma} &= \frac{\partial}{\partial \ell}
\end{aligned}$$

- Transformation of partials from $(a, e, i, \Omega, \omega, \sigma) \longrightarrow (a', e', h_2, k_2, \varpi, \ell)$

$$\begin{aligned}
\frac{\partial}{\partial a'} &= \frac{\partial}{\partial a} \\
\frac{\partial}{\partial e'} &= \frac{\partial}{\partial e} \\
\frac{\partial}{\partial h_2} &= \frac{\sin\Omega}{\cos i}\frac{\partial}{\partial i} + \frac{\cos\Omega}{\sin i}\left(\frac{\partial}{\partial\Omega} - \frac{\partial}{\partial\omega}\right) \\
\frac{\partial}{\partial k_2} &= \frac{\cos\Omega}{\cos i}\frac{\partial}{\partial i} - \frac{\sin\Omega}{\sin i}\left(\frac{\partial}{\partial\Omega} - \frac{\partial}{\partial\omega}\right) \\
\frac{\partial}{\partial \varpi} &= \frac{\partial}{\partial\omega} - \frac{\partial}{\partial\sigma} \\
\frac{\partial}{\partial \ell} &= \frac{\partial}{\partial\sigma}
\end{aligned}$$

- Transformation of partials from $(a, e, i, \Omega, \omega, \sigma) \longrightarrow (a', h_1, h_2, k_2, k_1, \ell)$

$$\begin{aligned}
\frac{\partial}{\partial a'} &= \frac{\partial}{\partial a} \\
\frac{\partial}{\partial h_1} &= \sin\varpi\frac{\partial}{\partial e} + \frac{1}{e}\cos\varpi\left(\frac{\partial}{\partial\omega} - \frac{\partial}{\partial\sigma}\right) \\
\frac{\partial}{\partial k_1} &= \cos\varpi\frac{\partial}{\partial e} - \frac{1}{e}\sin\varpi\left(\frac{\partial}{\partial\omega} - \frac{\partial}{\partial\sigma}\right) \\
\frac{\partial}{\partial h_2} &= \frac{\sin\Omega}{\cos i}\frac{\partial}{\partial i} + \frac{\cos\Omega}{\sin i}\left(\frac{\partial}{\partial\Omega} - \frac{\partial}{\partial\omega}\right) \\
\frac{\partial}{\partial k_2} &= \frac{\cos\Omega}{\cos i}\frac{\partial}{\partial i} - \frac{\sin\Omega}{\sin i}\left(\frac{\partial}{\partial\Omega} - \frac{\partial}{\partial\omega}\right) \\
\frac{\partial}{\partial \ell} &= \frac{\partial}{\partial\sigma}
\end{aligned}$$

and

$$\begin{aligned}
\frac{\partial}{\partial a} &= \frac{\partial}{\partial a'} \\
\frac{\partial}{\partial e} &= \sin\varpi\frac{\partial}{\partial h_1} + \cos\varpi\frac{\partial}{\partial k_1} \\
\frac{\partial}{\partial i} &= \cos i\sin\Omega\frac{\partial}{\partial h_2} + \cos i\cos\Omega\frac{\partial}{\partial k_2} \\
\frac{\partial}{\partial\Omega} &= e\cos\varpi\frac{\partial}{\partial h_1} - e\sin\varpi\frac{\partial}{\partial k_1} + \sin i\cos\Omega\frac{\partial}{\partial h_2} - \sin i\sin\Omega\frac{\partial}{\partial k_2} + \frac{\partial}{\partial\ell} \\
\frac{\partial}{\partial\omega} &= e\cos\varpi\frac{\partial}{\partial h_1} - e\sin\varpi\frac{\partial}{\partial k_1} + \frac{\partial}{\partial\ell} \\
\frac{\partial}{\partial\sigma} &= \frac{\partial}{\partial\ell}
\end{aligned}$$

A.2 Jacobian Matrices for Transformations of the Covariance Matrix

The Jacobian matrices J, which may be used e.g., for the transformation of covariance matrices from one parameter set to another, are given below for the transformations from the Keplerian elements to the five other element sets and vice versa.

- The Jacobian matrix of the transformation $(a, e, i, \Omega, \omega, \sigma) \longrightarrow (a', e', i', \Omega', \omega', \ell)$ reads

$$\frac{\partial(a', e', i', \Omega', \omega', \ell)}{\partial(a, e, i, \Omega, \omega, \sigma)} = \begin{pmatrix} 1 & 0 & 0 & 0 & 0 & 0 \\ 0 & 1 & 0 & 0 & 0 & 0 \\ 0 & 0 & 1 & 0 & 0 & 0 \\ 0 & 0 & 0 & 1 & 0 & 0 \\ 0 & 0 & 0 & 0 & 1 & 0 \\ 0 & 0 & 0 & 1 & 1 & 1 \end{pmatrix}$$

and the Jacobian matrix of the inverse transformation $\sigma \longrightarrow \ell$

$$\frac{\partial(a, e, i, \Omega, \omega, \sigma)}{\partial(a', e', i', \Omega', \omega', \ell)} = \begin{pmatrix} 1 & 0 & 0 & 0 & 0 & 0 \\ 0 & 1 & 0 & 0 & 0 & 0 \\ 0 & 0 & 1 & 0 & 0 & 0 \\ 0 & 0 & 0 & 1 & 0 & 0 \\ 0 & 0 & 0 & 0 & 1 & 0 \\ 0 & 0 & 0 & -1 & -1 & 1 \end{pmatrix}$$

- The Jacobian matrix of the transformation $(a, e, i, \Omega, \omega, \sigma) \longrightarrow (a', e', i', \Omega', \varpi, \ell)$ reads

$$\frac{\partial(a', e', i', \Omega', \varpi, \ell)}{\partial(a, e, i, \Omega, \omega, \sigma)} = \begin{pmatrix} 1 & 0 & 0 & 0 & 0 & 0 \\ 0 & 1 & 0 & 0 & 0 & 0 \\ 0 & 0 & 1 & 0 & 0 & 0 \\ 0 & 0 & 0 & 1 & 0 & 0 \\ 0 & 0 & 0 & 1 & 1 & 0 \\ 0 & 0 & 0 & 1 & 1 & 1 \end{pmatrix}$$

and for the inverse transformation $\sigma \longrightarrow \ell$

$$\frac{\partial(a, e, i, \Omega, \omega, \sigma)}{\partial(a', e', i', \Omega', \varpi, \ell)} = \begin{pmatrix} 1 & 0 & 0 & 0 & 0 & 0 \\ 0 & 1 & 0 & 0 & 0 & 0 \\ 0 & 0 & 1 & 0 & 0 & 0 \\ 0 & 0 & 0 & 1 & 0 & 0 \\ 0 & 0 & 0 & -1 & 1 & 0 \\ 0 & 0 & 0 & 0 & -1 & 1 \end{pmatrix}$$

- The Jacobian matrix for the transformation $(a, e, i, \Omega, \omega, \sigma) \longrightarrow (a', h_1, i', \Omega', k_1, \ell)$ reads

$$\frac{\partial(a', h_1, i', \Omega', k_1, \ell)}{\partial(a, e, i, \Omega, \omega, \sigma)} = \begin{pmatrix} 1 & 0 & 0 & 0 & 0 & 0 \\ 0 & \sin\varpi & 0 & e\cos\varpi & e\cos\varpi & 0 \\ 0 & 0 & 1 & 0 & 0 & 0 \\ 0 & 0 & 0 & 1 & 0 & 0 \\ 0 & \cos\varpi & 0 & -e\sin\varpi & -e\sin\varpi & 0 \\ 0 & 0 & 0 & 1 & 1 & 1 \end{pmatrix}$$

and for the inverse transformation $e, \omega \longrightarrow h_1, k_1$

$$\frac{\partial(a, e, i, \Omega, \omega, \sigma)}{\partial(a', h_1, i', \Omega', k_1, \ell)} = \begin{pmatrix} 1 & 0 & 0 & 0 & 0 & 0 \\ 0 & \sin\varpi & 0 & 0 & \cos\varpi & 0 \\ 0 & 0 & 1 & 0 & 0 & 0 \\ 0 & 0 & 0 & 1 & 0 & 0 \\ 0 & +\frac{1}{e}\cos\varpi & 0 & -1 & -\frac{1}{e}\sin\varpi & 0 \\ 0 & -\frac{1}{e}\cos\varpi & 0 & 0 & +\frac{1}{e}\sin\varpi & 1 \end{pmatrix}$$

- The Jacobian matrix for the transformation $(a, e, i, \Omega, \omega, \sigma) \longrightarrow (a', e', h_2, k_2, \varpi, \ell)$ reads

$$\frac{\partial(a', e', h_2, k_2, \varpi, \ell)}{\partial(a, e, i, \Omega, \omega, \sigma)} = \begin{pmatrix} 1 & 0 & 0 & 0 & 0 & 0 \\ 0 & 1 & 0 & 0 & 0 & 0 \\ 0 & 0 & \cos i \sin\Omega & \sin i \cos\Omega & 0 & 0 \\ 0 & 0 & \cos i \cos\Omega & -\sin i \sin\Omega & 0 & 0 \\ 0 & 0 & 0 & 1 & 1 & 0 \\ 0 & 0 & 0 & 1 & 1 & 1 \end{pmatrix}$$

and for the inverse transformation $i, \Omega \longrightarrow h_2, k_2$

$$\frac{\partial(a, e, i, \Omega, \omega, \sigma)}{\partial(a', e', h_2, k_2, \varpi, \ell)} = \begin{pmatrix} 1 & 0 & 0 & 0 & 0 & 0 \\ 0 & 1 & 0 & 0 & 0 & 0 \\ 0 & 0 & \sin\Omega/\cos i & \cos\Omega/\cos i & 0 & 0 \\ 0 & 0 & \cos\Omega/\sin i & -\sin\Omega/\sin i & 0 & 0 \\ 0 & 0 & -\cos\Omega/\sin i & \sin\Omega/\sin i & 1 & 0 \\ 0 & 0 & 0 & 0 & -1 & 1 \end{pmatrix}$$

- The Jacobian matrix for the transformation $(a, e, i, \Omega, \omega, \sigma) \longrightarrow (a', h_1, h_2, k_2, k_1, \ell)$ reads

$$\frac{\partial(a', h_1, h_2, k_2, k_1, \ell)}{\partial(a, e, i, \Omega, \omega, \sigma)} = \begin{pmatrix} 1 & 0 & 0 & 0 & 0 & 0 \\ 0 & \sin\varpi & 0 & e\cos\varpi & e\cos\varpi & 0 \\ 0 & 0 & \cos i \sin\Omega & \sin i \cos\Omega & 0 & 0 \\ 0 & 0 & \cos i \cos\Omega & -\sin i \sin\Omega & 0 & 0 \\ 0 & \cos\varpi & 0 & -e\sin\varpi & -e\sin\varpi & 0 \\ 0 & 0 & 0 & 1 & 1 & 1 \end{pmatrix}$$

and for the inverse transformation $e, i, \Omega, \omega \longrightarrow h_1, k_1, h_2, k_2$

$$\frac{\partial(a,e,i,\Omega,\omega,\sigma)}{\partial(a',h_1,h_2,k_2,k_1,\ell)} = \begin{pmatrix} 1 & 0 & 0 & 0 & 0 & 0 \\ 0 & \sin\varpi & 0 & 0 & \cos\varpi & 0 \\ 0 & 0 & \sin\Omega/\cos i & \cos\Omega/\cos i & 0 & 0 \\ 0 & 0 & \cos\Omega/\sin i & -\sin\Omega/\sin i & 0 & 0 \\ 0 & +\frac{1}{e}\cos\varpi & -\cos\Omega/\sin i & \sin\Omega/\sin i & -\frac{1}{e}\sin\varpi & 0 \\ 0 & -\frac{1}{e}\cos\varpi & 0 & 0 & +\frac{1}{e}\sin\varpi & 1 \end{pmatrix}$$

The transformations between the six element sets used in the context of this work are performed by the subroutine ODETRF, the transformations of the derivatives of vectors with respect to the different elements by the subroutine ODDTRF, and the transformation of the covariance matrix to different sets of elements by the subroutine ODQTRF.

B Combining Arcs Separated by a Manœuver

The formulae for combining consecutive arcs of a satellite orbit at the normal equation level are derived in Beutler et al. (1996b). Because — in contrast to the cited paper — not the special perturbation equations are used for the transformation of the partial derivatives at the manœuver epoch, the procedure used is shortly outlined in this appendix. The iterative procedure applied for combining two arcs of the satellite Meteosat 4 is discussed in section 3.1.4 and 5.4.

Given the two arcs described by the orbital element vectors $E_1|$ and $E_2|$ with osculation epochs t_1 and t_2 respectively and the dynamical parameters $q_1|$ and $q_2|$ (e.g. the radiation pressure coefficients):

$$\text{arc 1:} \quad p_1| = \{E_1|, q_1|\}, \qquad \text{arc 2:} \quad p_2| = \{E_2|, q_2|\}. \tag{B.1}$$

We assume that for both arcs an independent parameter determination is performed using the method of least squares. Starting with the a priori parameters $p_{10}|$ and $p_{20}|$ the corrections $\Delta p_1|$ and $\Delta p_2|$ are computed by solving the normal equation systems (NEQS)

$$\boldsymbol{N}_i \cdot \Delta p_i| = b_i| \qquad \text{for arc } i{=}1{,}2 \tag{B.2}$$

where

$\boldsymbol{N}_i = \boldsymbol{A}_i^T \cdot \boldsymbol{P}_i \cdot \boldsymbol{A}_i$ is the NEQS matrix of arc i,

$b_i| = \boldsymbol{A}_i^T \cdot \boldsymbol{P}_i \cdot \Delta\Phi_i|$ is the right hand side of the NEQS of arc i,

$\boldsymbol{A}_i$ is the fist design matrix,

$\boldsymbol{P}_i$ is the weight matrix matrix, and

$\Delta\Phi_i|$ is the (column-)matrix containing the values *observed − computed.*

We assume that the satellite performed a manœuver at epoch t_c. The manœuver shall be described by an instantaneous velocity change $\Delta\boldsymbol{v}$. Therefore the condition equations applied for connecting the two arcs are

$$\begin{aligned} \boldsymbol{r}_2(t_c) &= \boldsymbol{r}_1(t_c) \\ \boldsymbol{v}_2(t_c) &= \boldsymbol{v}_1(t_c) + \Delta\boldsymbol{v} \\ q_2| &= q_1| \quad . \end{aligned} \tag{B.3}$$

We write the first two equations (B.3) in the form of 6-component vectors (the first three elements containing the position vectors, the last three elements the velocity vectors)

$$r_2|(t_c) = r_1|(t_c) + \Delta r| = r_1|(t_c) + \boldsymbol{R}s| \tag{B.4}$$

where $s|$ represents the velocity change at t_c in the RSW-system which is transformed by the 6x3-matrix $\boldsymbol{R}$ into the xyz-system (computed from $r_1|$). Linearizing eq. (B.3) then gives

$$\begin{aligned} r_{20}|(t_c) + \left(\frac{\partial r_2}{\partial E_2}(t_c)\right) \Delta E_2| + \left(\frac{\partial r_2}{\partial q_2}(t_c)\right) \Delta q_2| &= \\ = r_{10}|(t_c) + \left(\frac{\partial r_1}{\partial E_1}(t_c)\right) \Delta E_1| + \left(\frac{\partial r_1}{\partial q_1}(t_c)\right) \Delta q_1| + \boldsymbol{R} s_0| + \boldsymbol{R} \Delta s| & \\ q_{20}| + \Delta q_2| = q_{10}| + \Delta q_1| \quad . & \end{aligned}$$

Eliminating $q_2|$ from the first equation and solving for $\Delta E_2|$ gives finally

$$\begin{aligned} \Delta E_2| &= \boldsymbol{H}_2^{-1} \boldsymbol{H}_1 \Delta E_1| + \boldsymbol{H}_2^{-1} (\boldsymbol{Q}_1 - \boldsymbol{Q}_2) \Delta q_1| + \boldsymbol{H}_2^{-1} \boldsymbol{R} \Delta s| + \\ &\quad + \boldsymbol{H}_2^{-1} \left[(r_{10}| - r_{20}|) - \boldsymbol{Q}_2 (q_{10}| - q_{20}|) + \boldsymbol{R} s_0| \right] \\ \Delta q_2| &= \Delta q_1| + (q_{10}| - q_{20}|) \end{aligned} \tag{B.5}$$

with the Jacobian matrices

$$\boldsymbol{H}_i = \left(\frac{\partial r_i}{\partial E_i}(t_c)\right) \qquad \boldsymbol{Q}_i = \left(\frac{\partial r_i}{\partial q_i}(t_c)\right) \quad . \tag{B.6}$$

Eq. (B.6) may be written in the compact form

$$\Delta p_2| = \boldsymbol{B}_{21} \Delta p_1'| + \Delta \rho_{21}| \tag{B.7}$$

with the parameter set $p_1'| = \{E_1|, q_1|, s|\}$, i.e. extended by the manœuver parameters. We have therefore expressed the corrections $\Delta p_2|$ of the parameters $p_2|$ of arc 2 by the corrections $\Delta p_1'|$ of the parameter set $p_1'|$. The NEQS for the new parameter set reads

$$\boldsymbol{N}_1' \cdot \Delta p_1'| = b_1'| \tag{B.8}$$

with

$$\begin{aligned} \boldsymbol{N}_1' &= \boldsymbol{B}_{21}^T \boldsymbol{N}_2 \boldsymbol{B}_{21} \\ b_1'| &= \boldsymbol{B}_{21}^T (b_2| - \boldsymbol{N}_2 \Delta \rho_{21}|) \end{aligned}$$

and after this transformation we may add the NEQS (B.8) and the NEQS (B.2) for arc 1. The result is a NEQS for the corrections $\Delta E|$, $\Delta q|$, and $\Delta s|$ for the combined arc.

C Radiation Pressure Model for the Meteosat Satellites

A simple radiation pressure model for the Meteosat satellites was proposed by Veillet et al. (1990). The satellite body is represented by three coaxial cylinders with dimensions as sketched in Figure C.1.

For each surface of the cylinders the coefficients are defined for diffuse scattering of light (d) and for specular reflection (s). Together with the absorption coefficient a the following identity holds

$$a + d + s = 1.$$

The radiation pressure acting on a plane surface tilted by an angle Θ to the incident light may be decomposed in a component parallel to the direction of the incident light $p_{\|}$ and a component orthogonal to it $p_{\perp}$

$$p_{\|} = \frac{S_{\odot}}{c} \cos\Theta \left[a + d + 2s\cos^2\Theta + \frac{2}{3} d \cos\Theta \right] \tag{C.1}$$

$$p_{\perp} = \frac{S_{\odot}}{c} \cos\Theta \left[\quad 2s\cos\Theta\sin\Theta + \frac{2}{3} d \sin\Theta \right] \tag{C.2}$$

where $S_{\odot}$ is the solar constant and c the velocity of light. The first term $a + d$ in the first equation describes the effect of light that is absorbed (either permanently or diffusely

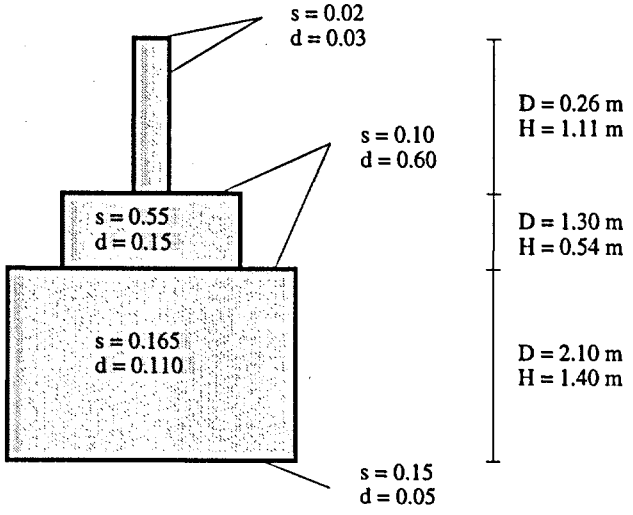

Figure C.1: Simple model for the Meteosat satellites proposed by Veillet et al. (1990). The satellite body is represented by three coaxial cylinders. For each surface the diffuse (d) and specular (s) reflection coefficient is given. Dimensions from Ferrand (1996).

re-emitted). The second term describes the acceleration due to specularly reflected light and the last term that of the diffused light.

For a cylinder with its symmetry axis inclined by the angle $\pi - \Theta$ relative to the incident light the radiation pressure may be decomposed as follows

$$p_{\parallel} = \frac{S_{\odot}}{c} \cos\Theta \left[a + d + \frac{4}{3} s \cos^2\Theta + \frac{\pi}{6} d \cos\Theta \right] \tag{C.3}$$

$$p_{\perp} = \frac{S_{\odot}}{c} \cos\Theta \left[\frac{4}{3} s \cos\Theta \sin\Theta + \frac{\pi}{6} d \sin\Theta \right]. \tag{C.4}$$

For a spherical object only a radiation pressure in the direction of the incident light exists

$$p_{\parallel} = \frac{S_{\odot}}{c} \left(1 + \frac{4}{9} d \right)$$

which depends only on the coefficient of diffusion of light for the surface.

Using the simple model presented at the beginning of the section and eqns. (C.1) to (C.4) the components of the radiation pressure parallel and orthogonal to the incident light may be computed. Because the symmetry axis of the satellite is very close to both, the rotation axis and the normal to the orbital plane, the incident angle of the light on all surfaces of the satellite can be obtained for any time. In addition, shadowing effects due to other parts of the satellite are taken into account.

As a result an 'effective' cross section of the satellite can be given as a function of the position of the Sun which corresponds to the cross section an ideally absorbing body would have to sense the same radiation pressure force. In Fig. C.2 this effective surface is given as a function of time for the direction parallel and orthogonal to the incident light together with the geometrical cross section of the satellite as viewed from the direction of the sun. The important differences to a simple model based on perfect absorption and fixed cross section consists of the increased value, the variation with time, and the existence of an orthogonal component.

For the orthogonal component the sign is defined to be positive if the force is acting northwards and negative when acting southwards. In Fig. C.2 we can see that the orthogonal component is negative or zero for all times (with the antenna of the satellite pointing northwards). This may be understood in the following way (see Fig. C.3, bottom left):

While the Sun is illuminating the satellite from 'below' the force acting on the lower surface due to specular reflection and diffusion pushes the satellite in northward direction while the forces acting on the cylindrical surfaces are perpendicular to the satellite's symmetry axis and has therefore a component pointing southwards relative to the direction of the incident light. According to the model the two effects nearly cancel if the Sun is below the orbital plane while the effect due to the flat upper surfaces outweighs the counteracting effect from the cylindrical surfaces. This asymmetry is due to the different optical properties of the upper and the lower surfaces of the satellite.

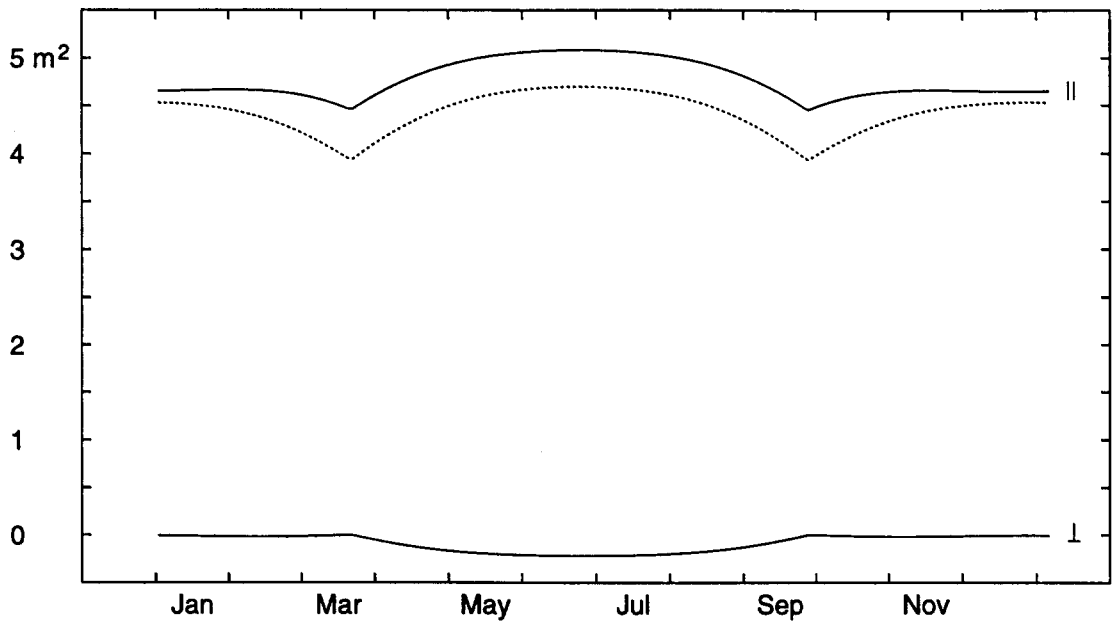

Figure C.2: Effective cross section for the direction parallel (||) and orthogonal (⊥) to the incident light and geometrical cross section (dotted line) according to the Meteosat radiation pressure model as a function of time.

In Fig. C.3 (right) the acceleration contributions due to permanent absorption, specular reflection, and diffusion of light are given. The absorption is the dominant effect for the direct radiation pressure (up to 80% of the total effect). Diffusion of light plays only a minor role for the parallel component. For the orthogonal component, on the other hand, the dominant effect is due to the diffusion of light whereas absorption has no effect.

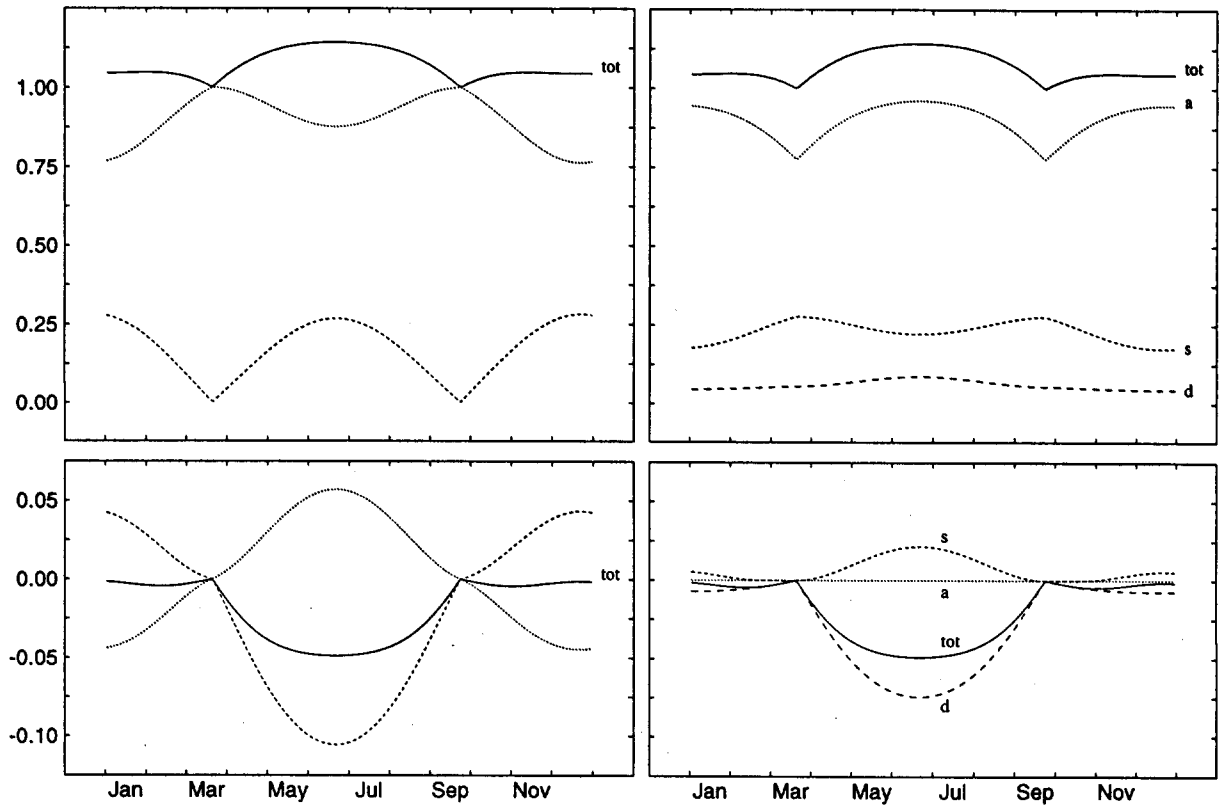

Figure C.3: Radiation pressure force sensed by the Meteosat satellites relative to the force sensed by a perfectly absorbing satellite as a function of time for the parallel component (top) and the orthogonal component (bottom). Left: Decomposition of the force into the parts due to the cylindrical surfaces (dotted lines) and to the upper and lower flat surfaces (dashed lines). Right: Decomposition of the force due to absorption (a), specular reflection (s), and diffused light (d). The total effect is given in all figures by the solid line.

Abbreviations

ABM	Apogee Boost Motor.
ACRS	Astrographic Catalogue Reference Stars.
AIUB	Astronomical Institute of the University of Berne.
BMK	Ballistische Messkamera.
CCD	Charge Coupled Device.
CDP	Crustal Dynamics Project.
CMC	Carlsberg Meridian Catalogue, astrometric catalogue (CMC, 1984).
COGEOS	International Campaign for Optical Observations for Geostationary Satellites, research project for geodynamic purposes.
COSPAR	Committee on Space Research.
CQSSP	Coupled Quasar, Satellite, and Star Positioning.
DASA	Deutsche Aerospace AG.
ESA	European Space Agency.
ESOC	European Space Operations Centre.
ESTEC	European Space Research and Technological Centre.
FGAN-FHP	Forschungsgesellschaft für Angewandte Naturwissenschaften e. V. – Forschungsinstitut für Hochfequenzphysik; Research Establishment for Applied Science – Research Institute for High Frequency Physics.
FK5	Fifth Fundamental Catalogue, fundamental astrometric catalogue defining the stellar reference frame.
FOV	Field of View.
GEM	Goddard Earth Model.
GEO	Geostationary Orbit.
GEODSS	Ground Electro-Optical Deep Space System.
GLONASS	Global Navigation Satellite System.

GMST	Greenwich Mean Sidereal Time.
GPS	Global Positioning Sytem.
GSFC	Goddard Space Flight Center.
GTO	Geostationary Transfer Orbit.
HA	Hour Angle.
HEO	Highly Elliptical Orbit.
HIPPARCOS	High Precision Parallax Collecting Satellite.
IAU	International Astronomical Union.
IERS	International Earth Rotation Service.
IGS	International GPS Service for Geodynamics.
INTEGRAL	International Gamma-Ray Astrophysics Laboratory.
ISO	Infra-red Space Observatory.
IUE	International Ultraviolet Explorer.
JGM	Joint Gravity Model.
JPL	Jet Propulsion Laboratory, Pasadena.
MEO	Medium Earth Orbit.
MTO	Medium Earth Transfer Orbit.
NASA	National Aeronautical and Space Administration.
NASDA	National Space Development Agency of Japan.
NGS	National Geodetic Survey.
NEQS	Normal Equation System.
NNSS	Navy Navigation Satellite System.
PAGEOS	Passive Geodetic Satellite.
PPM	Positions and Proper Motion astrometric catalogue (CMC, 1984).
RA	Right Ascension.
RAE	Royal Aerospace Establishment.

RCS	Radar Cross-Section.
RSA	Russian Space Agency.
SAO	Smithsonian Astrophysical Observatory.
SLR	Satellite Laser Ranging.
SNR	Signal-to-Noise Ratio.
SSN	Space Surveillance Network.
TIRA	Tracking and Imaging Radar.
TLE	Two Line Elements.
USSPACECOM	U.S. Space Command.
VLBI	Very Long Baseline Interferometry.
WEST	West European Satellite Triangulation.
ZIMLAT	Zimmerwald Laser Ranging and Astrometry Telescope (1 m).

Acknowledgements

I would like to thank Dr. D. Mehrholz from the Forschungsgesellschaft für angewandte Naturwissenschaften (FGAN), Wachtberg-Werthhoven, Germany, for providing Radar observations of geostationary satellites, Dr. M. Ploner from the Technical University Vienna, Austria, for his astrometric observations of Meteosat 5 and Meteosat 6 at Graz-Lustbühel, Dr. J. Klokočknik for fruitful discussions at the Ondřejov observatory, Czech Republic, Prof. G. Beutler for his support of this work as well as helpful discussions and comments, and, last but not least, for reviewing the manuscript and helping to translate it into readable English, and Dr. W. Gurtner for his final review of the text and comments. The work was supported by the Swiss National Science Foundation in the context of the project 'Satellite Geodesy and Fundamental Astronomy' (NSF grant nr. '20-40'933.94'). Funds for printing this volume were provided by the Swiss Academy of Sciences.

References

Abramowitz, M., I. A. Stegun (1965): 'Handbook of Mathematical Functions'. Applied Mathematics Series-55, National Bureau of Standards, U.S. Dept. of Commerce. Reprint Dover publications, inc., New York, p. 589ff.

Allan, R. R. (1963): 'Perturbations of Geostationary Satellite by the Longitude-Dependent Terms in the Earth Gravitational Field', *Planet. Space Sci.*, **11**, pp. 1325–1334.

Allan, R. R., G. E. Cook (1964): 'The Long-Period Motion of the Plane of a Distant Circular Orbit'. *Proc. Roy. Soc. London*, **280A**, pp. 97–109.

Allen, C. W. (1973): 'Astrophysical Quantities'. Third edition, Athlone Press, London, §56, p. 126.

Appleby, G., P. Gibbs (1995): 'Precise Optical Observations of Geostationary Satellites from Herstmonceux'. In *Proceedings of the Workshop: Accurate Orbit Determination and Observation of High Earth Satellites for Geodynamics*, A. Elipe et al. (Eds.), Cahiers du Centre Européen de Géodynamique et de Séismologie, Vol. 10, Luxembourg, pp. 3–9.

Appleby, G. (1995), private communication.

Ariane 4 User's Manual (1995). Arianespace, Evry, France.

Batyr, G., S. Veniaminov, V. Dicky, V. Yurasov (1993): 'The Current State of Russian Space Surveillance System and its Capability in Surveying Space Debris'. In *Proceedings of the First European Conference on Space Debris* (ESA SD-01), W. Flury (Ed.), Darmstadt, Germany, April 5–7, 1993, pp. 43–47.

Bauersima, I. (1984): 'Coupled Quasar, Satellite, and Star Positioning (CQSSP).' Mitteilungen der Satelliten-Beobachtungsstation Zimmerwald, Nr. 13, Universität Bern.

Beutler, G., M. Rothacher, U. Hugentobler (1987): 'First Orbit Determination from the Point of View of Modern Parameter Estimation'. Manuscript, University of Bern.

Beutler, G. (1990): 'Numerische Integration gewöhnlicher Differentialgleichungssysteme: Prinzipien und Algorithmen'. Mitteilungen der Satelliten-Beobachtungsstation Zimmerwald, Nr. 23, Universität Bern.

Beutler, G., A. Verdun (1992): 'Himmelsmechanik II: Der Erdnahe Raum'. Mitteilungen der Satelliten-Beobachtungsstation Zimmerwald, Nr. 28, Universität Bern.

Beutler, G. (1996): 'GPS Satellite Orbits'. In *GPS for Geodesy*, A. Kleusberg et al. (Eds.), Springer-Verlag, Berlin, Heidelberg, New York, pp. 37–101.

Beutler, G., I. I. Mueller, R. E. Neilan (1996a): 'The International GPS Service for Geodynamics (IGS): The Story'. In *GPS Trends in Precise Terrestrial, Airborne, and Apaceborne Applications*, G. Beutler et al. (Eds.), International Association of Geodesy Symposia, No. 115, Springer-Verlag, Berlin, Heidelberg, New York, pp. 3–13.

Beutler, G., E. Brockmann, U. Hugentobler , M. Mervart, M. Rothacher, R. Weber (1996b): 'Combining Consecutive Short Arcs Into Long Arcs for Precise and Efficient GPS Orbit Determination'. *J. of Geodesy*, **70**, pp. 287–299.

Blitzer, L. (1962): 'Effect of Ellipticity of the Equator on 24-Hour Nearly Circular Satellite Orbits'. *J. Geophys. Res.*, **67**, pp. 329–335.

Böhme, C. Eckardt, H. Potthoff (1995): 'Optical Observations of Geosynchronous Satellites — Results'. In *Proceedings of the Workshop: Accurate Orbit Determination and Observation of High Earth Satellites for Geodynamics*, A. Elipe et al. (Eds.), Cahiers du Centre Européen de Géodynamique et de Séismologie, Vol. 10, Luxembourg, pp. 29–36.

Brockmann, E. (1996): 'Combination of Solutions for Geodetic and Geodynamic Applications of the Global Positioning System (GPS)'. Ph.D. thesis, Druckerei der Universität Bern.

Chamberlain, S. A., T. A. Slauenwhite (1993): 'United States Space Command Space Surveillance Network Overview'. In *Proceedings of the First European Conference on Space Debris* (ESA SD-01), W. Flury (Ed.), Darmstadt, Germany, April 5–7, 1993, pp. 37–42.

Catalano, S., R. McCrosky, A. Milani, A. M. Nobili (1983): 'Optical Tracking of Synchronous Earth's Satellites for Geophysical Purposes'. *J. Geophys. Res.*, **88**, pp. 669–676.

Catalogue of the Carlsberg Meridian Circle, 1984–1990, Copenhagen University Observatory, Royal Greenwich Observatory, Istituto y Observatorio de Marina, La Palma.

Catastini, G., F. Blesa, A. M. Nobili, A. Rossi (1995): 'Analysis of ESOC range data to METEOSAT satellites with ORBIT10'. In *Proceedings of the Workshop: Accurate Orbit Determination and Observation of High Earth Satellites for Geodynamics*, A. Elipe et al. (Eds.), Cahiers du Centre Européen de Géodynamique et de Séismologie, Vol. 10, Luxembourg, pp. 55–62.

Clausen, K., C. Winkler (1994): 'Integral — A Challenging Scientific Mission'. *ESA Bulletin*, **79**, pp. 6–13.

Corbin, T. E., S. E. Urban (1991): 'Astrographic Catalogue Reference Stars'. U. S. Naval Observatory, Washington D. C.

Duma, D. P., Yu. N. Ivashchenko, Yu. Shokin (1986): 'An Experiment in the Determination of High-Precision Coordinates for Geostytionary Earth Satellites using a Wide-Angle Astrograph and a Special Plate Holder'. *Kinematika i Fizika Nebesnykh Tel*, **2**, No. 2, pp. 86–88.

Ferrand, G., (1996), ESTEC, private communication.

Fliegel, H. F., T. E. Gallini, E. R. Swift (1992): 'Global Positioning System Radiation Force Model for Geodetic Applications'. *J. Geophys. Res.*, **97**, pp. 559–568.

Flury, W. (1991): 'Collision Probability and Spacecraft Disposition in the Geostationary Orbit'. *Adv. Space Res.*, **11**, No. 12, pp. 67–79.

Flury, W. (1994): 'Vorlesung Raumfahrtmechanik'. Technische Hochschule Darmstadt.

Fricke, W., H. Schwan, T. Lederle, U. Bastian, R. Bien, G. Burkhardt, B. du Mont, R. Herint, R. Jährling, H. Jahreiss, S. Röser, H. M. Schwerdtfeger, H. G. Walter (1988): *Fifth Fundamental Catalogue (FK5), Part I. The Basic Fundamental Stars.* Veröff. Astron. Rechen-Institut Heidelberg No. 32.

Fricke, W., H. Schwan, T. Corbin, U. Bastian, R. Bien, C. Cole, E. Jackson, R. Jährling, H. Jahreiss, T. Lederle, S. Röser (1991): *Fifth Fundamental Catalogue (FK5), Part II. The FK5 Extension — New Fundamental Stars.* Veröff. Astron. Rechen-Institut Heidelberg No. 33.

Gooding, R. H., D. G. King-Hele (1989): 'Explicite Forms of Some Functions Arising in the Analysis of Resonant Satellite Orbits'. *Proc. Roy. Soc. London*, **422A**, pp. 241–259.

Grigoriev, K. V., A. S. Sochilina, A. N. Vershkov (1993): 'On Catalogue of Geostationary Satellites'. In *Proceedings of the First European Conference on Space Debris* (ESA SD-01), W. Flury (Ed.), Darmstadt, Germany, April 5–7, 1993, pp. 665–669.

Gurtner, W., E. Pop, J. Utzinger, T. Schildknecht, J. Barbe (1996): 'The New Laser and Astrometric Telescope in Zimmerwald'. In *Proceedings of Tenth International Workshop on Laser Ranging Instrumentation*, Shanghai, China, November 10–15, 1996.

Høg, E., U. Bastian, J. L. Halbwachs, F. van Leeuwen, L. Lindegren, V. V. Makarov, H. Pedersen, C. S. Petersen, P. Schwekendiek, K. Wagner, A. Wicenec (1995): 'Tycho Astrometry from Half of the Mission'. Astron. Astrophys., **304**, pp. 150–159.

Hugentobler, U., G. Beutler (1993): 'Resonance Phenomena in the Global Positioning System'. In *Dynamics and Astrometry of Natural and Artificial Celestial Bodies*, K. Kurzynska et al. (Eds.), Posnan, pp. 347–352.

Hugentobler, U., T. Schildknecht, A. Verdun (1995): 'CCD Astrometry of Geostationary Satellites at the Zimmerwald Observatory'. In *Proceedings of the Workshop: Accurate Orbit Determination and Observation of High Earth Satellites for Geodynamics*, A. Elipe et al. (Eds.), Cahiers du Centre Européen de Géodynamique et de Séismologie, Vol. 10, Luxembourg, pp. 23–28.

Hugentobler, U., T. Schildknecht, G. Beutler, (1996): 'Determination of Resonance Terms Using Optical Observations of Two Meteosat Satellites'. In IAU Colloquium 165 on *Dynamics and Astrometry of Natural and Artificial Celestial Bodies*, I. Wytrzyszczak et al. (Eds.), Posnan, in press.

IERS Standards (1992), D. McCarthy (Ed.), Central Bureau of IERS, Observatoire de Paris.

Interagency Report on Orbital Debris (1995), Office of Science and Technology Policy, The National Science and Technology Council.

Ivashchenko, Yu. N. (1989): 'Methods and Results of Observations of Geostationary Artificial Satellites with the Satellite Plateholder SKA-2'. *Kinematika i Fizika Nebesnykh Tel*, **5**, No. 2, pp. 16–22.

Janin, G. (1994): 'Lifetime of Ariane Third Stages on Geostationary Transfer Orbit'. In *Proceedings of the 19th ISTS*, Yokohama, Japan, May 15–24, 1994.

Janin, G. (1996): 'Log of Objects near the Geostationary Ring'. Issue 16, ESOC, February 1996.

Kardos, I., P. Pâquet, A. Drozyner (1995): 'Status Report on Geostationary Satellite Positioning by Time Measurements'. In *Proceedings of the Workshop: Accurate Orbit Determination and Observation of High Earth Satellites for Geodynamics*, A. Elipe et al. (Eds.), Cahiers du Centre Européen de Géodynamique et de Séismologie, Vol. 10, Luxembourg, pp. 11–22.

Kaula, W. M. (1966): *Theory of Satellite Geodesy.* Blaisdell Publ. Co., Waltham.

Kessler, D. J. (1993): 'Orbital Debris Environment'. In *Proceedings of the First European Conference on Space Debris* (ESA SD-01), W. Flury (Ed.), Darmstadt, Germany, April 5–7, 1993, pp. 251–262.

Kessler, M. F., A. Heske, C. Metcalfe, A. Salama (1991): 'The ISO Mission – A Scientific Overview'. *ESA Bulletin*, **67**, pp. 8–16.

Khan, M. (1993): 'The critically Inclined 16-Hour Orbit: 'An Unconventional Option for Improved Telecommunications on the Northern Hemisphere'. In *Dynamics and Astrometry of Natural and Artificial Celestial Bodies*, K. Kurzynska et al. (Eds.), Posnan, pp. 359–364.

Klokocnik, J. (1983): 'Orbital Rates of Earth Satellites at Resonances to Test the Accuracy of Earth Gravity Field Models'. *Celestial Mechanics*, **30**, pp. 407–422.

Klokocnik, J. (1988): 'Geopotential Research Mission (GRM): A Contribution to the Assessment of Orbit Accuracy, Orbit Determination and Gravity Field Modelling'. *Bull. Astron. Inst. Czechosl.*, **39**, pp. 45–67.

Klokocnik, J. (1991): 'A Note on Generalized Lumped Coefficients'. *Bull. Astron. Inst. Czechosl.*, **42**, pp. 389–392.

Kostelecky, J., J. Klokocnik (1982): 'Collocations and Thiertieth Order Resonant Harmonics'. *Planet. Space Sci.*, **31**, No.8, pp. 829–841.

Kovalevsky, J. (1961), First Int. Symposium on Analytical Astrodynamics, UCLA.

Kovalevsky, J., L. Lindegren, M. Froeschlé, F. van Leeuwen, M. A. C. Perryman, J. L. Falin, F. Mignard, M. J. Penston, C. Petersen, P. L. Bernacca, B. Bucciarelli, F. Donati, R. Hering, E. Høg, M. Lattanzi, H. van der Marel, H. Schrijver, H. G. Walter (1995): 'Construction of the Intermediate Hipparcos Astrometric Catalogue'. Astron. Astrophys., **304**, pp. 34–43.

Laplace, P. S. (1805): *Méchanique céleste.* Tome IV.

Macchetto, F., M. V. Penston (1978): 'The International Ultraviolet Explorer'. *ESA Bulletin*, **13**, pp. 9–14.

Massart, A. (1995), private communication.

Massart, A., G. Janin, W. Flury (1997): 'ESA's Use of the 1m Zeiss Telescope for Space Debris Observations'. In *Proceedings of the Second European Conference on Space Debris*, W. Flury (Ed.), Darmstadt, Germany, March 17–19, 1997, SP-393, pp. 105–110.

Mehrholz, D. (1993): 'Potentials and Limits of Space Object Observations and Data Analyses Using Radar Techniques'. In *Proceedings of the First European Conference on Space Debris* (ESA SD-01), W. Flury (Ed.), Darmstadt, Germany, April 5–7, 1993, pp. 59–64.

Mehrholz, D. (1995): 'Radar Detection of Mid-Size Debris'. *Adv. Space Res.*, **16**, No. 11, W. Flury (Ed.), pp. 17–27.

Mehrholz, D., L. Leushacke, U. Uschkerat, T. Schildknecht, U. Hugentobler (1997): 'Experimenteller Servicing Satellit-T, AP2000: Anflugziel, Anflug'. Forschungs- und Entwichlungsvertrag DJO/FGAN-2510/94. Wachtberg-Werthhoven.

Mehrholz, D. (1997): 'Radar Observations of Geosynchronous Orbits'. In *Proceedings of the Second European Conference on Space Debris*, W. Flury (Ed.), Darmstadt, Germany, March 17–19, 1997, SP-393, pp. 51–58.

Milani, A., A. M. Nobili, P. Farinella (1987): *Non-Gravitational Perturbations and Satellite Geodesy.* Adam Hilger, Bristol.

Morando, M. B. (1962): 'Libration d'un Satellite de 24h'. *Compt. rend.*, **254**, pp. 635–637.

Nauer, D. J. (1995): 'History of On-Orbit Satellite Fragmentation'. 9th edition, Teledyne Brown Engeneering.

Nobili, A. M. (1987): 'An International Campaign for Optical Observations of Geosynchronous Satellites (COGEOS): Scientific Aims and Organization'. *CSTG Bulletin*, **9**, pp. 19–30.

Orbital Debris — A Technical Assessment (1995), National Academy of Science, National Academy Press, Washington, D.C.

Ploner, M. (1996): 'CCD-Astrometrie von Objekten des geostationären Ringes'. Ph.D. thesis, *Geowissenschaftliche Mitteilungen*, **46**, Technische Universität Wien.

Plotkin, H. H., T. S. Johnson, P. Spadin, J. Moye (1965): 'Reflection of Ruby Laser Radiation from Explorer XXII'. *Proc. IEEE*, **53**, No. 7, pp. 301–302.

Potter, A. E. (1995): 'Ground-Based Optical Observations of Orbital Debris: A Review'. *Adv. Space Res.*, **16**, No. 11, pp. 35–45.

Potter, A. E., M. Mulrooney (1996): 'Optical Observations of Orbital Debris with the 3-Meter Liquid Metal Mirror Telescope'. In *Proceedings of the 31-th COSPAR Scientific Assebmly*, Birmingham, United Kingdom, to appear in *Adv. Space Res.*

Röser, S., U. Bastian (1991): *PPM Star Catalogue.* Astronomisches Rechen-Institut Heidelberg, Spektrum Akademischer Verlag, Heidelberg, Berlin, New York.

Rossi, A. (1988): 'ORBIT4 Simulations of the COGEOS Campaign'. First COGEOS Workshop, Pisa, February 11–12, 1988.

Rothacher, M. (1992): 'Orbits of Satellite Sytems in Space Geodesy'. *Geodätisch-geophysikalische Arbeiten in der Schweiz*, Vol. 46.

Rudenko, S. (1995): 'Software for the Analysis of Photographic Observations of Geosynchronous Satellites'. In *Proceedings of the Workshop: Accurate Orbit Determination and Observation of High Earth Satellites for Geodynamics*, A. Elipe et al. (Eds.), Cahiers du Centre Européen de Géodynamique et de Séismologie, Vol. 10, Luxembourg, pp. 63–70.

Schildknecht, T., U. Hugentobler, A. Verdun (1992): 'Optical Astrometry of Fast Moving Objects'. In *Proceedings of the Second International Workshop on Positional Astrometry and Celestial Mechanics*, A. Lopez Garcia et al. (Eds.), Valencia, pp. 321–325.

Schildknecht, T., U. Hugentobler, A. Verdun (1993): 'CCD Astrometry of Artificial Satellites'. In *Dynamics and Astrometry of Natural and Artificial Celestial Bodies*, K. Kurzynska et al. (Eds.), Poznan, pp. 103–108.

Schildknecht, T. (1994): 'Optical Astrometry of Fast Moving Objects Using CCD Detectors'. *Geodätisch-geophysikalische Arbeiten in der Schweiz*, Vol. 49.

Schildknecht, T., U. Hugentobler, A. Verdun, G. Beutler (1995a): 'CCD Algorithms for Space Debris Detection'. ESA Study Final Report (ESA/ESOC Contract No. 10623/93/D/IM).

Schildknecht, T., U. Hugentobler, A. Verdun (1995b): 'Algorithms for Ground Based Optical Detection of Space Debris'. *Adv. Space Res.*, **16**, No. 11, W. Flury (Ed.), pp. 47–50.

Schildknecht, T., U. Hugentobler, A. Verdun (1995c): 'Algorithms for Ground Based Optical Detection of Space Debris in GEO and GTO'. In *Proceedings of the First International Workshop on Space Debris*, Moscow, Russia, October 9 to 11, 1995.

Schildknecht, T., U. Hugentobler, A. Verdun (1996a): 'Algorithms for Optical Detection of Fast Moving Objects'. In *Proceedings of the Third International Workshop on Positional Astronomy and Celestial Mechanics*, A. Lopez Garcia et al. (Eds.), Cuenca, pp. 71–85.

Schildknecht, T., U. Hugentobler, A. Verdun (1996b): 'Optical Observations of Space Debris with the Zimmerwald 1 m Telescope'. In *Proceedings of the 31-th COSPAR Scientific Assebmly*, Birmingham, United Kingdom, to appear in *Adv. Space Res.*

Schmid, H. H. (1974): 'Worldwide Geometric Satellite Triangulation'. *J. Geophys. Res.*, **79**, pp. 5349–5476.

Sehnal, L. (1960): 'The Perturbations of the Orbit of the Stationary Satellite of the Earth'. *Bull. Astron. Inst. Czech.*, **11**, pp. 132–135.

Silva, D. R., M. E. Cornell (1992): 'A New Library of Stellar Optical Spectra'. *Astrophys. J. Suppl.*, **81**, pp. 865–881.

Sochilina, A. S., R. I. Kiladze, K. V. Grigoriev, A. N. Vershkov (1996): *Catalog of orbit of Geostationary Satellites.* Institute for Theoretical Astronomy of the Academy of Science of Russia, St. Petersburg.

Soop, E. M. (1994): *Handbook of Geostationary Orbits.* Kluwer Academic Publishers, Dortrecht, Boston, London.

Talent, D., T. Settecerri, A. Potter, K. Henize (1997): 'Report on the NASA/Schmidt GEO Survey Program'. In *Proceedings of the Second European Conference on Space Debris*, W. Flury (Ed.), Darmstadt, Germany, March 17–19, 1997.

Tapley, B. D., M. M. Watkins, J. C. Ries, G. W. Davis, R. J. Eanes, S. R. Poole, H. J. Rim, B. E. Schutz, C. K. Shum, R. S. Nerem, F. J. Lerch, J. A. Marshall, S. M. Klosko, N. K. Pavlis, R. G. Williamson (1996): 'The Joint Gravity Model 3'. *J. Geophys. Res.*, **101**, No. B12., pp. 28,029–28,049.

TELAS (1992): 'Zimmerwald 1 Meter Laser / Astrometric Telescope'. Rapport final de l'étude de définition. Technical report, TELAS.

Tisserand, F. (1888): *Traité de Mécanique Céleste.* New ed., Gauthier-Villars, Paris 1960, Vol I, p. 249ff.

U.S. Standard Atmosphere (1976), Washington D.C., U.S. Government Printing Office.

Veillet, Ch., G. Metris, Y. Boudon (1990): 'Status Report of Cerga/OCA'. Third COGEOS Workshop, Brussels, June 11–12, 1990.

Veis, G. (1963): 'The Precision Optical Satellite Tracking Net of the Smithsonian Astrophysical Observatory'. In *The Use of Artificial Satellites for Geodesy*, G. Veis (Ed.), North-Holland Publishing Company, Amsterdam, pp. 141–145.

Verdun, A. (1993): 'Objekterkennung und Zentroidbestimmung bei CCD-Richtungsbeobachtungen'. *Bericht Nr. 22 der Satelliten-Beobachtungsstation Zimmerwald*, Druckerei der Universität Bern.

Vilhena de Moraes, R., K. T. Fitzgibbon, M. Konemba (1995): 'Influence of the 2:1 Resonance in the Orbits of GPS Satellites'. *Adv. Space Res.*, **16**, No. 12, pp. 37–40.

Wagner, C. A. (1965): 'A Determination of Earth Equatorial Ellipticity from Seven Months of Syncom 2 Longitude Drift'. *J. Geophys. Res.*, **70**, pp. 1566–1568.

"Geodätisch-geophysikalische Arbeiten in der Schweiz"

(Fortsetzung der Publikationsreihe "Astronomisch-geodätische Arbeiten in der Schweiz") der Schweizerischen Geodätischen Kommission (ab Bd. 39):

39 1989 125 Jahre Schweizerische Geodätische Kommission
I. Bedeutung geodätischer Raumverfahren für Landesvermessung und Geodynamik. (R. Sigl)
II. Beitrag der Geodäsie zur Geodynamik. (H.-G. Kahle)
III. L'état actuel de la recherche sur les movements de l'écorce terrestre en Suisse. (F. Jeanrichard)
IV. Die Satellitengeodäsie im Dienste der globalen Geodynamik. (I. Bauersima)
V. Die Veranstaltungen zum 125 Jahr-Jubiläum der Schweizerischen Geodätischen Kommission. (W. Fischer). 62 Seiten.

40 1989 Integrale Schwerefeldbestimmung in der Ivrea- Zone und deren geophysikalische Interpretation. B. Bürki. 186 Seiten.

41 1990 ALGESTAR satellitengestützte Geoidbestimmung in der Schweiz. U. Marti. 61 Seiten plus Punktprotokolle.

42 1990 Höhensysteme, Schwerepotentiale und Niveauflächen: Systematische Untersuchungen zur zukünftigen terrestrischen und GPS-gestützten Höhenbestimmung in der Schweiz. B. Wirth. 204 Seiten.

43 1990 Gravimetrisches Geoid der Schweiz: Potentialtheoretische Untersuchungen zum Schwerefeld im Alpenraum. A. Geiger. 231 Seiten.

44 1991 Rapid Differential Positioning with the Global Positioning System (GPS). E. Frei. 178 Seiten.

45 1992 Dreidimensionales Testnetz Turtmann 1985-1990 Teil I. F. Jeanrichard (Hrsg.) Autoren: A.Geiger, H.-G. Kahle, R. Köchle, D. Meier, B. Neininger, D. Schneider, B. Wirth. 183 Seiten.

46 1993 Orbits of Satellite Systems in Space Geodesy. M. Rothacher. 243 Seiten.

47 1993 NFP 20. Beitrag der Geodäsie zur geologischen Tiefenstruktur und Alpendynamik. H.-G. Kahle (Hrsg.) Autoren: I. Bauersima, G. Beutler, B. Bürki, M. Cocard, A. Geiger, E. Gubler, W. Gurtner, H.-G. Kahle, U. Marti, B. Mattli, M. Rothacher, Th. Schildknecht, D. Schneider, A. Wiget, B. Wirth. 153 Seiten plus 90 Seiten Anhang.

48 1994 Ionosphere and Geodetic Satellite Systems: Permanent GPS Tracking Data for Modelling and Monitoring: Urs Wild, 155 Seiten.

49 1994 Optical Astrometry of Fast Moving Objects using CCD Detectors: Thomas Schildknecht, 200 Seiten.

50 1995 Geodätische Alpentraverse Gotthard: A. Elmiger, R. Köchle, A. Ryf und F. Chaperon. 214 Seiten.

51 1995 Dreidimensionales Testnetz Turtmann 1985-1993, Teil II (GPS-Netz). F. Jeanrichard (Hrsg.) Autoren: G. Beutler, A. Geiger, M. Rothacher, Stefan Schaer, D. Schneider, A. Wiget, 173 Seiten.

52 1995 High Precision GPS Processing in Kinematic Mode: M. Cocard. 139 Seiten.

53 1995 Ambiguity Resolution Techniques in Geodetic and Geodynamic Applications of the Global Positioning System. L. Mervart. 155 Seiten.

54 1997 SG 95: Das neue Schweregrundnetz der Schweiz: F. Arnet und E. Klingelé. 37 Seiten.

55 1997 Combination of Solutions for Geodetic and Geodynamic Applications of the Global Positioning System (GPS). Elmar Brockmann, 211 Seiten.

56 1997 Geoid der Schweiz 1997. Urs Marti, 140 Seiten.

57 1998 Astrometry and Satellite Orbits: Theoretical Considerations and Typical Applications. Urs Hugentobler, 209 Seiten.